
Novel Cavity Optomechanical Systems at the Micro- and Nanoscale and Quantum Measurements of Nanomechanical Oscillators

Georg Anetsberger



München 2010

Novel Cavity Optomechanical Systems at the Micro- and Nanoscale and Quantum Measurements of Nanomechanical Oscillators

Georg Anetsberger

Dissertation
an der Fakultät für Physik
der Ludwig–Maximilians–Universität
München

vorgelegt von
Georg Anetsberger
aus Landshut

München, den 9. November 2010

Erstgutachter: Prof. Dr. T. W. Hänsch

Zweitgutachter: Prof. Dr. J. P. Kotthaus

Tag der mündlichen Prüfung: 22. Dezember 2010

*In Erinnerung an
Johann Beck und
Georg Niedermaier.*

Contents

Table of Contents	vii
List of Publications	xi
List of Conference Contributions	xiii
List of Figures	xv
Zusammenfassung	xvii
Abstract	xix
1 Introduction	1
1.1 Cavity optomechanics	2
1.1.1 Linear Hamiltonian of cavity optomechanical systems	3
1.1.2 Quantum Langevin equations	5
1.1.3 Standard quantum limit of continuous position measurements	9
1.1.4 Radiation pressure force - dynamical backaction	15
1.1.4.1 Radiation pressure cooling	17
1.1.4.2 Heating and amplification	19
1.1.5 Optical spring effect	20
1.2 Toroid microresonators and their optical properties	23
1.2.1 Optical mode profile	23
1.2.2 Optical mode volume	26
1.2.3 Tapered fibre coupling	27
2 Near-field cavity optomechanics	29
2.1 Theoretical characterization of the optomechanical coupling	35
2.1.1 Perturbation theory	35
2.1.2 Analytic approximation for toroid microresonators	36
2.1.2.1 Micromechanical membrane	37
2.1.2.2 Nanomechanical string	39
2.1.3 Comparison to finite element modelling results	40
2.2 Static measurement of the optomechanical coupling	43

2.2.1	Dispersive optomechanical coupling	43
2.2.2	Simultaneous coupling to several optical modes	46
2.3	Transduction and actuation of nanomechanical motion	49
2.3.1	Effective mass of the nanomechanical oscillators	49
2.3.2	Transduction of Brownian motion	52
2.3.3	Radiation pressure actuation	54
2.3.4	Frequency dispersion and mode patterns of nanomechanical oscillators	58
2.3.5	Vacuum optomechanical coupling rate	60
2.4	Dynamical backaction	63
2.4.1	Backaction amplification - parametric instability	63
2.4.2	Radiation pressure cooling	66
2.5	Quantum measurements	69
2.5.1	Measurement techniques	69
2.5.1.1	Titanium-sapphire laser and homodyne measurement	69
2.5.1.2	Fibre laser and Pound-Drever-Hall measurement	72
2.5.2	Classical noise sources	72
2.5.2.1	Thermorefractive noise	72
2.5.2.2	Toroid mechanical modes	74
2.5.3	Sub-SQL imprecision	75
2.5.4	Backaction of the measurement	78
2.6	Optomechanical coupling to multiple optical modes	81
2.6.1	Modal coupling in whispering gallery microresonators	81
2.6.2	Transduction of motion and dynamical backaction using two optical modes	83
2.7	Quadratic optomechanical coupling to nanomechanical oscillators	87
2.8	Prospects for graphene sheets as mechanical oscillators	91
2.8.1	Characterization of graphene membranes	91
2.8.2	Optomechanical coupling of graphene	92
3	Monolithic ultra-low dissipation optomechanical resonators	95
3.1	Optomechanical coupling	95
3.2	Mechanical mode spectrum	97
3.3	General sources of mechanical dissipation	101
3.3.1	Gas damping	101
3.3.2	Clamping losses	101
3.3.3	Two-level systems	102
3.3.4	Thermoelastic damping	103
3.3.5	Phonon-phonon interaction	104
3.4	Clamping losses in toroid microresonators	105
3.5	Design of ultra-low dissipation spoke-supported resonators	109
3.5.1	Room-temperature quality factors	109
3.5.2	Temperature dependence of mechanical Q	110

4	Summary	113
A	Solution of the linearized quantum Langevin equations	115
A.1	Equations for the field quadratures	115
A.2	Solutions for the intracavity field quadratures	116
A.3	Solution for the output field quadratures	116
B	Experimental techniques for near-field cavity optomechanics	119
B.1	Microfabrication techniques	119
B.1.1	Fabrication of toroid near-field sensors	119
B.1.2	Fabrication of nanomechanical oscillators	122
B.2	Experimental setup	124
B.2.1	Compact tapered optical fibres	124
B.2.2	Coupling setup	125
B.3	Homodyne interferometer signal and frequency noise calibration	127
B.3.1	Homodyne signal	127
B.3.2	Frequency noise calibration	128
B.3.2.1	Calibrated phase modulation	128
B.3.2.2	Calibration of frequency noise spectra	129
C	Fabrication of spoke-supported microresonators	133
D	Code for FEM whispering gallery mode simulations	135
	Bibliography	156
	Danksagung	157

List of Publications

Publications during the course of this thesis

- [1] G. Anetsberger and T. J. Kippenberg. Cavity optomechanics at the nanoscale. *in preparation* (2010).
- [2] G. Anetsberger, E. Gavartin, O. Arcizet, Q. P. Unterreithmeier, E. M. Weig, M. L. Gorodetsky, J. P. Kotthaus and T. J. Kippenberg. Measuring nanomechanical motion with an imprecision below the standard quantum limit. *Physical Review A*, in press (2010).
- [3] M. L. Gorodetsky, A. Schliesser, G. Anetsberger, S. Deléglise and T. J. Kippenberg. Determination of the vacuum optomechanical coupling rate using frequency noise calibration. *Optics Express* **18**, 23236 (2010).
- [4] G. Anetsberger, O. Arcizet, Q. P. Unterreithmeier, R. Rivière, A. Schliesser, E. M. Weig, J. P. Kotthaus and T. J. Kippenberg. Near-field cavity optomechanics with nanomechanical oscillators. *Nature Physics* **5**, 909 (2009).
- [5] G. Anetsberger, R. Rivière, A. Schliesser, O. Arcizet and T. J. Kippenberg. Approaching the quantum world with nanospokes. *SPIE Newsroom*, doi: 10.1117/2.1200901.1423 (2009).
- [6] G. Anetsberger, R. Rivière, A. Schliesser, O. Arcizet and T. J. Kippenberg. Ultralow-dissipation optomechanical resonators on a chip. *Nature Photonics* **2**, 627 (2008).
- [7] A. Schliesser*, G. Anetsberger*, R. Rivière, O. Arcizet and T. J. Kippenberg. High-sensitivity monitoring of micromechanical vibration using optical whispering gallery mode resonators. *New Journal of Physics* **10**, 095015 (2008).
- [8] A. Schliesser*, O. Arcizet*, R. Rivière*, G. Anetsberger and T. J. Kippenberg. Resolved-sideband cooling and position measurement of a micromechanical oscillator close to the Heisenberg uncertainty limit. *Nature Physics* **5**, 509 (2009).
- [9] O. Arcizet*, R. Rivière*, A. Schliesser, G. Anetsberger and T. J. Kippenberg. Cryogenic properties of optomechanical silica microcavities. *Physical Review A* **80**, 021803 (2009).

- [10] A. Schliesser, R. Rivière, G. Anetsberger, O. Arcizet and T. J. Kippenberg. Resolved-sideband cooling of a micromechanical oscillator. *Nature Physics* **4**, 415 (2008).

Earlier publications

- [10]. R. Ma, A. Schliesser, P. Del’Haye, A. Dabirian, G. Anetsberger and T. J. Kippenberg. Radiation-pressure driven vibrational modes in ultrahigh-Q silica microspheres. *Optics Letters* **32**, 2200 (2007).
- [11]. R. Morrow, D. McKenzie, M. M. M. Bilek, C. MacDonald, M. Stindt, G. Anetsberger and A. Martin. Electric field effects on adsorption/desorption of proteins and colloidal particles on a gold film observed using surface plasmon resonance. *Physica B* **394**, 203 (2007).

* These authors contributed equally to this work.

List of Conference Contributions

- [1] Conference on Lasers, Electro-Optics, Quantum Electronics and Laser Science (Cleo/Qels). *San José, USA, May 2010*. Optical measurement of nanomechanical motion with an imprecision at the standard quantum limit. *Talk*
- [2] Conference on Lasers, Electro-Optics, Quantum Electronics and Laser Science (Cleo/Qels). *San José, USA, May 2010*. Near-field cavity optomechanics with nanomechanical oscillators. *Talk*
- [3] Gordon Research Conference on Mechanical Systems in the Quantum Regime, *Galveston, USA, Feb 2010*. Near-field cavity optomechanics with nanomechanical oscillators. *Poster*
- [4] 21st Edgar-Lüscher Seminar. *Klosters, Switzerland, February 2010*. Near-field cavity optomechanics with nanomechanical oscillators. *Talk*
- [5] Nanosystems Initiative Munich Workshop (Area D). *Munich, Germany, January 2010*. Near-field nano-optomechanics. *Talk*
- [6] Integrated Photonics and Nanophotonics Research and Applications Topical Meeting. *Honolulu, Hawaii, USA, July 2009*. Cavity optomechanics at the micro- and nanoscale. *Invited Talk*
- [7] European Conference on Lasers, Electro-Optics and Quantum Electronics (Cleo Europe). *Munich, Germany, June 2009*. Cavity nano-optomechanics using optical gradient fields. *Talk*
- [8] European Conference on Lasers, Electro-Optics and Quantum Electronics (Cleo Europe). *Munich, Germany, June 2009*. Ultra-low dissipation optomechanical resonators on a chip. *Invited Talk*
- [9] Conference on Lasers and Electro-Optics and International Quantum Electronics (Cleo/Iqec). *Baltimore, USA, May 2009*. Ultra-low dissipation optomechanical resonators on a chip. *Talk. Winner of the Theodore Maiman Award of the Optical Society of America Foundation*

- [10] Conference on Lasers and Electro-Optics and International Quantum Electronics (Cleo/Iqec). *Baltimore, USA, May 2009*. Cavity nano-optomechanics using optical gradient fields. *Talk*
- [11] Workshop on “Optical detection techniques at the nanoscale”. *University of Konstanz, Germany, April 2009*. Near-field cavity optomechanics with nanomechanical oscillators. *Invited Seminar*
- [12] Nanosystems Initiative Munich workshop (Area D). *Munich, Germany, April 2009*. Near-field cavity optomechanics with nanomechanical oscillators. *Talk*
- [13] Frühjahrstagung der Deutschen Physikalischen Gesellschaft. *Hamburg, Germany, March 2009*. Cavity nano-optomechanics using optical gradient fields. *Talk*
- [14] Ludwig-Maximilians-Universität, Chair of Solid State Physics. *Munich, Germany, Dec 2008*. Cavity optomechanics with toroid microresonators. *Invited Seminar*
- [15] Workshop on “Nanomechanical systems approaching the quantum regime”. *Munich, Sep 2008*. Ultra-low dissipation optomechanical resonators on a chip. *Poster*
- [16] Conference on Lasers and Electro-Optics, Quantum Electronics and Laser Science (Cleo/QELS). *San José, USA, May 2008*. Mechanical dissipation in micromechanical oscillators. *Poster*
- [17] Nanosystems Initiative Munich workshop on “Interactions in Hybrid Nanosystems”. *Frauenwörth, Germany, May 2008*. Ultra-low dissipation optomechanical resonators on a chip. *Poster. Winner of Best Poster Award*
- [18] Gordon Research Conference on Mechanical Systems in the Quantum Regime. *Ventura, USA, Feb 2008*. Ultra-low dissipation optomechanical resonators on a chip. *Poster*

List of Figures

1.1	Output field of a cavity as a function of laser detuning	7
1.2	Standard quantum limit of continuous position measurement	13
1.3	Radiation pressure induced photon-phonon scattering	15
1.4	Dynamical backaction rate	16
1.5	Optical spring effect	21
1.6	Fundamental TE- and TM-like optical modes of toroid microresonators . .	25
1.7	Optical mode volume of toroid microresonators	27
1.8	Tapered fibre coupling to toroid microresonators	27
2.1	Schematic of the experimental principle	30
2.2	Measurement imprecision of nanomechanical motion - approaching and by- passing the SQL	31
2.3	Scanning electron micrograph and optical properties of a toroid microres- onator near-field sensor	32
2.4	Definition of the coupling geometry	38
2.5	Induced optical cavity resonance frequency shift - comparison between ana- lytic model and FEM calculation	40
2.6	Distortion of the profile of TM- and TE-like optical microtoroid modes in- duced by a silicon nitride nanomechanical oscillator in the evanescent field	41
2.7	Experimental coupling coefficients at $\lambda \sim 1550$ nm wavelength	44
2.8	Optomechanical coupling between toroid and silicon nitride nanomechanical oscillator - theory and measurement at ~ 850 nm wavelength	45
2.9	Spatial profile of optical toroid microresonator modes	46
2.10	Avoided crossing and Fano-type interference of optical microresonator modes induced by silicon nitride nanostrings.	47
2.11	Effective mass of a nanomechanical string's eigenmodes	51
2.12	Brownian motion of a nanomechanical string	53
2.13	Experimental setup used for pump-probe measurements	55
2.14	Resonant response of a nanomechanical oscillator to radiation pressure . .	56
2.15	Comparison of static and dynamic optomechanical coupling coefficients . .	57
2.16	Frequency dispersion of a $50 \times 40 \times 0.03 \mu\text{m}^3$ silicon nitride membrane's mechanical eigenmodes.	58
2.17	Mode spectra and patterns of a $40 \times 0.7 \times 0.1 \mu\text{m}^3$ nanomechanical string .	59

2.18	Experimental determination of the vacuum optomechanical coupling rate	61
2.19	Radiation pressure parametric instability of a nanomechanical oscillator	63
2.20	Temporal behaviour of self-sustained oscillations	64
2.21	Threshold power for the onset of self-sustained oscillations	65
2.22	Dynamical backaction cooling and heating of a nanomechanical oscillator	66
2.23	Properties of the employed titanium-sapphire laser system	70
2.24	Homodyne measurement setup	71
2.25	Broadband frequency noise of a toroid microresonator	73
2.26	Measurement imprecision for a nanomechanical string as a function of coupling coefficient	76
2.27	Measurement imprecision below the SQL	77
2.28	Measurement results with respect to the SQL	78
2.29	Optical mode doublet in WGM resonators due to backscattering	82
2.30	Three mode interaction - Experiment	83
2.31	Dynamical backaction via two optical modes.	85
2.32	Quadratic optomechanical coupling to nanomechanical oscillators	88
2.33	Double-layer graphene membrane	92
3.1	Polarization spectroscopy	96
3.2	Mechanical mode spectrum of a toroid microresonator	98
3.3	Dispersion of crown and cantilever modes	99
3.4	Geometry dependence of mechanical Q	106
3.5	Spoke-supported microresonators	109
3.6	Material loss limited optomechanical microresonators	111
3.7	Temperature dependent mechanical Q factors	112
B.1	Fabrication of microcavity near-field sensors	121
B.2	Fabrication of silicon nitride nanomechanical oscillators	122
B.3	Compact tapered optical fibre	124
B.4	Experimental coupling setup for near-field cavity optomechanics	125
B.5	Homodyne interferometer signal	128
B.6	Calibration of the electro-optic phase modulator	130
C.1	Fabrication of spoke supported microresonators	134

Zusammenfassung

Diese Dissertation befasst sich mit der Kopplung optischer Mikroresonatoren an mikro- und nanomechanische Oszillatoren. Die auf Lichtdruck basierende wechselseitige optomechanische Kopplung zwischen Mikroresonator und einem mechanischen Freiheitsgrad, der die räumliche Struktur des Resonators moduliert, ermöglicht dabei, die Bewegung des mechanischen Freiheitsgrads durch das in den Resonator gekoppelte Lichtfeld sowohl auszulesen als auch zu steuern.

Der erste Teil der Dissertation beschreibt einen neuartigen experimentellen Ansatz, der auf evaneszenten, mittels eines Toroid-Mikroresonators überhöhten Nahfeldern beruht. Dieser Ansatz ermöglicht die Ausweitung dispersiver, resonatorverstärkter optomechanischer Kopplung auf subwellenlängenskalige nanomechanische Oszillatoren, die als Grundlage für eine Reihe hochauflösender Messmethoden dienen. Die experimentell analysierte optomechanische Kopplung stimmt dabei gut mit theoretischen Vorhersagen überein. Die entwickelte Plattform ermöglicht das Auslesen nanomechanischer Schwingungen mit außergewöhnlich hoher Empfindlichkeit, die den bisherigen Stand der Technik übertrifft. Dabei wird erstmals eine Messungenauigkeit erreicht, die unter der Schwelle, die dem Standard-Quanten-Limes entspricht, liegt. Bereits in den gegenwärtigen Messungen sollte die Quanten-Rückwirkung die Messempfindlichkeit dominieren, wird allerdings von thermischen Fluktuationen überdeckt. Dies könnte jedoch die Grundlage für den erstmaligen experimentellen Nachweis der Quanten-Rückwirkung des Strahlungsdrucks auf einen festkörperbasierten mechanischen Oszillator liefern. Zudem wird gezeigt, dass die durch Lichtdruck erzeugte Wechselwirkung zwischen evaneszentelem Resonatorfeld und nanomechanischem Oszillator zum Antreiben und Steuern des mechanischen Bewegungszustands des Oszillators verwendet werden kann. Sowohl Verstärkung dessen Bewegung, die zu sich selbst erhaltenden mechanischen Oszillationen führen kann, als auch Kühlung durch die dynamische Rückwirkung des Lichtdrucks wird erreicht. Des Weiteren wird gezeigt, dass die Nahfeld-Plattform auch resonante Kopplung eines nanomechanischen Oszillators an zwei optische Moden sowie quadratische Kopplung ermöglicht.

Im zweiten Teil der Dissertation werden monolithische, chip-basierte Resonatoren entwickelt, die ultraniedrige mechanische und optische Dissipation vereinen. Hierzu werden die intrinsischen mechanischen Moden von Toroid-Mikroresonatoren detailliert untersucht. Hochsensitive Messungen gestatten dabei, eine Fülle mechanischer Moden zu beobachten, welche gut mit den Ergebnissen aus Simulationen übereinstimmen. Insbesondere die Dissipationsmechanismen, die die mechanischen Güten bestimmen, werden dabei analysiert.

Aufhängeverluste werden als bei Raumtemperatur vorherrschender Verlustkanal identifiziert und durch eine neue geometrische Struktur systematisch minimiert. Dies führt zu Speichenresonatoren, deren mechanische Güten durch materialspezifische Verluste limitiert sind und den besten publizierten Werten für mechanische Oszillatoren ähnlicher Frequenzen gleichkommen.

Abstract

This thesis reports on coupling optical microresonators to micro- and nanomechanical oscillators. The mutual optomechanical coupling based on radiation pressure between the microcavity and a mechanical degree of freedom modulating its spatial structure thereby allows both transduction and actuation of the motion of the mechanical degree of freedom by the light field launched into the microcavity.

The first part of the thesis reports on a novel experimental approach based on cavity enhanced evanescent near-fields of toroid microresonators. It enables the extension of dispersive cavity optomechanical coupling to sub-wavelength scale nanomechanical oscillators which are at the heart of a variety of precision measurements. The optomechanical coupling present in the developed system is carefully analyzed experimentally and good agreement with theoretical expectations is found. The demonstrated platform allows transduction of nanomechanical motion with an exceptionally high sensitivity, outperforming the previous state-of-the-art transducers. Thereby, for the first time a measurement imprecision lower than the level of the standard quantum limit is achieved. In the present measurements, quantum backaction should already be the dominating contribution to the measurement sensitivity which is however masked by thermal noise. This may pave the way to the first experimental demonstration of radiation pressure quantum backaction on a solid-state mechanical oscillator. Moreover, the radiation pressure interaction between evanescent cavity field and nanomechanical oscillator is shown to enable actuating and controlling the motional state of the oscillator. Both amplification, leading to self-sustained mechanical oscillations, and cooling by radiation pressure dynamical backaction is reported. In addition, the capability of the near-field platform to implement resonant interaction of a mechanical mode with two optical modes is shown as well as the feasibility of quadratic coupling to the nanomechanical oscillators.

In the second part of the thesis monolithic on-chip resonators that combine ultra-low optical and mechanical dissipation are designed. To this end, the intrinsic mechanical modes of toroid microresonators are analyzed in detail. High-sensitivity measurements enable the observation of a plethora of mechanical modes and good agreement with finite element modelling is found. In particular the dissipation mechanisms limiting their mechanical quality are studied. Clamping losses are identified as the dominant loss mechanism at room temperature. Using a novel geometric design, these are systematically minimized which leads to spoke-supported microresonators with intrinsic material-loss limited mechanical quality factors rivalling the best published values at similar frequencies.

Chapter 1

Introduction

A harmonic oscillator is one of the simplest textbook examples in both classical and quantum physics. Its mechanical manifestation, i.e. a mechanical oscillator, is probably the most tangible and intuitive realization thereof. During the last decades, solid-state mechanical oscillators have been used in a variety of fields both in science and technology. Scientific applications range from micron-scale cantilevers used in atomic-force microscopy, to metre-scale mechanical oscillators in the form of interferometer mirrors intended for probing gravitational waves. Triggered by the compatibility with planar microelectronics, particularly microelectromechanical systems have vastly influenced technology [13] in the form of micromechanical accelerometers, steering micromirrors or inertial sensors.

In recent years, the combination of the fields *optical microcavities* [14] and *micromechanical systems* has triggered a rapid development of the research field *Cavity Optomechanics* [15–17]. Most generally speaking, this field of research investigates the interaction of light with a mechanical oscillator via radiation pressure where the strength of the interaction is enhanced using an optical cavity. Technological advances in micro- and nanofabrication have thereby brought about a variety of experimental systems spanning several orders of magnitude in size. A particularly intriguing aspect of this field is the prospect of realizing quantum mechanical experiments which have so far been restricted to single particles with tangible mechanical oscillators. This would open up a new arena for quantum physics.

The first chapter of this thesis will give an introduction into the basic principles of cavity optomechanics and set up a theoretical framework for the experimental work of this thesis. Moreover, the optical cavities employed in this thesis, toroid microresonators will be introduced.

Subsequently, the second chapter is dedicated to near-field cavity optomechanical experiments. Thereby the evanescent near-field of toroid microresonators is employed for radiation pressure coupling to sub-wavelength scale nanomechanical oscillators which enables the extension of cavity optomechanics to the nanoscale. Results of this chapter have partially been published in Ref. [4], Ref. [2] and Ref. [3].

In the third chapter, the dissipation of the internal mechanical modes of toroid microresonators is studied in detail, leading to the development of monolithic on-chip micro-optomechanical resonators combining ultra-low optical and mechanical dissipation. Those

results have partly been published in Ref. [6], Ref. [7] and Ref. [9].

1.1 Cavity optomechanics

Einstein's theory of general relativity [18] and the concomitant prediction of gravitational waves have triggered a century of experimental efforts to measure the tiny dilatations of space-time associated with gravitational waves. The most promising approach thereby uses an electromagnetic resonator parametrically coupled to a mechanical oscillator which has to date allowed relative displacement measurements down to a level of $< 10^{-21}$ [19, 20]. The fact that such an impressive sensitivity has still not proven to be sufficient for detecting direct experimental signatures of gravitational waves underpins the experimental challenge of these experiments. In the light of the outstanding sensitivities required in the search for gravitational waves, it has been realized that in fact quantum effects will be of relevance in the displacement measurements although dealing with macroscopic bodies. The associated quantum limits to displacement detection have thus been theoretically derived already more than two decades ago [21, 22]. These have their origin in the radiation pressure that is exerted by electromagnetic fields, which had interestingly already been postulated by Kepler in 1619. Moreover, it has been shown that the radiation pressure exerted by the electromagnetic field in a resonator may cause a bistability of the system [23] and it has been predicted that it can also lead to an oscillatory instability of the resonator, or contrarily cool the resonator [24, 25]. All these effects had to be considered when planning more and more advanced gravitational wave interferometers.

The transfer of these ideas and principles to the microscale, i.e. to low mass mechanical oscillators, which was facilitated by the progress in microfabrication techniques witnessed in recent years, has made them much more easily experimentally accessible and, even more important, changed their perception as caveats in gravitational wave astronomy to resources for a variety of experimental applications. Thus, gravitational wave detection may be regarded as the godfather of the recent surge in cavity optomechanical experiments.

In 2005, it was shown that in fact the radiation pressure of light can be used to drive laser-like oscillations of a micromechanical oscillator [26–28], also referred to as “phonon lasing”. The application of such compact, low-power photonic oscillators as frequency references is currently investigated [29–31]. Moreover, it has been demonstrated that micromechanical oscillators may be efficiently cooled by radiation pressure [32–34]. In particular the feasibility of ground state cooling using radiation pressure has been theoretically shown [35, 36]. Subsequently, a variety of research groups pursued experiments aiming at initializing a solid-state mechanical oscillator in its quantum-ground state using radiation pressure cooling [8, 10, 37–41]. This would provide a novel route to the new regime of quantum physics dealing with tangible mechanical oscillators which has recently been entered [42]. Just as reaching the ultimate limits in displacement detection and thus maximizing the performance of mechanical sensors of mass [43], charge [44] and magnetic field [45], this is an ongoing and very actively pursued paradigm in the field of Cavity Optomechanics.

The first part of this section is dedicated to the introduction of the basic theoretical

concepts in cavity optomechanics. It will start with the standard Hamiltonian of cavity optomechanical systems before a theoretical framework based on the quantum Langevin approach is derived. Then, building on this framework, the ability of cavity optomechanical systems to perform as nearly ideal transducers of mechanical motion is considered, in particular looking at the corresponding limitations due to quantum noise. Then, the effects of radiation pressure will be discussed, with a focus on dynamical backaction that provides a tool for controlling the motional state of mechanical oscillators. In the second part of this section, the optical properties of the cavities used in this thesis—toroid microresonators—will be discussed.

1.1.1 Linear Hamiltonian of cavity optomechanical systems

Here, a generic cavity optomechanical system which realizes parametric coupling between an optical resonator ¹ and a mechanical oscillator will be considered. The optical resonance frequency $\omega(x_0)$ shall first of all, however, depend on the position x_0 of the mechanical oscillator in a general fashion. It is only required that the typical harmonic oscillations x of the mechanical oscillator around its equilibrium position x_0 are sufficiently small to safely linearize the position dependent frequency around x_0 . This leads to the following linear dependence of the optical resonance frequency on the position fluctuations x :

$$\omega(x_0 + x) = \omega(x_0) + g \cdot x. \quad (1.1)$$

Here, we have introduced $g = \partial\omega/\partial x$ which is typically referred to as the optomechanical coupling coefficient. For simplicity we will from now on assume a fixed equilibrium position x_0 and identify $\omega(x_0) \equiv \omega$. The Hamiltonian H of the coupled optomechanical system may then be written as a sum of the optical and mechanical subsystems' Hamiltonians H_{opt} and H_{mech} , respectively, as well as the coupling Hamiltonian H_{om} [46]:

$$\begin{aligned} H = & \hbar\omega a_0^\dagger a_0 + i\hbar\sqrt{\kappa_{\text{ex}}}(s_0 a_0^\dagger e^{-i\omega_d t} - s_0^\dagger a_0 e^{i\omega_d t}) + H_\kappa \\ & + \hbar\Omega_m b^\dagger b + H_{\Gamma_m} \\ & + \hbar g_0 (b^\dagger + b) a_0^\dagger a_0. \end{aligned} \quad (1.2)$$

The creation (annihilation) operators of the optical and mechanical modes are denoted as a_0^\dagger (a_0) and b^\dagger (b) with corresponding resonance frequencies ω and Ω_m . The optical mode is coupled to an external port with a rate κ_{ex} , supplying a (laser) drive field $s_0 e^{-i\omega_d t}$ with photon flux $\langle s_0^\dagger s_0 \rangle$ and frequency ω_d . The Hamiltonians H_{Γ_m} and H_κ describe the damping of the mechanical [57] and optical [58] modes with energy decay rates Γ_m and κ . The latter consists of coupling to the external port κ_{ex} and losses within the resonator $\kappa_0 = \kappa - \kappa_{\text{ex}}$. The interaction energy between optical and mechanical degree of freedom is determined by the vacuum optomechanical coupling rate

$$g_0 \equiv g \times x_{\text{zpf}}, \quad (1.3)$$

¹ The theoretical description presented throughout this section is not restricted to the optical domain. It can be directly transferred to any *electromagnetic* resonator.

System	$g_0/2\pi$ [Hz]	$\kappa/2\pi$ [Hz]	$\Gamma_m/2\pi$ [Hz]	Ω_m/κ	x_{zpf} [fm]	Ref.
Crystalline microresonator	1	$2 \cdot 10^5$	$1 \cdot 10^3$	12	0.003	[47]
Movable mirror	$2 \cdot 10^{-3}$	$2 \cdot 10^4$	0.06	0.01	0.01	[48]
Microsphere	$1 \cdot 10^3$	$3 \cdot 10^7$	$8 \cdot 10^4$	5	0.04	[49]
Micromirror	1	$2 \cdot 10^6$	80	0.4	0.01	[32]
Micromirror	5	$8 \cdot 10^5$	30	1	0.5	[50]
Micromirror	300	$8 \cdot 10^8$	600	0.001	40	[51]
<i>Spoke-microresonator</i>	500	$5 \cdot 10^6$	500	5	0.2	[6]
Membrane-in-the-middle	5	$2 \cdot 10^5$	0.1	0.6	1	[37]
Double-microdisk	$8 \cdot 10^4$	$1 \cdot 10^8$	$2 \cdot 10^3$	0.06	3	[52]
Optomechanical crystal	$2 \cdot 10^5$	$5 \cdot 10^9$	$2 \cdot 10^6$	0.5	3	[53]
Photonic crystal cavity	$6 \cdot 10^5$	$2 \cdot 10^9$	$8 \cdot 10^4$	0.004	5	[49]
Nanomechanical rod	–	$8 \cdot 10^8$	300	0.002	–	[54]
<i>Near-field nanomechanics</i>	500	$5 \cdot 10^6$	100	2	20	[2]
Near-field nanomechanics	50	$2 \cdot 10^9$	$5 \cdot 10^4$	0.02	20	[55]
Microwave nanomechanics*	1	$3 \cdot 10^6$	10	0.4	30	[56]
Microwave nanomechanics*	2	$6 \cdot 10^5$	6	2	30	[41]

Table 1.1: Overview of recent cavity optomechanical systems (*requiring operation in a dilution refrigerator). Both systems developed in this thesis are in italics. The spoke-supported resonators (see chapter 3) exhibit the advantage of monolithic design and large resolved-sideband factors Ω_m/κ . The near-field platform (see chapter 2) displays essentially equal vacuum coupling rates g_0 and optical damping rates κ but offers the additional benefit of smaller mechanical damping rates Γ_m and larger zero-point motion x_{zpf} .

which is given by the product of optomechanical coupling coefficient g and the zero-point-fluctuations

$$x_{\text{zpf}} = \sqrt{\hbar/(2m\Omega_m)} \quad (1.4)$$

of the mechanical oscillator (m denotes the oscillator mass). The Hamiltonian $H_{\text{om}} = \hbar g_0(b^\dagger + b)a_0^\dagger a_0$ implements a *mutual* optomechanical coupling. It has its origin in the cavity resonance frequency which depends on the position of the mechanical oscillator via Eq. (1.1). It also, however, represents a radiation pressure force F that can be interpreted as

$$\langle F \rangle = - \left\langle \frac{\partial H}{\partial x} \right\rangle = -\hbar g \langle a_0^\dagger a_0 \rangle, \quad (1.5)$$

thus leading to a per-photon force $-\hbar g$ acting on the mechanical oscillator.

Table 1.1 shows an overview of recently studied cavity optomechanical systems that realize the Hamiltonian (1.2), along with both systems developed in this thesis. As can be seen, the corresponding system parameters vary over many orders of magnitude. A common feature of all studied systems is that the vacuum optomechanical coupling rate

g_0 is at least three orders of magnitude smaller than the optical decay rate κ . For a few systems, however, g_0 can exceed the mechanical decay rate Γ_m .

1.1.2 Quantum Langevin equations

Using the standard Heisenberg picture formalism, the above Hamiltonian allows the derivation of the Heisenberg-Langevin equations of motion for the relevant time dependent system operators a and x . Transforming all optical fields into the frame of the drive field (rotating at ω_d) these take the form:

$$\dot{a}_0 = (i\Delta - \kappa/2)a_0 - igxa_0 + \sqrt{\kappa_{\text{ex}}}s_0 + \sqrt{\kappa_0}s_{\text{vac}} \quad (1.6)$$

$$\ddot{x} = -\Omega_m^2x - \Gamma_m\dot{x} - \frac{\hbar g}{m}a_0^\dagger a_0 + \sqrt{\Gamma_m}\xi_{\text{th}}, \quad (1.7)$$

where $\Delta = \omega_d - \omega$ denotes the detuning of the drive field from cavity resonance. The mechanical oscillator is coupled to a thermal bath ξ_{th} at temperature T via Γ_m whereas the coupling of the optical field to the vacuum port s_{vac} ² is mediated by κ_0 .

In experimental situations, one mostly deals with large input fields $\langle s_0^\dagger s_0 \rangle$ leading to large occupation $\langle a_0^\dagger a_0 \rangle \gg 1$ of the intracavity field. Using a semiclassical approximation, we will correspondingly assume mean amplitudes for both drive and intracavity fields and introduce $s_0 =: \bar{s} + s$ and $a_0 =: \bar{a} + a$. Then, \bar{s} and \bar{a} denote the (large) mean amplitudes whereas s and a denote the small (quantum) fluctuations around these amplitudes. Keeping only first order terms, Eq. (1.7) yields the following expression for the intracavity mean-field

$$\bar{a} = \frac{\sqrt{\kappa_{\text{ex}}}}{\kappa/2 - i\Delta} \bar{s}, \quad (1.8)$$

which we can choose to be real. This simply requires an appropriate choice of the arbitrary phase of the input field $\bar{s} = e^{i\varphi_s} \cdot |\bar{s}|$, i.e.

$$e^{i\varphi_s} = \frac{\kappa/2 - i\Delta}{\sqrt{\kappa^2/4 + \Delta^2}}. \quad (1.9)$$

Note that then the mean intracavity photon number is simply given by \bar{a}^2 .

Looking at Eq. (1.7) one can see that the mean field \bar{a} exerts a static radiation pressure force onto the mechanical oscillator, shifting its mean position by $-\hbar g \bar{a}^2 / \Omega_m^2$. This subtlety can in fact lead to a bistability in oscillator position and intracavity power as experimentally demonstrated in 1983 [23] using a very low frequency mechanical oscillator ($\Omega_m \sim 1$ Hz). A detailed description of this effect is given for example in Ref. [59]. This bistability has been proposed as a resource for optomechanically induced squeezing of the light field [60],

² Here, the number of thermal photons, $\sim k_B T / (\hbar\omega) < 0.03$ (for $T < 300$ K and optical frequencies ω) is neglected. For systems operating at microwave frequencies, however, the thermal bath can be of relevance, even for cryogenic temperatures and would have to be considered, here.

analogous to Kerr squeezing [61]. Here, we assume for simplicity that the system resides in a stable solution for \bar{a} at equilibrium position x_0 .

Using a standard input-output formalism [62] combined with Eq. (1.8) then allows the derivation of the mean output field \bar{s}_{out} :

$$\bar{s}_{\text{out}} = \bar{s} - \sqrt{\kappa_{\text{ex}}} \bar{a} = \left(1 - \frac{\kappa_{\text{ex}}}{\kappa/2 - i\Delta} \right) \bar{s}. \quad (1.10)$$

Fig. 1.1 shows both the corresponding amplitude and phase of the output field \bar{s}_{out} as a function of the pump laser detuning Δ . Moreover, Eqs. (1.6)-(1.7) can be simplified to the following set of linearized quantum Langevin equations for the fluctuations s , a and x of the input field, the intracavity field and the mechanical oscillator position

$$\dot{a} = (i\Delta - \kappa/2) a - igx\bar{a} + \sqrt{\kappa_{\text{ex}}} s + \sqrt{\kappa_0} s_{\text{vac}} \quad (1.11)$$

$$\ddot{x} = -\Omega_{\text{m}}^2 x - \Gamma_{\text{m}} \dot{x} - \frac{\hbar g}{m} \bar{a}(a^\dagger + a) + \sqrt{\Gamma_{\text{m}}} \xi_{\text{th}}. \quad (1.12)$$

The corresponding output field fluctuations s_{out} are given by

$$s_{\text{out}} = s - \sqrt{\kappa_{\text{ex}}} a. \quad (1.13)$$

The above set of equations (1.11)-(1.13) forms a basic framework for cavity optomechanics which allows the description of a variety of cavity optomechanical phenomena.

It is very instructive to Fourier transform Eqs. (1.11)-(1.13). The Fourier transforms $c[\Omega]$ and $c^\dagger[\Omega]$ of operators $c(t)$ and $c^\dagger(t)$ are generally defined as ³:

$$c[\Omega] = \int_{-\infty}^{\infty} c(t) e^{i\Omega t} dt \quad (1.14)$$

$$c^\dagger[\Omega] = \int_{-\infty}^{\infty} c^\dagger(t) e^{i\Omega t} dt. \quad (1.15)$$

In Fourier space, the quantum Langevin equations obtained from Eqs. (1.11)-(1.12) then read:

$$-i\Omega a[\Omega] = (i\Delta - \frac{\kappa}{2}) a[\Omega] - i\bar{a}g x[\Omega] + \sqrt{\kappa_{\text{ex}}} s[\Omega] + \sqrt{\kappa_0} s_{\text{vac}}[\Omega] \quad (1.16)$$

$$-i\Omega a^\dagger[\Omega] = (-i\Delta - \frac{\kappa}{2}) a^\dagger[\Omega] + i\bar{a}g x[\Omega] + \sqrt{\kappa_{\text{ex}}} s^\dagger[\Omega] + \sqrt{\kappa_0} s_{\text{vac}}^\dagger[\Omega] \quad (1.17)$$

$$-\Omega^2 x[\Omega] = -\Omega_{\text{m}}^2 x[\Omega] + i\Omega \Gamma_{\text{m}} x[\Omega] - \frac{\hbar g}{m} \bar{a}(a^\dagger[\Omega] + a[\Omega]) + \sqrt{\Gamma_{\text{m}}} \xi_{\text{th}}[\Omega]. \quad (1.18)$$

The optical and mechanical noise operators $s_{\text{vac}}[\Omega]$ and $\xi_{\text{th}}[\Omega]$ are characterized by the

³ The inverse transform is then given by $c(t) = 1/(2\pi) \int_{-\infty}^{\infty} c[\Omega] e^{-i\Omega t} d\Omega$

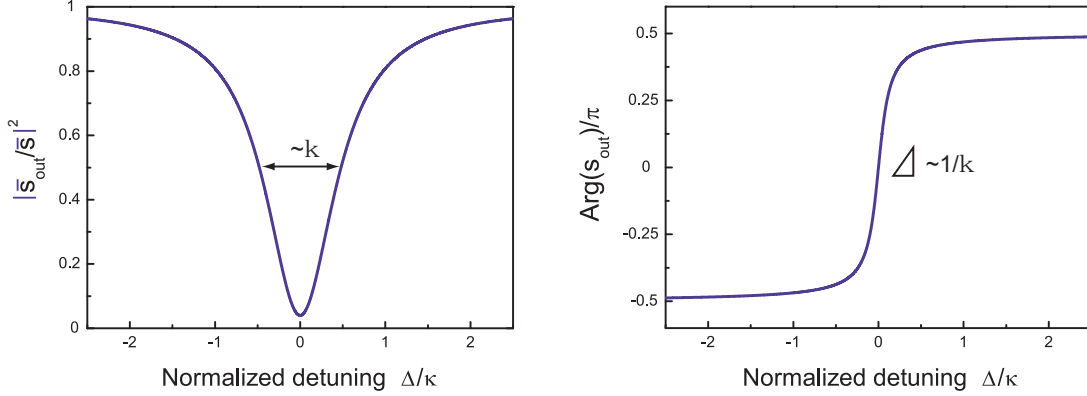


Figure 1.1: Output field \bar{s}_{out} of a cavity. The left panel shows the normalized power $|\bar{s}_{\text{out}}|^2$ transmitted by the cavity according to Eq. (1.13) as a function of normalized detuning (for $\kappa_{\text{ex}}/\kappa = 0.6$). The right panel shows the corresponding phase of the output field \bar{s}_{out} .

correlation functions [57, 58]⁴:

$$\langle s_{\text{vac}}[\Omega] s_{\text{vac}}^\dagger[\Omega'] \rangle = 2\pi \delta(\Omega + \Omega'), \quad (1.19)$$

$$\langle \xi_{\text{th}}[\Omega] \xi_{\text{th}}[\Omega'] \rangle = 2\pi \delta(\Omega + \Omega') \frac{1}{m} \hbar \Omega \left(\coth \left(\frac{\hbar \Omega}{2k_B T} \right) + 1 \right). \quad (1.20)$$

These non-zero correlation functions ensure non-zero fluctuations of x and a , respectively, even in the absence of external driving, as required by the fluctuation-dissipation theorem in the presence of the damping rates Γ_m and κ_0 . Note that a quantum-limited input field s (which can be obtained from a shot-noise limited laser source) has the same correlation function as the vacuum field s_{vac} given by Eq. (1.19).

From (1.16) and (1.17), the intracavity field fluctuations can be derived:

$$a[\Omega] = \frac{1}{\kappa/2 - i(\Delta + \Omega)} (-i\bar{a}g x[\Omega] + \sqrt{\kappa_{\text{ex}}} s[\Omega] + \sqrt{\kappa_0} s_{\text{vac}}[\Omega]) \quad (1.21)$$

$$a^\dagger[\Omega] = \frac{1}{\kappa/2 + i(\Delta - \Omega)} (i\bar{a}g x[\Omega] + \sqrt{\kappa_{\text{ex}}} s^\dagger[\Omega] + \sqrt{\kappa_0} s_{\text{vac}}^\dagger[\Omega]). \quad (1.22)$$

The fluctuations $x[\Omega]$ of the mechanical oscillator are thus imprinted into the intracavity field and transferred to the output field $s_{\text{out}}[\Omega]$ via Eq. (1.13)

$$s_{\text{out}}[\Omega] = \frac{i\sqrt{\kappa_{\text{ex}}}\bar{a}g}{\kappa/2 - i(\Delta + \Omega)} x[\Omega] + \frac{\frac{\kappa_0 - \kappa_{\text{ex}}}{2} - i(\Delta + \Omega)}{\kappa/2 - i(\Delta + \Omega)} s[\Omega] - \frac{\sqrt{\kappa_{\text{ex}}\kappa_0}}{\kappa/2 - i(\Delta + \Omega)} s_{\text{vac}}[\Omega] \quad (1.23)$$

⁴ The corresponding correlation functions in time domain are:

$$\begin{aligned} \langle s_{\text{vac}}(t) s_{\text{vac}}^\dagger(t') \rangle &= \delta(t - t'), \\ \langle \xi_{\text{th}}(t) \xi_{\text{th}}(t') \rangle &= \frac{1}{m} \int_{-\infty}^{\infty} \hbar \Omega e^{-i\Omega(t-t')} \left(\coth \left(\frac{\hbar \Omega}{2k_B T} \right) + 1 \right) \frac{d\Omega}{2\pi}. \end{aligned}$$

such that the mechanical oscillator's displacement $x[\Omega]$ can be retrieved from the cavity output field fluctuations. The fluctuations of the vacuum port $s_{\text{vac}}[\Omega]$ as well as the input field $s[\Omega]$ thereby constitute a background noise. In the next chapter the quantum limits associated with the measurement of x via the cavity output field will be discussed in detail.

Another interesting feature arising from Eq. (1.18) is the fluctuating radiation pressure force given by the fluctuations of the intracavity field $a[\Omega]$ and $a^\dagger[\Omega]$, respectively. Using expression (1.21) and (1.22), the radiation pressure force term in Eq. (1.18) can be written as

$$-\frac{\hbar g}{m} \bar{a} (a^\dagger[\Omega] + a[\Omega]) = -\frac{\hbar g}{m} \bar{a} (a_x \cdot x[\Omega] + a_q), \quad (1.24)$$

where

$$a_q = \frac{\sqrt{\kappa_{\text{ex}}} s[\Omega] + \sqrt{\kappa_0} s_{\text{vac}}[\Omega]}{\kappa/2 - i(\Delta + \Omega)} + \frac{\sqrt{\kappa_{\text{ex}}} s^\dagger[\Omega] + \sqrt{\kappa_0} s_{\text{vac}}^\dagger[\Omega]}{\kappa/2 + i(\Delta - \Omega)} \quad (1.25)$$

$$a_x = \bar{a} g \left[\left(\frac{\Delta - \Omega}{\kappa/2 + (\Delta - \Omega)^2} + \frac{\Delta + \Omega}{\kappa/2 + (\Delta + \Omega)^2} \right) + i \left(\frac{\kappa/2}{\kappa/2 + (\Delta - \Omega)^2} - \frac{\kappa/2}{\kappa/2 + (\Delta + \Omega)^2} \right) \right]. \quad (1.26)$$

The first term leads to a backaction force, randomly driving the mechanical oscillator. The second term, having both a component in phase and out of phase with the mechanical oscillator's motion, modifies its spring constant and damping rate as will be shown in the following.

Inserting the above expressions in Eq. (1.18), one obtains:

$$x[\Omega] m \underbrace{\left(\Omega_m^2 - \Omega^2 - i\Omega\Gamma_m + \frac{\hbar g}{m} \bar{a} \cdot a_x \right)}_{\chi_{\text{eff}}^{-1}} = m\sqrt{\Gamma_m} \xi_{\text{th}}[\Omega] - \hbar g \bar{a} \cdot a_q. \quad (1.27)$$

The right hand side of this equation has two contributions. The first one is the usual thermal Langevin force $m\sqrt{\Gamma_m} \xi_{\text{th}}[\Omega]$. The second term, arising from the (quantum) fluctuations of both the input field s and the vacuum port s_{vac} , constitutes a (quantum) backaction force $-\hbar g \bar{a} \cdot a_q$. Both forces drive the mechanical oscillator. Moreover, the in-phase and out-of-phase components of a_x modify the susceptibility of the mechanical oscillator with which it reacts to the aforementioned forces. The effective susceptibility χ_{eff} can be written as:

$$\chi_{\text{eff}}^{-1}/m = \underbrace{\left(\Omega_m^2 + \frac{\hbar g}{m} \bar{a} \cdot \text{Re}(a_x) \right)}_{\Omega_{\text{eff}}^2} - \Omega^2 - i\Omega \underbrace{\left(\Gamma_m - i \frac{\hbar g}{m} \bar{a} \cdot \text{Im}(a_x) / \Omega \right)}_{\Gamma_{\text{eff}}} \quad (1.28)$$

The real and imaginary parts of a_x thus change the effective resonance frequency Ω_{eff} and damping rate Γ_{eff} of the mechanical oscillator. Using Eq. (1.26), the modified resonance

frequency Ω_{eff} is given by:

$$\Omega_{\text{eff}} = \Omega_{\text{m}} \sqrt{1 + 2 \frac{g_0^2}{\Omega_{\text{m}}} \bar{a}^2 \left(\frac{\Delta + \Omega}{\kappa^2/4 + (\Delta + \Omega)^2} + \frac{\Delta - \Omega}{\kappa^2/4 + (\Delta - \Omega)^2} \right)}. \quad (1.29)$$

If we assume only weak perturbation, $|\Omega_{\text{eff}} - \Omega_{\text{m}}| \ll \Omega_{\text{m}}$ and $\Gamma_{\text{eff}} \ll \min\{\Omega_{\text{m}}, \kappa\}$, then the effective frequency shift can be approximated by

$$\Omega_{\text{dba}} \equiv \Omega_{\text{eff}} - \Omega_{\text{m}} \approx g_0^2 \bar{a}^2 \left(\frac{\Delta + \Omega_{\text{m}}}{\kappa^2/4 + (\Delta + \Omega_{\text{m}})^2} + \frac{\Delta - \Omega_{\text{m}}}{\kappa^2/4 + (\Delta - \Omega_{\text{m}})^2} \right), \quad (1.30)$$

Thus, the presence of a non-zero intracavity field can lead to a shift in the mechanical oscillator's eigenfrequency. This will be discussed in somewhat more detail in section 1.1.5.

In the same weak perturbation limit, the additional damping rate Γ_{dba} can be written as

$$\Gamma_{\text{dba}} \equiv \Gamma_{\text{eff}} - \Gamma_{\text{m}} \approx g_0^2 \bar{a}^2 \left(\frac{\kappa}{\kappa^2/4 + (\Delta + \Omega_{\text{m}})^2} - \frac{\kappa}{\kappa^2/4 + (\Delta - \Omega_{\text{m}})^2} \right). \quad (1.31)$$

As will be shown in detail in section 1.1.4, this change in effective damping rate can give rise to both cooling and amplification of the mechanical oscillator's motion.

1.1.3 Standard quantum limit of continuous position measurements

As can be seen in Fig. 1.1, close to resonance the properties of the field transmitted by a cavity very sensitively depend on the laser-cavity detuning Δ . This allows very sensitive measurements of mechanical motion using high-Q optomechanical cavities which can be understood in simple terms: First, close to the optical resonance the phase shift of the light transmitted through the optomechanical system induced by a position fluctuation x (leading to $\delta\omega = g \cdot x$) of the mechanical oscillator is amplified by $1/\kappa$, as indicated in Fig. 1.1 (right panel). Second, using optical fields these amplified phase-fluctuations can be measured in a quantum-limited fashion, i.e. without introducing excess classical noise during the measurement. Thus, this technique allows measurements of mechanical motion with a sensitivity whose limitations are only given by quantum noise. These limitations will be described in this section.

Using Eqs. (1.11)-(1.13) allows calculating the intracavity field fluctuations $a[\Omega]$, $a^\dagger[\Omega]$ (Eqs. 1.21 and 1.22) as well as the transmitted field's fluctuations $s_{\text{out}}[\Omega]$, $s_{\text{out}}^\dagger[\Omega]$ (cf. Eq. 1.23). These, in turn, allow the derivation of the associated quantum limits of displacement detection. It is convenient to perform the calculations for the respective in-phase and quadrature fluctuations.

In general, the fluctuations of the operators $c[\Omega]$ and $c^\dagger[\Omega]$ around the mean field \bar{c} may be expressed in terms of their respective amplitude and phase quadratures $p_c[\Omega]$ and

$q_c[\Omega]$ as

$$\begin{pmatrix} p_c[\Omega] \\ q_c[\Omega] \end{pmatrix} = R(\varphi) \begin{pmatrix} c[\Omega] \\ c^\dagger[\Omega] \end{pmatrix}, \quad (1.32)$$

where R is defined as

$$R(\varphi) = \begin{pmatrix} e^{-i\varphi} & e^{i\varphi} \\ -ie^{-i\varphi} & ie^{i\varphi} \end{pmatrix}, \quad (1.33)$$

and φ is the phase of the corresponding mean field, i.e. $e^{i\varphi} = \bar{c}/|\bar{c}|$.

Performing these transformations on Eqs. (1.16), (1.17) and using Eq. (1.13), the spectra of the output field's quadratures $S_{p_{\text{out}}}[\Omega]$, $S_{q_{\text{out}}}[\Omega]$ as well as the intracavity field's quadratures $S_{p_a}[\Omega]$, $S_{q_a}[\Omega]$ can be derived. Note that the double-sided spectrum $S_c^{\text{ds}}[\Omega]$ of a variably c can be defined via the correlation function in frequency domain as

$$2\pi \delta(\Omega + \Omega') S_c^{\text{ds}}[\Omega] = \langle c[\Omega]c[\Omega'] \rangle. \quad (1.34)$$

The corresponding symmetrized spectrum $S_c[\Omega]$ can then be defined as

$$S_c[\Omega] = (S_c^{\text{ds}}[\Omega] + S_c^{\text{ds}}[-\Omega]) / 2. \quad (1.35)$$

See appendix A for the general results for $S_{p_{\text{out}}}[\Omega]$, $S_{q_{\text{out}}}[\Omega]$, $S_{p_a}[\Omega]$ and $S_{q_a}[\Omega]$. For the special case of resonant probing ($\Delta = 0$) the output field's phase quadrature reads

$$\begin{aligned} S_{q_{\text{out}}}[\Omega] &= \left(1 - \frac{4\eta_c(1-\eta_c)}{1+4\Omega^2/\kappa^2}\right) S_{q_{\text{in}}}[\Omega] + \frac{4\eta_c(1-\eta_c)}{1+4\Omega^2/\kappa^2} S_{q_{\text{vac}}}[\Omega] \\ &+ \frac{16\eta_c^2}{1+4\Omega^2/\kappa^2} \frac{P}{\hbar\omega} \frac{4g^2}{\kappa^2} S_x[\Omega], \end{aligned} \quad (1.36)$$

where $P = |\bar{s}|^2$ denotes the input power launched to the resonator and $\eta_c = \kappa_{\text{ex}}/\kappa$ ($\eta_c \in [0, 1]$) is the coupling efficiency. In brief, this result can be obtained from Eq. (1.23) (and the respective expression for $s_{\text{out}}^\dagger[\Omega]$), taking into account the relative phases of input, output and intracavity mean fields (1.8)-(1.10) and assuming that all fields are uncorrelated.

Thus, the mechanical spectrum $S_x[\Omega]$ can be retrieved from the phase fluctuation spectrum $S_{q_{\text{out}}}[\Omega]$ of the output field s_{out} . The phase fluctuations of the input and vacuum fields $S_{q_{\text{in}}}$ and $S_{q_{\text{vac}}}$ (first and second terms in the above expression) thereby constitute a measurement background noise which is typically referred to as measurement imprecision. Assuming quantum limited correlations (1.19) for both input field and the vacuum port results in

$$S_{q_{\text{in}}} = S_{q_{\text{vac}}} = 1 \quad (1.37)$$

and expression (1.36) simplifies to:

$$S_{q_{\text{out}}}[\Omega] = \frac{16\eta_c^2}{1+4\Omega^2/\kappa^2} \frac{4g^2}{\kappa^2} \frac{P}{\hbar\omega} S_x[\Omega] + 1. \quad (1.38)$$

Thus, the signal proportional to S_x rides on top of a flat measurement background given by quantum shot noise. The equivalent mechanical noise amplitude corresponding to the shot-noise background in Eq. (1.38) can then be written as

$$S_x^{\text{imp}}[\Omega] = \frac{1 + 4\Omega^2/\kappa^2}{16\eta_c^2} \frac{\kappa^2}{4g^2} \frac{\hbar\omega}{P}. \quad (1.39)$$

The measurement imprecision caused by shot noise⁵ can thus, in principle, reach arbitrarily low values, provided sufficiently large power P and/or coupling g^2/κ^2 can be applied.

As the measurement imprecision is lowered, however, a second source of noise comes into play which has already been seen in Eq. (1.27): the radiation pressure quantum backaction of the measurement. From Eq. (1.27) one can derive that the (non-symmetrized) photon number fluctuations

$$S_N[\Omega] = \bar{a}^2 \frac{\kappa}{\kappa^2/4 + (\Delta + \Omega)^2} \quad (1.40)$$

inside the optical resonator lead to an additional force acting on the mechanical oscillator. Its motional spectrum while performing a measurement can then be written as

$$S_x[\Omega] = |\chi_{\text{eff}}[\Omega]|^2 \left(S_F^L + S_F^{\text{qba}}[\Omega] \right), \quad (1.41)$$

where the correlation functions (1.19)-(1.20) define the magnitude of the thermal Langevin force spectrum $S_F^L[\Omega]$ and the quantum backaction force spectrum $S_F^{\text{qba}}[\Omega]$:

$$S_F^L[\Omega] = 2m\Gamma_m k_B T \left[\frac{\hbar\Omega}{2k_B T} \left(1 + \coth\left(\frac{\hbar\Omega}{2k_B T}\right) \right) \right] \quad (1.42)$$

$$\begin{aligned} & \stackrel{k_B T \gg \hbar\Omega}{\approx} 2m\Gamma_m k_B T \\ S_F^{\text{qba}}[\Omega] &= (\hbar g)^2 \bar{a}^2 \frac{\kappa}{\kappa^2/4 + (\Delta + \Omega)^2}. \end{aligned} \quad (1.43)$$

The mechanical spectrum is thus driven not only by the thermal Langevin force but also by the measurement induced quantum backaction force. Note that the asymmetry of $S_F^{\text{qba}}[\Omega]$ with respect to frequency reflects the possibility of creating and annihilating energy quanta.

For resonant probing ($\Delta = 0$), the (symmetrized) measurement induced excess mechanical noise can be written as:

$$S_x^{\text{qba}}[\Omega] = |\chi_m[\Omega]|^2 \frac{16\eta_c}{1 + 4\Omega^2/\kappa^2} \frac{(\hbar g)^2}{\kappa^2} \frac{P}{\hbar\omega}, \quad (1.44)$$

where the identity of effective susceptibility $\chi_{\text{eff}}[\Omega]$ and intrinsic susceptibility

$$\chi_m[\Omega] = m^{-1} \left(\Omega_m^2 - \Omega^2 - i\Omega\Gamma_m \right)^{-1}, \quad (1.45)$$

⁵ The flat shot-noise becomes frequency dependent when scaled into units of mechanical displacement due to the resonator's cut-off frequency κ beyond which the transduction efficiency of the system reduces.

for vanishing detuning ($\Delta = 0$) is used. This contribution is typically termed the quantum backaction noise of the measurement [21, 22]. If one introduces the normalized coupling power

$$p \equiv 2\eta_c^{3/2} \frac{\hbar |\chi_m[\Omega]| g^2}{(\kappa/4)^2} \frac{P/(\hbar\omega)}{1 + 4\Omega^2/\kappa^2}, \quad (1.46)$$

the total noise of the measurement (at a fixed Fourier frequency Ω_{meas}), taking into account both sources of uncertainty, imprecision and backaction, and assuming resonant probing ($\Delta = 0$) can be written as:

$$S_x^{\text{tot}}[\Omega_{\text{meas}}] = \frac{\hbar |\chi_m[\Omega_{\text{meas}}]|}{2\sqrt{\eta_c}} \left(p + \frac{1}{p} \right). \quad (1.47)$$

This function is depicted in Fig. 1.2a, for a measurement at resonance, i.e. $\Omega_{\text{meas}} = \Omega_m$. For low power levels, $p \ll 1$, the measurement noise is dominated by imprecision noise which reduces $\propto 1/p$ for increased coupling. For large coupling power, $p \gg 1$, the measurement is on the other hand dominated by quantum backaction noise that increases $\propto p$ for increased coupling. At optimum coupling power, $p = 1$, the minimum measurement uncertainty is achieved

$$S_x^{\text{min}}[\Omega_{\text{meas}}] = \frac{1}{\sqrt{\eta_c}} \hbar |\chi_m[\Omega_{\text{meas}}]|. \quad (1.48)$$

The minimum uncertainty for an ideal measurement ($\eta_c = 1$) has been termed the standard quantum limit (SQL) of continuous position measurement:

$$S_x^{\text{SQL}}[\Omega_{\text{meas}}] = \hbar |\chi_m[\Omega_{\text{meas}}]|. \quad (1.49)$$

When considering a measurement at the resonance frequency of the mechanical oscillator it can be written as

$$S_x^{\text{SQL}}[\Omega_m] = S_x^{\text{zpf}}[\Omega_m], \quad (1.50)$$

where $S_x^{\text{zpf}}[\Omega_m] = \hbar/(m\Gamma_m\Omega_m)$ denotes the mechanical oscillator's (double sided) zero-point fluctuations.

The optimum coupling power $p = 1$ necessary to reach the standard quantum limit, then corresponds to an input power of

$$P_{\text{SQL}}/(\hbar\omega) = \frac{\Gamma_m (\kappa/2)^2}{16 g_0^2} (1 + 4\Omega_m^2/\kappa^2). \quad (1.51)$$

Correspondingly, the optimum power for reaching the minimum uncertainty $S_x^{\text{min}}[\Omega_m]$ in the case of $\eta_c \neq 1$ is given by $P_{\text{min}} = P_{\text{SQL}} \times \eta_c^{-3/2}$.

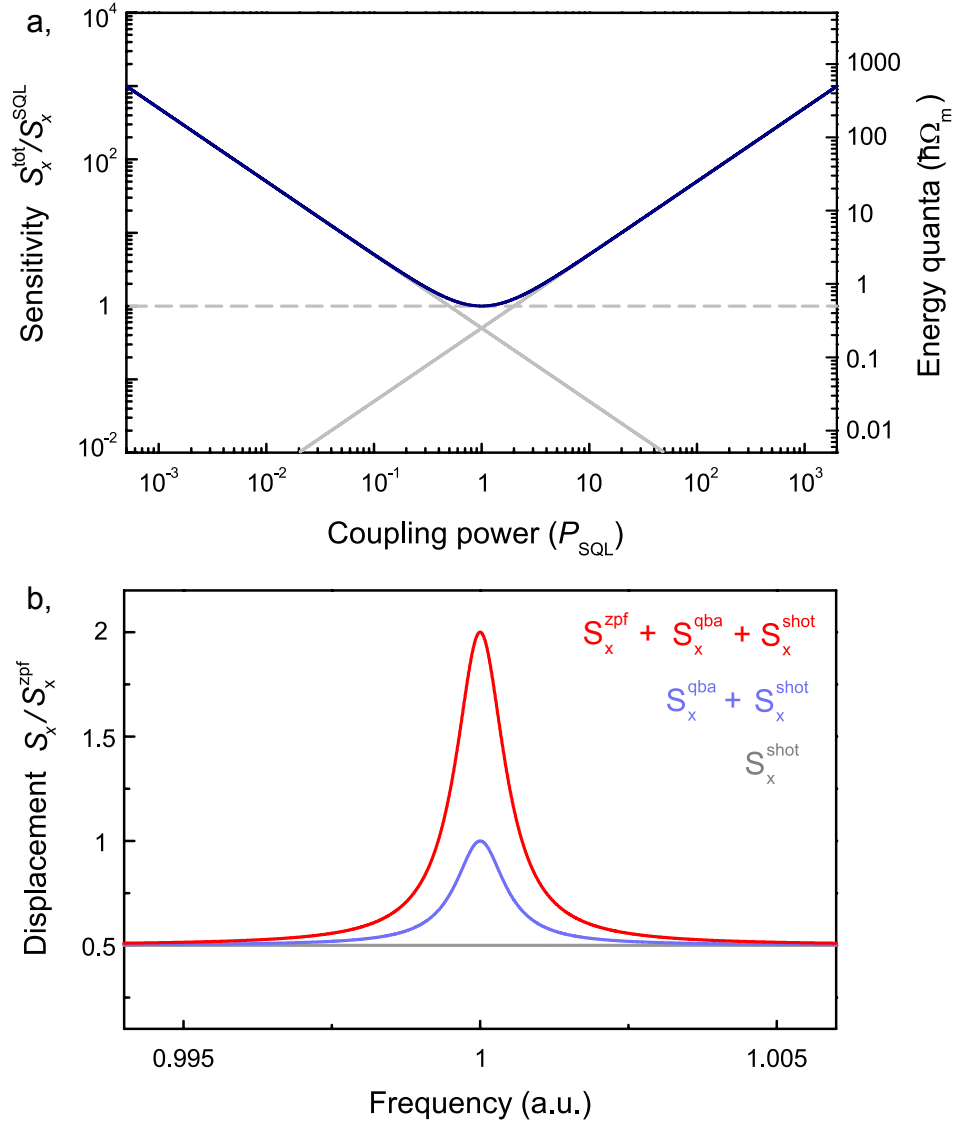


Figure 1.2: Standard quantum limit of continuous position measurement. a, Displacement sensitivity (for an ideal measurement, i.e. $\eta_c = 1$) at resonance ($\Omega_{\text{meas}} = \Omega_m$) as a function of normalized coupling power. The shot-noise (QBA-noise) decreases (increases) for increased coupling. At $P = P_{\text{SQL}}$ the optimum sensitivity equal to the zero-point fluctuations of the mechanical oscillator (dashed line) is achieved. b, Expected spectrum of a measurement at the SQL. The background is given by shot-noise and QBA-noise. At resonance, these add up to half an energy quantum of corresponding mechanical motion such that the measured mechanical peak lies at two times the zero-point fluctuations, even if the oscillator rests in its ground state, as assumed here. For $\eta_c < 1$, the minimum uncertainty, the optimum power and the shot-noise level are increased (by $\times\eta_c^{-1/2}$, $\times\eta_c^{-3/2}$, $\times\eta_c^{-2}$) whereas the quantum backaction is reduced (by $\times\eta_c$).

When the actually measured spectra at the SQL are considered, the measurement background

$$S_x^{\text{SQL}}[\Omega] = \frac{S_x^{\text{zpf}}[\Omega_m]}{2} \left(\frac{1 + 4\Omega^2/\kappa^2}{1 + 4\Omega_m^2/\kappa^2} + |\chi_m[\Omega]|^2 (m\Gamma_m\Omega_m)^2 \frac{1 + 4\Omega_m^2/\kappa^2}{1 + 4\Omega^2/\kappa^2} \right) \quad (1.52)$$

thus consists of the contribution caused by shot-noise at the detector (imprecision), as given by the first term in the above equation, which is flat around the mechanical resonance for a measurement within the cavity bandwidth, i.e. $\Omega < \kappa$. The second contribution is given by increased motion of the measured oscillator (backaction) caused by quantum backaction, as given by the second term and thus scales with the mechanical oscillator's susceptibility. This situation is depicted in Fig. 1.2b. Even if the mechanical oscillator resides in its quantum ground state, at resonance ($\Omega = \Omega_m$) a peak corresponding to $2 \times S_x^{\text{zpf}}[\Omega_m]$ is found due to the additive noise of $S_x^{\text{zpf}}[\Omega_m]/2$ contributed by both backaction and imprecision (cf. Eq. 1.52). In this context it is also instructive to normalize to the (apparent) mechanical noise quanta n_{meas} caused by the measurement. From Eq. (1.47) one obtains at resonance ($\Omega = \Omega_m$)

$$n_{\text{meas}} = \frac{1}{4\sqrt{\eta_c}} \left(p + \frac{1}{p} \right). \quad (1.53)$$

This expression further shows that at optimum coupling ($p = 1$, $\eta_c = 1$), the measurement adds $1/2$ energy quantum of excess noise to the intrinsic mechanical oscillator motional state. $1/4$ quantum of excess noise is thereby real motion imprinted onto the mechanical oscillator (caused by quantum backaction) and another $1/4$ quantum of apparent motion is imprinted onto the measured spectrum at the detector (caused by shot-noise at the detector). Thus, the measured mechanical peak is always increased by at least half a noise quantum due to both imprecision and backaction.

Operating at the shot-noise limit when measuring a mechanical oscillator's position can simply be achieved by employing a sufficiently low-noise laser. The situation where quantum backaction is the dominant source of uncertainty has, in contrast, to date never been experimentally accessed with solid-state mechanical oscillators. In principle, as mentioned earlier, it should simply be achieved by increasing the coupling power p . However, due to practical limitations both in g which cannot be engineered to arbitrarily high values and P which is limited by available laser power and adverse thermal effects typically present in real systems, this regime has to date not been reached. Besides the mere demonstration of the quantum limits in continuous displacement measurements this regime is interesting from several points of view.

First of all, if the mechanical oscillator is predominantly driven by radiation pressure shot-noise this can be used as a resource for squeezing the output field of the cavity [60, 63] since the optomechanical system behaves like an effective Kerr-medium. Moreover, as in such a regime the statistics of the light field fluctuations are imprinted onto the mechanical oscillator's motion, measuring its position (with a second laser field), in principle allows quantum-non-demolition measurements of the intracavity field [64–66].

In addition, measurement techniques have been proposed [67–69] that are sensitive only to a single quadrature of the mechanical motion and hence offer the possibility of back-action evasion. Thus, quantum non-demolition measurements of one quadrature of motion can be achieved. That such a measurement is feasible in principle has recently been demonstrated [70]. If applied in a situation where the quantum backaction would limit a linear measurement, a total sensitivity below the standard quantum limit can be achieved for the measured quadrature via backaction evasion. The further the transducer operates in the quantum backaction dominated regime, the better the attainable sensitivity thereby may become. Moreover, such a measurement offers the additional prospects of creating a squeezed mechanical oscillator state [69].

1.1.4 Radiation pressure force - dynamical backaction

Now, let us have a look at dynamical radiation pressure effects occurring in cavity optomechanical systems.

The optomechanical coupling rate g_0 indeed can give rise to Raman-like scattering of photons interacting with the mechanical degree of freedom via the radiation pressure quantum backaction term, cf. Eq. (1.43). Fig. 1.3a illustrates both Stokes and anti-Stokes scattering process which lead to creation and annihilation of a phonon accompanied by a photon energy shift corresponding to the phonon energy $\hbar\Omega_m$. Using Fermi's golden rule, the corresponding rates can be derived from the (non-symmetrized) photon number fluctuations $S_N[\Omega]$ (1.40), leading to radiation pressure force fluctuations as $S_F[\Omega] = (\hbar g)^2 S_N[\Omega]$

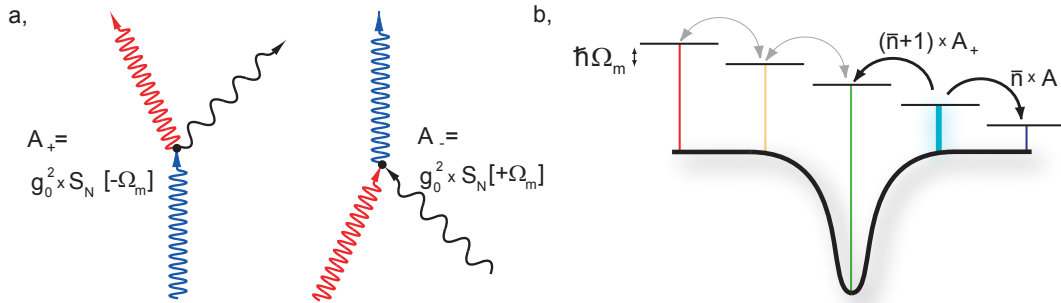


Figure 1.3: Radiation pressure induced photon-phonon scattering. a, Stokes (anti-Stokes) scattering processes with amplitude $A_+[\Omega_m]$ ($A_-[\Omega_m]$) lead to a red (blue)-shift of the photon energy by $\hbar\Omega$ and the creation (annihilation) of a phonon (black) with energy $\hbar\Omega_m$. b, The asymmetry provided by the optical resonance for non-zero detuning provides a net rate $|A_- - A_+| \neq 0$ extracting energy quanta ($\hbar\Omega_m$) from or transferring energy quanta to the mechanical oscillator. The latter corresponds to the depicted case of blue detuned pumping. It is noted that the probability of Stokes (anti-Stokes) process scales as $\propto \bar{n} + 1$ ($\propto \bar{n}$), where \bar{n} is the mechanical oscillator's mean occupation.

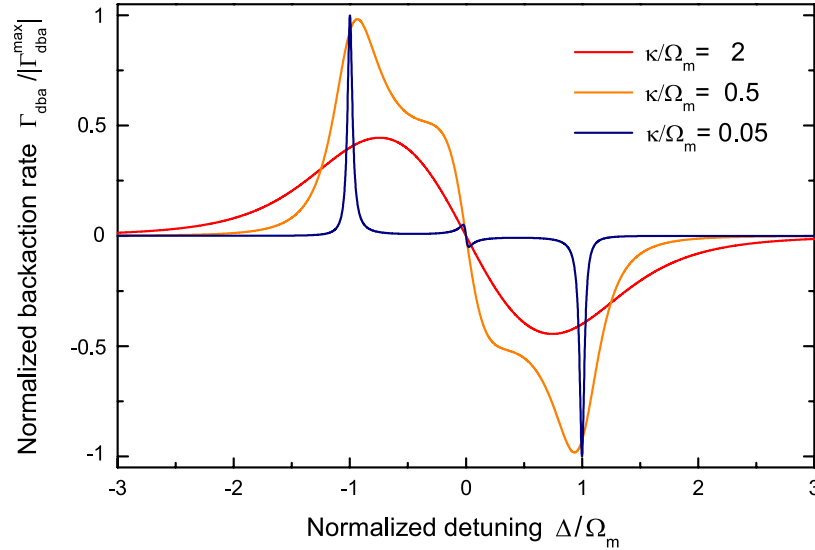


Figure 1.4: Normalized dynamical backaction rate $\Gamma_{\text{dba}}/|\Gamma_{\text{dba}}^{\text{max}}|$. For negative (positive) detuning the backaction rate is positive (negative) leading to (anti-) damping of the mechanical oscillator provided by the light field. Depending on the ratio κ/Ω_m , the functional form of Γ_{dba} changes from a broad dispersive feature around zero detuning ($\kappa/\Omega_m \gg 1$) to two sharp peaks centered around $\Delta = \pm\Omega_m$ ($\kappa/\Omega_m \ll 1$).

(1.43). The rates A_{\mp} for phonon annihilation/creation can then be written as [36]

$$A_{\mp} = g_0^2 \times S_N[\pm\Omega_m], \quad (1.54)$$

as long as the coupling is sufficiently weak ($\bar{a}g_0 \ll \kappa, \Omega_m$) and the mechanical damping is small enough ($Q_m = \Omega_m/\Gamma_m \gg 1$ and $\Gamma_m \ll \kappa$).

The sum of both rates gives rise to a net damping/amplification rate of the mechanical oscillator induced by the light field:

$$\Gamma_{\text{dba}} = A_- - A_+ = g_0^2 \bar{a}^2 \left(\frac{\kappa}{\kappa^2/4 + (\Delta + \Omega_m)^2} - \frac{\kappa}{\kappa^2/4 + (\Delta - \Omega_m)^2} \right). \quad (1.55)$$

This is exactly the additional damping rate given by Eq. (1.31), derived from the quantum Langevin equations in section 1.1.2. For negative detuning Γ_{dba} always exhibits positive values indicating additional damping of the mechanical oscillator provided by the light field. Contrarily, for positive detuning, Γ_{dba} is always negative leading to anti-damping or driving of the mechanical oscillator. For large κ/Ω_m the backaction rate follows a dispersive shape (as a function of detuning Δ) with a width given by $\kappa/2$. For smaller ratios, a crossover occurs into a regime where Γ_{dba} shows two sharp peaks around $\Delta = \pm\Omega_m$ whose linewidths approach κ . For given pump power P , couplings g_0 , η_c and mechanical frequency Ω_m the maximum backaction rate is indeed found at $\Delta = \pm\Omega_m$ for $\kappa \rightarrow 0$, where the variation of

the intra-cavity mean-field given by Eq. (1.8) is explicitly taken into account. One thus finds a maximum backaction rate of

$$\Gamma_{\text{dba}}^{\text{max}} = \mp 4 \eta_c \frac{g_0^2}{\Omega_m^2} \frac{P}{\hbar \omega}. \quad (1.56)$$

Fig. 1.4 shows the corresponding normalized shape of the dynamical backaction rate $\Gamma_{\text{dba}}/|\Gamma_{\text{dba}}^{\text{max}}|$ as a function of the normalized detuning Δ/Ω_m for different values of κ/Ω_m but constant input power P and couplings g_0 and η_c .

In the following two sections both the possibility of cooling and amplification mediated by Γ_{dba} will be discussed.

1.1.4.1 Radiation pressure cooling

In the case of negative detuning, the dynamical backaction rate is positive, which can give rise to cooling of the mechanical oscillator. The fact that a positive dynamical backaction rate which at first glance is simply an additional source of damping can give rise to cooling can be understood by considering the effective temperature of the equivalent heat-bath which the mechanical oscillator is coupled to via the dynamical backaction rate. Owing to the coherent laser input, which has quantum limited noise properties, this effective temperature is typically considerably lower than even cryogenic temperatures, provided that $\kappa \lesssim \Omega_m$, as will be shown below. Thus, coupling the mechanical oscillator to such a cold bath, leads to a net flux of energy from the mechanical oscillator into the cold bath until equilibrium is reached.

Detailed balance [71] demands that in equilibrium the rate of optomechanically created phonons $(n+1) \times A_+$ equals the rate of annihilated phonons $n \times A_-$. Using Eq. (1.54) and assuming Bose-Einstein statistics for the mechanical oscillator this would lead to an effective equilibrium temperature T_{qba} given by

$$\exp \left[\frac{\hbar \Omega_m}{k_B T_{\text{qba}}} \right] = \frac{\kappa^2/\Omega_m^2 + 4(\Delta/\Omega_m - 1)^2}{\kappa^2/\Omega_m^2 + 4(\Delta/\Omega_m + 1)^2}. \quad (1.57)$$

Thus, the temperature of the effective heat bath provided by the laser field T_{qba} vanishes if $\Delta = -\Omega_m$ and $\kappa/\Omega_m \rightarrow 0$, for which the right hand side of the above expression diverges. The equilibrium phonon number n_{qba} corresponding to Eq. (1.57) evaluates to

$$n_{\text{qba}} = \frac{\kappa^2/4 + (\Delta + \Omega_m)^2}{-4 \Delta \Omega_m}. \quad (1.58)$$

The same result can be derived from the quantum backaction force spectral density $S_F^{\text{qba}}[\Omega]$ obtained using the quantum Langevin approach (Eq. 1.43) which leads to excess motion of the mechanical oscillator $S_x^{\text{qba}}[\Omega]$ (cf. Eq. 1.41). The mean squared displacement caused by quantum backaction can be written as

$$\langle x^2 \rangle_{\text{qba}} = \frac{1}{2\pi} \int_{-\infty}^{\infty} |\chi_{\text{eff}}[\Omega]|^2 S_F^{\text{qba}}[\Omega] d\Omega, \quad (1.59)$$

and corresponds to excess motional quanta

$$n'_{\text{qba}} = \frac{1}{2\hbar} m \Omega_m \langle x^2 \rangle_{\text{qba}} - \frac{1}{2} \quad (1.60a)$$

$$= n_{\text{qba}} \quad (1.60b)$$

where the second equality is valid only in the relevant limit ($\bar{a}g_0 \ll \kappa, \Omega_m$; $Q_m \gg 1$ and $\Gamma_m \ll \kappa$), as derived in Ref. [72].

n_{qba} is minimized for a detuning of $\Delta_{\text{opt}} = -\Omega_m \sqrt{\kappa^2/(4\Omega_m^2) + 1}$ where one obtains the lowest, in principle achievable occupation number n_0 of

$$n_0 = \frac{1}{2} \left(\sqrt{1 + \frac{(\kappa/2)^2}{\Omega_m^2}} - 1 \right). \quad (1.61)$$

Thus, the cooling limit crucially depends on the ratio κ/Ω_m and small values are required in order to allow ground-state cooling. For $\kappa/\Omega_m = \sqrt{12}$ one obtains $n_0 = 1/2$ marking the threshold where the effective heat bath is sufficiently cold to achieve ground state-cooling. For reaching values $n_0 \rightarrow 0$ ratios $\kappa/\Omega_m \rightarrow 0$ are necessary. This regime has been termed resolved-sideband regime or good cavity limit [35, 36].

Very similar theoretical considerations and limits have been applied to laser cooling of trapped ions or atoms much earlier [73]. There, an essentially identical criterion of resolved sidebands was found, requiring a cooling transition (of the trapped ion or atom) that is narrower than the trapping frequency.

So far, the analysis completely neglected the thermal bath to which the mechanical oscillator is connected to via its intrinsic damping rate Γ_m . To complete our considerations we thus have to consider that the mechanical oscillator is in fact coupled to two competing temperature baths with temperatures T and T_{qba} (or equivalently two fluctuating force spectra, $S_F^L[\Omega]$ and $S_F^{\text{qba}}[\Omega]$), respectively, which will lead to an equilibrium occupation \bar{n} of the mechanical oscillator determined by the following rate equation [36]

$$\bar{n} (\Gamma_{\text{dba}} + \Gamma_m) = n_{\text{qba}} \Gamma_{\text{dba}} + n_{\text{th}} \Gamma_m, \quad (1.62)$$

where n_{th} denotes the mean thermal occupation of the mechanical oscillator caused by the thermal Langevin force in the absence of dynamical backaction. Since n_{th} is typically much larger than n_{qba} (since $T \gg T_{\text{qba}}$), the coupling to the thermal bath via Γ_m will prevent from reaching the cooling limit (1.61). We then obtain the equilibrium occupation

$$\bar{n} = \frac{\Gamma_m}{\Gamma_{\text{dba}} + \Gamma_m} n_{\text{th}} + \frac{\Gamma_{\text{dba}}}{\Gamma_{\text{dba}} + \Gamma_m} n_{\text{qba}}. \quad (1.63)$$

Again, this result can also be derived using the quantum Langevin approach. Integrating the spectra in Eq. (1.41) in the aforementioned limit directly yields Eq. (1.63), as shown in Ref. [72].

The above equation illustrates that the final equilibrium occupation number \bar{n} will lie between n_{th} and n_{qba} , depending on the relative weight of Γ_m and Γ_{dba} . Thus, in order to

be able to cool the mechanical oscillator to the ground state a second requirement has to be fulfilled, besides having small enough n_{qba} : The backaction rate Γ_{dba} has to be strong enough to overcome the fluctuations caused by the thermal environment. This is ensured for

$$\frac{\Gamma_{\text{dba}}}{\Gamma_{\text{m}}} \gtrsim 2 n_{\text{th}}. \quad (1.64)$$

As the framework of the above equations requires that the damping of the mechanical oscillator is smaller than its oscillation frequency, this leads to an additional constraint: the intrinsic quality factor of the mechanical oscillator has to be sufficiently large, $Q_{\text{m}} > 2 n_{\text{th}}$, such that after increasing the damping rate by the factor (1.64) one still has $Q_{\text{eff}} = \Omega_{\text{m}}/\Gamma_{\text{dba}} > 1$. Moreover, using Eq. (1.56), (1.64) can be recast into the following condition for ground-state cooling in terms of experimental parameters:

$$2 Q_{\text{m}} \frac{g_0^2}{\Omega_{\text{m}}^2} \frac{P}{\omega} > k_B T. \quad (1.65)$$

As mentioned earlier, the Stokes and anti-Stokes optical sidebands have relative weights of $(\bar{n} + 1) \times A_+$ and $\bar{n} \times A_-$ [35]. Once the mechanical oscillator is close to its ground state, i.e. $\bar{n} \rightarrow 0$, the anti-Stokes sideband is correspondingly expected to be strongly suppressed. Thus, spectroscopy of both sidebands may provide a convenient and unambiguous way to measure the equilibrium phonon number \bar{n} close to the ground state.

1.1.4.2 Heating and amplification

The opposite case, positive detuning, leads to an anti-damping of the mechanical oscillator, as depicted in Fig. 1.4. As long as $\Gamma_{\text{dba}} + \Gamma_{\text{m}} > 0$ this regime may be described, in analogy to the previous chapter, as coupling the mechanical oscillator to an effective bath whose temperature in this case has to be formally treated as a negative temperature bath [74], according to Eq. (1.57). Thus, the occupation \bar{n} of the mechanical mode is increased above its thermal equilibrium n_{th} , according to Eq. (1.63).

Note that as long as $|\Gamma_{\text{dba}}| < \Gamma_{\text{m}}$ the mechanical oscillator thus finds itself in a thermal state with an increased occupation dominated by the contribution n_{th} (in typical experimental situations for which $|n_{\text{qba}}| \ll n_{\text{th}}$).

The situation changes, however, when the threshold $\Gamma_{\text{dba}} + \Gamma_{\text{m}} \rightarrow 0$ is reached. There, the description of the dynamical backaction as an effective temperature bath breaks down. The mechanical oscillator becomes undamped and its motion can no longer be described as thermal but rather undergoes a driven, sinusoidal or coherent oscillation. This regime has been termed radiation pressure parametric instability [75, 76]. Using Eq. (1.55), the input power P_{th} , necessary to reach this regime at detuning $\Delta = \Omega_{\text{m}}$ (which is close to the optimum detuning for $\kappa \lesssim \Omega_{\text{m}}$) can be written as

$$\frac{P_{\text{th}}}{\hbar\omega} = \frac{\kappa}{\kappa_{\text{ex}}} \frac{\Gamma_{\text{m}}}{16} \frac{(\kappa/2)^2}{g_0^2} (1 + 4\Omega_{\text{m}}^2/\kappa^2) (4 + \kappa^2/(4\Omega_{\text{m}}^2)). \quad (1.66)$$

This power scale that also describes the power needed to cool the oscillator by a factor of $\times 2$ coincides (up to the factor $(4 + \kappa^2/4\Omega_m^2)/\eta_c$) with the power needed to reach the SQL (1.51) and thus can be regarded as a quite universal figure of merit. It describes both the transducer's ability to control the motional state of the oscillator and to read out its motion in a quantum limited way.

In the regime of the parametric instability, the mechanical oscillator can be rigorously described by solving Langevin equations (1.6, 1.7) for the intracavity mean-field \bar{a} and the mechanical oscillation amplitude, assuming a sinusoidal oscillation. Rich nonlinear dynamics can be found, giving rise to a complex attractor diagram for stable solutions of the mechanical oscillation amplitude \bar{x} [77–79]. Here, we will focus on considering a fixed positive detuning $\Delta = \Omega_m$. Then, the harmonic oscillation amplitude can be shown to depend solely on the normalized driving strength $D = 2\bar{a}^2\kappa^2g_0^2/\Omega_m^4$ [78], until the oscillation will eventually become chaotic [27].

The analogy of this transition to the threshold found in lasers has attracted significant interest recently among various physical realizations [80–83]. In particular the mechanical oscillator's linewidth is considerably narrowed above threshold. Indeed an expression very close to the formulae derived by Schawlow and Townes for lasers and masers [84, 85] is found [86] for the oscillator linewidth Γ_0

$$\Gamma_0 = \Gamma_m \frac{n_{\text{th}} + A_+}{n_c}. \quad (1.67)$$

Here, n_c denotes the number of phonons contributing to the coherent motion of the oscillator which is limited to $\sqrt{n_c} \lesssim \kappa/(4g_0)$ whereas n_{th} is the number of thermal phonons. A_+ describes the backaction limit to the linewidth in analogy to the spontaneous emission terms limiting laser and maser linewidths. The ability to thus create and control narrow linewidth optomechanical oscillators possibly ranging from medium to ultra-high frequencies triggered efforts to explore the suitability of such systems for frequency reference purposes [29–31].

1.1.5 Optical spring effect

The radiation pressure force arising from the imaginary part of a_x (cf. Eq. 1.26) modifies the linewidth of the mechanical oscillator and can be viewed as a viscous force. It can give rise to considerable cooling or heating/amplification of mechanical motion, as shown in the previous section. The radiation pressure force, however, can also have a component in phase with the mechanical oscillation originating from the real part of a_x (cf. Eq. 1.26) and thus affect the mechanical oscillator's eigenfrequency as given by Eq. (1.30). This so called optical spring effect can both soften or stiffen the mechanical oscillator's intrinsic rigidity and will be briefly discussed in this section.

It is interesting to note that Ω_{dba} can also directly be calculated from S_N (Eq. 1.40)

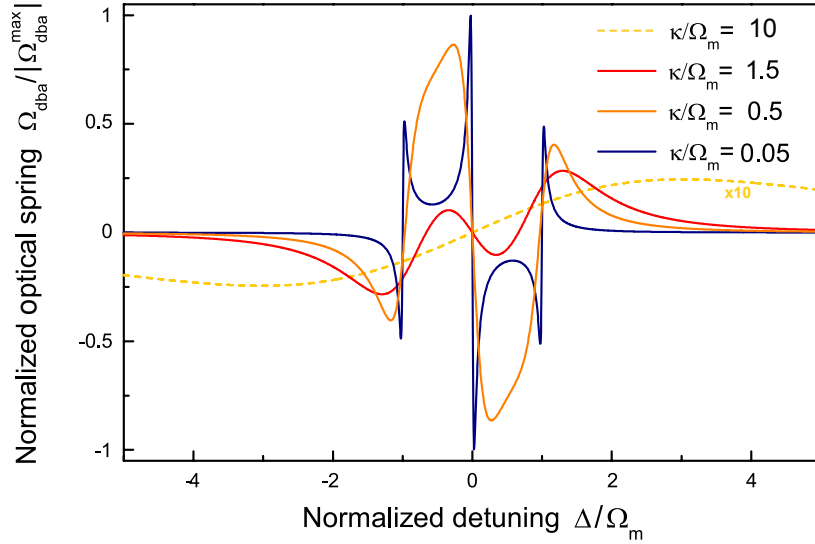


Figure 1.5: Normalized optical spring effect $\Omega_{\text{dba}}/|\Omega_{\text{dba}}|$, leading to a change of the mechanical oscillator's eigenfrequency. Depending on the ratio κ/Ω_m the sign of Ω_{dba} can be positive or negative for the same detuning. Moreover, the functional form of Ω_{dba} changes from a single, broad dispersive feature around zero detuning ($\kappa/\Omega_m \gg 1$) to three narrow dispersive features around $\Delta/\Omega_m = \pm 1$ and $\Delta = 0$ ($\kappa/\Omega_m \ll 1$).

using a Kramers-Kronig type relation [36]

$$\Omega_{\text{dba}} = g_0^2 \int_{-\infty}^{\infty} S_N[\Omega] \left(\frac{1}{\Omega_m - \Omega} - \frac{1}{\Omega_m + \Omega} \right) \frac{d\Omega}{2\pi}. \quad (1.68)$$

Using the residue theorem, one then obtains the corresponding shift Ω_{dba} induced by a particular S_N . For the case of a single optical resonance (i.e. using Eq. 1.40), Eq. (1.30) is recovered.

Similar to the case of the dynamical backaction rate Γ_{dba} (1.55), Ω_{dba} for given input power P , couplings g_0 , η_c and mechanical frequency Ω_m is maximized for $\kappa \rightarrow 0$, however at $\Delta = \pm\kappa/2$. Then, the maximum frequency shift

$$\Omega_{\text{dba}}^{\text{max}} = \mp 2 \frac{g_0^2}{\Omega_m^2} \eta_c \frac{P}{\hbar\omega} \quad (1.69)$$

is obtained. The normalized frequency shift $\Omega_{\text{dba}}/|\Omega_{\text{dba}}^{\text{max}}|$ is shown in Fig. 1.5 as a function of normalized detuning (Δ/Ω_m) and for various ratios κ/Ω_m . For large ratios κ/Ω_m , one obtains a dispersive feature around zero detuning, leading to a softening (stiffening) of the mechanical oscillator for $\Delta < 0$ ($\Delta > 0$). The maxima in this regime are located at $\Delta \approx \pm\kappa/(2\sqrt{3})$. Similar to the dynamical backaction rate, also the optical spring effect exhibits a more complex dependence on detuning if the mechanical oscillation frequency is

in the range of the optical bandwidth, as shown in Fig. 1.5. In the limit $\kappa/\Omega_m \rightarrow 0$, one obtains three dispersive features at $\Delta = \pm\Omega_m$ and $\Delta = 0$.

If the maximum optical spring effect (1.69) is compared to the attainable dynamical backaction rate (1.56), one obtains $\Omega_{\text{dba}}^{\text{max}}/\Gamma_{\text{dba}}^{\text{max}} = 1/2$, for the resolved-sideband regime ($\kappa \ll \Omega_m$). Thus, both effects are comparable in absolute terms. However, when considering high Q mechanical oscillators, i.e. $\Omega_m \gg \Gamma_m$, the relative dynamical backaction induced shift is much larger for the oscillator's linewidth than for its frequency. Cooling by a factor $\times 2$, for example, i.e. a factor $\times 2$ increase in linewidth, implies the possibility to obtain a relative resonance frequency shift of only $1/(2Q_m) \ll 1$. Thus, for experiments with $\kappa \lesssim \Omega_m$ the optical spring effect is typically less important. In the Doppler regime ($\kappa \gg \Omega_m$), however, the ratio of both quantities scales as (κ/Ω_m) and strong optical springs may be obtained despite comparatively low dynamical backaction rates [48, 87].

1.2 Toroid microresonators and their optical properties

The work presented in this thesis is based on toroid microresonators [88]. These monolithic on-chip whispering gallery mode optical microcavities exhibit an exceptional combination of small mode volume and very long photon storage times leading to an optical finesse that can exceed one million. The optical properties of toroid microresonators have been exploited for various research areas ranging from non-linear optics, such as frequency comb generation [89–91] or Raman lasing [92], to molecular recognition [93] and cavity QED [94–96].

In this thesis, they are exploited for cavity optomechanics. Thereby, two conceptionally entirely different approaches to cavity optomechanics are studied, both based on toroid microresonators. The first one exploits the evanescent optical near-field of the toroid microresonators to couple their optical modes to separate nanomechanical oscillators. This approach extends dispersive cavity optomechanics to sub-wavelength scale nanomechanical oscillators and constitutes a *nano*-optomechanical system. The experiments performed with this system will be presented in chapter 2. The second approach explores the interaction of the toroid microresonator’s optical with its intrinsic mechanical modes that are naturally parametrically coupled to each other as discovered in 2005 [26–28]. This study and the resulting system, monolithic ultra-low dissipation *micro*-optomechanical resonators, will be presented in chapter 3. Since both build upon the same optical resonator its fundamental optical properties will be presented in this section.

First, an analytic approximation for the optical modes of toroid microresonators along with the respective mode volume will be discussed and compared to results from finite element simulations. Then tapered fibre coupling to the optical modes will be briefly described.

1.2.1 Optical mode profile

The eigenmodes $\vec{E}_j(\vec{r}, t) = \vec{E}_j(\vec{r}) e^{-i\omega_j t}$ ($j \in \mathbb{N}$) of a dielectric body are in principle given by the solutions of the wave equation:

$$\left(\nabla^2 - \frac{\epsilon(\vec{r})}{c^2} \right) \frac{\partial^2 \vec{E}_j(\vec{r}, t)}{\partial t^2} = 0, \quad (1.70)$$

where c denotes the speed of light in vacuum and $\epsilon(\vec{r})$ denotes the position dependent relative dielectric constant, reflecting the geometric structure of the dielectric. Solutions of the wave equation follow the dispersion relation $k_j(\vec{r})^2 = \epsilon(\vec{r})(\omega_j/c)^2$ and fulfill the Helmholtz equation:

$$\left(\nabla^2 + \epsilon(\vec{r}) \frac{\omega_j^2}{c^2} \right) \vec{E}_j(\vec{r}) = 0. \quad (1.71)$$

For spherical resonators, this equation can be solved exactly by separation of variables. Due to their resemblance to toroids, the solution for spheres will briefly be described here.

Using spherical coordinates and assuming transverse electric (TE) and transverse magnetic (TM) modes, respectively, Eq. (1.71) leads to the well known whispering gallery modes of spheres [97, 98] characterized by the mode number triplet (ℓ, m, q) . The azimuthal dependence of these is simply sinusoidal in nature ($\propto e^{\pm i\ell\varphi}$), with the azimuthal mode number $\ell \in \mathbb{N}$ describing the number of full wave trains along the sphere's equator. The polar dependence of the modes can be expressed in terms of associated Legendre polynomials $P_m^\ell(\cos(\theta))$ with the polar mode number $m \in \{-\ell, \dots, \ell\}$ related to the number of field nodes in polar direction via $|l - m|$. Finally, the radial dependence of the field can be written in terms of cylindrical Bessel functions $J_{m+1/2}$ within the sphere and cylindrical Hankel functions $H_{m+1/2}$ outside the sphere. Continuity relations of the field across the sphere boundary fix the third, radial mode number $q \in \mathbb{N}$ which also indicates the number of field nodes $q - 1$ in radial direction. The full solutions and their detailed derivation can be found in Refs. [97, 98].

For toroids, in contrast, no such closed analytic solutions exist. However, an analytic approximation based on a spheroid approximation in cylindrical coordinates (φ, ρ, z) has been developed [99, 100]. For a toroid with major radius R and minor radius r , the optical field of a fundamental ($|m - \ell| = 0, q = 1$) mode with mode number ℓ may, in the vicinity of the equatorial plane, be expressed as:

$$E_\zeta \approx \begin{cases} E_0 \exp\left[-\frac{z^2}{2r_z^2}\right] J_\ell\left(T_{\ell 1} \frac{\rho}{R}\right) e^{i\ell\varphi}, & \rho < R, \\ \frac{1}{P} E_0 \exp\left[-\frac{z^2}{2r_z^2}\right] J_\ell\left(T_{\ell 1} \frac{R}{R}\right) e^{i\ell\varphi} e^{-\alpha(\rho-R)}, & \rho > R, \end{cases} \quad (1.72)$$

where $\bar{R} = R + \frac{P}{k_0\sqrt{n^2-1}}$ is an effective radius and $T_{\ell 1}$ denotes the first zero of J_ℓ ⁶. The refractive index of the toroid is denoted by n and k_0 is the (vacuum) wavenumber $k_0 = 2\pi/\lambda$, where λ denotes the (vacuum) wavelength. Note that unlike for spheres the optical modes of spheroids and toroids respectively are strictly speaking not pure transverse electric (TE) or transverse magnetic (TM) [99]. The modes can however be approximately treated as TE-like modes, for which $P = 1$ and $\zeta \approx z$ and TM-like modes for which $P = 1/n^2$ and $\zeta \approx \rho$. The mode width r_z in z direction is given by

$$r_z = \frac{R^{3/4} r^{1/4}}{\sqrt{\ell}} \frac{1}{(1 - R/(4\ell^2 r))^{1/4}}. \quad (1.73)$$

The evanescent part of the field decays on a length scale $\alpha^{-1} \sim \lambda/(2\pi)$. More precisely, the decay length α^{-1} can be approximated by:

$$\alpha^{-1} \approx \frac{\lambda}{2\pi} \left(\frac{1}{\sqrt{n^2-1}} - \frac{\alpha_1 n^2 (3-2P^2)}{6(n^2-1)^{3/2}} \left(\frac{\ell}{2}\right)^{-2/3} \right) \approx \frac{\lambda}{2\pi\sqrt{n^2-1}}, \quad (1.74)$$

⁶ for $\ell \gg 1$, as is the case here, these can be approximated by $T_{\ell 1} = \ell + 1.8558\ell^{1/3} + \mathcal{O}(\ell^{-1/3})$

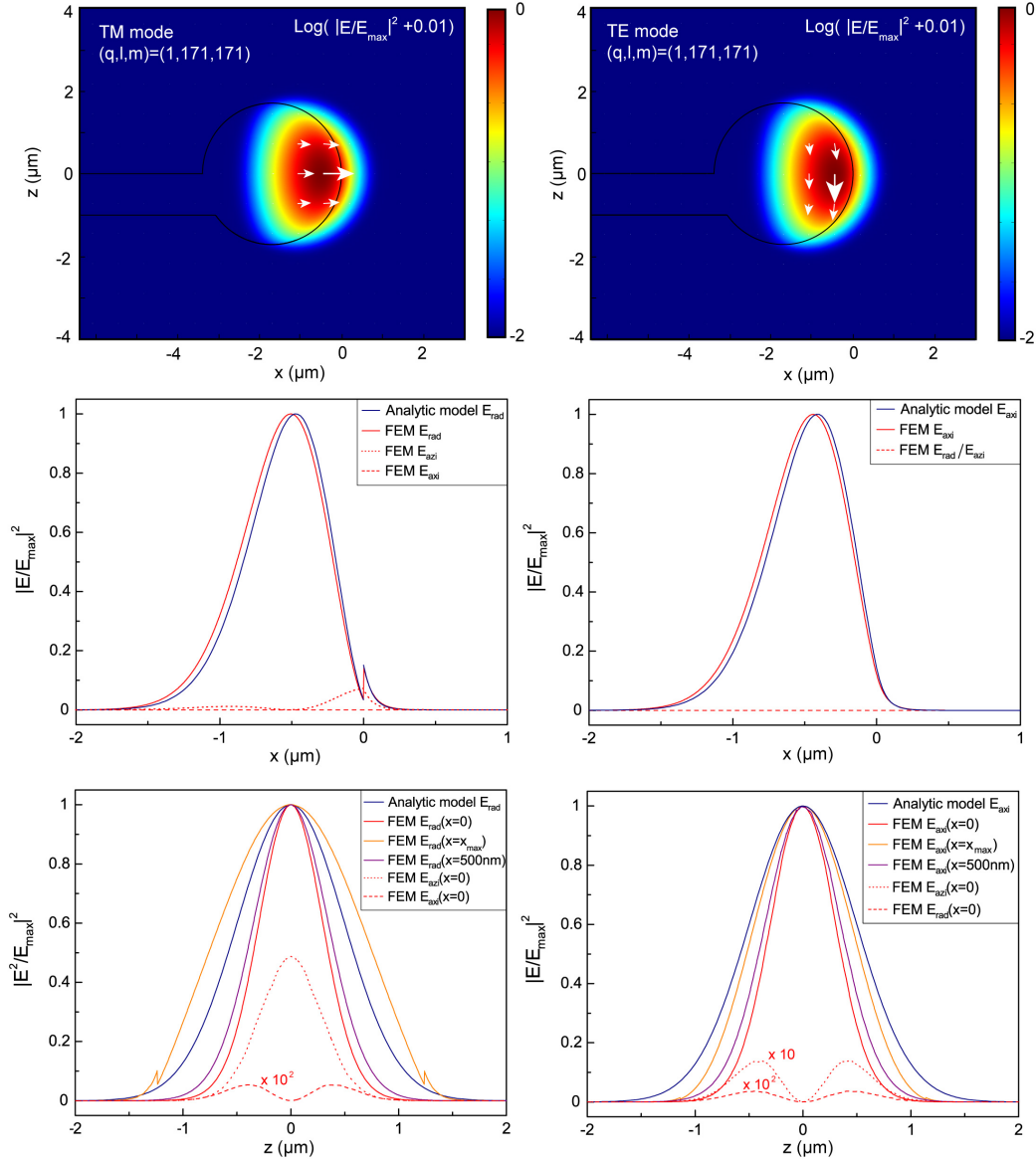


Figure 1.6: Fundamental optical mode of toroid microresonators (left column: TM-like mode at 797 nm; right column: TE-like mode at 800 nm; both for $n = 1.45$). Top row: colour-coded field distribution obtained by finite element simulations (E_{\max} denotes the field maximum). Second row: radial, axial and azimuthal field components as a function of the position x (at $z = 0$) obtained from both the finite element simulation and the analytic model in Eq. (1.72). Bottom row: field components as a function of z for various values of x . The TM-like mode has a considerable admixed azimuthal field component whereas the TE-like mode has a more pure polarization (x_{\max} denotes the x -coordinate of the field maximum position). Overall, the analytic model yields a good approximation of the finite element simulation results.

where α_1 denotes the negative first zero of the Airy function ($\alpha_1 \approx 2.33811$). In the same approximation, the mode number ℓ of the fundamental modes can be expressed via the following equation:

$$nk_0R = \sqrt{T_{\ell 1}^2 + \ell\sqrt{R/r}} - \frac{Pn}{\sqrt{n^2 - 1}}. \quad (1.75)$$

Fig. (1.6) shows an overview of the normalized field amplitudes of TE and TM modes for a toroid with typical geometry ($R = 16 \mu\text{m}$, $r = 1.7 \mu\text{m}$) calculated both by the above approximation and by finite element method (FEM) simulations⁷. Good agreement between Eq. (1.72) and the FEM results to a level of a few percent is typically found. Also the resonance frequencies predicted by Eq. (1.75) typically deviate less than 1% from the FEM values.

1.2.2 Optical mode volume

The volume of an optical cavity mode is an important quantity that is influencing the coupling of the resonator to other systems such as atoms studied in cavity quantum electrodynamics [102, 103] but also to mechanical oscillators explored in the field of cavity optomechanics [15, 16]. In particular, it will be of relevance in chapter 2 of this thesis. Usually [92, 104], it is defined as

$$V_\ell = \frac{\int \epsilon(\vec{r}) |\vec{E}_\ell(\vec{r})|^2 d\vec{r}}{\epsilon(\vec{r}_{\max}) \max_{\vec{r}} |\vec{E}_\ell(\vec{r})|^2}, \quad (1.76)$$

for a particular mode \vec{E}_ℓ (\vec{r}_{\max} denotes the position of the electric field maximum). Using the above approximation, the cavity mode volume of a toroid microresonator can then (for both TE- and TM-like modes) be approximated as:

$$V_\ell = \pi^{3/2} \bar{R}^2 r_z \frac{J_\ell'(T_{\ell 1})^2}{J_\ell^2(T_{\ell 1}')}, \quad (1.77)$$

where $T_{\ell 1}' > 0$ is the the first local maximum of J_ℓ and J_ℓ' denotes its derivative. Keeping only first order terms, the mode volume can thus be written as

$$V_\ell \approx 15.1 \frac{R^{11/4} r^{1/4}}{\ell^{7/6}} \approx 1.15 R^{19/12} r^{1/4} \lambda^{7/6}. \quad (1.78)$$

It is interesting to note that the toroid's minor radius r has evidently only very little influence on the cavity mode volume. Fig. 1.7 shows the mode volume as a function of wavelength for different major and minor radii according to the above equation as well as using FEM simulations. Due to the approximations used in Eq. (1.72) the accuracy is best for large ℓ and small R/r . For the most relevant parameter space used in this thesis, excellent agreement ($< 10\%$) between model and FEM simulation is found.

⁷ The code used for these simulations using Comsol Multiphysics is adapted from [101] and given in appendix D.

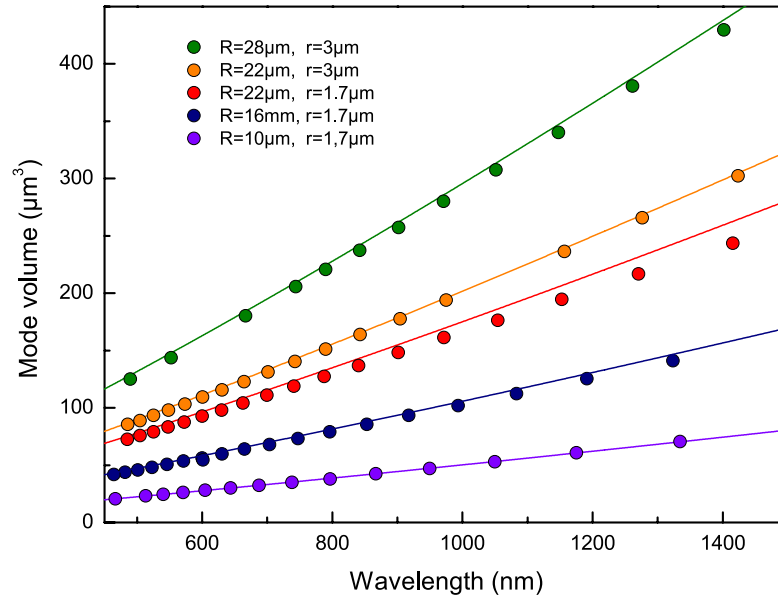


Figure 1.7: Optical mode volume of fundamental TM-like toroid microresonator modes. For a variety of parameters (see inset) the mode volume is evaluated as a function of wavelength using both finite element simulation (dots) and the simplified analytic model (lines) given by Eq. (1.78). Good agreement, in particular for small R/r , is found.

1.2.3 Tapered fibre coupling

Coupling light in and out of whispering gallery mode microresonators has been achieved using several different methods. Prism coupling (see e.g. Ref. [105]) has provided a flexible and also efficient method to couple free-space laser beams to whispering gallery modes. It requires, however, a rather bulky setup and is not easily compatible with micron scale systems. Subsequently, also side-polished fibres were used for coupling, providing

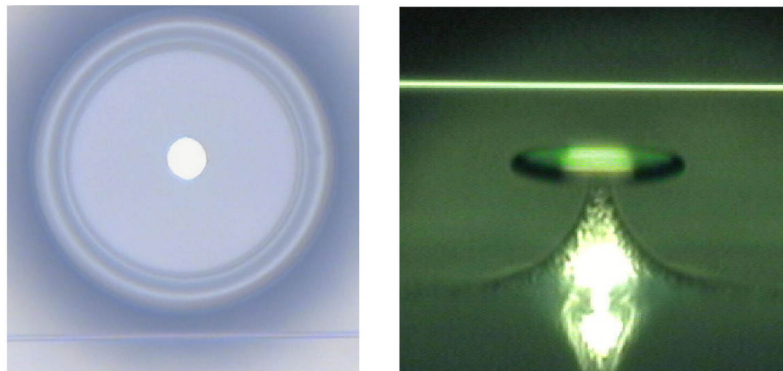


Figure 1.8: Micrographs of a toroid microresonator coupled to a single-mode tapered optical fibre. Top view (left, field of view $\sim 100 \mu\text{m}$) and side view (right, $\sim 200 \mu\text{m}$).

the convenience of having a single-mode optical fibre as input and output coupler. The efficiency of this method, however, is comparatively low. With tapered fibre coupling a method has been found [106] that combines both the convenience of fibre coupling and an efficiency that enables coupling of more than 99% of the input field into a whispering gallery mode [107]. Thereby, a single-mode optical fibre is adiabatically tapered down to a diameter of only a few hundred nanometres. The mode guided within the fibre becomes partially evanescent and thus spatially overlapping evanescent fields of tapered fibre and whispering gallery mode (of toroid microresonators in our case) can couple light in and out of the resonator. Fig. 1.8 shows a micrograph of a toroid coupled to a tapered optical fibre. The diameter of the fibre taper is thereby adjusted such that the propagation constants of the fields within the taper and the toroid match. Highly efficient and stable coupling to toroid microresonators of various sizes is achieved at wavelenghts ranging from 800 nm to 1550 nm with tapers that can maintain a transmission exceeding 99%. The fabrication of the fibres used in this thesis is described in appendix B.2.1.

Chapter 2

Near-field cavity optomechanics

The mutual coupling of optical resonators and mechanical degrees of freedom has in recent years become an area of intense research [15–17], as introduced in the previous chapter. Until 2009, the vast majority of cavity optomechanical systems relied on Fabry-Perot type resonator configurations where a light beam is trapped between a fixed and a moveable mirror. This experimental setting which has its origin in the power recycling cavities of laser gravitational wave interferometers enabled extremely sensitive measurements of the moveable mirror’s motion down to a sensitivity of $10^{-19} \text{ m}/\sqrt{\text{Hz}}$ already in the 1990s [108, 109]. In the subsequent decade, advances in microfabrication have, moreover, allowed miniaturization of the employed cavity mirrors and thus a concomitant drastic increase of their susceptibility to external forces. This led to the observation of dynamic radiation pressure phenomena that were predicted already decades ago, such as radiation pressure cooling of micromechanical oscillators [25, 32–34]. Using the aforementioned experimental configuration, the miniaturization of the resonators is, however, fundamentally bound by the optical diffraction limit. The reflecting element must not be smaller than the diffraction limited optical spot size in order to prevent diffraction from degrading the optical quality factor of the employed cavity. Thus, this approach does not allow straightforward extension of quantum-limited measurements of mechanical motion or radiation pressure actuation to nanomechanical oscillators.

Such an extension, in turn, would be interesting from several points of view. First, nanomechanical oscillators have been successfully used as ultra-sensitive probes of mass and external forces, allowing single atomic-mass resolution [43] or single electron-spin detection [45] despite the fact that the detection methods were partially far from being quantum-limited. Improved and possibly quantum-limited transduction of nanomechanical motion could thus lead to further leaps in the performance of nanomechanical oscillators as sensitive probes. Second, the fact that in recent years nanomechanical elements that combine high mechanical quality, i.e. low coupling to the thermal environment, with extremely small effective mass (when compared to micromechanical elements) have been developed makes them highly interesting for probing quantum limits of mechanical motion.

In this thesis an approach based on cavity-enhanced optical near-fields (schematically shown in Fig. 2.1) will be reported that for the first time enabled extending quantum-

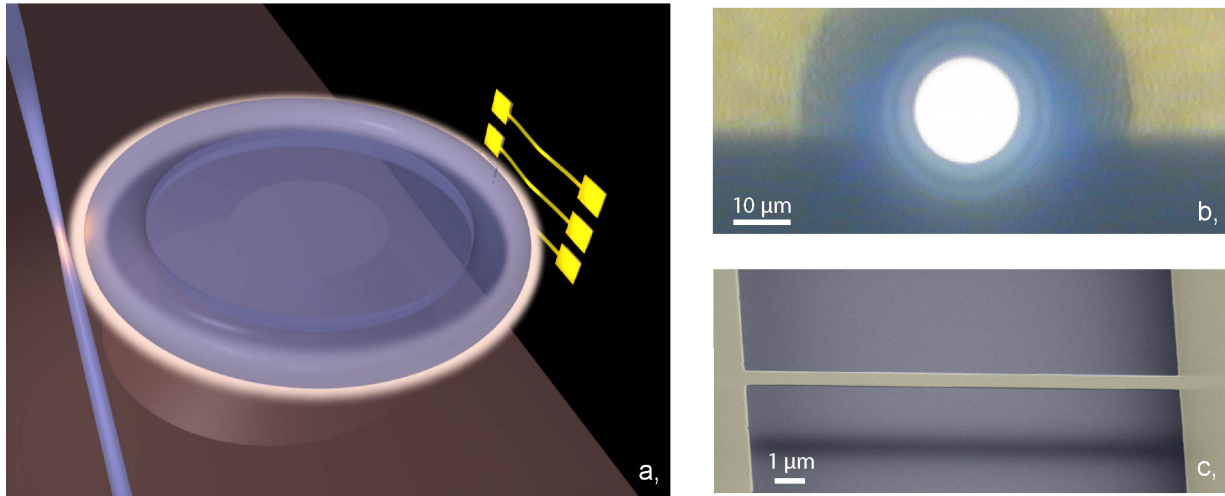


Figure 2.1: Schematic of the experimental principle. a, A toroid microresonator is pumped using a tapered optical fibre. The near-field of the optical cavity mode allows dispersive coupling to nanomechanical oscillators, here in the form of nanomechanical strings. b, Microscope top view of a toroid microresonator ($R = 16 \mu\text{m}$) suitable for near-field probing, as explained in the text. c, (False colour) scanning electron micrograph of a typical silicon nitride string used for the experiments shown in this chapter ($15 \times 0.5 \times 0.1 \mu\text{m}^3$).

limited cavity optomechanical coupling to nanomechanical oscillators. The developed system, moreover, allowed for the first time a measurement imprecision below the standard quantum limit for nanomechanical oscillators, a long sought-after goal [49, 110–115], as shown in Fig. 2.2.

In a sense, the employed approach bypasses the optical diffraction limit by resorting to evanescent optical near-fields which have also been very successfully used in the domain of near-field microscopy [116]. Already in 1983, Braginsky and Vyatchanin envisioned to use the evanescent near-field of an optical whispering-gallery resonator to couple to a dielectric “stick” parallel to the propagation direction of the optical field [117]. Several years later, around 1990, the optical forces between microspheres evanescently coupled to each other were studied both experimentally and theoretically [118, 119]. In the light of the advances in microfabrication, the idea of near-field coupling was then, during the last five years, extended to optical waveguides [120–122]. The mechanical element and the photons in such a near-field coupling configuration exchange momentum via the optical gradient force, as opposed to the scattering force used in the traditional Fabry-Perot setups. The pioneering work of Ashkin [123, 124] experimentally demonstrated that optical gradient fields can be used to exert considerable forces on particles and indeed provide a powerful tool for a variety of applications such as optical tweezers, complementing the impressive capabilities of the scattering force for cooling or amplifying a solid state mechanical oscillator’s motion [25] or for cooling atoms and ions [73], as first proposed by Hänsch and Schawlow [125] and widely used today. In Ref. [126], a recent overview of the optical gradient force and

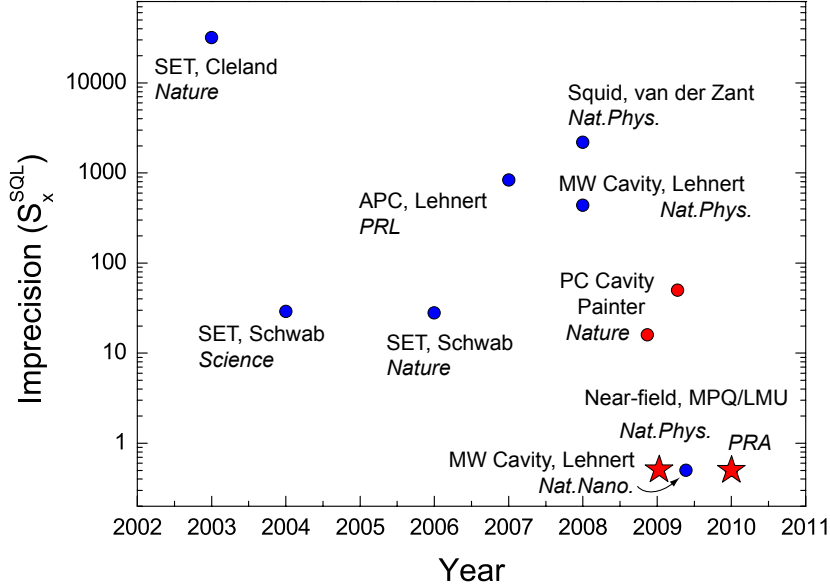


Figure 2.2: Measurement imprecision of nanomechanical motion approaching and bypassing the SQL in the past years, using various techniques. The approach reported in this section (stars) allowed for the first time a measurement imprecision below the level of the SQL in 2009 [4] and a ~ 100 times reduction of necessary input power in 2010 [2]. The blue data points represent experiments requiring cryogenic operation, performed in the groups of Cleland [44], Schwab [111, 112], Lehnert [56, 113, 114] and van der Zant [115] (SET: single-electron transistor, APC: atomic point contact, Squid: superconducting quantum interference device, MW Cavity: microwave cavity). The red data points correspond to systems operating at room temperature realized in the group of Painter [49, 53] (PC Cavity: photonic crystal cavity) and in the course of this thesis [2, 4].

its applications in the context of optomechanical systems is given.

The first experimental implementation of a nanomechanical element whose motion was actuated and transduced by optical gradient fields was reported in 2008 [127] and an electrical implementation thereof soon afterwards [128]. In 2009, the first cavity-enhanced systems incorporating a nanomechanical element were studied using a photonic crystal structure [49] and a toroid microresonator [4]. The latter work has been performed in the context of this thesis and will be reported on in this section: an experimental platform that for the first time enabled dispersive cavity optomechanics with sub-wavelength scale nanomechanical oscillators.

The evanescent near-field of toroid microresonators (see chapter 1.2) is used to couple their optical modes to the motion of dielectric nanomechanical oscillators. One type of nanomechanical oscillators studied in this thesis are strained silicon nitride nanomechanical strings as shown in Fig. 2.1c. In order to be able to bring nanomechanical oscillators which are fabricated on a silicon chip (see appendix B.1.2 for fabrication details) into the

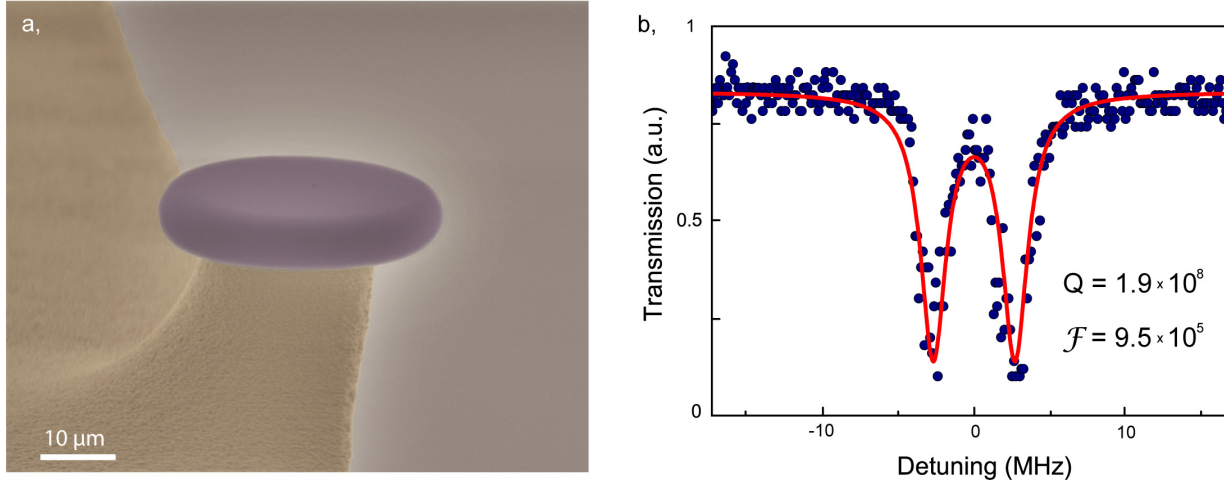


Figure 2.3: Toroid microresonator near-field sensor. a, (False colour) scanning electron micrograph of a toroid microresonator ($R = 18\ \mu\text{m}$) near-field sensor. The silica toroid (blue) resides on top of a silicon pedestal (brown) such that the toroid extends across the chip support. b, Transmission through the tapered fibre around a WGM resonance of a toroid near-field sensor. The spectrum reveals a doublet of coupled clock- and counter-clockwise modes [129] with linewidths of $\kappa/2\pi = 1.9\ \text{MHz}$. This corresponds to an optical quality factor of $Q = 1.9 \times 10^8$ and a finesse of $\mathcal{F} = 0.95 \times 10^6$.

vicinity of the optical modes of a toroid—which rests on a separate chip—the toroid has to be fabricated at the edge of its chip support such that the silica torus extends across the silicon chip. Such a toroid is shown in Fig. 2.3a (see also Fig. 2.1b). This requirement makes the fabrication of toroids suitable for near-field interactions slightly more complex than for normal on-chip toroids. The fabrication of such toroids is described in detail in appendix B.1.1. Here it shall suffice to mention that these devices can be fabricated with similarly high finesse ($\sim 10^6$) as regular toroids, which is shown in Fig. 2.3b. They are probed using regular tapered fibre coupling (cf. section 1.2.3). The tapered fibre is thereby attached to a compact mount (cf. appendix B.2.1) such that the evanescent near-field of the free-standing cavity part can be accessed by nanomechanical oscillators. These, residing on a silicon chip, are mounted on a three axis piezo cube (Attocube) that allows both translational fine- and coarse-positioning of the nanomechanical oscillators. Using a mirror mount, the respective rotational degrees of freedom of the nanomechanical oscillators can be fine-tuned. All experiments reported in this thesis are carried out in a vacuum chamber in order to rule out any gas damping of the nanomechanical oscillators. The optomechanical coupling region is however designed sufficiently close to a window in the chamber to allow optical access by a long working distance ($\sim 25\ \text{mm}$) microscope. The actual experimental apparatus and its alignment are explained in more detail in appendix B.2.

In the first section of this chapter, the optomechanical coupling in this system is theoretically analyzed. Good agreement is found with the experimental values derived in

the static measurements of the second section. The dynamic optomechanical coupling to nanomechanical oscillators is thoroughly characterized in the third section. The fourth section describes the first observation of radiation pressure dynamical backaction on nanomechanical oscillators giving rise to laser-like coherent nanomechanical oscillations as well as cooling of nanomechanical motion. Quantum limited measurements of nanomechanical motion that allowed for the first time measurements of nanomechanical motion with an imprecision below the standard quantum limit are reported in the fifth section. After section six which reports optomechanical coupling to multiple optical modes, an experiment exhibiting quadratic optomechanical coupling is described in section seven. Section eight gives the prospects of coupling to graphene mechanical oscillators.

2.1 Theoretical characterization of the optomechanical coupling

Before discussing the experimental results, the evanescent optomechanical coupling between the optical modes of a toroid microresonator and a dielectric positioned in its evanescent near-field is examined. First, a general expression based on perturbation theory is derived. Then, using this general expression and the approximations presented in section 1.2, specific results for toroid microresonators are given. Finally, these are compared to results of a finite element simulation.

2.1.1 Perturbation theory

In this section, a general analytic expression for the optomechanical coupling based on perturbation theory is derived. Starting from the general wave equation, a perturbative expression for the optomechanical coupling between an optical resonator and a dielectric can be obtained.

Let $\vec{E}_j^{(0)}(\vec{r}, t) = \vec{E}_j^{(0)}(\vec{r}) e^{-i\omega_j^{(0)}t}$ ($j \in \mathbb{N}$) be a set of normalized, orthogonal eigenmodes of the wave equation (1.70) with the dispersion relations $k_j^{(0)}(\vec{r})^2 = \epsilon^{(0)}(\vec{r})(\omega_j^{(0)}/c)^2$ and $E_j^{(0)}(\vec{r})$ fulfilling the Helmholtz equation (1.71). We will now choose a particular mode $E_i^{(0)}(\vec{r})$ and calculate the shift of the resonance frequency induced by a small external perturbation. Let $\epsilon^{(1)}(\vec{r})$ describe this perturbation of the system caused by positioning a dielectric object of volume V_{diel} in the evanescent near-field of the toroid. The approach used below does not necessitate $\epsilon^{(1)}(\vec{r}) \ll \epsilon^{(0)}(\vec{r})$, in fact the experimental situation implies $\epsilon^{(1)}(\vec{r}) > \epsilon^{(0)}(\vec{r})$. However, locality of the perturbation, that is $\int (\epsilon^{(1)}(\vec{r}) - 1) d\vec{r} \ll \int (\epsilon^{(0)}(\vec{r}) - 1) d\vec{r}$, is required. The new solution of the perturbed system may then be expressed as a linear combination of the unperturbed solutions $\vec{E}_j^{(0)}(\vec{r})$:

$$\vec{E}_i^{(0)}(\vec{r}) + \vec{E}_i^{(1)}(\vec{r}) = \left(1 + c_i^{(1)}\right) \vec{E}_i^{(0)}(\vec{r}) + \sum_{j \neq i} c_j^{(1)} \vec{E}_j^{(0)}(\vec{r}). \quad (2.1)$$

Inserting this perturbative solution into equation (1.71) one obtains (keeping only first order terms):

$$\begin{aligned} & \sum_{j \neq i} c_j^{(1)} \epsilon^{(0)}(\vec{r}) \left((\omega_j^{(0)})^2 - (\omega_i^{(0)})^2 \right) \vec{E}_j^{(0)}(\vec{r}) \\ & - \vec{E}_i^{(0)}(\vec{r}) \left(2\epsilon^{(0)}(\vec{r}) \omega_i^{(0)} \omega_i^{(1)} + \epsilon^{(1)}(\vec{r}) \left((\omega_i^{(0)})^2 + 2\omega_i^{(0)} \omega_i^{(1)} \right) \right) \\ & - \sum_j c_j^{(1)} \epsilon^{(1)}(\vec{r}) \vec{E}_j^{(0)}(\vec{r}) (\omega_i^{(0)})^2 = 0. \end{aligned} \quad (2.2)$$

Multiplying the above expression by $\left(\vec{E}_i^{(0)}(\vec{r})\right)^*$ and integrating over the entire volume,

only the second line yields relevant first order contributions ¹ and one obtains:

$$\frac{\omega_i^{(1)}}{\omega_i^{(0)}} = -\frac{1}{2} \frac{\int \epsilon^{(1)}(\vec{r}) |\vec{E}_i^{(0)}(\vec{r})|^2 d\vec{r}}{\int \epsilon^{(0)}(\vec{r}) |\vec{E}_i^{(0)}(\vec{r})|^2 d\vec{r}}. \quad (2.3)$$

Using the optical resonator's mode volume, Eq. (2.3) can be written as

$$\frac{\omega_i^{(1)}}{\omega_i^{(0)}} = -\frac{1}{2} \frac{\int_{V_{\text{diel}}} (\epsilon_{\text{diel}}(\vec{r}) - 1) |\vec{E}_i^{(0)}(\vec{r})|^2 d\vec{r}}{n^2 V_i |E_{\text{max}}|^2}. \quad (2.4)$$

Here, \vec{E}_{max} denotes the maximum of the electric field $\max_{\vec{r}} |\vec{E}_i^{(0)}(\vec{r})|$, $\epsilon_{\text{diel}}(\vec{r})$ is the relative dielectric constant of the material causing the perturbation and n is the refractive index of the optical resonator, which is assumed to be constant.

2.1.2 Analytic approximation for toroid microresonators

In the following, we will use the analytical approximations for the eigenmodes of a toroid (major radius R and minor radius r) introduced in section 1.2 in order to obtain analytic approximations of Eq. (2.4) and thus the optomechanical coupling coefficient. Let us define ξ as the ratio of the field amplitude at the toroid's (vacuum) surface and the maximum field amplitude

$$\xi = \frac{|E(\rho = R, z = 0, \varphi)|^2}{|E_{\text{max}}|^2}. \quad (2.5)$$

For a fundamental mode with angular mode number ℓ this ratio is given by

$$\xi = \frac{1}{P^2} \left(\frac{J_\ell(T_{\ell 1} R / \bar{R})}{J_\ell(T'_{\ell 1})} \right)^2. \quad (2.6)$$

To first order, this ratio can (for both TE- and TM-like modes) be approximated by $\xi \approx 1.2 (\lambda/R)^{2/3}$, i.e. it increases for smaller cavity radii and for larger wavelengths. The relative frequency shift (2.4) can then be written as

$$\frac{\omega_i^{(1)}}{\omega_i^{(0)}} = -\frac{1}{2} \frac{\xi}{V} \int_{V_{\text{diel}}} (\epsilon^{(1)}(\vec{r}) - 1) e^{-\frac{z^2}{r^2}} e^{-2\alpha x_0} d\vec{r}, \quad (2.7)$$

with the distance of the toroid's rim to the surface of the dielectric $x_0 = \rho - R$. Thus, we are now in a position to calculate the optomechanical coupling coefficient $g \equiv \partial\omega^{(1)}/\partial x_0$:

$$g = \alpha \omega^{(0)} \frac{\xi}{V} \int_{V_{\text{diel}}} (\epsilon^{(1)}(\vec{r}) - 1) e^{-\frac{z^2}{r^2}} e^{-2\alpha x_0} d\vec{r}. \quad (2.8)$$

¹ Note the orthonormality of the unperturbed eigenmodes $\int \vec{E}_j^{(0)}(\vec{r}) \vec{E}_i^{(0)}(\vec{r})^* = \delta_{ji}$ and the locality of the perturbation $\int (\epsilon^{(1)}(\vec{r}) - 1) d\vec{r} \ll \int (\epsilon^{(0)}(\vec{r}) - 1) d\vec{r}$.

Using equations (1.77) and (2.6) a simple first order expression can be found for the term ξ/V

$$\frac{\xi}{V} = \frac{\sqrt{2}}{\pi} \frac{n^{5/2}}{n^2 - 1} \lambda^{-1/2} R^{-9/4} r^{-1/4}. \quad (2.9)$$

Keeping only first order terms and assuming a point-like dielectric with refractive index n_{diel} positioned in the equatorial plane, the following simple expression for the coupling coefficient g is found (for both TE- and TM-like modes):

$$g = \frac{\omega}{\lambda} \left(\frac{2^{3/2} n^{5/2}}{\sqrt{n^2 - 1}} \right) (n_{\text{diel}}^2 - 1) \frac{V_{\text{diel}}}{R^{9/4} r^{1/4} \lambda^{1/2}} \exp \left[-\frac{4\pi\sqrt{n^2 - 1}}{\lambda} x_0 \right]. \quad (2.10)$$

Employing the traditional Fabry-Perot type cavity approach enables coupling coefficients $g = \omega/L$ where for the characteristic cavity length one typically has $L \gg \lambda$. The term ω/λ in the above equation implies that, in principle, using the gradient field approach, much larger optomechanical coupling can be achieved. Indeed to fully harness this possibility and enable $g \sim \omega/\lambda$, the gap x_0 has to be considerably smaller than the corresponding typical $1/e$ distance, i.e. $x_0 \ll 100 \text{ nm}$ (for $\lambda \sim 850 \mu\text{m}$ and $n = 1.45$), which is experimentally feasible. Moreover, for typical geometry parameters of a toroid ($R \sim 16 \mu\text{m}$, $r \sim 2 \mu\text{m}$) and assuming $n_{\text{diel}} = 2$, a sampled volume of order $V_{\text{diel}} \sim (3 \mu\text{m})^3$ is necessary in order to reach a coupling of $g = \omega/\lambda$. This is large considering that a point-like dielectric was assumed earlier on. So, a more detailed analysis is necessary to conclude how closely $g = \omega/\lambda$ can be approached and will be given in the next section.

Moreover, it is interesting to note that using the near-field approach a stronger scaling of the optomechanical coupling with wavelength is found compared to the scattering force approach. There, the coupling g is simply inversely proportional to wavelength, whereas here—in the case of a point-like dielectric—it scales as $g \propto \lambda^{-2.5}$. Regarding the coupling coefficient, short wavelengths therefore seem to be highly advantageous.

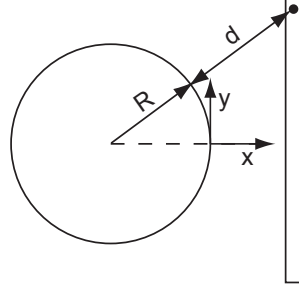
Two types of dielectric mechanical oscillators have been studied during the course of this thesis: micromechanical membranes (typical dimensions: $(50 - 1000 \mu\text{m})^2 \times 30 \text{ nm}$) and nanomechanical strings ($30 \mu\text{m} \times 500 \text{ nm} \times 100 \text{ nm}$). In the following the optomechanical coupling coefficients for these particular geometries will be evaluated.

2.1.2.1 Micromechanical membrane

We first consider a thin dielectric membrane positioned tangentially at a distance x_0 from the toroid, as depicted in Fig. 2.4. The electric field amplitude at volume element (x, y, z) can be expressed in terms of z and its in-plane distance $d = \sqrt{(R+x)^2 + y^2} - R$ from the toroid. The optomechanical coupling between toroid and a membrane of area $A = l_y \times l_z$ and thickness t is thus given by:

$$\alpha \omega \frac{\xi}{V} (n_{\text{diel}}^2 - 1) \int_{x=x_0}^{x_0+t} \int_{y=-l_y/2}^{l_y/2} \int_{z=-l_z/2}^{l_z/2} e^{-\frac{z^2}{r^2}} e^{-2\alpha\sqrt{(x+R)^2+y^2}-R} dx dy dz. \quad (2.11)$$

Figure 2.4: Typical geometry (top view) for a thin dielectric positioned tangentially at a distance x_0 from the toroid. The electric field at position (x, y) can be expressed as a function of the distance $d(x, y) = \sqrt{(x + R)^2 + y^2} - R$.



The integral over the z -coordinate yields the sampling length in this direction ²:

$$\bar{l}_z = \int_{z=-l_z/2}^{l_z/2} e^{-\frac{z^2}{r_z^2}} dz = \sqrt{\pi} r_z \text{Erf} \left(\frac{l_z}{2r_z} \right). \quad (2.12)$$

In all practical cases of this thesis $l_z/2 \geq 25 \mu\text{m}$ is much larger than $r_z \sim 1 \mu\text{m}$ (for typical parameters) and thus to a very good approximation $\text{Erf} \left(\frac{l_z}{2r_z} \right) = 1$. The sampling length in z -direction is thus given by

$$\bar{l}_z = \sqrt{\pi} r_z \approx \frac{\lambda^{1/2} r^{1/4} R^{1/4}}{\sqrt{2n}}, \quad (2.13)$$

where Eqs. (1.73) and (1.75) are used.

Assuming $y \ll R$ the integral over x and y can be simplified. This approximation is justified since for all relevant experimental realizations $|E(x, y)|^2 < 0.01 \times |E(x, 0)|^2$ as soon as $y > 0.2 \times R$. The integral over x and y can then be broken into two independent integrals such that the sampling length along the y -axis can be approximated as

$$\bar{l}_y = \sqrt{\pi} \sqrt{R\alpha^{-1}} \approx \sqrt{\frac{R\lambda/2}{\sqrt{n^2 - 1}}}, \quad (2.14)$$

using Eq. (1.74). The coupling coefficient is thus given by:

$$\begin{aligned} g(x_0) &= \alpha \omega \frac{\xi}{V} (n_{\text{diel}}^2 - 1) \bar{l}_z \bar{l}_y \int_{x=x_0}^{x_0+t} e^{-2\alpha x} dx \\ &= \frac{1}{2} \omega \frac{\xi}{V} (n_{\text{diel}}^2 - 1) \bar{l}_z \bar{l}_y (1 - e^{-2\alpha t}) e^{-2\alpha x_0}. \end{aligned} \quad (2.15)$$

Keeping terms to first order, one arrives at a coupling coefficient of

$$g(x_0) = \frac{1}{2^{3/2} \pi} \frac{\omega}{R} \frac{n^2 (n_{\text{diel}}^2 - 1)}{(n^2 - 1)^{5/4}} \sqrt{\frac{\lambda}{R}} (1 - e^{-2\alpha t}) e^{-2\alpha x_0}, \quad (2.16)$$

² The usual convention of defining the error function as $\text{Erf}(x) = \frac{2}{\sqrt{\pi}} \int_0^x e^{-t^2} dt$ is used.

or a corresponding optical frequency shift $\omega^{(1)}(x_0) = -g(x_0)/2\alpha$

$$\omega^{(1)}(x_0) = -\frac{\omega}{2^{7/2}\pi^2} \left(\frac{\lambda}{R}\right)^{3/2} \frac{n^2(n_{\text{diel}}^2 - 1)}{(n^2 - 1)^{7/4}} \sqrt{\frac{\lambda}{R}} (1 - e^{-2\alpha t}) e^{-2\alpha x_0}. \quad (2.17)$$

The above coupling coefficient (2.16) is approximately $\times 20$ smaller than the intrinsic optomechanical coupling to the internal mechanical modes of the toroid microresonator ω/R , assuming $x_0 \ll 2/\alpha$ and typical parameters ($l_y \times l_z \times t = 50 \times 40 \times 0.03 \mu\text{m}^3$, $n_{\text{diel}} = 2.1$). This loss in coupling coefficient is, however, overcompensated by typically more than $\times 20$ larger zero-point-motion of the membrane's fundamental mode (compared to a typical toroid mode, cf. sections 2.3.1 and 3) such that even larger vacuum optomechanical coupling rates g_0 are expected for evanescent near-field coupling to a membrane. For the point-like coupling shown in the previous section, the optomechanical coupling scales as $\propto \lambda^{-5/2}$. Here, in this three-dimensional analysis the scaling is reduced to $\propto \lambda^{-3/2}$ (in the limit $t \ll \alpha$) since for shorter wavelengths the optical mode is more strongly confined leading to reduced sampling lengths $\bar{l}_y, \bar{l}_z \propto \sqrt{\lambda}$. Moreover, using this configuration, optomechanical coupling coefficients up to $g \sim 0.005 \times \omega/\lambda$ are expected for typical parameters.

2.1.2.2 Nanomechanical string

The second geometrical structure which is used in the experiments described in this thesis are nanomechanical strings. These can, based on the calculations in the previous section, be treated as a membrane with a strongly reduced width. The width of the employed (rectangular) strings, i.e. their extension in z -direction, l_z varies from 300 nm to 1000 nm whereas their thickness t is typically ~ 100 nm. In order to calculate the effective length sampled in z -direction \bar{l}_z , the error function $\text{Erf}\left(\frac{l_z}{2r_z}\right)$ in Eq. (2.12) has therefore to be evaluated individually as its argument $\frac{l_z}{2r_z}$ may take values approximately spanning the interval $[0.1, 1]$.

The sampling length $\bar{l}_y \leq 5 \mu\text{m}$, however, is typically much smaller than the length of the nanomechanical strings ($\geq 15 \mu\text{m}$) such that all other expressions derived in the previous section on micromechanical membranes can be used. The optomechanical coupling may thus be expressed as:

$$g(x_0) = \frac{1}{2^{3/2}\pi} \frac{\omega}{R} \sqrt{\frac{\lambda}{R}} \frac{n^2(n_{\text{diel}}^2 - 1)}{(n^2 - 1)^{5/4}} \text{Erf}\left(\frac{l_z}{2r_z}\right) (1 - e^{-2\alpha t}) e^{-2\alpha x_0}, \quad (2.18)$$

with the corresponding frequency shift $\omega^{(1)}(x_0) = -g/2\alpha$ given by

$$\omega^{(1)}(x_0) = -\frac{\omega}{2^{7/2}\pi^2} \left(\frac{\lambda}{R}\right)^{3/2} \frac{n^2(n_{\text{diel}}^2 - 1)}{(n^2 - 1)^{7/4}} \text{Erf}\left(\frac{l_z}{2r_z}\right) (1 - e^{-2\alpha t}) e^{-2\alpha x_0}. \quad (2.19)$$

For a $l_z = 0.8 \mu\text{m}$ wide string, the loss in coupling compared to the membrane case $l_z \geq 40 \mu\text{m}$, as described by the error function in the above expression, is typically only a factor

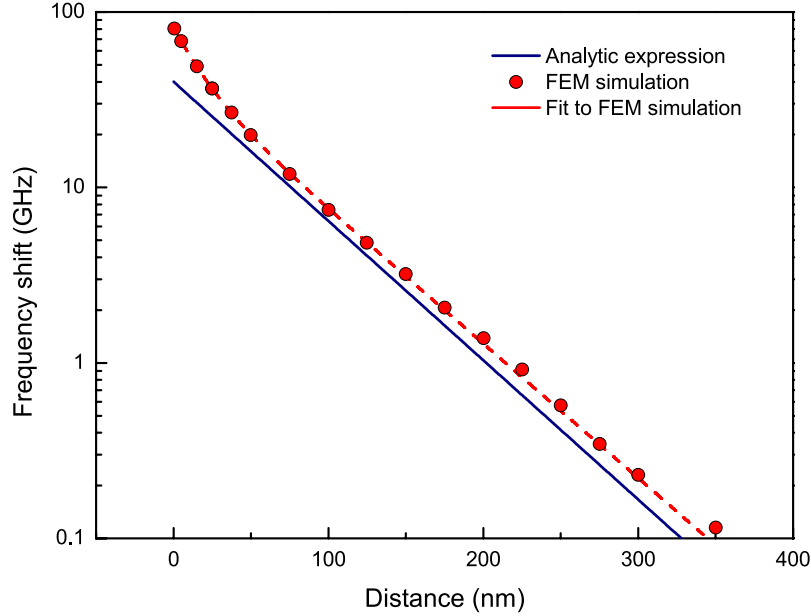


Figure 2.5: Negative optical resonance frequency shift according to the analytic approximation 2.19 and FEM simulations as explained in the text for a TM-like mode, with typical parameters $R = 16 \mu\text{m}$, $r = 1.7 \mu\text{m}$, $\ell = 171$ (corresponding to $\lambda \sim 800 \text{ nm}$) and a nanomechanical string with cross-section $100 \text{ nm} \times 700 \text{ nm}$ (Fit model: sum of two exponentials).

of ~ 2 . This reflects the optimized geometry where $l_z/2$ is now comparable to r_z and thus minimizes the mass of the dielectric without considerable loss of optomechanical coupling coefficient which results in optimized vacuum optomechanical coupling rates g_0 .

2.1.3 Comparison to finite element modelling results

As introduced in chapter 1.2, FEM simulations provide a powerful tool for calculating the optical properties of microtoroids. Here, these are applied to simulate the optomechanical coupling between a silica microtoroid and a dielectric in its evanescent field. The simulation assumes an axisymmetric geometry which holds true for the toroid itself, but not the nanomechanical element. To correct for this, the frequency shifts calculated in the axisymmetric simulation are re-scaled by the actual tangential sampling length \bar{l}_y of the evanescent cavity field as derived in the previous section 2.1.2, cf. Eq. (2.14).

Fig. 2.5 shows the cavity resonance frequency shift according to Eq. (2.19) as well as calculated by FEM simulations for a TM optical mode and typical experimental parameters. See appendix D for the code used for implementing the FEM simulations. Good agreement on a level of 15% is found between the analytic approximations of the resonance frequency shift and the results of the FEM simulation. Only for very small distances $x_0 < 50 \text{ nm}$, the frequency shift evaluated by FEM shows a deviation from first order perturbation theory. This deviation is caused by the fact that for small distances the

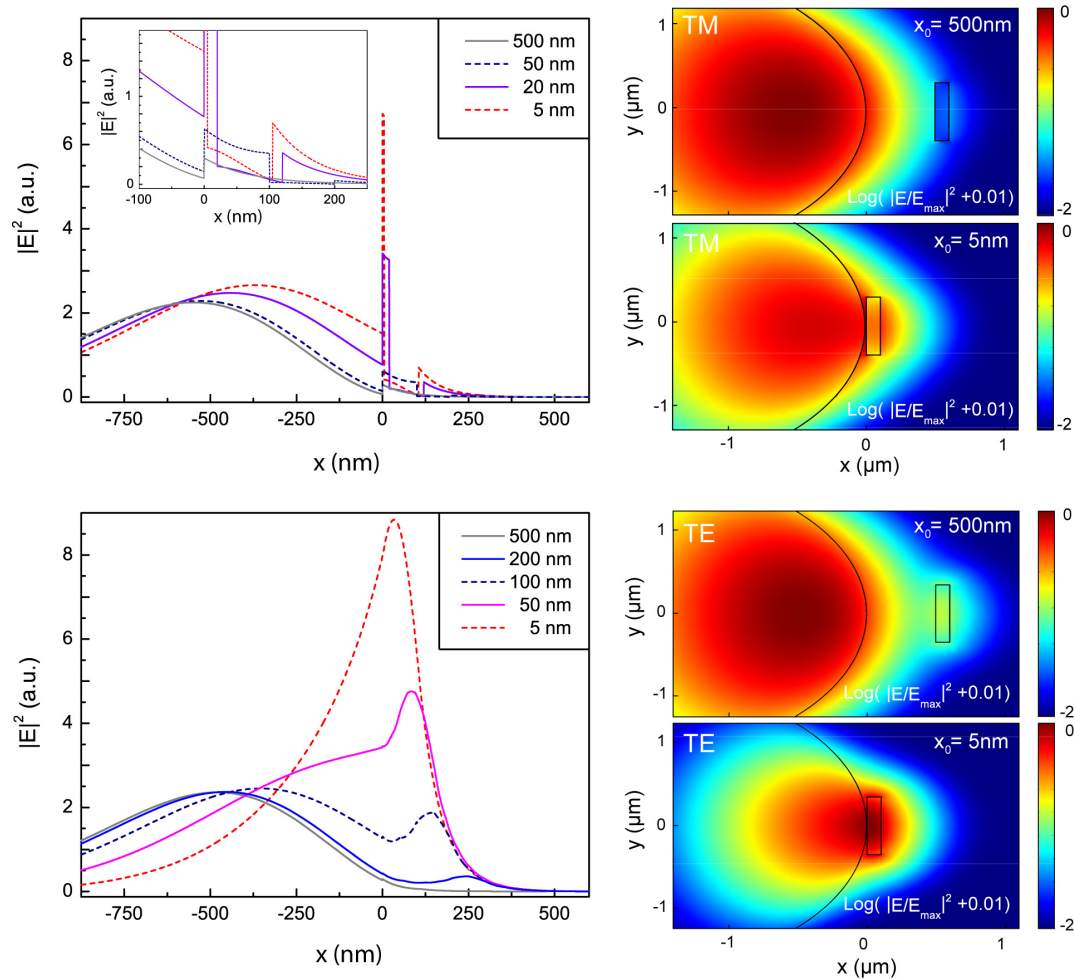


Figure 2.6: Distortion of the profile of TM- and TE-like optical microtoroid modes induced by a silicon nitride nanomechanical oscillator in the evanescent field. The top left panel shows the radial distribution of a TM mode for varying distances x_0 to the nanomechanical oscillator ($100 \text{ nm} \times 700 \text{ nm}$). The top right panel shows the corresponding field distribution for $x_0 = 500 \text{ nm}$ and $x_0 = 5 \text{ nm}$, respectively. For small x_0 a perturbation of the optical mode becomes evident, pulling the mode locally towards the vacuum. The field is sharply enhanced in the gap between nanomechanical oscillator and silica toroid. This leads to the deviation from first order perturbation theory, as described in the text. In the case of a TE mode (bottom panels) which is also pulled towards the vacuum an even stronger perturbation might arise if the short nanomechanical string supports an optical mode at the toroid resonance frequency. Then the mode can be pulled into the nanomechanical oscillator which then acts as a waveguide.

dielectric can significantly disturb the optical mode profile, pulling it slightly out of the silica structure and thus leading to larger frequency shifts. This effect is shown in Fig. 2.6 where the dependence of the mode pattern on the nanomechanical oscillator's position is shown for both TE and TM mode. For large distances x_0 the modes are only slightly perturbed by the presence of the dielectric. For smaller gaps, however, the optical modes are considerably pulled towards the vacuum side. The TM mode is thereby sharply enhanced in the gap between dielectric cavity and nanomechanical oscillator. This explains the aforementioned discrepancy of the optical frequency shift predicted by the analytic model (Eq. 2.19) and the values calculated via FEM for small gaps (≤ 50 nm). There, the first order modifications of the optical mode profile caused by the dielectric mechanical oscillator cannot be neglected anymore and lead to a deviation from first order perturbation, as developed in section 2.1.1. In the case of TE modes, the field can be pulled into the dielectric nanomechanical oscillator which can lead to a resonant coupling of light into the nanomechanical oscillator (then acting like an optical waveguide), as shown in Fig. 2.6. This phenomenon is, however, not studied in this thesis.

2.2 Static measurement of the optomechanical coupling

After having characterized the optomechanical coupling both analytically and using FEM simulations, we will now turn to the experimental side of this chapter. This section will be dedicated to a careful experimental examination of the static optomechanical coupling (the dynamic coupling coefficients will be considered in section 2.3) between toroid microresonator and nanomechanical oscillators via the evanescent optical field. First the coupling to a single optical mode is analyzed, resulting in good agreement with the numerical values obtained in the previous section. Second, effects related to the simultaneous coupling to two different optical modes of similar optical frequency will be shown.

2.2.1 Dispersive optomechanical coupling

The simplest way to characterize the optomechanical coupling coefficient g is based on static measurements of the cavity resonance frequency. To this end, the nanomechanical oscillator's distance x_0 to the cavity is gradually changed while a sweeping laser tracks the cavity resonance frequency $\omega(x_0)$. By taking the derivative $\partial\omega/\partial x_0$ of the measured frequency shift, the position dependent optomechanical coupling coefficient $g(x_0)$ can thus be derived.

In the first series of measurements the convenient telecommunication wavelength range is used ($\lambda \sim 1550$ nm). Fig. 2.7 shows the measured optical frequency shift as a function of the distance to the microresonator for both a silicon nitride membrane ($50 \times 40 \times 0.03 \mu\text{m}^3$, commercially available at SPI Supplies) and a nanomechanical string ($25 \times 0.8 \times 0.11 \mu\text{m}^3$, see appendix B.1.2 for fabrication details). As expected from the considerations in the previous chapter, an exponential shift of the cavity resonance frequency is found. The cavity linewidth is, moreover, not altered by the presence of the dielectric in the evanescent field even for the smallest distances x_0 . Thus, the coupling is purely dispersive. An exponential fit allows the extraction of an optical decay length $\alpha^{-1} = 226$ nm (string) and $\alpha^{-1} = 249$ nm (membrane). The experimental parameters are $n = 1.44$, $R = 29 \mu\text{m}$, $r = 2.9 \mu\text{m}$, $\lambda = 1539$ nm (string), $\lambda = 1557.4$ nm (membrane) and refractive indices of $n_{\text{diel}}^{\text{st}} = 2.0$ [130, 131] and $n_{\text{diel}}^{\text{m}} = 2.1$ [130, 132] for the silicon nitride string and membrane are assumed³. The value expected from Eq. 1.74 is thus $\bar{\alpha}^{-1} \sim 220$ nm, yielding good agreement of order 10% with the measured values (since experimentally TE and TM like modes are not distinguished, the average $\bar{\alpha}^{-1} \equiv (\alpha_{\text{TE}}^{-1} + \alpha_{\text{TM}}^{-1})/2$ is used for comparison, here). The measured maximum absolute optical frequency shifts are 0.72 GHz (string) and 2.25 GHz (membrane). The right axes in Fig. 2.7 show the corresponding optomechanical coupling coefficients obtained by taking the derivative of the exponential fit (which simply leads to a scaling weighted by the decay constant). Values of order $g/2\pi = 10$ MHz/nm

³ The refractive index depends on the silicon concentration of the silicon nitride. An error of ± 0.1 is estimated [130, 132], larger than the index variation ~ 0.05 as a function of wavelength between 600 nm and 1600 nm [133, 134].

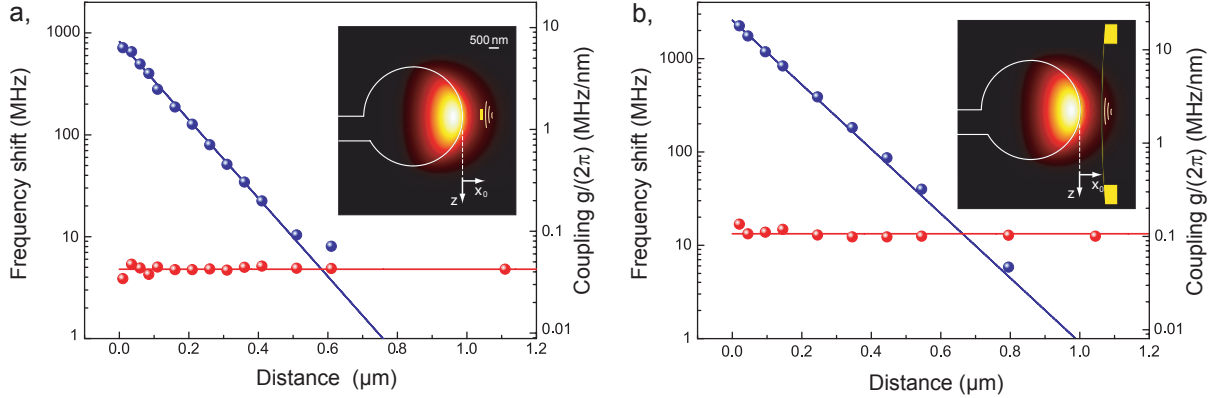


Figure 2.7: Evanescent coupling coefficients at $\lambda \sim 1550$ nm wavelength. Linewidth (red) and negative optical frequency shift (blue) of a $R = 29 \mu\text{m}$ microtoroid as a function of the distance x_0 to a silicon nitride string ($25 \times 0.8 \times 0.11 \mu\text{m}^3$, left panel) and a Si_3N_4 membrane ($50 \times 40 \times 0.03 \mu\text{m}^3$, right panel). The frequency shifts follow an exponential dependence and the data reveal in both cases purely dispersive coupling without introducing a measurable degradation of the microcavities' optical linewidth. The right axes show the dispersive optomechanical coupling $g(x_0)/2\pi$, as given by the negative derivative of the fitted frequency shift data (blue alone). Note that the absolute position of $x_0 = 0$ has an uncertainty of ~ 100 nm. Fig. adapted from Ref. [4].

are achieved for both the silicon nitride string and the membrane.

The above coupling coefficients are significantly smaller than the ones expected from the analytic model which predicts values of $g/2\pi \sim 100$ MHz/nm for both elements at vanishing distance $x_0 \rightarrow 0$. For the membrane, whose lateral dimensions are larger than the optical sampling lengths l_x and l_y , the rotational degree of freedom along the y -axis is most critical when optimizing its position in the evanescent optical field. For the nanomechanical strings, however, both the rotation along y - and x -axes as well as the absolute position in z -direction are very critical. All degrees of freedom are carefully optimized experimentally. The discrepancy between calculated and measured values is, however, caused by the fact that the absolute distance between nanomechanical element and toroid in the experiments does not approach zero⁴. The optomechanical coupling renders the cavity resonance frequency very sensitive to relative vibrations between nanomechanical oscillator and microresonator chips within the experimental apparatus. These practically limited the gaps which allowed stable measurements to an estimated value of $x_0 \sim 100$ nm in this first series of experiments.

In a second experimental step, efforts were made to increase the accessible optomechanical coupling coefficients. First, the vibration isolation of the experimental chamber was improved by mounting the chamber on a passive rubber vibration isolation system which

⁴ The silicon nitride membranes were observed to break when touching the optical cavity, i.e. at $x_0 = 0$. Contrarily, the silicon nitride strings which are under larger tension do not break nor degrade the optical resonator upon touching, thus allowing in principle values down to $x_0 = 0$.

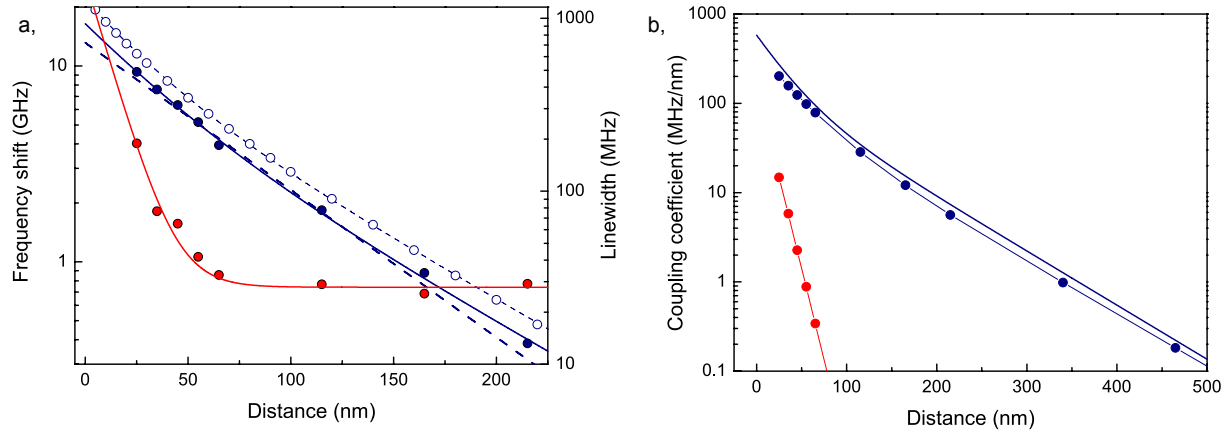


Figure 2.8: Optomechanical coupling between toroid and silicon nitride nanomechanical string—theory and measurement. a, Negative optical frequency shift (full blue dots) and cavity linewidth (red dots) as a function of the distance to a nanomechanical string ($30 \times 0.3 \times 0.1 \mu\text{m}^3$) along with fits using a double (single) exponential decay for the frequency shift (linewidth). Empty dots: FEM simulation; dashed line: analytic approximation (Eq. 2.18), both for TM-like mode. b, Red and blue dots represent the reactive and dispersive optomechanical coupling coefficients γ and g , as given by the derivative of the exponential fits in a. Good agreement of the measured dispersive coupling with the FEM results (solid blue line) is found.

was found to significantly reduce the vibrations transmitted through the floating optical table on which the experiment was mounted. Moreover, the vibration isolation to the vacuum pumping station was improved reducing the vibrations induced by the vacuum pumps. In particular aiming, moreover, at improved coupling to nanomechanical strings, the experimental parameters according to Eqs. (2.18) and (1.74), $g \propto (1 - e^{-13.2t/\lambda})/\sqrt{\lambda R^3}$, were optimized. First, working at shorter wavelength was pursued, moving from the telecommunication wavelength band to the range of a titanium-sapphire laser ($\lambda \sim 800 \text{ nm}$) enhancing the attainable coupling by a factor ~ 2 . Second, the fabrication of the toroid near-field sensors was optimized (see appendix B.1.1) to allow for smaller cavity radii strongly increasing the coupling (at the cost of making the experimental alignment more challenging). High-finesse cavities with radii down to $16 \mu\text{m}$ and a finesse $\sim 10^6$ were achieved with the fabrication steps described in appendix B.1.1. This lower bound in radius is similar to the one found for standard toroid microresonators in Ref. [135].

Fig. 2.8a shows the measured frequency shift induced by a narrower nanomechanical string ($30 \times 0.3 \times 0.1 \mu\text{m}^3$) for a resonance at 838 nm wavelength of a $18.4 \mu\text{m}$ -radius cavity along with the shift expected from both FEM simulations and the analytic approximation (see Eq. 2.19). A maximum frequency shift of 9 GHz is measured and good agreement with both FEM simulation and analytic model is found, assuming a closest distance of 25 nm . For very small gap sizes $x_0 < 50 \text{ nm}$ the measured frequency shift deviates from the uniform

exponential behaviour and follows a steeper slope, in agreement with the FEM simulation. This is attributed to the deviation from first order perturbation, as described in section (2.1.3). Another important aspect is that given the increased dispersive coupling, now for small x_0 also the cavity linewidth considerably increases, as shown in Fig. 2.8a. This effect cannot be explained by absorption of photons in silicon nitride. Based on an upper bound for the ratio of imaginary to real part of the refractive index (the complex refractive of high stress SiN was measured to be $\lesssim 0.6 \cdot 10^{-5}$ at a wavelength of 935 nm in Ref. [136]), absorption should, in the case of Fig. 2.8a, lead to an increase of the linewidth by < 1 MHz, two orders of magnitude smaller than the observed value. The increased optical losses are rather attributed to increased surface scattering at both silicon nitride and silica surfaces since for small gap sizes, the optical mode is considerably pulled towards these, as depicted in Fig. 2.6. Fig. 2.8b shows the dispersive and reactive coupling coefficients derived from the data shown in panel a. For all values of x_0 the dispersive contribution by far dominates the interaction. The measured dispersive coupling coefficients show very good agreement with the coefficients obtained from FEM simulations reaching values $g/2\pi > 200$ MHz/nm. This corresponds to a one order of magnitude improvement compared to the initial values, attributed to shorter wavelength, smaller cavity radius and improved stability, i.e. smaller x_0 . The reactive coupling, in turn, reaches values up to $\gamma/2\pi \leq 13$ MHz/nm.

The largest dispersive coupling was measured using wider nanostring oscillators with a cross-section of 700×100 nm² reaching a value of $g/2\pi = 290$ MHz/nm which corresponds to a vacuum optomechanical coupling rate of $g_0/2\pi \sim 5$ kHz (with the zero-point fluctuations of this particular string given by $x_{zpf} \sim 18$ fm, cf. section 2.3).

2.2.2 Simultaneous coupling to several optical modes

In the previous section the optomechanical coupling of a nanomechanical oscillator to a single optical resonance was described. Due to the rich mode spectrum of toroid micros-

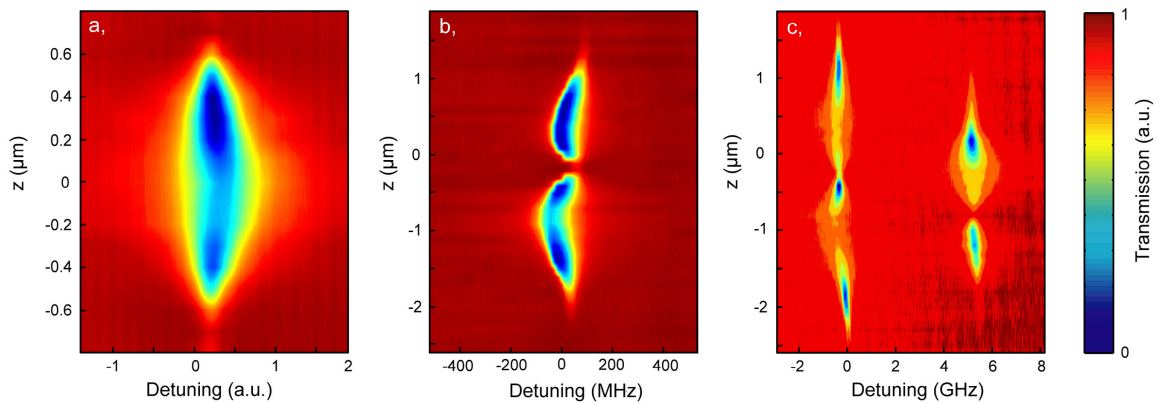


Figure 2.9: Spatial profile of optical toroid microresonator modes as inferred by the transmission of the tapered optical fibre at varying distance. Fundamental (a, $|m| = \ell$), second order (b, $|m| = \ell - 1$), second and third order (c, $|m| = \ell - 2$) modes can be distinguished.

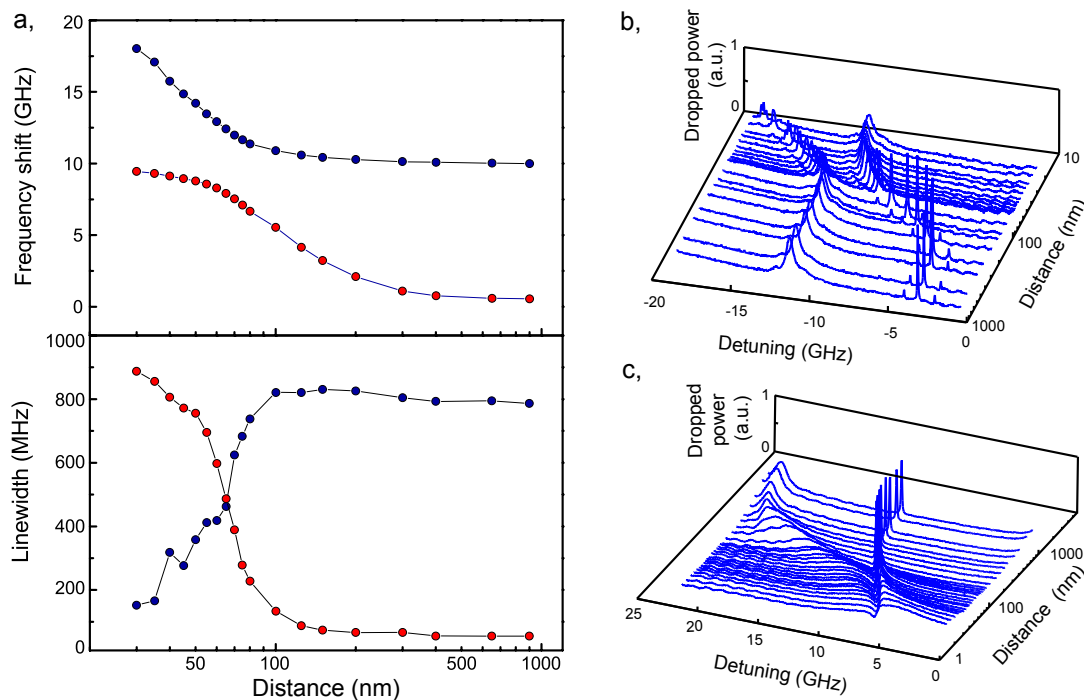


Figure 2.10: Avoided crossing and Fano-type interference of optical microresonator modes induced by dielectric nanostrings. a, Negative optical resonance frequency shift (top) and linewidth (bottom) of two adjacent optical WGM microtoroid modes as a function of the distance to a nanomechanical silicon nitride string. For large distances only the higher frequency mode is coupled to the nanomechanical oscillator. Correspondingly, it is pulled towards the lower frequency mode as the nanomechanical string is approached. The dielectric nanomechanical oscillator distorts and couples both modes to each other via scattering which gives rise to an avoided crossing. b, shows the corresponding cavity absorption spectra. c, Fano-like interference of optical microresonator modes. The situation is similar to b. Here, however, the higher frequency mode has a broad linewidth (broader than the coupling rate between both modes). Thus, it effectively acts as a continuum leading to a Fano-type interference.

onators, however, a situation might arise where two or more optical resonances closely spaced in frequency couple to the nanomechanical oscillator simultaneously.

Fig. 2.9 shows the measured vertical optical mode profiles of several optical modes. These are acquired by measuring the transmission of the tapered fibre while scanning both its position along the z -axis (the distance to the toroid is kept fixed) and the laser frequency. Fig. 2.9a shows a fundamental optical mode characterized by a single lobe along the z -coordinate. Fig. 2.9b and c, however, show higher order optical modes with two and three lobes along the z -coordinate. Obviously, the coupling of a nanomechanical string to an optical mode doublet, as shown in Fig. 2.9c, will strongly depend on its position along

the z -axis. Depending on the exact location of the nanomechanical string both optical modes should experience different optical frequency shifts and indeed interesting effects can be observed.

Fig. 2.10a-b shows a situation where a nanomechanical string is coupled to an optical mode doublet. It is positioned close to a maximum (minimum) of the higher (lower) frequency mode. As the nanostring is approached to the toroid the higher frequency mode is exponentially shifted towards lower frequencies whereas the lower frequency mode is not affected. As the frequencies of both optical modes approach each other, the scattering induced by the nanomechanical oscillator strongly couples both modes, leading to an avoided crossing. During the avoided crossing both optical modes also switch their respective optical linewidth, as expected from a simple coupled oscillator model. It is noted that the corresponding coupling frequency is as large as ~ 3 GHz, much larger than in a previously studied microsphere system [137] which could be caused by a Purcell enhancement of the scattering [137, 138] into the adjacent high Q optical modes ($Q \sim 5 \cdot 10^5$ and $Q \sim 3 \cdot 10^7$). For the closest distance $x_0 \sim 25$ nm, the higher frequency optical mode is shifted by 18 GHz and a dispersive coupling coefficient of $g/2\pi = 270$ MHz/nm is achieved in this configuration. If the coupling between both optical modes is weaker than one of the optical mode's intrinsic decay rates, a Fano-type interference is observed as both modes are tuned into resonance with each other. This situation is depicted in Fig. 2.10c where a very broad resonance (linewidth ~ 5 GHz) is used.

2.3 Transduction and actuation of nanomechanical motion

With the previously characterized static optomechanical coupling coefficients which were obtained by displacing the nanomechanical oscillator as a whole, we will now turn to the intrinsic mechanical modes of the employed nanomechanical oscillators. To this end, nanomechanical oscillators positioned at a fixed distance x_0 to the microresonator will be considered. We will both actively drive the resonators and passively examine the motion of their eigenmodes via the dispersive optomechanical coupling g . The Brownian motion of the nanomechanical oscillators (section 2.3.2) as well as their response to a modulated light field (section 2.3.3) will be used to calibrate the optomechanical coupling in an independent, *dynamic* way confirming the *static* values obtained in section 2.2.1 and yielding an absolute calibration of the nanomechanical oscillators' displacement. First, however, the notion of a mechanical oscillator's effective mass will be introduced which is crucial for the correct scaling of the optomechanical interaction.

2.3.1 Effective mass of the nanomechanical oscillators

In chapter 2.2.1 the optomechanical coupling was defined as the static optical resonance frequency shift induced by an infinitesimal change in oscillator position x_0 , $\Delta\omega \equiv \Delta x_0 \cdot g$. Here, we will consider the cavity frequency noise $S_\omega[\Omega]$ induced by the Brownian position fluctuations $S_x[\Omega]$ of a particular mechanical mode of the nanomechanical oscillator $S_\omega[\Omega] = g_{\text{dyn}} \cdot S_x[\Omega]$. The cavity frequency noise spectrum S_ω can be measured in absolute terms, as will be shown in section 2.3.2 (see also appendix B.3). The quantities on the right hand side of the above equation are, however, a-priori not that well-defined. Typically, the convention of matching static and dynamic coupling coefficients $g_{\text{dyn}}(x_0) \equiv g(x_0)$ has been pursued in the optomechanical literature (which leads to the well-known $g(l) = \omega/l$ for a Fabry-Perot cavity of length l). This convention necessitates to carefully define the actually measured effective coordinate of each mechanical oscillator mode, taking into account the spatial overlap of the optical and mechanical mode shape used for measurement. Moreover, this convention requires the notion of an effective mass [139] for each mechanical oscillator mode in order to fulfill the equipartition theorem. Following a different convention, one could e.g. also absorb the overlap between optical and mechanical modes into an effective optomechanical coupling which would then lead to different optomechanical coupling for each individual mechanical mode and in particular different static and dynamic coupling coefficients. Then, in turn, the notion of constant motional mass for all mechanical modes could be adopted.

Here, we follow the former, more frequently used convention as then both static and dynamic coupling coefficients are identical for all mechanical modes. Since each convention is somewhat arbitrary a simple method for characterizing the optomechanical coupling via the vacuum optomechanical coupling rate without having to introduce effective masses or effective coupling coefficients will be described in section 2.3.5. In the following, the effec-

tive coordinates and corresponding effective masses for a nanomechanical string positioned horizontally in the evanescent optical microresonator field will be derived. The results for vertical coupling, as well as nanomechanical membranes will also be given.

The j -th eigenmode of a doubly clamped rectangular string of length L , Young's modulus Y and cross-sectional inertia $I = wt^3/12$ (where the thickness t is understood along the axis of oscillation and the width w corresponds to the lateral dimension) oscillates at frequencies given by [140]:

$$\Omega_m^j/(2\pi) = \frac{j^2\pi}{2L^2} \sqrt{\frac{YI}{\rho A}} \sqrt{1 + \frac{ASL^2}{j^2YI\pi^2}}. \quad (2.20)$$

In the limit of large internal tensile stress ($S \gg (j\pi t/L)^2 Y/12$), the mode patterns of a nanomechanical string extending from $y = 0$ to $y = L$ are given by

$$u_j(y) = u_{j,0} \sin\left(\frac{j\pi}{L}y\right). \quad (2.21)$$

Each mechanical mode fulfills the equipartition theorem:

$$\frac{1}{2}m\Omega_m^2 \langle u_j^2 \rangle = k_B T, \quad (2.22)$$

where $m = \rho t w L$ denotes the oscillator's physical mass and $\langle u_j^2 \rangle = 1/L \int_L u_j(y)^2 dy$ is the mean squared displacement amplitude averaged along the string's length⁵.

In general, however, the measured coordinate deviates from $\langle u_j^2 \rangle$ since it is weighted by the geometry of the measurement apparatus. For the presented system the measured coordinate is given by the spatial distribution of the normalized optical mode profile $v_0(y)$ ($\int_{-\infty}^{\infty} v_0(y)^2 dy = 1$), sampling the nanomechanical string. This results in a normalized squared displacement of

$$\langle u_j \rangle_{v_0}^2 = \left(\int_L u_j(y) v_0(y)^2 dy \right)^2, \quad (2.23)$$

which generally does not equal $\langle u_j \rangle^2$. In order to maintain equipartition for the actually measured coordinate the oscillator's mass correspondingly has to be adjusted. This leads to an individual effective mass m_{eff} for each mechanical mode. Using Eq. (2.22), the effective mass of the j -th mode can then generally be written as

$$m_{\text{eff}}^{(j)} = m \frac{\langle u_j^2 \rangle}{\langle u_j \rangle_{v_0}^2} = m \frac{1/L \int_L u_j(y)^2 dy}{\left(\int_L u_j(y) v_0(y)^2 dy \right)^2}. \quad (2.24)$$

Assuming for example a point like measurement at the centre of the string, i.e. $v_0(y)^2 = \delta(y - L/2)$, the effective mass of the eigenmodes which are symmetric around $y = L/2$ (i.e.

⁵ Note that for the space *and* time averaged root mean square amplitude \bar{u}_j one obtains $\bar{u}_j^2 = \langle u_j^2 \rangle / 2$ and thus the usual $m\Omega_m^2 \bar{u}_j^2 / 2 = k_B T / 2$.

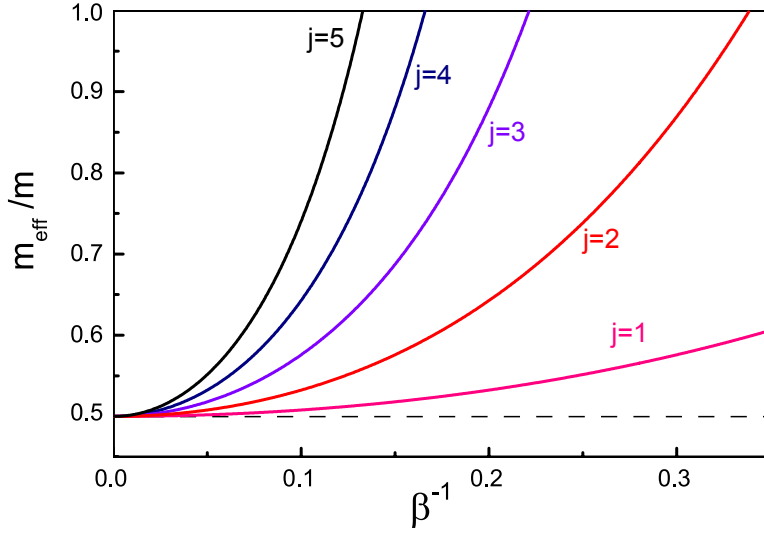


Figure 2.11: Effective mass of the lowest mechanical modes of a nanomechanical string for symmetric probing around a central antinode as a function of β^{-1} , according to Eq. (2.27). The effective mass m_{eff} of the fundamental mode is always close to half its physical mass m whereas for higher order modes small β^{-1} is required to maintain small effective masses.

$j \in 2\mathbb{N} - 1$) evaluates to $m/2$. The effective mass of all antisymmetric modes (i.e. $j \in 2\mathbb{N}$) in contrast diverges for any symmetric probing around $y = L/2$.

The approximate expression of the toroid field as obtained in the previous section reads

$$v_0^2(y) = \sqrt{\frac{\alpha}{\pi R}} e^{-\alpha(y-y_0)^2/R}, \quad (2.25)$$

with the field maximum along the string residing at $y = y_0$. Inserting this expression as well as the fundamental mode pattern of the strings (2.21) into Eq. (2.24) one obtains the following expression for the effective mass m_{eff}^j of the j -th mode:

$$\frac{m_{\text{eff}}^j}{m} = \frac{\pi R}{L\alpha} \frac{\int_0^L \sin^2(\frac{j\pi}{L}y) dy}{\left(\int_0^L \sin(\frac{j\pi}{L}y) e^{-\alpha(y-y_0)^2/R} dy \right)^2} \quad (2.26)$$

or

$$m_{\text{eff}}^j = \frac{m}{2} \left(\int_0^1 \beta \sin(j\pi u) \text{Exp} \left[-\pi\beta^2 \left(u - \frac{y_0}{L} \right)^2 \right] du \right)^{-2}, \quad (2.27)$$

where $\beta^2 = \frac{L^2\alpha}{\pi R} = L/\bar{l}_y$ reflects the string's length L weighted by the transverse optical sampling length \bar{l}_y .

Typical experimental parameters used during this thesis yield $\beta \gg 1$. For the fundamental mechanical modes ($j = 1$) and symmetric probing around the string's centre ($y_0 = L/2$), the integrand in the above expression thus approximately represents a normalized Gaussian (centered at $u = 1/2$ with a width $\ll 1$). Correspondingly, values close to 1 are found for the integral. Thus, the effective mass of the fundamental modes is typically given by half the oscillator's physical mass, i.e. $m_{\text{eff}} \approx m/2$. This can be intuitively understood as follows: $\beta \gg 1$ indicates a point like measurement of the mode at the centre of the string. Thus, the measured coordinate is given by the the squared peak displacement

$u_{1,0}^2$ which is $\times 2$ larger than the mean squared displacement $\langle u_1^2 \rangle$ averaged along the full length of the string. Accordingly, the measured mechanical oscillator mode effectively can be described by a $\times 2$ smaller mass, i.e. its effective mass is given by $m_{\text{eff}} = m/2$. For higher order mechanical modes whose motion is more localized, however, the deviation from $m_{\text{eff}}^j = m/2$ can be large. Fig. 2.11 illustrates the effective mass of the first five fundamental modes as a function of β for symmetric probing around a central antinode of the mechanical mode.

Equivalently, the effective mass for vertical coupling (string positioned along the z -axis) is given by:

$$m_{\text{eff},v}^j = \frac{m}{2} \left(\int_0^1 \beta_z \sin(j\pi u) e^{-\pi\beta_z^2(u-\frac{z_0}{L})^2} du \right)^{-2}, \quad (2.28)$$

where $\beta_z^2 = L/\bar{l}_z$ (cf. Eq. 2.13). Similarly one can show that the effective mass for membrane modes is given by:

$$m_{\text{eff}}^{j,k} = \frac{m}{4} \left(\int_0^1 \beta_y \sin(j\pi u) e^{-\pi\beta_y^2(u-\frac{y_0}{L_y})^2} du \times \int_0^1 \beta_z \sin(k\pi u) e^{-\pi\beta_z^2(u-\frac{z_0}{L_z})^2} du \right)^{-2}, \quad (2.29)$$

where $\beta_\zeta^2 = L_\zeta/\bar{l}_\zeta$ ($\zeta \in \{y, z\}$). For all experimental cases studied in this thesis the effective mass of the fundamental mode can be safely approximated by $m_{\text{eff}}^{(1,1)} = m/4$.

Employing the correct effective mass as defined above for the thermal Langevin force spectrum $S_F^L[\Omega]$ (cf. Eq. 1.42) as well as the susceptibility $\chi_m[\Omega]$ ($\chi_m[\Omega]^{-1} = m_{\text{eff}}(\Omega_m^2 - \Omega^2 - i\Gamma_m\Omega)$) of each mechanical mode then ensures that equipartition (2.22) is fulfilled.

2.3.2 Transduction of Brownian motion

The dispersive optomechanical coupling g transduces the Brownian motion of the nanomechanical oscillators into cavity frequency noise $S_\omega[\Omega]$ via:

$$S_\omega[\Omega] = g^2 \times S_x[\Omega]. \quad (2.30)$$

When the cavity is probed by a laser field, the Brownian noise S_x will thus be imprinted onto phase and amplitude noise of the field transmitted through the tapered optical fiber coupled to microresonator and nanomechanical oscillator (cf. appendix A). In the following the cavity will be probed on resonance to avoid dynamical backaction (cf. section 1.1.4) and thus all the cavity frequency noise is encoded in the phase quadrature of the transmitted field according to Eq. (1.36). The phase fluctuations of the transmitted light can be analyzed in several ways. Here, a Pound-Drever-Hall [141] technique is used, as depicted in Fig. 2.12b whereas in chapter 2.5 also homodyne measurements will be performed. By adding a well-known frequency modulation to the measurement laser using an electro-optic modulator (EOM), the cavity frequency noise can be calibrated in absolute terms (cf. appendix B.3.2). The frequency noise spectra recorded at varying distances between toroid and a nanomechanical string are depicted in Fig. 2.12a. Note that all

determine the mode temperature of each mechanical mode from the measured frequency noise spectra.

We will however turn this reasoning around. Here, the heating of the nanomechanical oscillators induced by light absorption can be shown to be negligible and, in the presented measurements, a mode temperature of 300 K, i.e. thermalization with the environment can be safely assumed. No dependence of the mechanical oscillator's mode temperature on the optical input power could be found within the measurement error bars (unless dynamical backaction effects come into play). This is in agreement with FEM simulations based on the complex refractive index of SiN ($n_{\text{im}} \lesssim 0.6 \times 10^{-5}$, [136]). Very conservative estimates yield a maximum heating power of < 500 nW (for the highest coupling power levels employed) leading to a maximum relative temperature increase of less than 1% (for a typical nanostring). Thus, the Brownian motion of the nanomechanical oscillators at ambient temperature is *well-known* and can be used in order to extract the optomechanical coupling coefficients from the Brownian noise measurements. Thereby, the optomechanical coupling can be measured in a second independent way, based on the actual mechanical modes of the nanomechanical oscillators. Good agreement on a level of 30% is hereby typically found with the statically determined values, as shown in section 2.2.1. In the next section, the agreement between static and dynamic coupling will be quantified in more detail.

2.3.3 Radiation pressure actuation

In this section, the nanomechanical oscillators are actuated by an intensity modulated laser beam. It will be shown that the most dominant contribution to the nanomechanical oscillators' response is given by radiation pressure whose magnitude is in excellent agreement with the values expected for the optical dipole force. Within our measurement accuracy, no thermal contribution can be found. The coupling coefficients extracted from this force response measurement correspondingly are in good agreement with the statically measured values. Moreover, the sign of the dipole force can be determined confirming the attractive nature of the optical dipole force interaction.

Fig. 2.13 shows the setup employed for measuring the nanomechanical oscillator's response. Two lasers emitting at around 1550 nm are employed. A fibre-coupled diode laser operating at 1530 nm serves as *pump* laser. Together with a fibre-coupled amplitude modulator it provides a sinusoidally modulated input power $\delta P(t)$, which in turn causes the optical resonances to periodically shift in frequency via thermal effects due to light absorption, via light-force induced mechanical displacement of both the toroid and the nanomechanical oscillator, but also via the Kerr-nonlinearity of silica (i.e. its intensity dependent refractive index). These shifts are read out with a weak 1560 nm *probe* laser resonantly locked to a microcavity resonance. Its transmitted phase reflecting the induced cavity resonance frequency shifts is read out using a Pound-Drever-Hall technique. Modulating the power of the strong pump laser and demodulating the detected probe error signal with the same (swept) frequency via a network analyzer, allows observation and discrimination of the different mechanisms contributing to the system's response. The light transmitted by

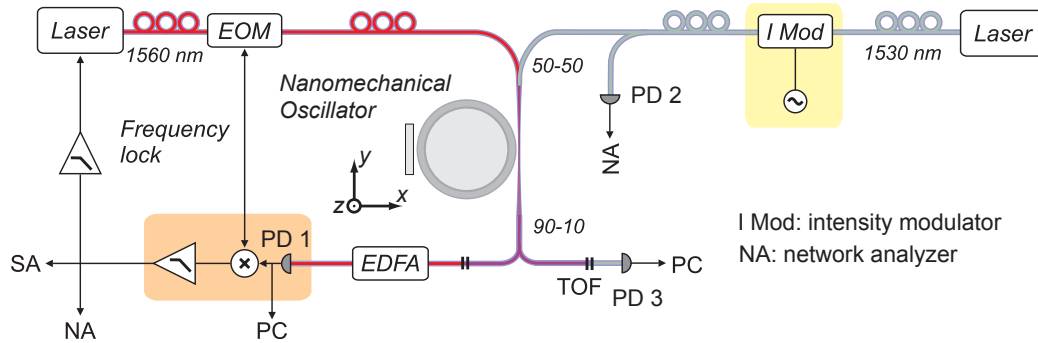


Figure 2.13: Experimental setup used for radiation pressure response measurements. The amplitude modulated pump and the probe beam (both at resonance of two separate optical modes) are sent to the cavity via a fibre coupled beam combiner. The transmitted signals of both pump and probe beam are accessed individually via a fibre coupled splitter and tunable optical filters (TOF). The probe beam is amplified via an EDFA before detection to allow probing of the cavity-nanomechanical-oscillator system’s response to the pump beam (via a Pound-Drever-Hall technique) at low probe power.

the oscillator-cavity system is split using a 90/10 coupler and the separation between the pump and probe fields (separated by 30 nm) is ensured by means of tunable optical filters. The main port serves for probing as well as locking the probe laser. The probe beam is amplified *after* the microresonator by an erbium doped fibre amplifier (EDFA) in order to read out the response of the cavity resonance frequency with simultaneously low input power and large signal to noise ratio. This ensures that the measurement is not perturbed by the presence of the probe beam inside the optomechanical system. The weak port is used to maintain the pump laser on resonance. It is made sure that residual crosstalk is more than 10 dB below the weakest signals detected.

Fig. 2.14 (inset) shows the broadband response of the system which is the sum of several phenomena. At low frequencies, the microcavity response to the intensity modulation is dominated by thermal mechanisms, described in detail in Ref. [142]. The most prominent is the temperature induced refractive index change that affects the optical path length of the cavity. The thermorefractive contribution strongly reduces with frequency, and above 1 MHz a plateau corresponding to the silica Kerr effect contribution is observed as well as a few resonances corresponding to the first mechanical modes of the toroid (the mechanical modes of the nanomechanical oscillator are not resolved due to their high mechanical Q). Note that we do not see a change of any broad-band noise when the cavity is probed with and without nanomechanical oscillator which implies that the thermal response of the nanomechanical oscillator is much smaller than the toroid’s thermal response.

Let us now turn to the resonant response of the nanomechanical oscillators which is shown in Fig. 2.14 for a silicon nitride membrane ($50 \times 40 \times 0.03 \mu\text{m}^3$) at different gap sizes x_0 . The measured response is made up of the Lorentzian response of the nanomechanical oscillator around its eigenfrequency, interfering with the flat Kerr background. The Kerr

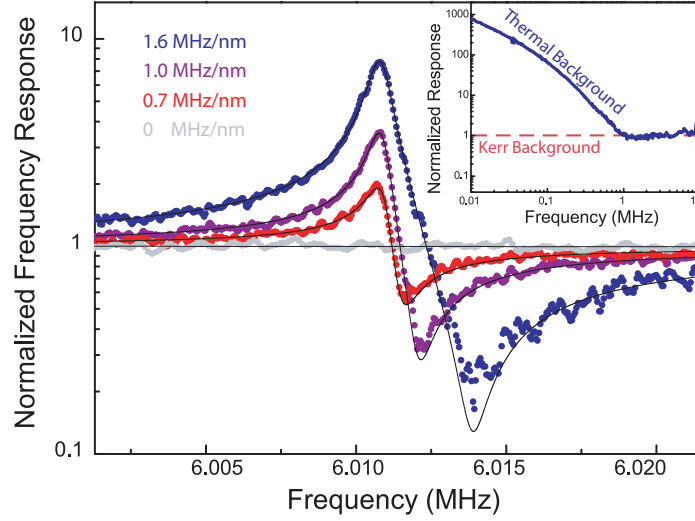


Figure 2.14: Resonant response of a silicon nitride membrane’s fundamental mechanical mode to radiation pressure interfering with the constant Kerr response of the cavity, for constant modulated laser power. The magnitude of the mechanical oscillator’s response compared to the Kerr plateau allows the extraction of the optomechanical coupling coefficient $g/2\pi$ (inset) as explained in the text, confirming the statically measured values. Inset: Broadband response of the cavity-nanomechanical oscillator system. Fig. adapted from Ref. [4].

response of silica can be used as a reference, calibrating the response of the nanomechanical oscillators. Under a modulation δP of the intracavity power, the Kerr effect causes an optical resonance frequency modulation given by:

$$\delta\omega^{\text{Kerr}}[\Omega] = -\omega \frac{n_2}{nA_{\text{mode}}} \delta P_{\text{intra}}[\Omega], \quad (2.32)$$

where $n_2 = 3 \cdot 10^{-16} \text{ cm}^2 \text{ W}^{-1}$ is the Kerr coefficient of silica and A_{mode} the optical mode area. The intracavity power modulation δP_{intra} is linked to the input power modulation δP by $\delta P_{\text{intra}} = \frac{\mathcal{F}}{\pi} \delta P$ in the case of critical coupling, where $\mathcal{F} = c/(nR\kappa)$ denotes the optical finesse (the linewidth of the pump mode is 120 MHz, such that the cavity cut-off can be safely neglected for the modulation frequencies below 15 MHz considered here). From the flat Kerr background an effective mode area of $A_{\text{mode}} = 34 \mu\text{m}^3$ (where $\delta P = 8 \mu\text{W}$ was used) can be extracted.

Moreover, via the optomechanical coupling g , the modulated intracavity power also exerts a modulated dipolar force $\delta F[\Omega]$ on the nanomechanical oscillator that in turn modulates the microcavity optical resonance according to:

$$\delta\omega^{\text{nano}}[\Omega] = g_{\text{probe}} \delta x[\Omega] = g_{\text{probe}} \chi_{\text{m}}[\Omega] \delta F[\Omega], \quad (2.33)$$

where g_{probe} is the coupling rate of the probe optical mode and $\delta x[\Omega]$ is the oscillation amplitude of the nanomechanical oscillator. The modulated optical force applied to the

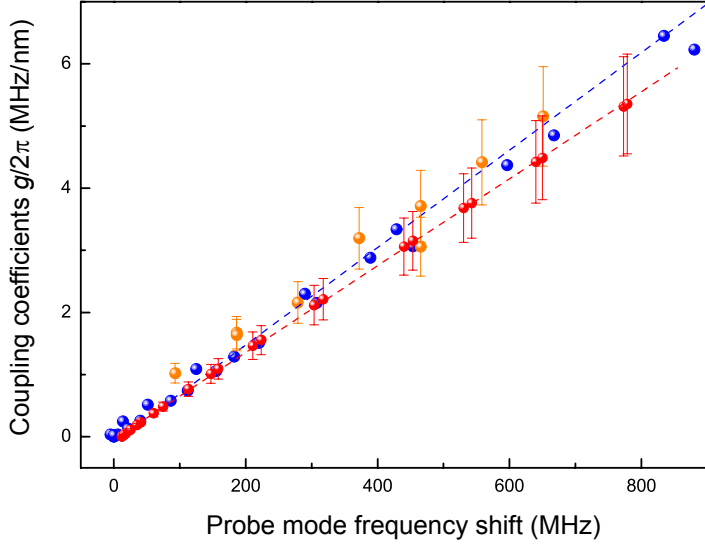


Figure 2.15: Coupling coefficients g_{pump} (red), g_{probe} (blue) evaluated from static measurements and effective coupling rate g_{eff} determined by the force-response measurement (orange). Error bars represent the uncertainties in scaling the different data sets to a common base. Within the measurement uncertainty, the magnitude expected for the dipolar force is confirmed. This demonstrates independently that the force on the nanomechanical oscillator is dominated by the optical dipole force.

oscillator can be written as:

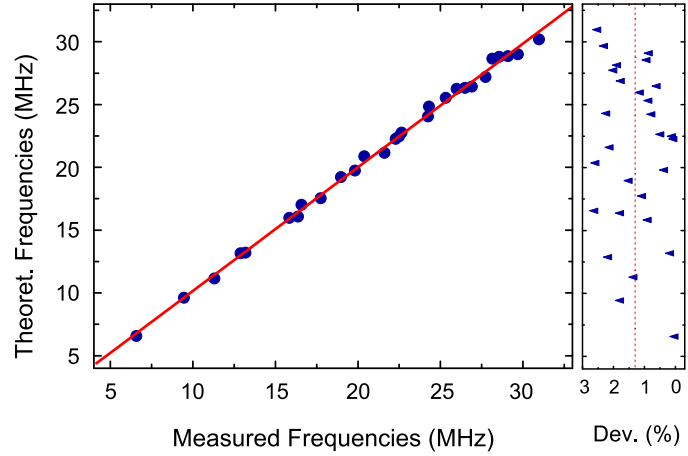
$$\delta F[\Omega] = -\hbar g_{\text{pump}} \frac{2\pi Rn}{c} \frac{\delta P[\Omega]}{\hbar\omega}. \quad (2.34)$$

We have assumed equal effective mass associated with both optical modes, here. We have, however, differentiated between the coupling parameters for the pump (g_{pump}) and probe (g_{probe}) modes since they exhibit slightly different spatial profiles. Both coupling parameters have been separately measured, statically. The total response of the system is the coherent sum of the various mechanisms contributing. Since here we are only interested in the local response around the nanomechanical oscillator's resonance, we only consider Kerr and mechanical responses:

$$\frac{\delta\omega^{\text{tot}}}{\delta\omega^{\text{Kerr}}}[\Omega] = 1 + \frac{a_1}{\Omega_m^2 - \Omega^2 - i\Omega\Gamma_m}, \quad \text{where } a_1 = \frac{g_{\text{probe}}g_{\text{pump}}}{\omega^2} \frac{2\pi Rn^2 A_{\text{mode}}}{cn_2 m_{\text{eff}}}. \quad (2.35)$$

The frequency response data, normalized to the Kerr background, is accordingly fitted using this model which represents the coherent sum of a damped driven harmonic mechanical oscillator and a unity (Kerr) background response. The interference between the response of the mechanical mode and the instantaneous Kerr response is due to the fact that the former gets out of phase with the latter when the modulation frequency is swept over the resonance frequency (at resonance the mechanical oscillator response is $\pi/2$ out of phase with the driving force). Thus, a dispersive shape of the total response curve is expected. As shown in Fig. 2.14, this effect is indeed observed with an excellent agreement between the data and the fit model. The frequency dependence of the mechanical susceptibility, i.e. the fact that it responds in phase (out of phase) at frequencies lower (higher) than its eigenfrequency, allows accessing the sign of the measured force. Importantly, the fact that the interference dip is present at frequencies higher than the mechanical resonance

Figure 2.16: Frequency dispersion of a $50 \times 40 \times 0.03 \mu\text{m}^3$ silicon nitride membrane's eigenmodes. The frequencies expected from the strain model (2.36) are fitted to the measured frequencies using the ratio $\sqrt{S/\rho}$ as fit parameter. Excellent agreement up to the (7, 2) mode is found with an average deviation of less than 2% (dashed line, right). The full red line (left) simply represents a linear fit.



frequency confirms the *attractive nature of the optical force*, oriented towards the region of higher optical intensity.

The results from the fits for different oscillator positions (the coefficients a_1) yield the effective force-response coupling rate $g_{\text{eff}} = \sqrt{g_{\text{pump}} g_{\text{probe}}}$ using an effective mass of $m_{\text{eff}} = m/4 = 4 \cdot 10^{-14} \text{ kg}$ ⁸. Good agreement at a level of 10%, within the experimental errorbars, is found between the static and the force-response based determination of the coupling coefficient g_{eff} , underpinning the fact that the force acting on the nanomechanical oscillator is dominated by the optical dipole force.

2.3.4 Frequency dispersion and mode patterns of nanomechanical oscillators

In this section the properties of the employed nanomechanical oscillators will be characterized in somewhat more detail. For the nanomechanical strings and membranes intrinsic mechanical quality factors ranging from 10^4 to $> 10^5$ are found (for frequencies of 5 MHz to 15 MHz) in vacuum (pressure $< 10^{-5}$ mbar) depending on the cleanliness of the samples. These are similar to the values reported elsewhere for nanostrings [128, 131]. To our knowledge, however, similarly small membranes have not been examined by other researchers so far. For much larger membranes (edge lengths $\geq 500 \mu\text{m}$) considerably higher mechanical Q has been found [37, 136]. The measured mechanical quality factors are most likely limited by two level systems within the amorphous silicon nitride [143, 144] (see also section 3 for an in-depth analysis of different mechanical damping mechanisms). In the following, we will focus on the mode structure of both nanomechanical strings and membranes.

The eigenmodes of a thin membrane (thickness t , edge lengths l_y and l_z , mass density

⁸ Here, a density of $\rho = 2.5 \cdot 10^3 \text{ kg/m}^3$ [37] is assumed for the low-stress silicon nitride.

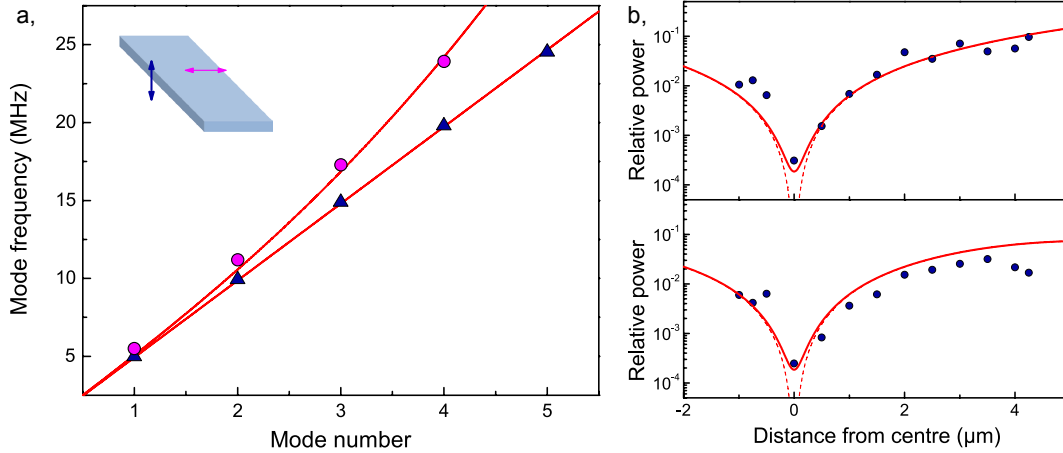


Figure 2.17: Modes of a $40 \times 0.7 \times 0.1 \mu\text{m}^3$ nanomechanical string. a, Out-of-plane (triangles) and in-plane mechanical modes (circles). The out-of-plane mode family follows a harmonic frequency ladder whereas the in-plane mode family increases faster in frequency owing to the larger in-plane cross-sectional inertia. Displacing the toroid along the string's axis allows recording the nanomechanical string's spatial mode patterns, as shown in b: peak squared displacement of the second (upper panel) and fourth (lower panel) out-of-plane mode normalized to the fundamental mode. Good agreement with Eq. (2.20) (dashed lines) is found, when the finite sampling length of the microresonator \bar{l}_y (cf. Eq. 2.14) is taken into account (full lines).

ρ) dominated by its internal tensile stress S (force per cross-sectional area) are given by

$$\Omega_m^{(j,k)}/(2\pi) = \frac{1}{2} \sqrt{\frac{S}{\rho}} \sqrt{j^2/l_y^2 + k^2/l_z^2}. \quad (2.36)$$

Fig. 2.16 shows the measured frequencies of the first 28 eigenmodes of a $50 \times 40 \times 0.03 \mu\text{m}^3$ membrane (up to order (7, 2)) along with the expected frequencies according to Eq. (2.36). For the latter, the ratio $\sqrt{S/\rho}$ is adjusted in a least square fit to the measured values. Excellent agreement is found between theory and experiment with the membrane frequencies fully described by the strain model. From this fit one obtains a value of $S/\rho = (1.0 \pm 1) \times 10^5 \text{ m}^2/\text{s}^2$. Using the density of $\rho = (2.5 \pm 0.5) \text{ kg}/\text{m}^3$ [37] for low-stress silicon nitride, this yields a tensile stress of $(260 \pm 70) \text{ MPa}$.

For the strained nanomechanical strings, however, deviations from the purely strain-dominated model are found. Their frequencies for arbitrary intrinsic stress are given by Eq. (2.20). Fig. 2.17a shows the nine lowest order eigenmodes of a $40 \times 0.7 \times .1 \mu\text{m}^3$ nanomechanical string. The out-of-plane modes follow a linear dependence on mode number, here up to the fifth mode at 25 MHz since their motion is dominated by the internal tensile stress, i.e. $S \gg (j\pi t/L)^2 Y/12$ (cf. Eq. 2.20). The spatial displacement patterns of these modes can be measured by displacing the toroid microresonator with respect to the centre of the nanostring. Fig. 2.17b shows the squared oscillation amplitude of the

second and fourth out-of-plane modes normalized to the fundamental out-of-plane mode. The measured amplitudes are in good agreement with the theoretical expectation taking into account the transverse optical sampling length \bar{l}_y (see Eq. 2.14). In fact, minimizing the signal of even eigenmodes constitutes a simple way to find the centre of the nanostrings and thus optimize the transduction of the fundamental mode. The measured out-of-plane modes allow inferring the ratio $S/\rho = (1.6 \pm 0.1)10^5 \text{ m}^2/\text{s}^2$. For LPCV deposited high-stress silicon-nitride a density of $(3 \pm 0.5)10^3 \text{ kg/m}^3$ is expected, see Ref. [131] and references therein. Thus, the resulting tensile stress in this particular sample is given by $S = (0.5 \pm 0.1) \text{ GPa}$. Values up to $S = 0.8 \text{ GPa}$ were, however, obtained using other samples. The measurement is moreover also sensitive to in-plane modes of the string (a higher order optical mode is used for this measurement). Owing to the high aspect-ratio of the nanomechanical oscillators, these exhibit considerably different frequencies and in particular do not follow linear dispersion, as shown in Fig. 2.17a. This is due to the increased value of the cross-sectional inertia (by a factor $(w/t)^2$) for modes oscillating along the longer axis of the string. With this additional mode family, the Young's modulus of the employed strings can be calculated. Using the above value for density and stress in order to fit expression (2.20) to this mode family (see Fig. 2.17a), one obtains a Young's modulus of $Y = (55 \pm 9) \text{ GPa}$ which is lower than the value measured in Ref. [131] for higher stress ($S \approx 1.2 \text{ GPa}$) LPCVD silicon nitride ($Y \approx 200 \text{ GPa}$).

2.3.5 Vacuum optomechanical coupling rate

In the previous section, we followed the convention of normalizing the nanomechanical oscillator's displacement by the overlap of optical and mechanical modes. This is a very intuitive approach and has its origin in Fabry-Perot type cavities [139] following the aforementioned conceptual identity of static and dynamic optomechanical coupling coefficients g for all mechanical modes. Using integrated structures, however, the notion of static coupling rates is far less intuitive. In complex structures, e.g. photonic crystal cavities with very complex three-dimensional displacement patterns, the choice of a single one-dimensional coordinate becomes less obvious and thus the separation of coupling coefficient and displacement becomes somewhat arbitrary. A quantity that is, however, a-priori well-defined is the cavity frequency noise spectrum S_ω induced by the mechanical oscillator's motion. In order to characterize the optomechanical coupling without the necessity of introducing a coupling coefficient g and a corresponding effective mass that both depend on the definition of the displacement coordinate, the zero-point coupling rate $g_0 = g \times x_{zpf}$ (cf. section 1.1.1) is ideally suited as it is independent of the actual definition of the measured displacement. It can be expressed solely in terms of the cavity frequency noise spectrum and thus avoids the ambiguity in the definition of coupling coefficient and corresponding displacement. It can be written as [3]

$$g_0 = \sqrt{\frac{\hbar\Omega_m}{2k_B T} \int_0^\infty S_\omega^{\text{ss}}[\Omega] \frac{d\Omega}{2\pi}}, \quad (2.37)$$

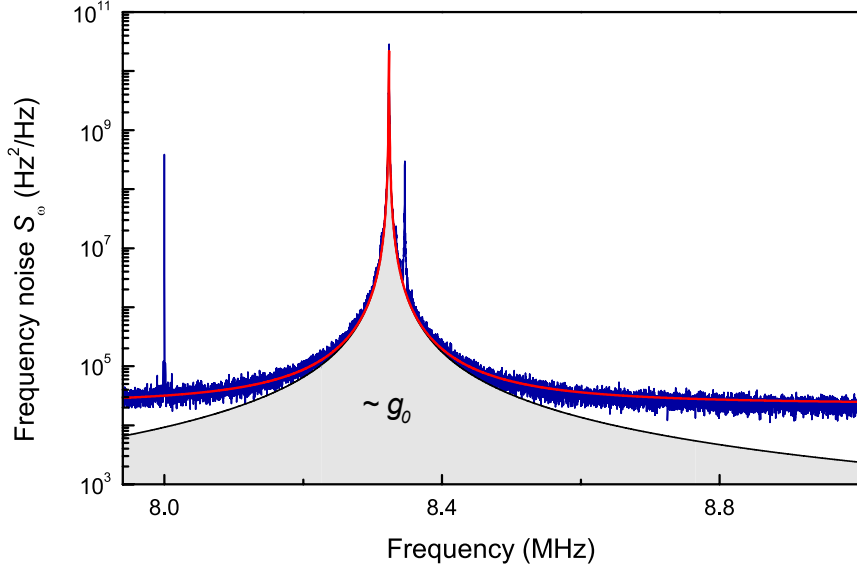


Figure 2.18: Experimental determination of the vacuum optomechanical coupling rate. The (single-sided) frequency noise induced by the fundamental mode of a nanomechanical string is fitted with a Lorentzian. The integral of the corresponding trace (shaded area) directly yields the vacuum optomechanical coupling rate $g_0/2\pi$ according to Eq. (2.37), without having to introduce effective masses or coupling coefficients.

where the superscript in S_ω^{ss} stresses the fact that here, the experimentally acquired single-sided spectrum is used⁹. Provided that the mechanical mode thermalizes to its surrounding bath (which can be easily verified e.g. by measuring the frequency spectrum S_ω at varying input power levels), this quantity is thus most easily experimentally accessible. Besides the cavity frequency noise spectrum $S_\omega[\Omega]$ only the mechanical oscillator's eigenfrequency Ω_m is required which can be simply extracted from the measured spectrum. Fig. 2.18 shows a calibrated frequency noise spectrum $S_\omega[\Omega]$ (see appendix B.3.2 for details on the calibration), reflecting the Brownian motion of a nanomechanical string ($30 \times 0.7 \times 0.1 \mu\text{m}^3$). Fitting the measured trace and directly integrating the Lorentzian frequency noise spectrum (without the constant measurement background) yields a value of $g_0/2\pi = (520 \pm 50)$ Hz. The error bar reflects both the uncertainty in the frequency noise calibration and in the Lorentzian fit. Using the conventions introduced in the previous chapters, a zero-point motion of $x_{\text{zpf}} \sim 20$ fm and correspondingly a coupling coefficient of $g/2\pi \sim 30$ MHz/nm is obtained. In contrast to these, the evaluated zero-point coupling g_0 is independent of the particular definition of the oscillator mass and thus yields an unambiguous measure for the optomechanical interaction strength. Here, g_0 is larger than the typical mechanical dissipation rates $\Gamma_m/2\pi \sim 100$ Hz. However, it is considerably smaller than the typical optical dissipation rates $\kappa/2\pi \sim 5$ MHz. Compared to other cavity optomechanical systems one finds a huge variation of attainable coupling rates, ranging from $g_0/2\pi \sim 1$ Hz in

⁹ Double-sided spectra correspondingly have to be integrated also over negative frequencies.

moveable mirror setups (e.g. Ref. [39]) up to $g_0/2\pi \sim 100$ kHz in optomechanical crystals [53]. All systems, however, share the common feature that the optomechanical coupling rate is orders of magnitude smaller than the optical cavity decay rate κ . Thus, in order to reach the regime of strong optomechanical coupling, which leads to normal mode splitting [36, 145], a strong intracavity field \bar{a} , enhancing the vacuum optomechanical coupling rate to an effective coupling rate $\bar{a} \times g_0$, is required. Strong coupling was first experimentally demonstrated in Ref. [39] using an input power of 11 mW.

2.4 Dynamical backaction

In this section dynamical backaction effects are presented. In particular the first demonstration of radiation pressure dynamical back-action on a nanomechanical oscillator [4] allowing the creation of laser-like mechanical oscillations is discussed. Exceptionally low threshold power levels ($P < 1 \mu\text{W}$) for the onset of regenerative nanomechanical oscillations are found. Moreover, the feasibility of cooling nanomechanical motion by radiation pressure is demonstrated.

2.4.1 Backaction amplification - parametric instability

In section 1.1.4 the radiation pressure parametric instability was discussed. Its first experimental observation was reported in 2005 [26, 28]. Here, it is for the first time possible to transfer this effect into the domain of nanomechanical oscillators. To this end, the microcavity is excited with a blue detuned cw laser beam leading to anti-damping of the employed nanomechanical string which can lead to maser/laser-like [85] amplification of mechanical motion, as described in section 1.1.4. Thereby, the mechanical oscillator resumes the role of the photon field in the laser. The cavity, in turn, has the role of the

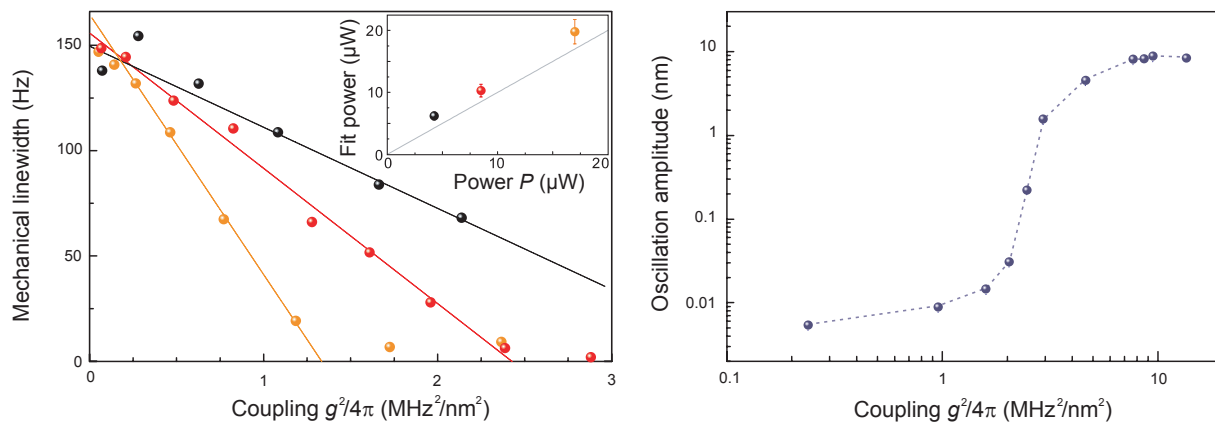


Figure 2.19: Radiation pressure parametric instability of a nanomechanical oscillator. Left panel: Dynamical backaction for blue detuned pumping ($\Delta/2\pi = 6 \text{ MHz}$) leads to linewidth narrowing of the nanomechanical oscillator ($\Omega_m/2\pi = 10.8 \text{ MHz}$, $Q_m = 70'000$, $m_{\text{eff}} = 3.6 \cdot 10^{-15} \text{ kg}$) when increasing the optomechanical coupling g . Fitting the data obtained for different input power levels yields good agreement with the dipolar force (inset). Right panel: Oscillation amplitude of the nanomechanical string (derived from a 30-Hz bandwidth power measurement). It increases as the effective damping is reduced by dynamical backaction. Once the backaction rate exceeds the intrinsic damping rate there is a clear threshold for the onset of large self-sustained oscillations driven by the the light field. The amplitude saturates for amplitudes of several nanometres. Fig. adapted from Ref. [4].

(phonon) gain medium. As in the case of a laser, the canonical signs of this phenomenon are linewidth narrowing, threshold behaviour and eventual saturation of the oscillation. All of these features are observed with the nanomechanical strings as shown in Fig. 2.19.

In the experiment a $31 \mu\text{m}$ radius cavity is pumped by a laser with fixed blue-detuning $\Delta = \kappa/2$. The resonator is evanescently coupled to a nanomechanical string. This leads to a dynamical backaction rate increasing as $\Gamma_{\text{dba}} \propto -g^2 \cdot P$ (cf. Eq. 1.31) and correspondingly to a reduced linewidth of the nanomechanical oscillator, as depicted in Fig. 2.19a. Fitting the measured oscillator linewidths yields good quantitative agreement with the actually employed input power levels (Fig. 2.19a, inset), confirming that the dynamical backaction is indeed caused by the dispersive radiation pressure optomechanical coupling via the optical dipole force. The narrowing of the mechanical linewidth is connected to a increase of the oscillator's temperature, as shown in section 1.1.4. Correspondingly, its mean oscillation amplitude increases for increased optomechanical coupling which is shown in Fig. 2.19b. When the backaction rate eventually equals the intrinsic mechanical damping rate Γ_m , the nanomechanical oscillator experiences net gain causing an onset of coherent mechanical oscillations and its linewidth is narrowed below the resolution limit (1 Hz) of the employed spectrum analyzer. A clear threshold of the mechanical oscillation amplitude can be seen in Fig. 2.19b, followed by a saturation of the mechanical motion once the frequency shift caused by the mechanical oscillator exceeds the cavity linewidth, leading to gain saturation. These large coherent oscillations of up to 10 nm in amplitude can lead, remarkably and

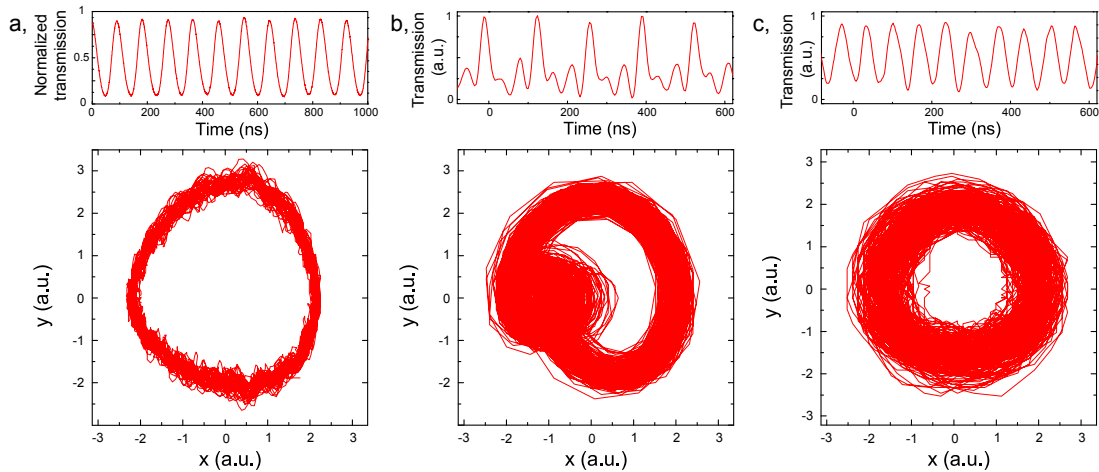


Figure 2.20: Temporal behaviour of self-sustained oscillations. The coherent nanomechanical oscillations cause near-unity modulation of the cavity transmission (a, same oscillator as shown in Fig. 2.19). Here, an input power of $\sim 10 \mu\text{W}$ and a coupling coefficient of $g \sim 5 \text{ MHz/nm}$ is used. For higher coupling power the transmission through the optical resonator becomes nonlinear as depicted in b and period doubling can be observed, c. These data were obtained for a 7.8 MHz nanomechanical string ($P \sim 5 \mu\text{W}$, $g \sim 25 \text{ MHz/nm}$). The nonlinear oscillations are, however, less stable in amplitude as can be seen in the corresponding phase diagrams.

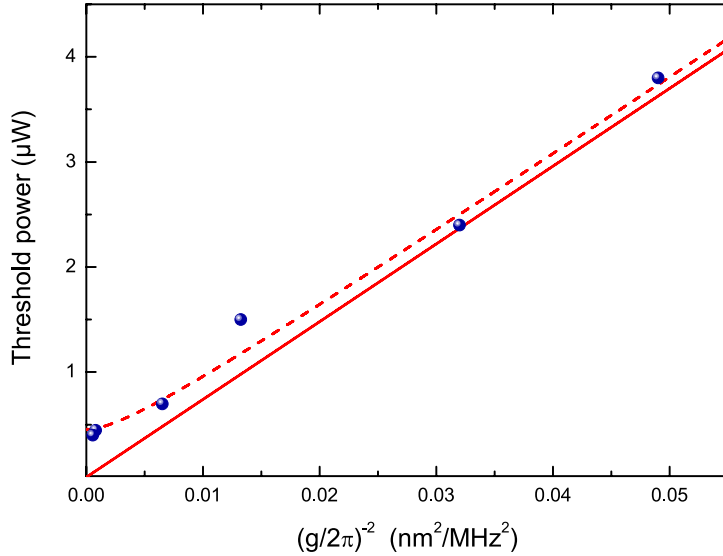


Figure 2.21: Threshold power for the onset of self-sustained mechanical oscillations. P_{th} is shown as a function of the optomechanical coupling g . The lowest threshold power obtained is 400 nW. The solid line is the theoretical expectation from Eq. (1.66) with no fit parameters. The dashed line is a guide to the eye.

despite the nanoscale nature of the strings, to near-unity modulation depth of the optical-cavity transmission, as shown in Fig. 2.20a, when the oscillation amplitude is close to $\kappa/(2g)$. The corresponding phase diagram, recorded over more than 4000 oscillation cycles, shows the coherent nature of these oscillations.

The observation of radiation pressure induced coherent oscillations constitutes the first report of dynamical backaction amplification or cooling of nanomechanical motion using radiation pressure (in contrast to thermal effects [49, 146]), and in particular using optical gradient or dipole forces. A radiation pressure induced optical spring effect within a nano-optomechanical system has been reported in Ref. [49] using a photonic crystal cavity. Dynamical backaction cooling or amplification of nanomechanical oscillators had earlier on, however, been achieved only using single electron transistors [112] or microwave fields [38] which require cryogenic operation and, owing to more than four orders of magnitude longer wavelength, show much lower coupling coefficients.

As the coupling coefficient g (or equivalently \sqrt{P}) is increased in the presented near-field system, the mechanical oscillations may shift the cavity resonance frequency by more than its linewidth such that the transmission of the optomechanical system becomes non-linear. This is shown in Fig. 2.20b-c. These nonlinear oscillations are achieved with minute input powers of only $P \sim 5 \mu\text{W}$. This is about three orders of magnitude less than the power levels used in [27] where similar behaviour is reported for a micromechanical oscillator.

The threshold power P_{th} needed to reach the regime of self-sustained mechanical oscillations has been given in Eq. (1.66). Fig. 2.21 shows the measured threshold power as a function of the employed optomechanical coupling. A remarkably low value of $P_{\text{th}} = 400 \text{ nW}$ is found for a nanomechanical string ($\Omega_{\text{m}}/2\pi = 8.4 \text{ MHz}$, $Q_{\text{m}} = 60'000$, $m_{\text{eff}} = 3 \cdot 10^{-15} \text{ kg}$) using a coupling coefficient of $g/2\pi = 45 \text{ MHz/nm}$.

The radiofrequency signal caused by the mechanical oscillator in the parametric oscillation regime have been proposed to serve as a photonic clock [31] motivated by their

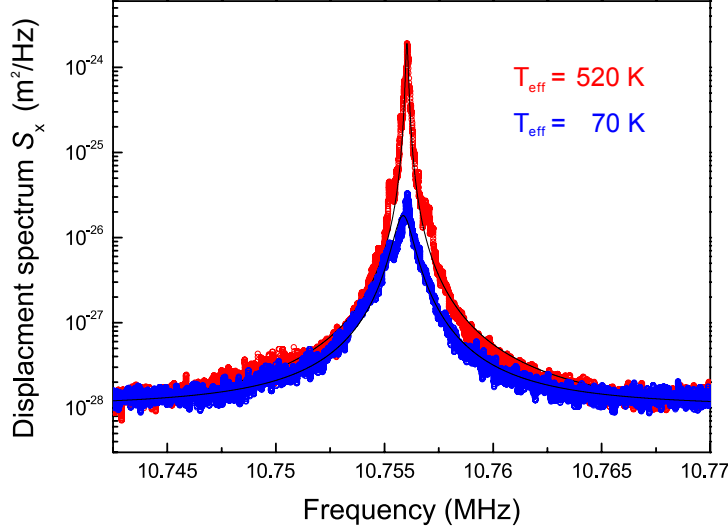


Figure 2.22: Dynamical backaction cooling and heating of a nanomechanical oscillator. The blue (red) trace shows the (single-sided) motional spectrum of a nanostring (properties as described in the text) measured with a negative (positive) detuning of $|\Delta| \sim 10$ MHz. Correspondingly its effective temperature is reduced (increased) to 70 K (520 K).

ultra-narrow linewidth (cf. section 1.1.4). As such, low-power, radiation pressure driven nanomechanical oscillators might be able to serve as on-chip frequency references replacing the commonly used bulkier quartz crystals. Such an application, however, requires a thorough study and minimization of the signal’s phase noise [29–31] to reach the quality of a quartz oscillator.

2.4.2 Radiation pressure cooling

In the previous chapter dynamical backaction amplification was described. The opposite regime, namely dynamical backaction cooling, is also feasible, yielding a tool for radiation pressure cooling nanomechanical motion which had earlier on only been demonstrated using cryogenic microwave resonators [38]. Fig. 2.22 shows the spectra recorded with a nanomechanical string ($\Omega_m/2\pi = 10.8$ MHz, $Q_m = 50'000$, $m_{\text{eff}} = 3.2 \cdot 10^{-15}$ kg, $\kappa/2\pi = 8$ MHz, $P = 14 \mu\text{W}$, $g/2\pi = 4$ MHz/nm) with both a positively and negatively detuned diode laser. The former ($\Delta/2\pi \sim 10$ MHz) leads to linewidth narrowing, and a corresponding effective temperature increase to $T_{\text{eff}} = 570$ K. The latter ($\Delta/2\pi \sim -10$ MHz) increases the oscillator’s intrinsic linewidth $\Gamma_m/2\pi = 220$ Hz via dynamical backaction to $\Gamma_{\text{eff}} = 940$ Hz which leads to cooling by a factor $\Gamma_{\text{eff}}/\Gamma_m \sim 4.3$, i.e. a temperature of 70 K¹⁰.

Recent experiments with micromechanical oscillators have demonstrated much stronger backaction cooling, reaching temperatures of ~ 5 K [10, 32–34] (i.e. cooling by $\times 10^2$) or even in the low mK-range [37] (i.e. cooling by $\times 10^4$), starting from room temperature.

¹⁰ The effective temperature is in both cases inferred by the oscillator linewidth.

Cryogenic implementations of micro-optomechanical systems have, moreover, reached occupation numbers of only ten or a few tens of quanta [8, 40, 50, 147] with a backaction cooling contribution ranging within $10 - 10^3$. Radiation pressure backaction cooling of nanomechanical oscillators, however, has previously only been shown using superconducting microwave systems which have been able to realize cooling factors of $\times 5$ [38] and $\times 100$ [41], limited by thermal effects.

With the employed parameters $\kappa/\Omega_m = 0.74 < \sqrt{12}$ as used here, in principle cooling to a final occupation below $1/2$ is possible (cf. Eq. 1.61). In order to achieve this goal, considerably larger cooling factors would, however, have to be achieved. This corresponds to using larger optomechanical coupling, larger input power or higher mechanical Q. A $\times 10$ larger coupling coefficient as well as two times higher mechanical Q are in principle easily accessible. This would hypothetically then require a still realistic but nevertheless very large input power, i.e. $P = 9.4 \text{ mW}$, to reach an occupation below unity from room temperature. The strong thermal bistability of toroid microresonators [105, 142, 148, 149] would certainly render it very difficult to reliably lock such a high power beam to the red wing of the optical resonance. At temperatures accessible using He-4 cryostats ($T = 1.6 \text{ K}$), however, cooling below unity should be feasible with an estimated (based on the above parameters) input power of only $P = 50 \mu\text{W}$, where the expected increase in mechanical Q of silicon nitride based resonators at cryogenic temperatures [143] is not even taken into account.

2.5 Quantum measurements

One of the major research directions in the context of nanomechanical oscillators has been the design of transducers enabling quantum limited measurements of nanomechanical motion (cf. section 1.1.3). Here we will examine the ability of the near-field system to perform quantum-limited measurements. As will be shown in this section, it enabled for the first time measurements of nanomechanical motion with an imprecision at the SQL [4].

The first part of this section will introduce the two different employed measurement techniques. Then, the classical noise sources that may limit the measurements at room temperature will be discussed. Both have their origin in the finite temperature of the optical resonator serving as transducer: mechanical Brownian motion and thermorefractive frequency noise of the optical microresonator. Despite these noise sources an imprecision 3 dB below the SQL is reached, as will be shown in the third section. Moreover, the quantum-limited imprecision is shown to reach values more than 10 dB below the SQL [2]. This chapter concludes with an estimation of the radiation pressure quantum backaction present in the current measurements and an outlook.

2.5.1 Measurement techniques

The total effective displacement spectrum $S_x[\Omega]$ carried by the measurement laser after coupling to the near-field cavity optomechanical system consists of the following contributions:

$$S_x[\Omega] = S_x^{\text{nano}}[\Omega] + \frac{1}{g^2} \left(S_\omega^{\text{laser}}[\Omega] + S_\omega^{\text{thr}}[\Omega] + \frac{\omega^2}{R^2} S_x^\mu[\Omega] \right), \quad (2.38)$$

where S_ω^{thr} and $\omega^2/R^2 S_x^\mu$ are the frequency fluctuations caused by thermorefractive and mechanical noise within the microcavity which will be discussed in the next section. S_x^{nano} and S_ω^{laser} denote the actual motion of the nanomechanical oscillator and the equivalent frequency noise caused by laser noise. In order to reduce the latter to shot-noise S_ω^{shot} , a quantum-noise limited laser (at the Fourier frequencies of interest) is required. In this thesis two quantum-limited laser sources have been employed: an Erbium-doped fibre laser (emitting at $\lambda = 1550$ nm) and a titanium-sapphire laser (emitting at $\lambda = 800$ nm).

2.5.1.1 Titanium-sapphire laser and homodyne measurement

The layout of the employed titanium-sapphire laser (Coherent MBR-110) is sketched in Fig. 2.23. A 10 W pump laser emitting at 532 nm (Coherent Verdi V-10) is used to pump a titanium-sapphire crystal embedded in a monolithic bow-tie cavity, yielding more than 1 W continuous wave (cw) output power over a wide wavelength range from ~ 700 nm to ~ 900 nm. The coarse tuning of the laser wavelength is accomplished by manually tuning a birefringent filter within the resonator. The electronics supplied with the laser allow single-frequency operation as well as fine-tuning of the laser frequency by using an error signal created by the internal etalon. Moreover, the laser can be locked to the Invar reference

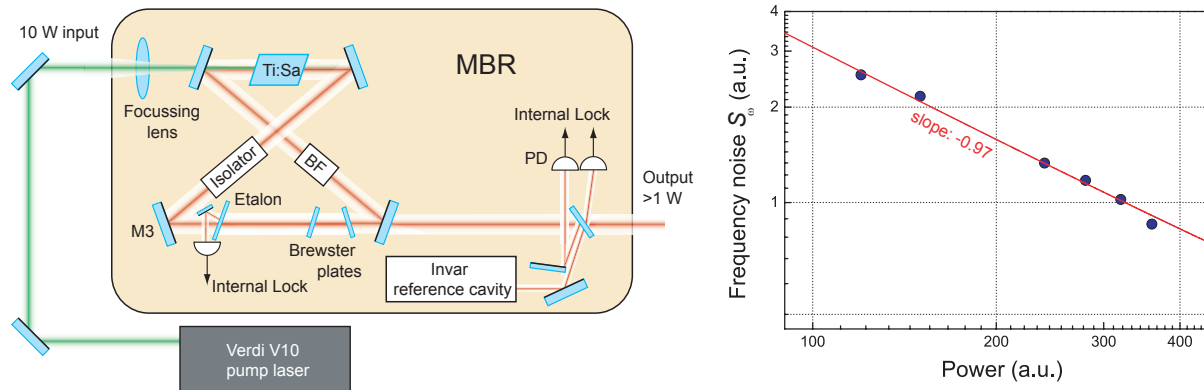


Figure 2.23: The titanium-sapphire laser system. The left panel shows a schematic of the laser system (PD: photodiode, BF: birefringent filter). The right panel shows the measured level of frequency noise S_ω as a function of laser power along with a fit yielding an exponent of -0.97 , close to -1 , as expected for quantum noise.

cavity (typical finesse ~ 50) which is tunable via a piezo. Brewster plates and a small piezo mounted on mirror M3 (cf. Fig. 2.23) provide additional slow and fast actuation of the laser frequency. Overall, the laser can be tuned mode-hop free over a range of 40 GHz. The reference cavity can moreover be locked to an external error signal using the integrated electronic feedback circuit supplied by the manufacturer (locking bandwidth ~ 10 kHz). The measured laser noise performance is quantum-limited in both phase and amplitude at the Fourier frequencies of interest (> 500 kHz) for sufficiently large power levels ($> 200 \mu\text{W}$) at the detectors. Fig. 2.23 shows a measurement of the laser frequency noise for varying power levels. The magnitude of the frequency noise spectrum S_ω thereby reduces linearly with power, as expected for quantum noise.

The homodyne detection scheme which is used in combination with this laser system is depicted in Fig. 2.24. Using a polarizing beam-splitter (PBS 2, cf. Fig. 2.24), the laser light is divided into a high-power local oscillator beam and a low power signal beam (PBS 1 is used for controlling the overall laser power). Both beams are fiber-coupled and the signal beam is sent into the vacuum chamber where it couples to the nanomechanical oscillator via the toroid microresonator and tapered optical fiber. Its polarization is only partly ($\approx 50\%$) adjusted to the optical WGM. The fraction of the light ($\approx 50\%$) that has due to the wrong polarization not coupled to the microresonator and nanomechanical oscillator (signal arm probe beam) is picked off by a combination of waveplates and PBS 3. The local oscillator polarization is adjusted such that most of its power (≥ 1 mW) is transmitted through PBS 3. The small portion of the local oscillator beam reflected by PBS 3 is brought to interference with the signal arm probe beam using PBS 4. This interference signal is used to actively lock the relative phase of both interferometer arms to zero, as depicted in Fig. 2.24b, employing a movable mirror and a motorized translation stage, similar to Ref. [7]. The signal arm measurement beam that has interacted with the cavity is reflected off

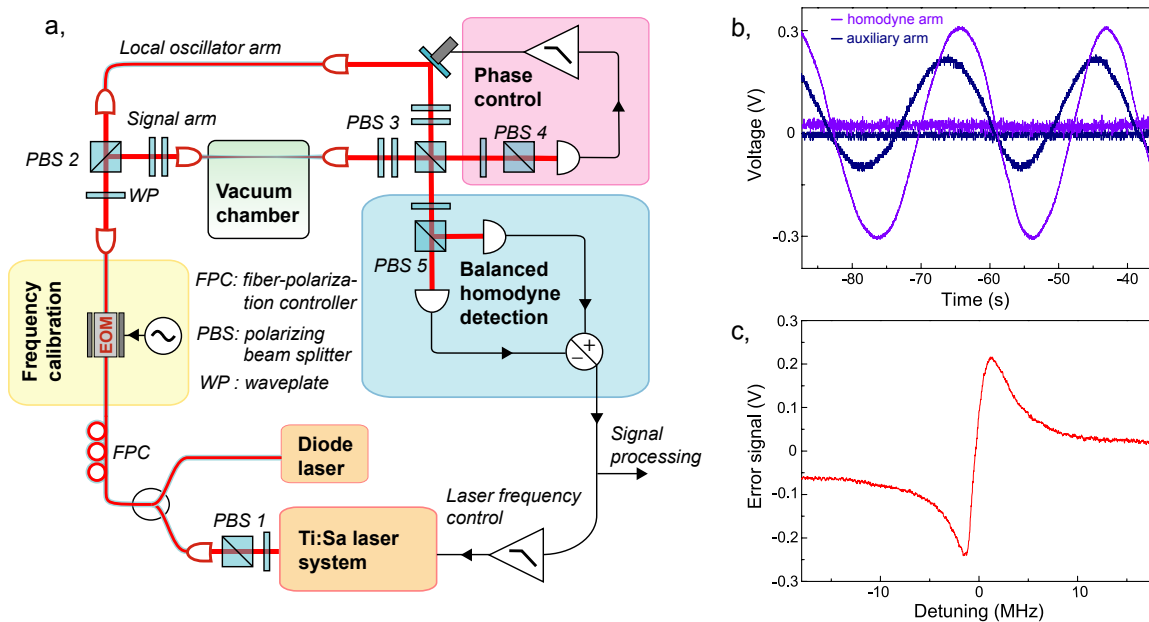


Figure 2.24: Homodyne measurement setup. a, Schematic of the employed setup. See text for details. b, Sinusoidal error signals at the phase control detector (auxiliary arm) and the homodyne detector (note that the x -axis has arbitrary units for these traces). By locking the auxiliary arm signal (phase control lock), the phase difference of signal and local oscillator can be controlled. The locked traces are shown versus time, reflecting the stability of the setup. c, Homodyne error signal obtained when coupling to the optical microresonator for zero phase difference between local oscillator and signal arm.

PBS 3 and brought to interference with the local oscillator at a balanced photo detector after passing through PBS 5. The resulting dispersive signal indicates the phase difference between local oscillator and signal measurement beam. Since the relative phases of both beams acquired by propagating through the system are exactly equal (as ensured by the phase control lock), the phase difference is solely due to interaction of the signal beam with the optical microresonator. Thus, the interference signal indicates the laser detuning with respect to the cavity and its low frequency (≤ 10 kHz) part is used to lock the laser to cavity resonance. The corresponding error signal for a $\kappa/2\pi = 7$ MHz resonance is shown in Fig. 2.24c. The high frequency part of the interference signal is sent to an electronic spectrum analyser thus recording the cavity frequency noise spectrum which is calibrated via a known frequency modulation by means of an electro-optic modulator (cf. Fig. 2.24a, see appendix B.3.2 for calibration details). The optomechanical coupling coefficients g allow the transformation of the frequency noise spectra into equivalent displacement spectra of the nanomechanical oscillators, which can be thus recorded in a shot-noise limited fashion. An additional diode laser proved very helpful for quick characterization and diagnostics.

2.5.1.2 Fibre laser and Pound-Drever-Hall measurement

The second laser source that was used for high-sensitivity monitoring in the course of this thesis is an Erbium-doped fibre laser (Koheras Basik E15). It is a turn-key style laser, that emits in a band of 1 nm in the range of 1550 nm. The laser employed here, yields an output power of ~ 10 mW around 1547 nm. Its wavelength can be tuned via applying voltages to two separate input ports. The first one controls the laser temperature and provides (slow) coarse tuning of the wavelength. The second one actuates a piezo that allows fast (bandwidth: ~ 20 kHz) fine tuning (responsivity: ~ 10 MHz/V) of the laser frequency.

It is a convenient laser system with quantum-limited noise performance for Fourier frequencies above ~ 5 MHz and has been used combined with a Pound-Drever-Hall detection scheme (see Fig. 2.12b for the corresponding measurement setup). However, its comparatively small tunability (1 nm) combined with the large free-spectral range of toroid microcavities (13 nm for $R = 20 \mu\text{m}$) are limiting its application.

2.5.2 Classical noise sources

Let us first discuss the classical sources of frequency noise leading to measurement imprecision, given by thermorefractive noise S_ω^{thr} and Brownian motion of the microresonator $\omega^2/R^2 S_x^\mu$. A broadband measurement illustrating these is shown in Fig. 2.25.

2.5.2.1 Thermorefractive noise

The thermodynamic temperature fluctuations within a given volume element scale inversely proportional to its size [150]. By means of a temperature dependent refractive index, these temperature fluctuations lead to a fluctuating phase of electromagnetic waves when propagating through the volume element. In an electromagnetic resonator this effect thus causes fluctuations of its resonance frequency: thermorefractive frequency noise, which particularly plays a role for small mode-volume resonators. The fundamental temperature fluctuations $S_T[\Omega]$ within the cavity mode volume lead to thermorefractive frequency noise given by

$$S_\omega^{\text{thr}}[\Omega] = (\omega/n \cdot dn/dT)^2 \times S_T[\Omega]. \quad (2.39)$$

For spherical optical WGM microresonators an analytic model of the temperature fluctuation spectrum $S_T[\Omega]$ has been developed [150]. This model is adapted to the toroid microresonators employed in this work [2]. To this end, the optical mode profile is approximated by a Gaussian ellipse with semi-axes r_z given by Eq. (1.73) and r_x given by $b = 0.77 R/\ell^{2/3}$ ¹¹. From Eq. (1.75) (see also Ref. [151]), the angular mode number ℓ of the fundamental optical mode can be deduced:

$$\ell + 1.8558\ell^{1/3} + \frac{1}{2}\sqrt{\frac{R}{r}} - \frac{Pn}{\sqrt{n^2 - 1}} = nk_0R. \quad (2.40)$$

¹¹ This corresponds to the equivalent mode radius when the Bessel function in Eq. (1.72) is approximated by a Gaussian.

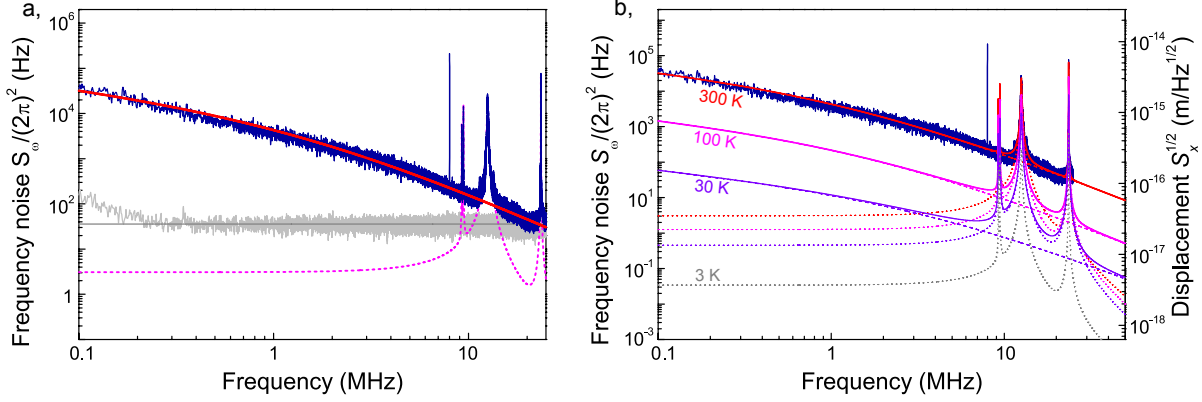


Figure 2.25: Broadband frequency noise (single-sided) of a toroid microresonator. a, The predominant noise source is thermorefractive noise. A fit according to Eq. (2.41) yields good agreement (red line). The equivalent frequency noise caused by shot-noise (grey) is much lower due to sufficiently high input power ($P_{\text{in}} \sim 10 \mu\text{W}$). The mechanical modes of the microresonator (pink dashed line) have negligible off-resonant contribution (8 MHz: calibration marker), here. b, Thermorefractive cavity frequency noise is expected to continuously reduce for lower temperatures, particularly taking the temperature dependence of silica's material parameters into account. For 30 K, a suppression of 25 dB compared to room temperature is expected. Also the toroid mechanical background noise reduces with temperature despite the concomitant decrease of mechanical quality factors (see section 3.5.2 for details) which is explicitly taken into account, here. The right axis shows the corresponding noise floor in displacement units, assuming a coupling coefficient of $g/2\pi = 50 \text{ MHz/nm}$.

The optical mode volume is given by $V = 2\pi^2 r_x r_z R$. Defining a cut-off time τ via $\tau^{-1} = (4/\pi)^{1/3} D (1/r_x^2 + 1/r_z^2)$, where D denotes the thermal diffusivity of silica one arrives at the following approximation for the (single-sided) thermorefractive frequency noise for a fundamental mode:

$$S_{\omega}^{\text{thr}}[\Omega] = \left(\frac{\omega}{n} \frac{dn}{dT} \right)^2 \times \frac{(16\pi)^{1/3} k_B T^2 \tau}{V \rho C \sqrt{\Omega \tau}} \frac{1}{(1 + (\Omega \tau)^{3/4})^2}, \quad (2.41)$$

where C and ρ are the heat capacity (per unit mass) and density of silica. The approximation is valid for Fourier frequencies $\Omega/2\pi \gg D/(2\pi r^2) \sim 40 \text{ kHz}$.

The resonator used for obtaining the data shown in Fig. 2.25 has a major radius of $R = 18.4 \mu\text{m}$ and a minor radius of $r = 1.8 \mu\text{m}$. For a temperature of $T = 300 \text{ K}$, the probe wavelength of $\lambda = 853 \text{ nm}$ and the refractive index of silica $n = 1.45$, expression (2.41) and the constant shot-noise background of $S_{\omega}^{\text{shot}}[\Omega] = (2\pi \cdot 6 \sqrt{\text{Hz}})^2$ are fitted to the measured data by keeping all parameters fixed and using only the mode axes r_x and r_z as fit parameters. Increasing r_z by $\times 1.42$ and decreasing r_x by $\times 0.75$ (thus increasing the mode volume by 7%), the fit yields excellent agreement with the measured data as shown in

T	dn/dT (K^{-1})	C (J/kgK)	k (J/msK)
300 K	$8.7 \cdot 10^{-6}$	730	1.38
100 K	$3.5 \cdot 10^{-6}$	260	0.64
30 K	$1.2 \cdot 10^{-6}$	60	0.26

Table 2.1: Material parameters of silica from Refs. [153] and [154].

Fig. 2.25. The parameter adjustments are attributed to the deviation of the actual mode profile from its Gaussian approximation and the simplified boundary conditions assumed in the analytic approximation.

In total, to a level of $\sim 10\%$ good agreement between measurement and model is found. Thus, thermorefractive noise which may be of relevance also for other nano-optomechanical transducers [49, 152] is well understood in our system. This allows an extrapolation of its behaviour to lower temperatures. In addition to its direct temperature dependence, expression (2.41) also indirectly depends on temperature via the temperature dependent material parameters $\frac{dn}{dT}$, C and $D = k/(\rho C)$, where k is the thermal conductivity of silica. In order to extrapolate the temperature dependence we fit the tabulated values of these parameters [153, 154] via polynomials. Table 2.1 shows values of $\frac{dn}{dT}$, C and k for a few representative temperatures. The overall temperature dependence of Eq. (2.41) predicts a steady reduction of thermorefractive noise for lower temperatures. In Fig. 2.25b, the thermorefractive noise contributions expected for 100 K and 30 K are compared to the room temperature data. At 30 K the level of thermorefractive noise is reduced by approximately 25 dB compared to the room temperature value. Thus, already at 30 K its contribution to the measurement imprecision would be negligible. Since the temperature dependence of the refractive index of silica is known only above 30 K we cannot estimate its exact quantitative behavior for lower temperatures. Most likely it will, however, continue to decrease further for lower temperatures and in similarly sensitive measurements [8] no evidence for thermorefractive frequency noise in toroid microresonators was found.

2.5.2.2 Toroid mechanical modes

As can be seen in Fig. 2.25, also mechanical modes of the toroid contribute to the measurement background. Other than thermorefractive noise, these are, however, peaked around their respective resonance frequencies. By appropriate choice of the cavity geometry, no mechanical mode will be present below 12 MHz, i.e. the frequency range of interest, here. Thus, it is essentially the low frequency tail of all mechanical modes present in the toroid that contributes to the background noise in the frequency band of interest. Since the low frequency tail of a mechanical mode scales as $S_x \stackrel{\Omega \rightarrow 0}{\propto} \Gamma_m / \Omega_m^4$ it is desirable to maximize both the quality factors and the resonance frequencies of the toroid modes. The latter can be simply accomplished by minimizing the size of the cavity and the undercut of the silica disk. This requirement thus nicely coincides with the properties needed for large optomechanical coupling. In order to obtain high mechanical quality factors of the mechanical modes, the rotational symmetry of the toroid as well as the supporting silicon pillar are cru-

cial since asymmetries always give rise to low quality factor mechanical modes. Satisfying symmetry can be achieved although the resonators are fabricated at the edge of their chip support by careful microfabrication (see appendix B.1.1 for details) and thus the current measurements are not limited by mechanical noise of the microresonator. In chapter 3, the mechanical modes of the toroid microresonator will be analyzed more extensively. As will also be shown there, the mechanical quality factor of the intrinsic silica microcavity modes deteriorates at lower temperatures (see section 3.5.2), as opposed to the mechanical quality factor of silicon nitride nanomechanical oscillators [143]. The micromechanical background noise expected for different cryogenic temperatures taking into account the known temperature dependence of the mechanical quality factors of toroid microresonators (see section 3 for details) is depicted in Fig. 2.25b. Despite the reduced quality factors, this noise source also reduces sufficiently fast with temperature and should not limit the sensitivity to values above the shot-noise level. Consequently, at low temperatures shot-noise should be the only relevant contribution to the measurement imprecision and an imprecision at the level of $10^{-17} \text{ m}/\sqrt{\text{Hz}}$ should be feasible (assuming a coupling coefficient $g/2\pi = 50 \text{ MHz/nm}$), as shown in Fig. 2.25b.

2.5.3 Sub-SQL imprecision

Having characterized the different background noise contributions, now the actual measurements of nanomechanical motion will be presented. It is interesting to note that according to Eq. (2.38), all sources of both classical and quantum-mechanical noise are uniformly suppressed by increasing the coupling coefficient g . This is depicted in Fig. 2.26, where the measurement imprecision for a nanomechanical string ($30 \times 0.7 \times 0.1 \mu\text{m}^3$, $\Omega_m = 8.3 \text{ MHz}$, $Q_m = 30'000$, $m_{\text{eff}} = 3 \cdot 10^{-15} \text{ kg}$) is shown as a function of optomechanical coupling for two different input power levels. For large enough coupling coefficients, the imprecision is lowered below the SQL.

As a second variable of the measurements, the input power can be used to vary the shot noise contribution S_{ω}^{shot} , which as opposed to the other contributions to S_x depends on the optical input power $S_{\omega}^{\text{shot}} \propto 1/P$ (cf. Eq. 1.39). Correspondingly, it is limiting for low input power levels. For large enough power levels, it can however be reduced below the classical noise sources, as already shown in Fig. 2.25.

The first measurements with an imprecision below the SQL for a nanomechanical oscillator were obtained using a 1550 nm Erbium-doped fibre laser combined with Pound-Drever-Hall detection, as described in section 2.5.1.2. Employing a $\kappa/2\pi = 50 \text{ MHz}$ resonance, a coupling coefficient of $g/2\pi = 3.8 \text{ MHz/nm}$ and $65 \mu\text{W}$ input power, an imprecision of $S_x = (0.5_{-0.25}^{+0.5}) S_x^{\text{SQL}}$ is achieved for a $4.9 \cdot 10^{-15} \text{ kg}$ nanomechanical string ($\Omega_m/2\pi = 8 \text{ MHz}$, $Q_m = 40'000$) [4]. This measurement represents the first time that a nanomechanical oscillator is measured with an imprecision below the SQL. In absolute terms, the imprecision corresponds to a displacement noise floor of $\sqrt{S_x} = 570 \cdot 10^{-18} \text{ m}/\sqrt{\text{Hz}}$. The error bar in this measurement however amounts to 3 dB. The exceptional dynamic range of $> 60 \text{ dB}$ in addition to the nanomechanical oscillator's narrow linewidth leads to a washing out of the peak of the spectrum in the presence of small drifts of the mechanical resonance frequency

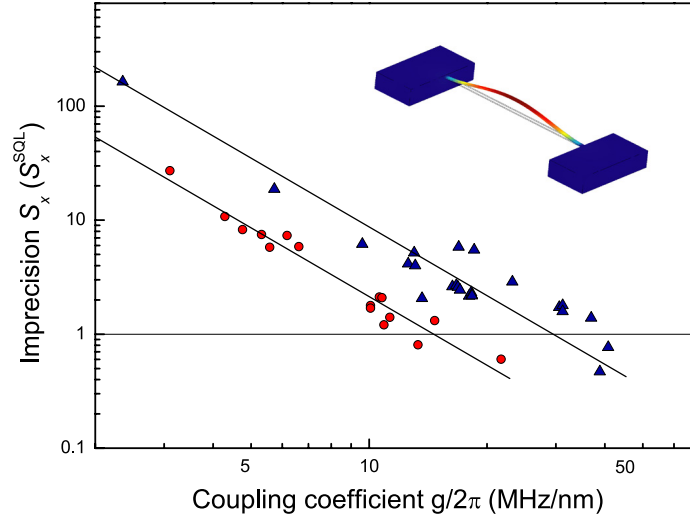


Figure 2.26: Measurement imprecision for a nanomechanical string as a function of coupling coefficient. The measurement imprecision reduces with increased coupling g , irrespective of its origin. It can be lowered below the SQL for both $P = 1 \mu\text{W}$ (red) and $P = 8 \mu\text{W}$ (blue), using homodyne detection. The black lines are guides to the eye. Inset: FEM simulation of the fundamental mode of a nanomechanical string.

on the Hz-level. Thus, the mechanical quality factor (and hence the level of the SQL for the respective measurement) can only approximately be determined from the data which leads to a 3 dB error bar.

As mentioned earlier, in order to increase the optomechanical coupling the experiment was transferred to shorter wavelength and smaller cavities. This allowed an increase of the optomechanical coupling by more than one order of magnitude. Consequently the power needed to reach the SQL (cf. Eq. 1.51) could be reduced by two orders of magnitude. These measurements were performed with the titanium-sapphire laser system presented in section 2.5.1.1. Fig. 2.27a shows a spectrum acquired with a coupling coefficient of $g/2\pi = 40 \text{ MHz/nm}$ and a cavity resonance with a critically coupled linewidth of $\kappa/2\pi = 20 \text{ MHz}$ ($Q_0 = 7.2 \cdot 10^7$). Already $1 \mu\text{W}$ of input power is sufficient to obtain an imprecision below the SQL, $S_x = (0.47 \pm 0.2) S_x^{\text{SQL}}$ ¹². By increasing the input power, the shot-noise limited imprecision can be lowered to values $> 10 \text{ dB}$ below the SQL, using only $8 \mu\text{W}$, as depicted in Fig. 2.27b. Due to the thermal instability of toroid microresonators in connection with residual vibrations in the optomechanical system, however, the coupling coefficient has to be slightly reduced for this measurement (to $g/2\pi = 15 \text{ MHz/nm}$) in order to allow a stable laser lock. Consequently, the higher power measurement is partly limited by thermorefractive frequency noise ($S_\omega^{\text{thr}} \sim (2\pi 14)^2 \text{ Hz}$ at $\Omega \sim 8 \text{ MHz}$).

¹² The mechanical quality factor is evaluated using small coupling. Data whose fitted quality factor deviates by more than 15% from the low coupling value are discarded. This leads to the reduced error bar compared to the previous measurement.

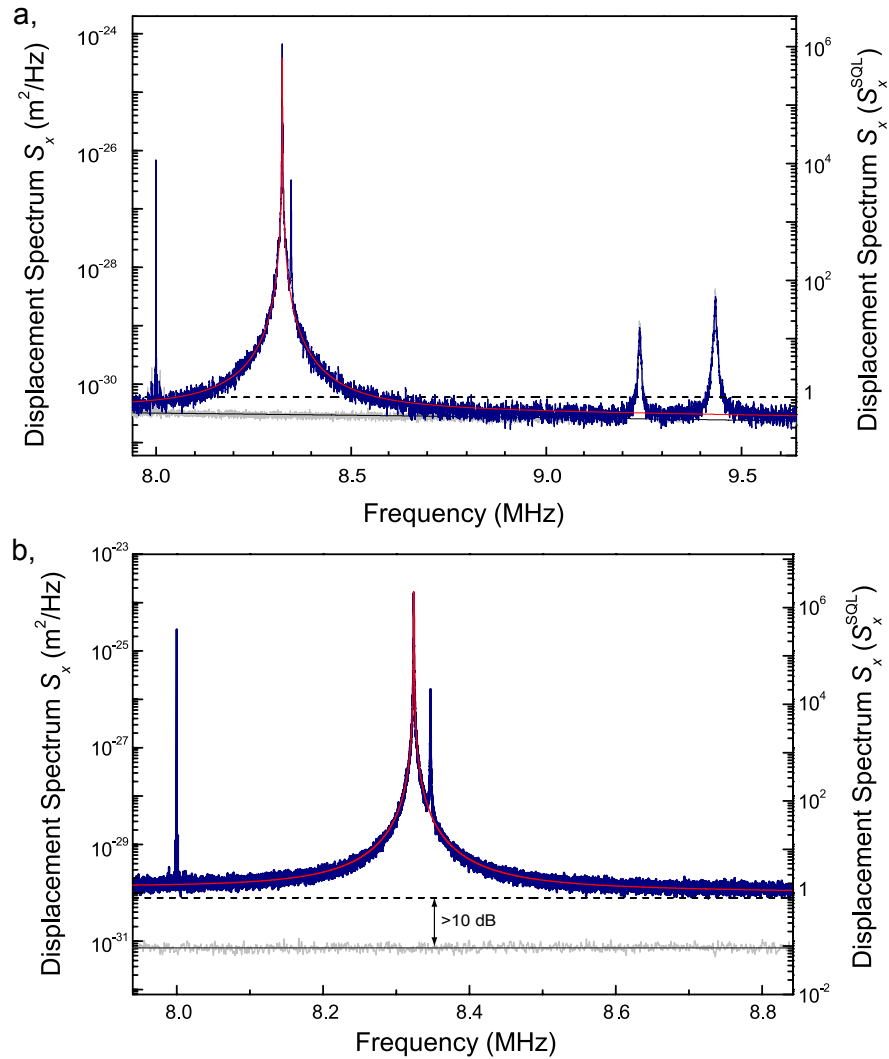


Figure 2.27: Measurement imprecision below the SQL for a nanomechanical string ($30 \times 0.7 \times 0.1 \mu\text{m}^3$, $Q_m = 30'000$, $m_{\text{eff}} = 3 \cdot 10^{-15} \text{ kg}$). Spectra (blue, single-sided) and corresponding fits (red) of the nanomechanical oscillator's fundamental mode at 8.35 MHz. a, The measurement imprecision (grey, acquired by removing the nanomechanical oscillator from the microresonator, i.e. at $g = 0$) lies 3 dB below the SQL (dashed line). 8.4 MHz: in-plane mode of the nanomechanical oscillator, 8 MHz: calibration marker, 9 MHz: mechanical modes of the microtoroid. b, Using higher input power ($P = 8 \mu\text{W}$), the shot-noise level (grey, measured by detuning the laser from cavity resonance) is lowered more than 10 dB below the SQL (dashed line).

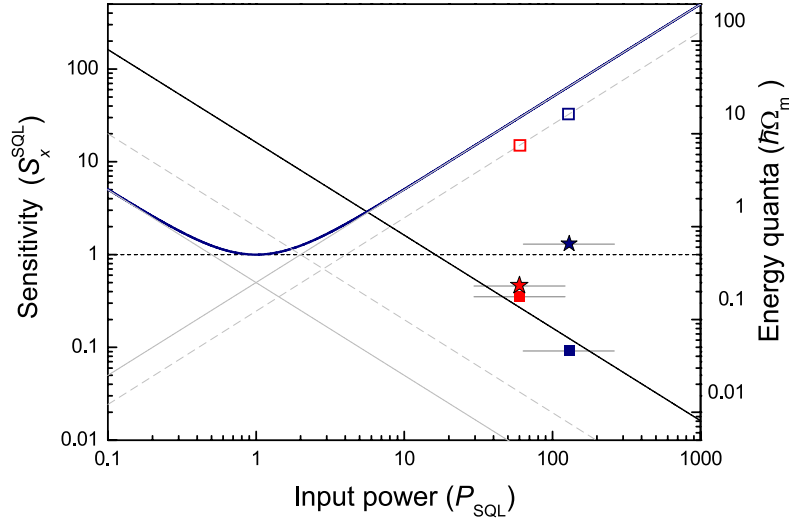


Figure 2.28: Measurement sensitivity (blue line) for an ideal measurement as a function of normalized coupling power. Both shot-noise and quantum backaction (grey) whose values are also given for an impedance matched measurement (dashed grey lines) contribute. The full squares correspond to the measured shot-noise of the traces in Fig. 2.27 whereas the stars mark the corresponding measured total imprecision. The measured shot-noise is fitted by the black line. The empty squares denote the *calculated* quantum backaction, corresponding to approximately $n_{\text{qba}} = 10$ and $n_{\text{qba}} = 20$ noise quanta, respectively.

The measurements shown here are so far the only measurements of nanomechanical motion enabling an imprecision at and below the SQL at room temperature (cf. Fig. 2.2). With the coupling coefficients $g/2\pi > 200$ MHz/nm demonstrated in section 2.2.1 even an imprecision deeply below the SQL would be possible. As mentioned above, the thermal bistability of the toroid microresonator as well as residual vibrations prevent from obtaining a sufficiently stable laser lock in that parameter range for the continuous measurements shown here. By increasing the stability of the employed experimental apparatus (e.g. by exchanging the employed turbomolecular with a vibration free ion-getter pump) and thus the accessible optomechanical coupling, considerable further improvements should be possible.

2.5.4 Backaction of the measurement

Let us point out once again that achieving an imprecision below the SQL does not imply that we have beaten a quantum limit. In principle, the measurement imprecision can be arbitrarily low, as outlined in section 1.1.3. Thus, there is no fundamental obstacle to reaching sub-SQL imprecision. Such an imprecision has however in the past not been achieved for nanomechanical oscillators merely due to a lack of quantum limited detection (this would correspond to large $S_{\omega}^{\text{laser}}$ in Eq. 2.38) combined with low coupling coefficients. Being able to lower the measurement imprecision below the SQL is, however, prerequisite

for a quantum-limited measurement which requires an imprecision that corresponds to exactly $0.5 \times S_x^{\text{SQL}}$. This was enabled for the first time by the demonstrated near-field system as described in the previous section. It might thus facilitate measurements at the SQL in the future and in particular the observation of quantum backaction which comes into play once the imprecision is lowered below the SQL (cf. Fig. 1.2). Let us now turn to an estimation of the level of quantum backaction that should be present in the measurements shown in the previous section. The fact that a critically coupled resonator is employed for the measurements ($\kappa_0 = \kappa_{\text{ex}} = \kappa/2$) gives in fact rise to a shot-noise (quantum-backaction) level that is increased (reduced) compared to the case of an ideal measurement by a factor $\times 4$ ($\times 2$), according to Eq. (1.39) and (1.44). Fig. 2.28 shows the position of both measurement traces depicted in Fig. 2.27 with respect to the SQL. In both cases, the power needed to reach the SQL, P_{SQL} , is evaluated and the input power is scaled to the respective value of P_{SQL} . Corresponding power levels of $P = 60 \times P_{\text{SQL}}$ in the first and $P = 130 \times P_{\text{SQL}}$ in the second case are found. Although the measured shot-noise is slightly larger than expected (which is attributed to losses in the tapered optical fibre and imperfect photo-detectors), a lowest shot-noise level of $0.09 \times S_x^{\text{SQL}}$ is achieved for $P = 130 \times P_{\text{SQL}}$. Based on P_{SQL} , the expected quantum backaction contribution can be estimated. For the second measurement ($P = 130 \times P_{\text{SQL}}$) a quantum backaction contribution of $n_{\text{qba}} \approx 20$ quanta is found, as shown in Fig. 2.28. Hence, QBA should already in the present measurements be the dominating contribution to the measurement sensitivity, much larger than the imprecision caused by thermorefractive ($n_{\text{thr}} \approx 0.5$) and shot noise ($n_{\text{shot}} < 0.1$). But in the current experiment the QBA contribution is masked by the large number of thermal quanta ($\bar{n} \approx 7.5 \times 10^5$) in the nanomechanical oscillator.

It is, however, not unrealistic to envisage experimental parameters that would allow a level of quantum backaction that is comparable to the thermal occupation even at room temperature. The ratio of quantum backaction and thermal noise may, using Eqs. (1.44) and (2.31b), be written in simple terms

$$\frac{S_x^{\text{qba}} [\Omega]}{S_x^{\text{thermal}} [\Omega]} = 4 \frac{g_0^2}{\kappa \Gamma_m} \frac{n_{\text{cav}}}{n_{\text{th}}} \frac{1}{1 + 4\Omega^2/\kappa^2}, \quad (2.42)$$

where $n_{\text{cav}} = \bar{a}^2$ denotes the number of intracavity photons (1.8) and n_{th} is the number of thermal phonons. It can be seen that in order to enhance the QBA contribution it is desirable to combine large vacuum optomechanical coupling rates (requiring large coupling coefficients and zero-point motion) with low optical and mechanical damping κ and Γ_m , respectively. Transforming to more accessible experimental parameters, this expression reads:

$$\begin{aligned} \frac{S_x^{\text{qba}} [\Omega]}{S_x^{\text{thermal}} [\Omega]} &= \left(\frac{g/2\pi}{50 \text{ MHz/nm}} \right)^2 \left(\frac{P}{20 \mu\text{W}} \right) \left(\frac{\lambda}{850 \text{ nm}} \right) \left(\frac{300 \text{ K}}{T} \right) \left(\frac{5 \text{ MHz}}{\kappa/2\pi} \right)^2 \frac{2 \kappa_{\text{ex}}/\kappa}{1 + 4\Omega_m^2/\kappa^2} \\ &\times \left(\frac{15 \text{ pg}}{m_{\text{eff}}} \right) \left(\frac{Q_m}{10^6} \right) \left(\frac{1 \text{ MHz}}{\Omega_m/2\pi} \right). \end{aligned} \quad (2.43)$$

Thus, by combining a nanomechanical silicon nitride string with the properties demonstrated in Ref. [155] ($\Omega_m/2\pi = 1 \text{ MHz}$, $Q_m = 10^6$, $m_{\text{eff}} = 15 \cdot 10^{-15} \text{ kg}$, dimensions:

$275 \times 0.35 \times 0.11 \mu\text{m}^3$) with the already demonstrated optomechanical parameters, a ratio of unity should be well within experimental reach. In particular, assuming $\kappa/2\pi = 5$ MHz at $\lambda = 850$ nm and $T = 300$ K as well as critical coupling, only an input power of $24 \mu\text{W}$ is required to reach a ratio of unity. These intriguing numbers provide a promising outlook for an experiment demonstrating for the first time radiation pressure quantum backaction acting on a solid state mechanical oscillator. This would allow quantum optomechanical experiments [156] such as QND measurements of the intracavity field [64–66] or optomechanically induced squeezing [60, 63] of the optical output field *at room temperature*. Moreover, beating the SQL for one quadrature of the mechanical oscillator using backaction evading techniques would become feasible [67–70] (cf. also section 1.1.3).

2.6 Optomechanical coupling to multiple optical modes

So far, we have only considered a single electromagnetic mode coupled to a single mechanical mode, according to Eq. (1.2). In the literature, however, also the interaction of several optical modes with a mechanical oscillator has been studied both theoretically [75, 76, 157] and experimentally [82, 158]. Such an interaction can considerably enhance both dynamical backaction and transduction of motion.

As mentioned earlier, the power needed to reach the SQL, cf. Eq. (1.51) (or similarly the threshold power for reaching the parametric instability, Eq. 1.66) is a universal figure of merit describing the performance of an optomechanical system. In general, P_{SQL} is reduced by using high quality factor optical resonances, i.e. by using small κ . In the case ($\kappa \ll \Omega_m$) the optical resonator's response, however, becomes too slow to follow the mechanical oscillator's dynamics which cancels the effects of high optical Q. Thus, the system's performance saturates to a value independent of the cavity bandwidth κ . It has been shown that coupling a mechanical oscillator to three optical modes spaced by its mechanical resonance frequency, allows overcoming this limitation [157]. Pumping the central resonance, the motional sidebands at $\pm\Omega_m$ are resonant with the adjacent optical modes, enhancing the transduction of motion. Thus, the SQL may be reached at $P \sim \kappa^2/(4\Omega_m^2) \times P_{\text{SQL}}$, which can be much lower than in the case of a single optical mode.

Similarly, if two optical modes spaced by exactly the mechanical oscillator's resonance frequency are both parametrically coupled to a mechanical mode, the radiation pressure dynamical backaction can be significantly enhanced. When pumping the higher or lower optical resonance, the weight of the Stokes and anti-Stokes sidebands are strongly asymmetric, very similar to the resolved sideband case of a single resonance (cf. section 1.1.4). However, the fact, that the pump laser is now, in contrast to the resolved sideband case, resonantly coupled to one of the optical cavity's resonances enhances the dynamical backaction roughly by a factor $\sim 4\Omega_m^2/\kappa^2$. This may allow a drastic reduction of the power levels needed to achieve ground-state cooling.

Here the feasibility of three-mode interactions—two optical modes coupled to one mechanical mode—using toroid microresonators is discussed. Thereby, the fact that clock- and counterclockwise propagating modes in toroid microresonators, that are intrinsically degenerate, can be coupled via scattering [129, 159, 160] and thus form a doublet is the key ingredient. Before looking at the experimental data, we will first have a look at back-scattering induced mode splitting in whispering gallery mode microresonators.

2.6.1 Modal coupling in whispering gallery microresonators

Following a coupled mode approach [62] the two equations governing coupled clock- and counterclockwise modes a_{cw} and a_{ccw} may be written as

$$\dot{a}_{\text{cw}} = \left(i\Delta - \frac{\kappa}{2}\right) a_{\text{cw}} + \sqrt{\kappa_{\text{ex}}} s + i\frac{\gamma}{2} a_{\text{ccw}} \quad (2.44)$$

$$\dot{a}_{\text{ccw}} = \left(i\Delta - \frac{\kappa}{2}\right) a_{\text{ccw}} + i\frac{\gamma}{2} a_{\text{cw}}. \quad (2.45)$$

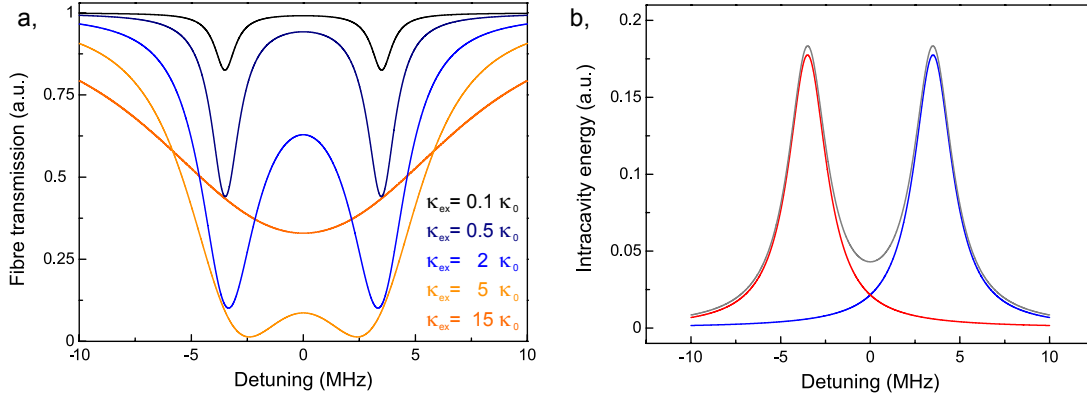


Figure 2.29: Mode doublet of a WGM resonator. a, Transmission of a $\kappa_0/2\pi = 1$ MHz mode doublet with $\gamma/2\pi = 7$ MHz for various external coupling κ_{ex} , as explained in the text. b, Total intracavity energy $|a_{\text{cw}}|^2 + |a_{\text{ccw}}|^2$ (black) as well as the individual contributions of the hybridized lower frequency $|b_1|^2$ (red) and higher frequency mode $|b_2|^2$ (blue) for $\kappa/2\pi = 2.6$ MHz and $\gamma/2\pi = 7$ MHz.

For simplicity it is assumed that both modes exhibit the same decay rates κ . Only the clockwise mode is pumped via the input field s (cf. Eq. 1.7). The former is, however, also coupled to the counterclockwise mode via the scattering rate γ . Here, the detuning Δ is defined with respect to the frequency of the originally degenerate optical modes. The steady state solution to this set of equation can be readily found (see Ref. [160] for further details):

$$a_{\text{cw}} = \sqrt{\kappa_{\text{ex}}} \frac{i\Delta - \kappa/2}{\Delta^2 - \kappa^2/4 - \gamma^2/4 + i\Delta\kappa} s \quad (2.46)$$

$$a_{\text{ccw}} = -i \frac{\gamma/2}{i\Delta - \kappa/2} a_{\text{cw}}. \quad (2.47)$$

Only a_{cw} is coupled to the output mode s_{out} . The output field s_{out} , which is shown in Fig. 2.29a, thus only depends on a_{cw} via $s_{\text{out}} = s - \sqrt{\kappa_{\text{ex}}} a_{\text{cw}}$ (cf. Eq. (1.13)). The population of the mode a_{ccw} , in turn, leads to light being partly reflected from the cavity, $s_{\text{r}} = -i\kappa_{\text{ex}} a_{\text{ccw}}$.

It can be clearly seen that the coupling of both modes to each other leads to the formation of a mode doublet. The doublet can be transformed into a pair of symmetric and antisymmetric modes $b_1 = 1/\sqrt{2}(a_{\text{cw}} + a_{\text{ccw}})$ and $b_2 = 1/\sqrt{2}(a_{\text{cw}} - a_{\text{ccw}})$, representing the lower (higher) frequency mode. This is shown in Fig. 2.29b, along with the total intracavity field energy $|a_{\text{cw}}|^2 + |a_{\text{ccw}}|^2$. Both modes form sine- and cosine-shaped standing wave patterns [137].

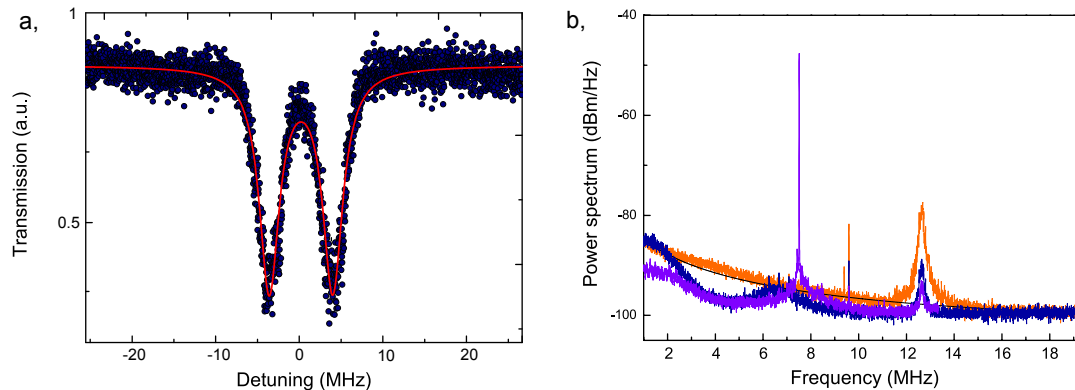


Figure 2.30: Three mode interaction. a, Transmission of the tapered fibre when scanning across a mode doublet with a splitting of $\gamma/2\pi = 7$ MHz and an intrinsic linewidth of $\kappa_0/2\pi = 2$ MHz. b, Recorded frequency noise spectra. The orange trace is taken in the overcoupled regime ($g = 0$). At low frequency, thermorefractive noise dominates, whose magnitude decreases with frequency. The blue trace is recorded in the undercoupled regime ($g = 0$). The transduction of thermorefractive noise decays faster. It is, however, enhanced for frequencies around γ . The violet trace is recorded when coupling to a nanomechanical oscillator whose resonance matches the splitting γ . Since the higher frequency optical mode is used for transduction, the motion of the nanomechanical oscillator is amplified due to dynamical backaction.

2.6.2 Transduction of motion and dynamical backaction using two optical modes

Experimentally, coupling an optical mode doublet to a mechanical oscillator, requires some tunability of either the optical splitting frequency or the mechanical oscillator's resonance frequency in order to match both. This is difficult to achieve using systems that incorporate optical and mechanical degrees of freedom within the same element and do not allow tuning optical and mechanical properties independently.

In toroid microresonators, the optical mode splitting is defined by the density of scattering centres within each optical mode's volume [160] which determines the scattering rate γ . Thus, although the order of magnitude of typical splitting frequencies can be increased by deliberately implanting defect centers [138], its exact value is random and cannot be tuned in-situ. Thus, the mechanical degree of freedom has to act as the tunable element. Using the near-field approach, this can be nicely implemented since the mechanical resonance frequency can be chosen independently. To this end, arrays of nanomechanical oscillators with gradually changing lengths (and thus gradually changing resonance frequency) are fabricated. Thus, exactly matching mechanical oscillation frequency and optical mode splitting can be achieved.

Fig. 2.30a shows the transmission of a toroid microresonator resonance doublet with a splitting of $\gamma/2\pi \sim 7$ MHz. When tuning the laser to either sideband, the transduction of

equivalent cavity frequency noise is expected to be enhanced at frequencies matching the optical splitting frequency γ . This is shown in Fig. 2.30b ($\gamma/2\pi = 7$ MHz). The blue resonance of the optical doublet is pumped with a diode laser (slightly blue-detuned) and the corresponding amplitude noise spectrum is recorded consisting of thermorefractive noise and mechanical noise of both the cavity itself and the nanomechanical oscillator. When the cavity is strongly overcoupled and thus the splitting is removed (cf. Fig. 2.29a), the thermorefractive noise exhibits the typical shape (cf. section 2.5.2.1), as shown in Fig. 2.30b. When the same measurement is performed in an undercoupled regime, the transduction of thermorefractive frequency noise shows a fast cut-off, due to narrow cavity bandwidth ($\kappa/2\pi \sim 2$ MHz). However, an apparent peak at 7 MHz is found, which corresponds to the enhancement of frequencies $\sim \gamma/2\pi$ due to the presence of the second optical mode. If, in addition, a nanomechanical oscillator ($\Omega_m/2\pi = 7.5$ MHz) is coupled to the cavity, the degree of coincidence between splitting $\gamma/2\pi$ and mechanical frequency $\Omega_m/2\pi$ can be directly derived from the recorded RF spectrum. This is shown in Fig. 2.30b where pumping the blue resonance in addition leads to dynamical backaction, amplifying the nanomechanical oscillator's motion.

The dynamical backaction rate in the case of three-mode coupling can be derived from the photon statistics within the cavity, as shown in section (1.1.4). In Ref. [157], the spectrum of the intracavity photon number fluctuations has been derived for the case of resonantly pumping the red (blue) sideband of a mode doublet

$$S_N[\Omega] = |\bar{a}|^2 \frac{4\kappa(-2\Omega \pm \gamma)^2}{4\Omega^2(\pm\gamma - \Omega)^2 + \kappa^2(\pm\gamma - 2\Omega)^2}. \quad (2.48)$$

The dynamical backaction rate (for pumping the red and blue sidebands, respectively) is then calculated to be:

$$\begin{aligned} \Gamma_{\text{dba}}^{(2)} &= \pm |\bar{a}|^2 \frac{1}{9 + 16\Omega_m^2/\kappa^2} \frac{64g_0^2\Omega_m^2}{\kappa^3} \\ &\underset{\Omega_m \gg \kappa}{\approx} \pm 4 |\bar{a}|^2 \frac{g_0^2}{\kappa}, \end{aligned} \quad (2.49)$$

where the geometric factor describing the overlap between both optical and mechanical modes [75] is neglected for simplicity. If one compares this result with the corresponding limit for a single optical resonance ($\Omega_m \gg \kappa$), one arrives at the result that the dynamical backaction rate per intracavity photon is *reduced* in the two-mode case by a factor $(1 + 16\Omega_m^2/\kappa^2) / (9 + 16\Omega_m^2/\kappa^2)$ which approaches unity for $\kappa/\Omega_m \rightarrow 0$. Thus, if the backaction rate is limited by effects due to absorption within the cavity, one does not gain in the regime of two optical modes. One does, however, gain considerably in terms of necessary input power. Since in the two-mode case, the cavity can be pumped resonantly, the dynamical backaction rate can be written as ¹³

$$\Gamma_{\text{dba}}^{(2)} \approx \pm 8 \eta_c \frac{g_0^2}{\kappa^2} \frac{P}{\hbar\omega}. \quad (2.50)$$

¹³ Note that in the presence of splitting the resonant intracavity photon number is reduced by $\times 2$ compared to the case without splitting (1.8).

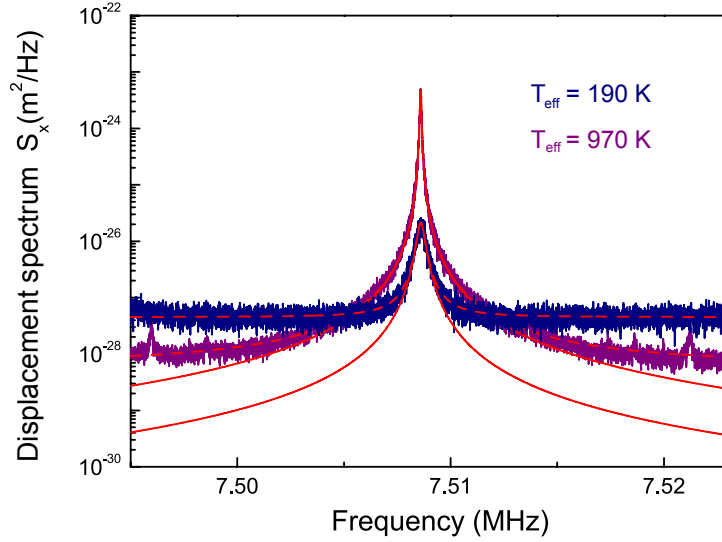


Figure 2.31: Dynamical backaction via two optical modes. Pumping the red (blue) resonance of an optical doublet (splitting $\gamma/2\pi = 7$ MHz) leads to dynamical backaction cooling (heating) of the nanomechanical oscillator ($m_{\text{eff}} = 1.6 \cdot 10^{-15}$ kg, $\Omega_m/2\pi = 7.51$ MHz, $Q_m = 30'000$).

Compared to the single-mode case (Eq. 1.56), this corresponds to an enhancement of $\times 2 \Omega_m^2 / \kappa^2$, which can be considerable and correspondingly may significantly lower the input power levels necessary for a certain cooling factor. Moreover, the fact that resonant pumping can be used, may facilitate strong cooling from room-temperature since operating in the thermally unstable regime of red detuned locking [105, 142, 148, 149] is not necessary, as opposed to the single resonance case. Fig. 2.31, shows that both cooling and amplification of nanomechanical oscillators is possible using two optical resonances. Dynamical backaction rates of order 100 Hz are achieved. Eq. (2.50) suggests that considerably stronger backaction rates should in principle be feasible. However, the non-unity overlap of both optical and mechanical modes would have to be taken into account for a quantitative comparison. Further experiments along these lines would therefore be interesting in order to explore the corresponding limitations. At least in principle, cooling rates bringing the nanomechanical oscillator close to the quantum ground state even from room temperature are accessible. However, also the limitations owing to the finite mechanical Q factor ($Q_m > n_{\text{th}} \approx 8 \cdot 10^5$, is required for ground state cooling [35, 36]) and the thermorefractive noise floor have to be considered in future studies. The latter constraint is a fundamental obstacle, whereas the former may be met by employing mechanical oscillators with larger quality factors $Q_m > n_{\text{th}}$, as demonstrated e.g. in Ref. [136].

2.7 Quadratic optomechanical coupling to nanomechanical oscillators

In this section, the feasibility of leaving the regime of linear optomechanical coupling and realizing quadratic coupling to nanomechanical oscillators using toroid microresonators is demonstrated. Quadratic optomechanical coupling was proposed in 2008 [37]. Thereby, the first order derivative of the optical resonance frequency with respect to the nanomechanical oscillator's position vanishes. The position dependent optical resonance frequency may thus be written as $\omega(x_0 + x) = \omega(x_0) + g^{(2)} \cdot x^2$, where the quadratic coupling term $g^{(2)} = \partial^2 \omega(x_0) / \partial^2 x_0$ is introduced. The corresponding interaction Hamiltonian $H(x_0) = \hbar(\omega(x_0 + x) - \omega(x_0)) a_0^\dagger a_0$ may then, using the rotating wave approximation, be written as [37]

$$H_{\text{om}}^{(2)} = \hbar g^{(2)} x_{\text{zpf}}^2 \left(b^\dagger b + \frac{1}{2} \right) a_0^\dagger a_0. \quad (2.51)$$

In contrast to the linear interaction Hamiltonian (1.2), $H_{\text{om}}^{(2)}$ commutes with the occupation number of the mechanical oscillator, i.e. $[H_{\text{om}}^{(2)}, b^\dagger b] = 0$. Thus, in principle, the quadratic interaction Hamiltonian $H_{\text{om}}^{(2)}$ allows QND measurements of mechanical quanta [37]. QND measurements in various contexts have in the past allowed impressive experiments, demonstrating e.g. quantum jumps of electrons [161–163] or the occupation number of microwave modes [164]. Similarly, observing quantum jumps of a tangible mechanical oscillator may become reality employing quadratic optomechanical coupling [165].

A scheme allowing access to quadratic coupling has first been proposed using a Fabry-Perot cavity and a silicon nitride membrane within the cavity [37]. Here the feasibility of such a situation using nanomechanical oscillators coupled to toroid microresonators will be discussed. Thereby, the fact that clock- and counterclockwise propagating modes in toroid microresonators, that are intrinsically degenerate, can be coupled via scattering plays a key role.

As outlined in the previous chapter, optical WGM resonators can enter a regime where the doubly degenerate clockwise and counterclockwise optical modes form doublets [129, 159, 160]. So far, the nanomechanical oscillators have been coupled *horizontally* to the optical microresonator modes. In order to harness the standing wave patterns of the mode doublets for quadratic optomechanical coupling and to selectively couple to the sine or cosine modes b_1 and b_2 (cf. Fig. 2.29b), we use *vertical* coupling, as depicted in Fig. 2.32, i.e. the strings are positioned perpendicular to the propagation of the light field. When a nanomechanical string is approached to the toroid vertically, the frequency shift of the respective optical mode is proportional to the squared field amplitude at the string's position (cf. section 2.1 for details). Correspondingly, the relative frequency shifts experienced by modes b_1 and b_2 which exhibit standing wave patterns, changes as the nanomechanical oscillator's position is scanned tangentially to the toroid's equator. This is shown in Fig. 2.32a, where the color-coded cavity transmission is depicted as a function

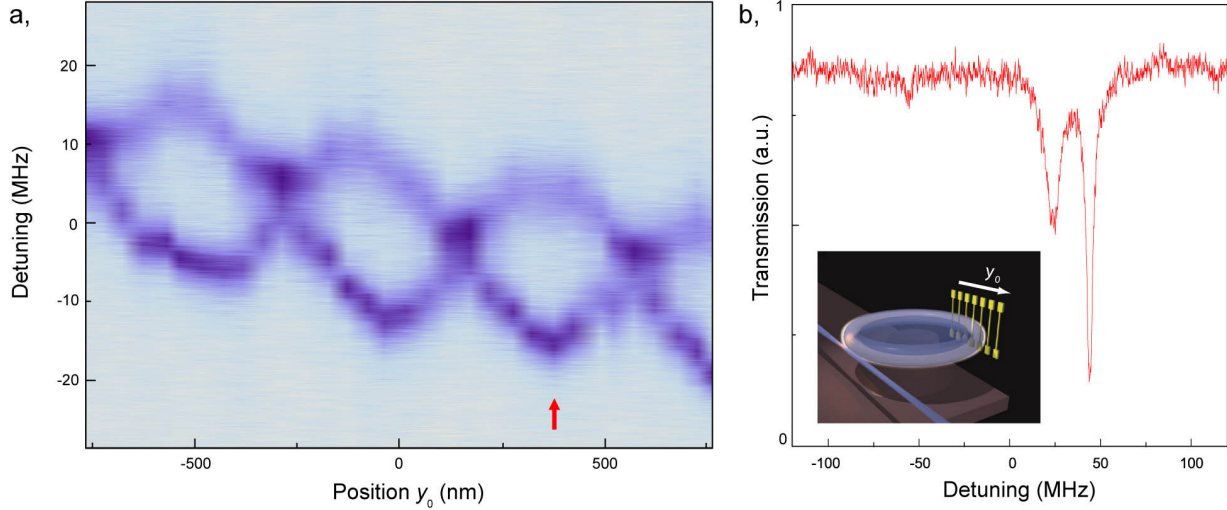


Figure 2.32: Quadratic optomechanical coupling to nanomechanical oscillators. a, Colour-coded transmission spectrum of a toroid microresonator doublet (arbitrary units) as a function of the lateral nanomechanical oscillator position y_0 which is oriented vertically (cf. inset b). At the turning points of the sinusoidal oscillations, the linear optomechanical coupling vanishes and the interaction is quadratic. This is the case at e.g. the location indicated by the red arrow, for which the transmission spectrum is plotted in b.

of the lateral position of a nanomechanical string. The lateral periodicity corresponds as expected to half the wavelength within the optical resonator ($\lambda/2n \approx 500\text{nm}$ for $\lambda \approx 1550\text{nm}$).

At the turning points of the sinusoidally oscillating cavity resonance frequencies indicated by the red arrow in Fig. 2.32a (corresponding to the transmission plotted in panel b) the system exhibits a quadratic optical frequency shift with respect to the in-plane motion of the string (see section 2.3.4), i.e. a non-zero $\frac{\partial^2}{\partial y^2}\omega_0 = g^{(2)}$, whereas $\frac{\partial}{\partial y}\omega_0 = 0$. In this vertical coupling configuration scattering due to the nanostring is observed which is unequally distributed among the two modes, as shown in Fig. 2.32b, since they sense either a maximum (leading to non-negligible scattering) or a node (leading to negligible scattering) at the nanomechanical oscillator's position. The regions where both optical modes cross each other in frequency should in fact exhibit avoided crossings, since both modes are coupled to each other via scattering by the nanomechanical oscillator, leading to additional quadratic coupling points. These are, however, not well resolved in the current measurements. Fitting the data shown in Fig. 2.32a nevertheless yields quadratic coupling coefficients (at the region of the red arrow) of $g^{(2)}/2\pi \sim 1\text{ kHz/nm}^2$.

The data shown here was recorded before the optimization of the optomechanical coupling (cf. section 2.2.1). Using shorter wavelength ($\lambda \sim 800\text{ nm}$) and smaller cavities ($R \sim 16\ \mu\text{m}$) as employed in section 2.2.1, quadratic coupling coefficients of order $g^{(2)}/2\pi \sim 20\text{ kHz/nm}^2$ are expected, similar to the values initially shown in Ref. [37]. In Ref. [166] considerably larger coupling $g^{(2)}/2\pi \sim 30\text{ MHz/nm}^2$ has recently been demon-

strated. In order to assess the feasibility of measuring quantum jumps, however, one has to compare the frequency shift induced by a single phonon $\propto g^{(2)} \times x_{\text{zpf}}^2$ to the shot-noise limit of the measurement [37], given by Eq. (1.39). Thus, using the low-mass nanomechanical strings employed here, which have a $\sim \sqrt{500}$ times larger zero-point motion than the mechanical oscillators (silicon nitride membranes with $1000 \times 1000 \times 0.05 \mu\text{m}^3$) of Ref. [166] makes the expected single-phonon frequency shift expected for the toroid near-field system comparable. Still, resolving the expected quantum jumps is currently a few orders of magnitude out of experimental reach [166]. However, measuring non-classical phonon shot-noise [167] might be feasible with current systems.

2.8 Prospects for graphene sheets as mechanical oscillators

In this section, the feasibility of coupling to nanomechanical oscillators fabricated from graphene will be examined.

Since its experimental realization [168, 169] graphene has attracted enormous interest in recent years due to its exceptional electronic [170, 171], thermal [172] and mechanical properties [173–175] (see Ref. [176] for a recent review). The fact that graphene can be fabricated as single atomic layer sheet of carbon (single-layer graphene) makes it the ultimate version of a two-dimensional solid state mechanical oscillator. Its exceptionally small motional mass combined with large surface makes it very interesting for applications such as mass detection or force/charge sensing. So far, nanomechanical oscillators have been fabricated out of single- [177, 178] to few-layer [174, 177] graphene sheets with width and length of one to a few micron. Thereby, oscillation frequencies around 100 MHz have been found in single-layer graphene and an inverse dependence on the length of the respective ribbon/string has been found [178], indicating internal tensile stress. The room temperature quality factors found were only around 100, similar to the values found in early studies of carbon nanotubes whose mechanical quality factors have meanwhile been improved up to $Q_m > 10^5$ [179]. Recently, mechanical quality factors as high as 14'000 have been reported for a 130 MHz single-layer graphene mechanical mode [178]. This value has been measured at low temperature ($T = 50$ K). However, it is not clear if this is a pristine temperature effect or simply due to the increased tensile stress within the graphene resonator obtained for the specific setup used in Ref. [178].

All the so far employed transducers have fallen short of being able to measure the Brownian motion of single-layer graphene. Here, we will show that this should in principle be possible using a graphene resonator coupled to the near-field of a microtoroid.

2.8.1 Characterization of graphene membranes

One of the experimental challenges, the fabrication of well defined and free-standing graphene membranes has been solved. Fig. 2.33 shows a microscope image of a double-layer graphene sheet suspended over a $5 \times 5 \mu\text{m}^2$ window etched into a silicon chip fabricated in the group of Jannik Meyer. The layer thickness can be reliably examined by Raman spectroscopy [180]. Even simpler, one can exploit the fact that each layer of graphene absorbs an astounding 2.3% of incident light over the whole visible spectrum. This value is surprisingly solely defined by the fine structure constant α which leads to transmittivity T given by $T = 1 - \pi\alpha \approx 97.7\%$ [181]. Fig. 2.33 shows the transmission through a double-layer graphene sheet and the corresponding measurement using an empty window. From these measurements an absorption of $(2.4 \pm 0.2)\%$ per layer can be deduced, in good agreement with the expected 2.3%. Although the reflectivity of a single graphene layer is very small ($R = (\pi\alpha/2)^2 T \approx 10^{-4}$, [181]), the graphene layer can also be detected in reflection (cf. Fig. 2.33, inset) when exposed to a bright source.

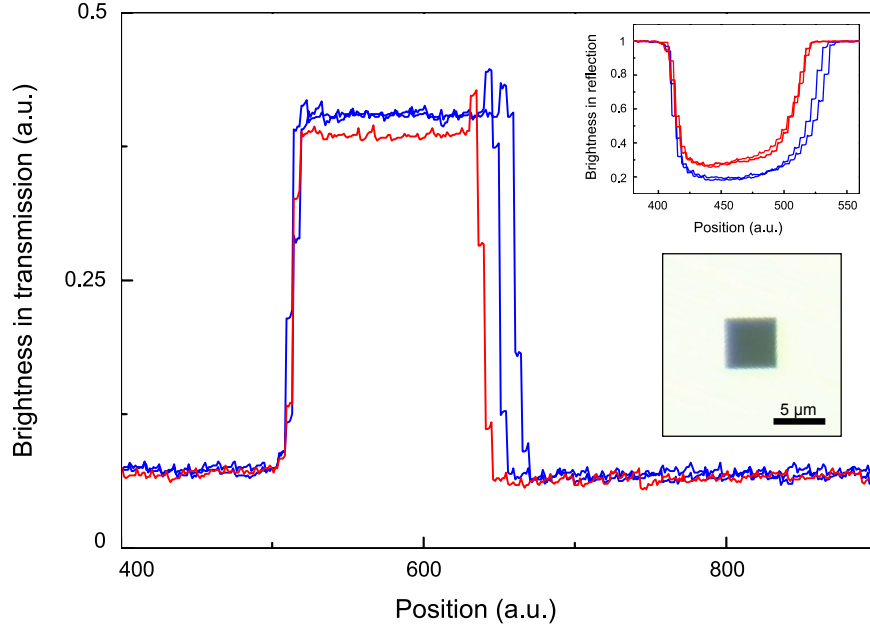


Figure 2.33: Double-layer graphene membrane. The transmission of white light across the center of a double-layer graphene sheet suspended over a $5 \times 5 \mu\text{m}^2$ window (red) and of empty windows (blue) is shown. The averaged absorption per layer is measured to be $(2.4 \pm 0.2)\%$. Despite its low reflectivity, the presence of a graphene sheet on the window can also be verified in reflection (upper inset). The lower inset shows a microscope image of a suspended double-layer graphene membrane.

2.8.2 Optomechanical coupling of graphene

In this section the optomechanical coupling properties of a $5 \times 5 \mu\text{m}^2$ single-layer graphene sheet coupled to the optical near-field of a microtoroid will be estimated. From Eqs. (2.16) and (2.18) one can deduce that for optimum positioning, the coupling coefficients of a $5 \mu\text{m}^2$ graphene sheet should be smaller than the respective coupling to a silicon nitride string (width l_z , thickness t) by a factor

$$\chi \sim \frac{n_g^2 - 1}{n_{\text{SiN}}^2 - 1} \frac{1}{\text{Erf}(l_z/(2r_z))} \frac{1 - e^{-2\alpha t_g}}{1 - e^{-2\alpha t}} \quad (2.52)$$

where n_g and t_g denotes the refractive index and thickness of the graphene membrane. We will, in the following, assume real and imaginary refractive index of graphene to be identical to the values measured for bulk graphite: $n_g = 3$, $n_g^{\text{im}} = 1.9$ [182]. Moreover, the thickness t_g is assumed to be given by the lattice constant in graphite $t_g = 0.3 \text{ nm}$. For typical values ($R = 18 \mu\text{m}$, $r = 1.8 \mu\text{m}$, $\lambda = 850 \text{ nm}$, $l_z = 300 \text{ nm}$, $t = 100 \text{ nm}$), one then obtains $\chi \sim 7 \times 10^{-2}$. For an ideally positioned graphene sheet, the dispersive coupling coefficient is therefore expected to be ~ 15 times smaller than the ones accessible for silicon nitride nanostrings. Thus, coupling coefficients of $g/2\pi \lesssim 10 \text{ MHz/nm}$ or equivalently

static frequency shifts of $\Delta\omega/2\pi \lesssim 500$ MHz may be expected. These values should in principle allow the observation of the Brownian motion of a single-layer graphene sheet. Assuming a frequency of $\Omega_m/2\pi \sim 15$ MHz (extrapolated from Refs. [173, 178]) a mechanical Q of 100 and a mass of $m_{\text{eff}} = 4 \cdot 10^{-18}$ kg (based on a density of $\rho = 2000$ kg/m³), the (single-sided) Brownian noise at resonance evaluates to $S_x[\Omega_m] \sim 5 \cdot 10^{-25}$ m²/Hz. With a dispersive coupling coefficient of $g/2\pi = 1$ MHz/nm this should lead to a frequency noise of $S_\nu = 5 \cdot 10^5$ Hz. For such a coupling coefficient the cavity linewidth is estimated to be broadened to $\kappa/2\pi \sim 1$ GHz using a simple model based on the real and imaginary refractive indices. Nevertheless, this should still allow the detection of the frequency noise $S_\nu = 5 \cdot 10^5$ Hz induced by the graphene sheet (the role of the dispersive coupling coefficient is neglected, here).

The experimental challenge, however, is the correct positioning of the graphene samples with respect to the toroid. Using silicon nitride oscillators, the dispersive cavity resonance frequency shift caused by the silicon nitride in the evanescent field can be conveniently used as a signal for coarse positioning as it is distinct from the predominantly reactive shift induced by the silicon substrate¹⁴. When considering graphene, each induced dispersive frequency shift will always be accompanied by a considerable increase of the cavity linewidth owing to its relatively large imaginary refractive index. Thus, the static shifts exerted by graphene and the silicon substrate are expected to be very similar to each other and might not easily be distinguished experimentally. In order to simplify “finding” the graphene membrane’s modes, a piezo actuator that drives the mechanical resonances could be used in order to facilitate locating these.

¹⁴ This is caused by light leaking into the large refractive index bulk silicon substrate which supports a continuum of optical modes, see also appendix B.2

Chapter 3

Monolithic ultra-low dissipation optomechanical resonators

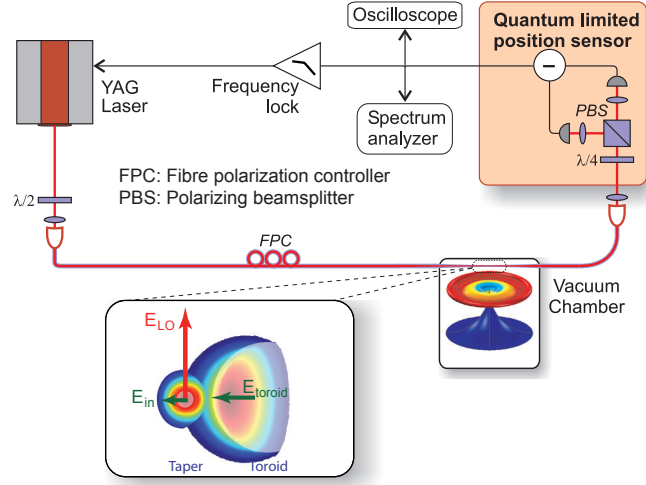
Since their inception in 2003 [88], the exceptional optical properties of toroid microresonators have been exploited in a variety of fields. Applications range from non-linear optics, e.g. frequency comb generation [89–91] or Raman lasing [92] to molecular recognition [93] and cavity QED [94–96]. In 2005, it was found that they also host a variety of mechanical modes which are naturally parametrically coupled to their optical whispering gallery modes and can be driven via radiation pressure [26–28]. One year later, toroid microresonators [34] were among the first solid-state mechanical oscillators that were cooled via radiation pressure dynamical backaction [32–34]. Moreover, they enabled for the first time resolved-sideband cooling of a micromechanical oscillator [10]. In this chapter, the mechanical properties of toroid microresonators are thoroughly analyzed. First, the optomechanical coupling within toroid microresonators is briefly reviewed before their mechanical mode structure is analyzed in detail. Following a summary of relevant loss mechanisms leading to mechanical dissipation in general, clamping losses are elucidated in detail and identified as the leading contribution limiting the quality factors of the most prominent microtoroid mode, the fundamental radial breathing mode. Subsequently, spoke-supported microresonators that minimize clamping losses are presented. They allow realizing the ultimate material-loss limit of the attainable mechanical quality factor in silica-based systems.

3.1 Optomechanical coupling

As already shown in chapter 2, the presence of thermally excited mechanical modes within toroid microresonators leads to clear signatures in their optical frequency noise spectra. The displacement of the cavity boundaries caused by the Brownian motion of the toroid's eigenmodes leads to a change in the effective round-trip length of the cavity ¹ and thus its

¹ The concomitant strain-fields also contribute an effective length change via a strain dependent refractive index. Their contribution can be estimated to be only on the order of 20% compared to the displacement contribution [142] and are thus neglected, here.

Figure 3.1: Polarization spectroscopy. Only a small polarization component of the Nd:YAG laser is adjusted to match the toroid's whispering gallery mode polarization. The larger fraction (with orthogonal polarization) of the field bypasses the cavity and serves as a local oscillator. It is brought to interference with the output field of the cavity using a quarter waveplate and a polarizing beam splitter. The resulting signal is recorded using a balanced detector. Figure adapted from Ref. [6].



resonance frequency. To model this optomechanical coupling, a universal coupling coefficient of $g = \omega/R$ is chosen, irrespective of the actual optical or mechanical modes involved. This choice is motivated by the experimentally most interesting mode, the radial breathing mode (RBM). As shown in more detail later on, this mode comprises predominantly radial motion. Considering this radial motion of the toroid's boundary within a simple ray picture, a change Δx of the toroid's radius R would lead to a frequency shift given by $\Delta\omega/\Delta x = \omega/R$, i.e. exactly the shift described by the assumed coupling g . Moreover, as a photon travels along the cavity boundary over an angle φ it transfers a momentum of $\Delta p = -\varphi p$ (p denotes the photon momentum within the cavity) to the cavity which leads to a per-photon force of $F = -\hbar\omega/R$. Thus, also the per-photon force in this picture is correctly reproduced by the choice $g = \omega/R$. As outlined in section 2.3.1, the choice of a uniform coupling coefficient, however, necessitates the notion of an individual effective mass for each particular combination of optical and mechanical mode which can be extracted either from measurements or finite element simulations.

3.2 Mechanical mode spectrum

In this section, the mechanical mode spectrum of toroid microresonators will be thoroughly examined. In order to obtain high sensitivity which is desirable for a detailed characterization of the spectrum, a quantum-noise limited Nd:YAG laser (neodymium-doped yttrium aluminum garnet; type Mephisto from Innolight GmbH) emitting at $\lambda = 1064 \text{ nm}$ is employed. Combined with a polarization spectroscopy (Hänsch-Couillaud) technique [183], as shown in Fig. 3.1, it enables shot-noise limited detection of the cavity frequency noise. The laser is fibre-coupled and sent to the vacuum chamber where a tapered-fibre region allows coupling to the microresonators. The laser polarization is chosen such that only a small fraction of the field matches the polarization of the respective WGM. The larger fraction thus bypasses the resonator and is used as local oscillator which is brought to interference with the signal emerging from the resonator using a waveplate and a polarizing beam splitter (cf. Fig. 3.1). This enables a dispersive error signal as a function of the laser detuning from cavity resonance [183]. Its low frequency part is used to lock the laser to resonance whereas the high frequency part enables extracting the respective cavity frequency noise. Compared to the homodyne detection scheme employed in the previous chapter, this setup is considerably less complex as it does not need any active stabilization. The strong asymmetry between local oscillator ($P_{\text{lo}} \gg 50 \mu\text{W}$) and signal power levels ($P_{\text{s}} < 5 \mu\text{W}$), however, makes the measured signals very sensitive to drifts of the input field's polarization. In practice, this limits the long-term stability and applicable power ratios $P_{\text{lo}}/P_{\text{s}}$ using polarization spectroscopy.

Fig. 3.2a shows the displacement spectrum of a toroid ($R = 23 \mu\text{m}$) which reveals 16 mechanical modes in the range $0 - 100 \text{ MHz}$. Using FEM simulation, all measured frequencies can be attributed to a particular mechanical eigenmode. To this end, the geometry parameters obtained from a microscope image of the sample are used as start values and subsequently fine-tuned in order to fit the simulated to the measured frequencies. Excellent agreement with an average deviation of less than 2% is found, as shown in Fig. 3.2b. The corresponding mode patterns are depicted in Fig. 3.2c. Only three out of the 19 modelled modes are experimentally not observable which is attributed to a combination of low mechanical Q and large effective mass. Due to the composite geometric structure of microtoroids, resulting in a relatively complex geometry (when e.g. compared to strings or membranes) microtoroids exhibit a diverse set of eigenmodes. Several mode families can nevertheless be distinguished in which the motion of the silica disk, the silica torus and the silicon pillar partially decouple. The mode showing the lowest effective mass and hence the most interesting mode is the RBM (mode 14 in Fig. 3.2). Most previous work has therefore focused on this mode [26, 34]. An equivalent mode has been studied in a microdisk structure [184] where it was termed radial contour mode. In contrast, the torsional mode (mode number 4 in Fig. 3.2) where the silica disk shows an in-plane rotation should not be optomechanically coupled at all to first order. Interestingly, this torsional mode can nevertheless be observed experimentally. One particular mode family that can be identified are the radially symmetric flexural modes (modes 2 and 8 in Fig. 3.2) in which the motion of the free standing part of the silica disk resembles the modes

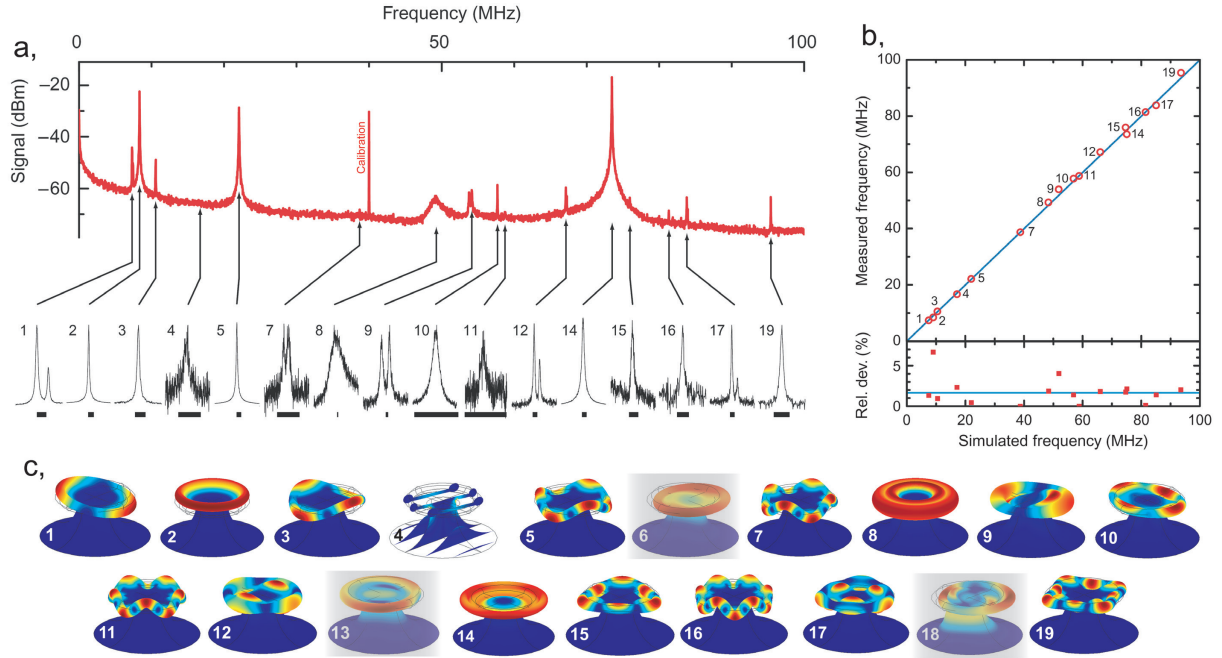


Figure 3.2: Mechanical mode spectrum of a toroid microresonator. a, Displacement noise spectrum of a $R = 23 \mu\text{m}$ microtoroid in the range 0 – 100 MHz. All measured frequencies can be attributed to a particular mode as derived by FEM simulations with an average deviation of less than 2%, b. The corresponding mode patterns are shown in c (colour code: total displacement in arbitrary units), where the shaded modes are not observed experimentally. Fig. adapted from Ref. [7].

of a cantilever. The fundamental frequencies of a cantilever of length L can in general be expressed as $\Omega_i/2\pi = C \cdot \sqrt{k_i}/2\pi$, where C is a material constant and the wavenumber k_i satisfies [185]

$$\cos(k_i \cdot L) \cdot \cosh(k_i \cdot L) + 1 = 0. \quad (3.1)$$

Fig. 3.3 shows the measured frequencies of the two lowest order flexural modes (modes 2 and 8 from Fig. 3.2) and, in addition, the first five flexural modes of a different sample plotted as a function of the wavenumber k_i , where the free standing part of the silica disk is taken as equivalent cantilever length L ($13.2 \mu\text{m}$ and $39.6 \mu\text{m}$, respectively). Both sets of data allow an accurate uniform quadratic fit of the fundamental radially symmetric modes. Thus, the latter can indeed be regarded as cantilever modes following the same quadratic dispersion for microtoroids of different sizes. The absolute measured frequencies deviate only by -25% from the crude approximation of an ideal cantilever [185] with length L , taking into account the material parameters of silica. A further separate mode family which is characterized by sinusoidal oscillations of the torus itself (modes 1, 3, 5, 7, 11 and 16 in Fig. 3.2) can be identified. The dispersion diagram of these modes, which are referred to as crown-modes, is depicted in Fig. 3.3. The respective wavelength λ_i is

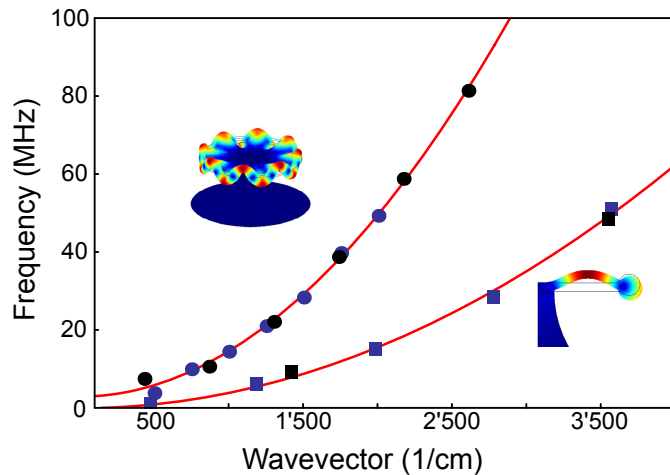


Figure 3.3: Dispersion of crown (circles) and cantilever modes (squares). Both mode families follow a uniform quadratic dependence on wavenumber measured for two different samples (black: $R = 23 \mu\text{m}$, blue: $R = 45 \mu\text{m}$). Inset: FEM mode patterns of eighth order crown and second order cantilever modes (colour code: total displacement in arbitrary units). Fig. adapted from Ref. [7].

defined by twice the distance between two adjacent nodes of each mode. The frequencies $\Omega_i/2\pi$ of the crown modes observed in microtoroids of different major and minor radius ($23 \mu\text{m}/2.6 \mu\text{m}$ and $45 \mu\text{m}/2.8 \mu\text{m}$) allow a simultaneous fit following a quadratic dependence on the wavenumber $k_i = 2\pi/\lambda_i$. The uniform dependence shows that the silica torus, despite its attachment to the silica disk, behaves effectively like an independent element. The quadratic dispersion, moreover, rules out the presence of radial tensile stress within the torus as this would lead to linear dispersion characteristic of a vibrating string, cf. Eq. (2.20). This can be explained by the laser reflow process which the microtoroids undergo [88] and which relaxes all potentially present stress. The absolute frequencies of the crown modes, however, are $\times 4$ larger than predicted by Eq. (2.20) for an ideal silica string which is due to the attachment to the silica disk causing additional stiffness.

3.3 General sources of mechanical dissipation

It became evident already in the previous section that the various mechanical modes present in microtoroids exhibit vastly different mechanical quality (cf. Fig. 3.2). In this section, relevant contributions which lead to mechanical dissipation in general and thus determine the mechanical quality will briefly be reviewed. When modelling a damped harmonic oscillator, all damping contributions are typically summed up to a single damping rate Γ_m and correspondingly to a total mechanical quality factor $Q_m = \Omega_m/\Gamma_m$. Thereby, the total damping rate is given by the sum of the rates relating to the individual sources of loss, i.e. $\Gamma_m = \sum_i \Gamma_i$. Correspondingly, the mechanical quality factor can be written as

$$Q_m^{-1} = \sum_i Q_i^{-1}. \quad (3.2)$$

In the following, we start with the loss mechanisms that can in principle be eliminated completely (or at least to a negligible amount) by using a suitable experimental setting (gas damping, clamping losses) before more fundamental sources are discussed (two-level systems, thermoelastic damping and phonon-phonon interaction).

3.3.1 Gas damping

Operating a mechanical oscillator in a gaseous environment will lead to energy dissipation from the mechanical oscillator into the heat bath provided by the surrounding gas molecules. For large pressures, the gas may thereby be treated as a fluid. Correspondingly, the viscosity of the gas dominates the damping, leading to a quality factor $Q \propto p^{-1}$ [186]. This regime is typically referred to as viscous damping regime. For lower pressures, this source of damping becomes negligible. Another component has, however, to be taken into account, given by individual collisions of gas molecules with the mechanical oscillator. The resulting damping mechanism leads to a weaker pressure dependence $Q \propto p^{-1/2}$ [186, 187] and has been termed molecular gas damping regime. However, for practically all mechanical oscillators gas damping can be lowered to negligible values by using moderate pressure levels in or even above the high-vacuum range.

3.3.2 Clamping losses

The fact that typically, solid state mechanical oscillators are not freely suspended but rather attached to some kind of support leads to dissipation into the supporting structure. This is typically referred to as clamping losses. In principle this source of loss can be eliminated to a level where the loss is only given by phonon-tunneling [188]. Although universal for all “clamped” structures, clamping losses can vary to a large amount within different resonator geometries and thus have to be specifically optimized for each particular mechanical oscillator, individually. In particular, the support of test masses employed for gravitational wave detection has been extensively studied in the past [189–191]. But also

in the micromechanics community considerable efforts have been devoted to a clever design of the mechanical oscillators' support [192–194].

3.3.3 Two-level systems

In virtually all amorphous materials, a loss mechanism which can be regarded as more fundamental than the previously mentioned ones is present. It is caused by the lack of long-range order characteristic of amorphous solids and the concomitant structural defects [195]. The precise microscopic origin of these defects is not known to date. The phenomenology of the mechanical damping that is associated with these defects, however, can be accurately reproduced by modelling them as a distribution of effective two-level systems (TLS) which can change their conformation. Thereby, the defects (that may be comprised of single atoms or groups of atoms) have two equilibrium positions which are given by the two minima of an asymmetric double well potential [196–201]. Following the notation of Ref. [202], the phonon strain field e deforms the lattice of the solid which modulates the energy difference Λ between the energy minima. This leads to a coupling between strain field and the TLS described by $2\gamma = \partial\Lambda/\partial e$. Combined with a relaxation of the population at rate τ^{-1} this perturbation gives rise to a frictional force acting on the mechanical mode which limits the quality factor to [202]

$$Q_{\text{tls}}^{-1} = \frac{\gamma^2}{\rho v^2 k_B T} \int_{-\infty}^{+\infty} d\Lambda \int_0^{+\infty} dV P(\Lambda, V) \operatorname{sech}^2\left(\frac{\Lambda}{2k_B T}\right) \frac{\Omega\tau}{1 + \Omega^2\tau^2}, \quad (3.3)$$

where v and ρ denote the speed of sound in and the density of the particular material. $P(\Lambda, V)$ is the density of TLS with energy splitting Λ and barrier height V (the energy maximum lies $V + \Lambda/2$ above the ground state of the lower energy well). Note that Q_{tls} depends on both temperature and frequency. The relaxation time is given by

$$\tau = \tau_0 e^{V/T} \operatorname{sech}\left(\frac{\Lambda}{2k_B T}\right), \quad (3.4)$$

where τ_0 is inversely proportional to the oscillation frequency within the individual wells. Assuming a phenomenological density function

$$P(\Lambda, V) \propto \left(\frac{V}{V_0}\right)^{-\zeta} \exp\left(-\frac{1}{2} \frac{V^2}{V_0}\right) \exp\left(-\frac{1}{2} \frac{\Lambda^2}{\Lambda_c}\right), \quad (3.5)$$

with cut-off energies V_0 and Λ_c ($\zeta < 1$), expression (3.3) can be approximated by:

$$Q_{\text{tls}}^{-1} = \mathcal{C} \operatorname{Erf}\left(\frac{\sqrt{2}k_B T}{\Lambda_c}\right) \frac{1}{k_B T} \int_0^{\infty} \left(\frac{V}{V_0}\right)^{-\zeta} \exp\left(-\frac{1}{2} \frac{V^2}{V_0}\right) \frac{\Omega\tau_0 \exp(V/(k_B T))}{1 + \Omega^2\tau_0^2 \exp(2V/(k_B T))} dV. \quad (3.6)$$

Thus, the temperature and frequency dependent damping due to TLS is characterized by the material coefficients \mathcal{C} , Λ_c , V_0 , ζ and τ_0 . The model (3.6) universally describes the damping found in virtually all amorphous materials [195]. For silica, taking into account measurements spanning from 11 kHz to above 200 MHz and from a few up to a few hundred Kelvin allows the extraction of $\zeta = 0.28 \pm 0.03$, $V_0/k_B = (667 \pm 21)$ K, $V_0/\Lambda_c = 7.7 \pm 0.7$, $\tau_0 = 10^{-12.2 \pm 0.18}$ s and $\mathcal{C} = (1.45 \pm 0.35) \times 10^{-3}$ [202].

TLS can be the dominant loss channel in amorphous solids. In order to avoid this source of dissipation one has to resort to crystalline materials. These can exhibit almost perfect long-range order and thus negligible damping due to defect induced two-level fluctuators.

3.3.4 Thermoelastic damping

A fundamental source of dissipation inherent to all material (also crystals) is given by thermoelastic damping. It can be understood from the fact, that the strain fields associated with a mechanical mode alter the temperature of the lattice via the coefficient of thermal expansion (which is a consequence of non-linear terms in the lattice potential). Delayed heat flow between regions of different strain (and thus temperature) thereby cause damping of the mechanical mode. This thermodynamic source of dissipation (requiring a phonon mean-free path that is smaller than the dimensions of the oscillator) has first been described already in the 1930s by Zener [203, 204]. For a vibrating beam, the mechanical damping associated with this phenomenon can be written as [203]

$$Q_{\text{ted}}^{-1} = \Delta_E \frac{\Omega \tau_w}{1 + \Omega^2 \tau_w^2}. \quad (3.7)$$

The time scale τ_w is defined by the thermal diffusivity and the width of the beam in the direction of oscillation w , $\tau_w = w^2/(\pi^2 D)$ [203, 205]. The prefactor Δ_E is given by

$$\Delta_E = \frac{Y \alpha^2 T}{\rho C_p}, \quad (3.8)$$

where α denotes the linear coefficient of thermal expansion, C_p is the heat capacity per unit mass for constant pressure and Y is the Young's modulus. Thus, for oscillation periods both much larger and smaller compared to the time scale τ_w , thermoelastic damping tends to negligible values. Its maximum of $Q_{\text{ted}}^{-1} = \Delta_E/2$ is found at $\Omega = 1/\tau_w$. Besides its frequency dependence, thermoelastic damping should also show both a direct temperature dependence $\propto T$ and an indirect dependence via the material parameters Y , α and C_p . This source of dissipation has been shown to be the dominant loss mechanism in a range of materials [190, 206, 207] resulting in Q factors between 10^4 and 10^7 , depending on material, geometry and frequency. It can be mitigated by interrupting the heat-flow within the mechanical oscillator via voids [208] or resorting to low temperatures where it is expected to vanish. Using the material parameters of silica ($Y = 73$ GPa, $\alpha = 5 \cdot 10^{-7}$ K $^{-1}$, $\rho = 2200$ kg/m 3 , $C_p = 730$ J/(kg · K)), expression (3.7) yields a lower limit for the attainable quality factor of $Q_{\text{ted}} \geq 2/\Delta_E \approx 5 \cdot 10^5$ at room temperature.

3.3.5 Phonon-phonon interaction

Dissipation of mechanical modes can also be caused by interaction of individual phonon modes with each other, i.e. phonon-phonon scattering. In crystals, this damping mechanism is known as Akhiezer effect as first studied by Akhiezer in 1938 [209]. The interaction can be viewed as an effective anharmonicity of the local phonon potential. A modulation of the lattice constant caused by the excitation of phonons modulates the frequencies of the individual phonon modes and thus their effective temperatures. As the phonon modes relax to the equilibrium temperature on a certain time scale this gives rise to damping [210]. Although this process has been originally studied for crystals, it has also been shown to be of relevance in amorphous materials where propagating phonon modes can interact with localized phonon modes [211].

The dependence of the mechanical Q factor caused by Akhiezer damping is phenomenologically given by

$$Q_{\text{akh}}^{-1} = \gamma_{\text{G}}^2 \frac{C_p T v}{2 v_{\text{D}}^3} \frac{\Omega \tau_{\text{anh}}}{1 + \Omega^2 \tau_{\text{anh}}^2}, \quad (3.9)$$

where γ_{G} is the Grüneisen parameter characterizing the mean anharmonicity, C_v is the volumetric specific heat, v is the speed of sound, v_{D} is the Debye velocity. The anharmonic relaxation time τ_{anh} is a material specific function of temperature.

For crystals this effect has often been found to be limiting the measured mechanical quality (see e.g. Ref. [212] and references therein). For amorphous materials, however, Akhiezer damping is typically smaller than the damping caused by two-level fluctuators (cf. section 3.3.3). For silica, in particular, the parameter $\gamma_{\text{G}}^2 = 3.6$ (assuming $v_{\text{D}}^3 = 0.322v^3$) has been found [202, 211] and the temperature dependence of τ_{anh} has been measured in Ref. [211].

3.4 Clamping losses in toroid microresonators

In this section, the relevant dissipation mechanisms limiting the mechanical Q of the RBM (cf. section 3.2) in toroid microresonators will be discussed. All experiments are performed in a vacuum chamber with a pressure below 0.1 mbar (unless otherwise specified) such that gas damping is negligible [6]. Clamping losses are experimentally found and theoretically confirmed as the dominant sources of damping at room temperature.

In an ideal radial breathing mode, such as the case e.g. in a freely suspended ring, only in-plane motion is present. The asymmetric clamping conditions of a microtoroid—the torus is clamped with an offset to the silica disk [213] which in turn is rigidly attached to the silicon pillar at its bottom but free on its top face—lead to an out-of-plane oscillation component which is always admixed to the radial breathing mode. It is precisely this out-of-plane motional component that is found to strongly influence the clamping losses. The coupling between radial and out-of-plane flexural modes thereby strongly depends on the toroid geometry. Fig. 3.4a, shows the Q factors and frequencies of radial breathing and adjacent third order cantilever modes of a microtoroid for varying relative undercut u (defined as the length of the free-standing part of the cavity divided by its radius, cf. Fig. 3.4b, inset). The breathing mode's frequency only slightly changes with varying relative undercut whereas the cantilever mode is more strongly affected (in fact, its frequency approximately scales as $\propto u^{-2}$, as shown in section 3.2). As the toroid's undercut is gradually increased, the frequencies of both modes therefore approach each other. They do not, however, cross but rather show an avoided crossing. This behaviour can accurately be described by a coupled harmonic oscillator model:

$$\ddot{x}_{r/f} + \Gamma_{r/f}\dot{x}_{r/f} + \Omega_{r/f}^2 x_{r/f} + \varsigma^2 x_{f/r} = 0, \quad (3.10)$$

where $x_{r/f}$, $\Omega_{r/f}$, $\Gamma_{r/f}$ denote the amplitude, bare frequency and damping rate of the radial and flexural modes which are coupled by ς . The complex eigenvalues of the coupled system can then be calculated to satisfy

$$\lambda_{\pm} = \frac{\Omega_r + \Omega_f}{2} + i\frac{\Gamma_r + \Gamma_f}{4} \pm \sqrt{\left(\frac{\Omega_r - \Omega_f}{2} + i\frac{\Gamma_r - \Gamma_f}{4}\right)^2 + \frac{\varsigma^4}{4\Omega_r\Omega_f}}, \quad (3.11)$$

with eigenfrequencies $\Omega_{\pm} = \text{Re}(\lambda_{\pm})$ and quality factors $Q_{\pm} = \text{Re}(\lambda_{\pm}) / (2\text{Im}(\lambda_{\pm}))$. First, the bare frequencies and Q factors are approximated as linear functions of the relative undercut and fitted to the measured data, as shown in Fig. 3.4a. Then, the coupled oscillator model according to Eq. (3.11) is fitted to the measured coupled frequencies and quality factors, where the coupling rate ς serves as fit parameter. Good agreement between model and data is found, as shown in Fig. 3.4, and a relatively large coupling rate of $\varsigma/2\pi = 14$ MHz is extracted ($\varsigma \gg \Gamma_{r/f}$). It leads not only to an avoided crossing of the coupled frequencies but also to a mixing of the mechanical quality factors Q_{\pm} . The originally higher quality mode described by λ_+ turns into a low Q mode after the avoided crossing (and vice versa). In the avoided crossing region, the quality factor of both modes is low. This leads to a strong modulation of the radial breathing mode's Q factor

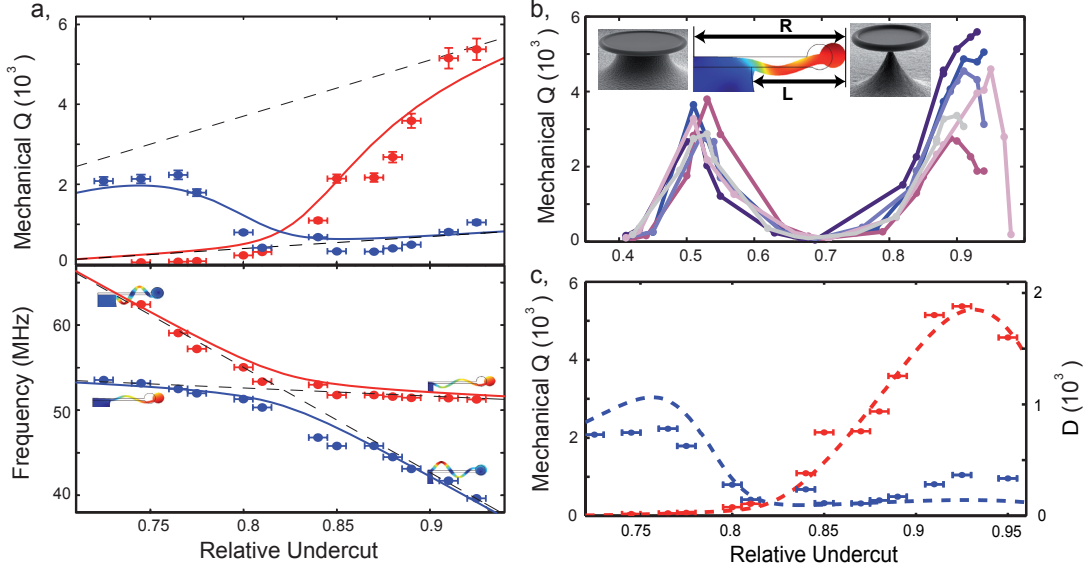


Figure 3.4: Geometry dependence of mechanical Q. a, Mechanical Q and frequencies of RBM and third order flexural mode ($R = 28 \mu\text{m}$, oxide thickness: $t = 1 \mu\text{m}$) for varying relative undercut $u = L/R$ (cf. inset of b). Mutual coupling of both modes leads to an avoided crossing. The coupled oscillator model (full lines) yields good agreement with the data, assuming a linear dependence of the bare frequencies and Q on undercut (dashed lines). b, The normal mode coupling leads to a strong dependence of the RBM's mechanical Q on the relative undercut ($R \approx 28 \mu\text{m}$, $t = 2 \mu\text{m}$). Data in b, is recorded at atmospheric pressure. Inset: Definition of undercut $u = L/R$ and scanning electron micrographs of toroids with small (left) and large (right) u . c, The measured mechanical Q factors accurately follow the model D up to a constant scaling factor ~ 3 . Fig. adapted from Ref. [6].

as the undercut is varied. Fig. 3.4b shows the measured Q factors of the RBM for six different samples of similar geometry over a wide range of undercut. Three dips can be distinguished. These, can all be attributed to normal mode coupling to the three lowest order flexural modes and the concomitant avoided crossing as their frequency approaches the RBM frequency. The mechanical quality might thus be optimized by choosing undercut regions where the coupling between radial and flexural modes and hence the out-of-plane motional component of the RBM is minimized, e.g. $u \sim 0.9$ in Fig. 3.4b.

With the insight that the out-of-plane motion (induced by coupling to flexural modes) predominantly influences the mechanical quality, the phenomenological parameter

$$D = \left(\frac{v\rho}{E_{\text{mech}}} \Omega_{\text{m}} \int_{A_{\text{p}}} |\Delta z(r)|^2 dA \right)^{-1}, \quad (3.12)$$

is devised, describing the emission of sound waves from the silica disk into the silicon pillar

(ρ , v : density and speed of sound in silica; E_{mech} : total energy stored in the mechanical oscillation). The out-of plane oscillation amplitude Δz of the silica disk, integrated across the clamping region A_p , as described by D indeed follows the measured quality factors for both radial and flexural mode remarkably well, as shown in Fig. 3.4c. A relation of $Q \approx 3 \cdot D$ is found, clearly confirming that the mechanical quality factor of the RBM is dominated by the geometry-dependent clamping losses modelled by D . The clamping losses can thus be conveniently *calculated* using FEM simulations. This provides a useful tool for an overall optimization of the toroid design, as described in the next section.

3.5 Design of ultra-low dissipation spoke-supported resonators

Having shown that the clamping losses within toroid microresonators can be a-priori *calculated* with the model described in the previous section, we can now use it as a tool to devise optimized geometries mitigating clamping losses. One such geometry will be described in this section: spoke-supported microtoroids. The basic idea is to replace the silica disk, which usually connects the torus to the silicon pillar and mediates clamping losses, by a few thin silica bridges. The length of these bridges can then precisely be chosen such that they do not support modes at the radial breathing mode's resonance frequency. Thus, the radial breathing mode is decoupled from the supporting silicon pillar and clamping losses can be strongly suppressed. Following a procedure shown in detail in appendix C, such toroids can in fact be fabricated using a combination of standard wet- and dry-etching techniques. Fig. 3.5 shows a corresponding electron micrograph of a spoke-supported toroid.

3.5.1 Room-temperature quality factors

Finite element simulations predict that the clamping losses as described by Eq. (3.12) may be reduced by several orders of magnitude by integrating a spoke-support into the silica disk and choosing appropriate geometries. The measurements confirm this expectation. Fig. 3.6 shows the actually measured mechanical quality factors of spoke-supported toroids (and also regular toroids) as a function of the corresponding simulated value D . The fabricated samples exhibit values of D that are increased by more than three orders of magnitude

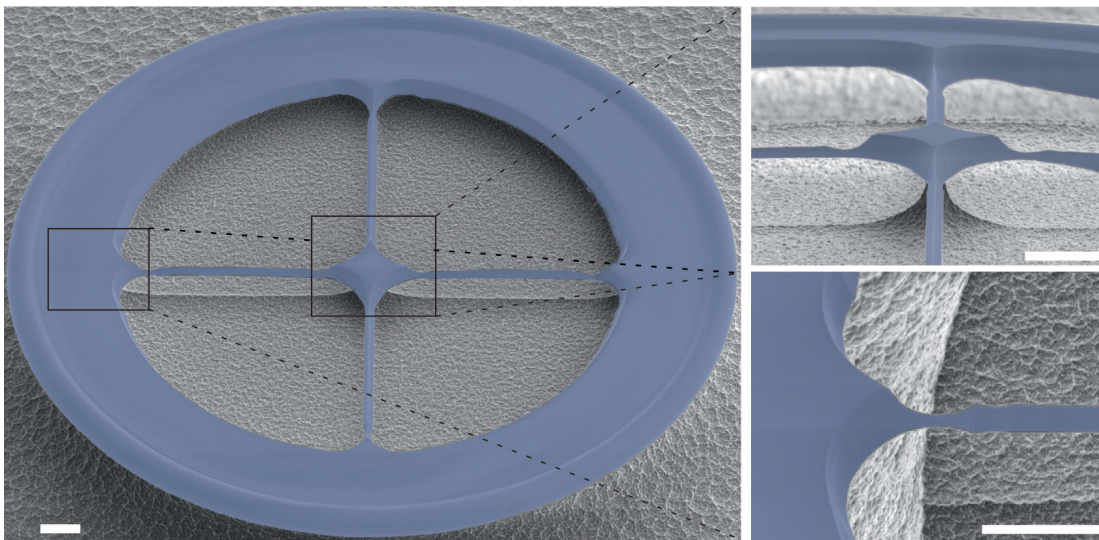


Figure 3.5: Scanning electron micrographs of spoke-supported microresonators (scale bar: $5\ \mu\text{m}$). Fig. adapted from Ref. [6].

compared to regular toroids. Correspondingly, larger mechanical Q factors are obtained, as shown in Fig. 3.6a. However, Fig. 3.6a also clearly indicates a saturation of the Q factors for large D . Nevertheless Q factors up to 50'000 are achieved (corresponding to approximately one order of magnitude increase in Q compared to the values at the initial stage of the study [34]). As will be shown in the next section, the saturation of the Q factors is due to intrinsic losses caused by TLS present in amorphous silica. Thus, using a spoke-support that minimizes the clamping losses D^{-1} , in fact material loss limited Q factors are achieved.

It is emphasized that the optical properties of the optomechanical resonator are not affected by using the spokes design, since the laser reflow process enabling ultra-high optical Q can still be applied, as shown in appendix C. This is exemplified by Fig. 3.6c, where the transmission of a spoke-supported microtoroid is shown, indicating a cavity finesse of $\mathcal{F} = 230'000$. The mechanical degrees of freedom within microtoroids can thus be optimized individually via the spokes length, width and position without compromising the exceptional optical properties. Meanwhile, similar spoke geometries in connection with double-disk structures have been used for static and dynamic tuning of the device geometry via optical forces [214, 215].

3.5.2 Temperature dependence of mechanical Q

In the previous chapter, the clamping losses in toroid microresonators were successfully understood and modelled. Consequently, these could be considerably reduced by an optimized geometric design. As shown in Fig. 3.6, however, the measured mechanical quality factors saturate at values of approximately 50'000 despite a much stronger reduction of clamping losses. In order to elucidate this saturation the temperature dependence of the mechanical quality factors is studied across a wide range of temperatures, both above and below room temperature. Fig. 3.7 shows the inverse quality factor of the RBM at 38 MHz as a function of temperature. The damping of $Q_m^{-1} = 1/32'000$ measured for this sample at room temperature continuously decreases when the temperature is increased. In particular, at 410 K a highest value of $Q_m = 80'000$ is attained. The corresponding frequency-Q product $Q_m \cdot \Omega_m/2\pi = 3 \cdot 10^{12}$ Hz is amongst the best values for micromechanical oscillators achieved to date [216]. Besides demonstrating a further reduction of dissipation, the observed temperature dependence allows a detailed understanding of the limitations to the mechanical quality. The inset in Fig. 3.7 shows the damping $Q_m^{-1}(T)$ obtained with a 34 MHz sample measured from 10 K to 300 K. A strong temperature dependence becomes evident. In order to fit the measured data, the relevant losses caused by TLS (cf. section 3.3.3), the Akhiezer contribution (cf. section 3.3.5) and a constant background attributed to clamping losses are included. The constant background and the variables τ_0 and \mathcal{C} in the TLS term (Eq. 3.6) are used as fit parameters, keeping all other variables both within the TLS and the Akhiezer term (Eq. 3.9) fixed (but taking the measured temperature dependence of the material parameters [153, 211] into account). Excellent agreement with the data over the full temperature range is found. The fit parameters $\tau_0 = 10^{-12.1}$ s and $\mathcal{C} = 1.8 \cdot 10^{-3}$ fall within the range reported in Ref. [202] (see section 3.3.3). Using the

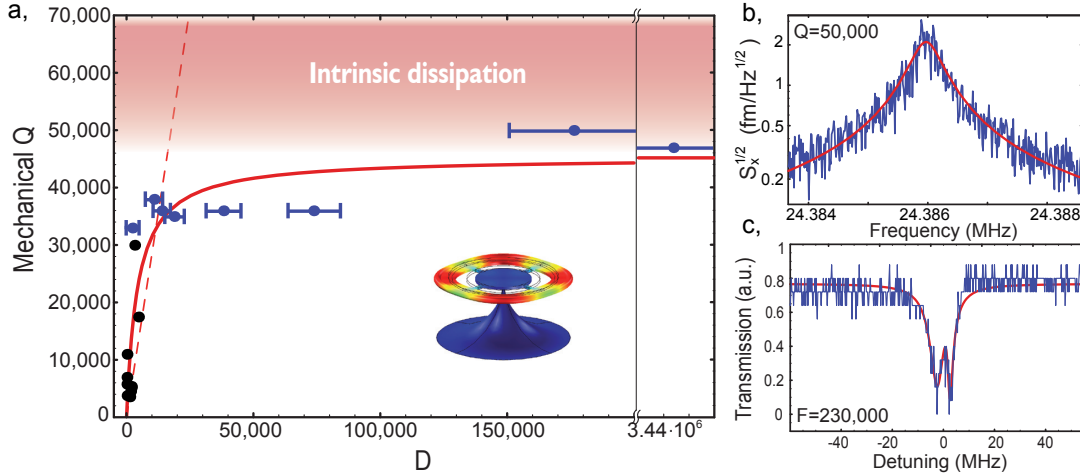


Figure 3.6: Material loss-limited optomechanical microresonators. a, The measured mechanical Q factor (blue: RBM of spoke-supported resonators, black: radially symmetric modes of optimized regular toroids) is shown for the corresponding simulated values of D . For small D the linear relation between D and Q is confirmed (the dashed line corresponds to the fit shown in Fig. 3.4c). For large D , a saturation towards the material loss limit is found (cf. section 3.5.2). The red line denotes a fit according to $Q_m^{-1} = a/D + b$, where a and b are used as fit parameters. Inset: FEM simulation of the RBM of a spoke-supported toroid. b, Single-sided displacement spectrum of the RBM, showing a Q of 50'000 at 24 MHz. c, Optical transmission spectrum of a spoke-supported microtoroid exhibiting mode splitting (cf. section 2.6.1) and an intrinsic finesse of 230'000. Fig. adapted from Ref. [6].

same fit for the high-temperature data (295 K to 410 K) also yields excellent agreement ($\tau_0 = 10^{-12.05}$ s and $\mathcal{C} = 1.8 \cdot 10^{-3}$). Moreover, the extracted temperature-independent background sets an upper bound for the remaining clamping losses of $Q_{cl}^{-1} = 1/140'000$, experimentally confirming that indeed a strong reduction of clamping losses is achieved. For this specific sample the D model, however, predicts even six times lower clamping losses. Thus, it is likely that slight asymmetries in the structure cause additional clamping losses not taken into account in the above FEM model and lead to the observed background of $Q_{cl}^{-1} = 1/140'000$. The intrinsic losses of silica (that is, those caused by TLS and Akhiezer damping) are known to exhibit a local minimum at a temperature of around 500 K [195] and thus a further increase in temperature would likely yield even higher Q factors than those achieved at 410 K. It is noted that thermoelastic damping, for which an upper bound of $Q_{ted}^{-1} = \Delta_E/2 = 2 \times 10^{-6}$ is found at room temperature (cf. section 3.3.4), can safely be neglected in this analysis.

For operation at cryogenic temperatures, which is required for experiments pursuing ground-state cooling of the RBM [8], the presence of TLS leads to a strong degradation of the mechanical quality factors compared to the room temperature values. Particularly in the frequency range of interest here (10-100 MHz), the Q factors exhibit a minimum of

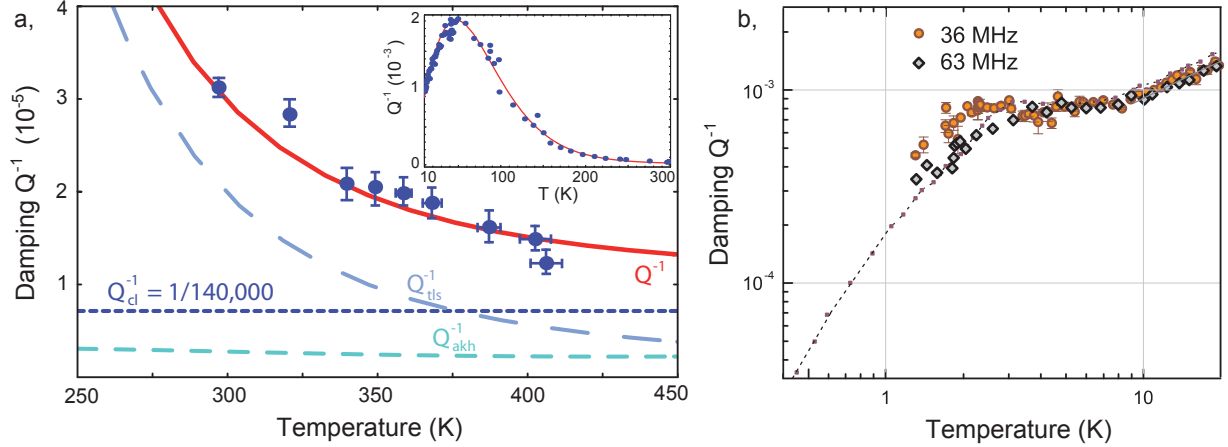


Figure 3.7: Temperature dependent mechanical Q factors. a, The mechanical damping (for a RBM at 38 MHz) reduces down to a value of $1/80'000$ at 410 K, as the temperature is increased. The data are fitted using a constant clamping loss background Q_{cl}^{-1} , the contributions of Akhiezer damping Q_{akh}^{-1} and TLS losses Q_{tls}^{-1} . The fit yields good agreement with the data and a clamping loss limit of $Q_{cl} = 1/140'000$ can be extracted. Inset: The dependence of the low-temperature (from 300 K to 10 K) damping is dominated by TLS losses. The fit as explained in the text yields excellent agreement with the data. b, Q factors at low temperatures. Below $T = 10$ K, the Q factors of two different samples (dots and diamonds) first show a plateau, before increasing $\propto T^3$ below a frequency dependent threshold. The dotted line denotes a measurement from Ref. [195] at 43 MHz. Fig. adapted from Refs. [6] and [9].

$Q_{tls} \sim 600$ at $T \sim 50$ K (cf. Fig. 3.7a, inset). For even lower temperatures, the mechanical quality factors recover slightly and a temperature independent plateau of $Q_{tls} \sim 1'000$ is measured for $T < 10$ K [9], which is in agreement with previous measurements [195]. Note that in this temperature regime Q_{tls}^{-1} is no longer accurately described by Eq. (3.6) since the tunneling term which dominates at low temperatures is neglected, there. Below a frequency dependent cut-off temperature, the Q factors increase again according to $Q_{tls} \propto \Omega_m/T^3$ [217], as can be seen in Fig. 3.7b, for two measurements at different RBM frequencies. The threshold for this increase approximately lies at $T \sim 2$ K for frequencies $\Omega_m/2\pi \sim 50$ MHz and is moved to higher temperatures for higher oscillation frequencies. For a frequency of 43 MHz, a Q of $50'000$ has been recovered at $T \sim 450$ mK [195]. Measurements in a He-3 cryostat show that indeed Q factors well above 10^4 are accessible within microtoroids at temperatures of $T \sim 500$ mK and the clamping loss limit of regular toroid microresonators is reached again at these low temperatures [147]. Spoke-supported microresonators with low clamping losses may in this regime enable sufficiently high mechanical Q to achieve ground-state cooling.

Chapter 4

Summary

In this thesis, two conceptionally entirely different approaches to cavity optomechanics have been reported. Both are, however, based on the exceptional optical properties of toroid microresonators whose whispering gallery modes exhibit a combination of ultra-high optical quality factors and small mode volume.

First, nanomechanical oscillators were dispersively coupled to the optical modes of toroid microresonator using their evanescent near-field. The resulting hybrid system allowed the extension of dispersive cavity optomechanics to the realm of *nanomechanical* oscillators. In particular, radiation pressure actuation and cooling of nanomechanical oscillators were achieved. Moreover, for the first time nanomechanical motion was measured with an imprecision lower than the standard quantum limit using this system. It is shown that the versatility of the developed platform also offers the capability of coupling mechanical motion resonantly or quadratically to an optical mode doublet. In currently ongoing experiments, the developed system may enable the demonstration of radiation pressure quantum backaction on a solid-state mechanical oscillator which has remained an elusive goal so far. Moreover, the near-field approach has the flexibility to be combined with almost arbitrary mechanical oscillator geometries and materials and thus offers wide applicability. For example graphene oscillators may be studied and, combined with low frequency oscillators, the application as a sensitive probe for small forces can be envisioned.

Second, the properties of the intrinsic mechanical modes of toroid microresonators were elucidated in detail. Both the spectrum and the origin of the mechanical quality factors of the mechanical modes were analyzed experimentally as well as using finite element simulation. A thorough understanding of the mechanical quality factors allowed their subsequent optimization which resulted in the development of spoke-supported microresonators. These combine both ultra-low optical and state-of-the-art mechanical dissipation in a single monolithic device. Their properties might, in a next generation of experiments, enable the first observation of a solid-state mechanical oscillator which is cooled to its quantum ground-state using radiation pressure.

Appendix A

Solution of the linearized quantum Langevin equations

In this appendix the solutions of the linearized quantum Langevin equation (1.11) and (1.13) will be given and general expressions for the intracavity field as well as the output field fluctuations will be derived.

A.1 Equations for the field quadratures

First, taking the Fourier transform of the quantum Langevin equation (1.11) and its hermitian conjugate one obtains:

$$-i\Omega a[\Omega] = \left(i\Delta - \frac{\kappa}{2}\right) a[\Omega] - i\bar{a}g x[\Omega] + \sqrt{\kappa_{\text{ex}}} s[\Omega] + \sqrt{\kappa_0} s_{\text{vac}}[\Omega] \quad (\text{A.1a})$$

$$-i\Omega a^\dagger[\Omega] = \left(-i\Delta - \frac{\kappa}{2}\right) a^\dagger[\Omega] + i\bar{a}g x[\Omega] + \sqrt{\kappa_{\text{ex}}} s^\dagger[\Omega] + \sqrt{\kappa_0} s_{\text{vac}}^\dagger[\Omega]. \quad (\text{A.1b})$$

These expressions may be written in matrix form as follows:

$$M \begin{pmatrix} a \\ a^\dagger \end{pmatrix} + \begin{pmatrix} i \\ -i \end{pmatrix} \bar{a}g x - \sqrt{\kappa_{\text{ex}}} \begin{pmatrix} s \\ s^\dagger \end{pmatrix} - \sqrt{\kappa_0} \begin{pmatrix} s_{\text{vac}} \\ s_{\text{vac}}^\dagger \end{pmatrix} = 0, \quad (\text{A.2})$$

where

$$M = \begin{pmatrix} \frac{\kappa}{2} - i(\Delta + \Omega) & 0 \\ 0 & \frac{\kappa}{2} + i(\Delta - \Omega) \end{pmatrix} \quad (\text{A.3})$$

and, for simplicity, the argument of the fields Ω is omitted. Now, the optical field operators are replaced by the corresponding amplitude and phase quadratures p and q , respectively. To this end, one has to consider that for a mean field \bar{c} with phase φ , these can be written in terms of the field fluctuations c and c^\dagger via the rotation matrix R as described in Eq. (1.32) and (1.33). The intracavity mean-field \bar{a} was assumed to be real in section (1.1.2) and thus has a vanishing phase. The corresponding phases of \bar{s} and \bar{s}_{out} , φ_s and $\varphi_{s_{\text{out}}}$ (with respect to \bar{a}) can be obtained from Eqs. (1.8) and (1.10), respectively.

Thus re-writing Eq. (A.2), the amplitude and phase quadratures of the intracavity field fluctuations may be written as

$$\begin{pmatrix} p_a \\ q_a \end{pmatrix} = R(0)M^{-1} \left[\begin{pmatrix} -i \\ i \end{pmatrix} \bar{a}gx + \sqrt{\kappa_{\text{ex}}}R(\varphi_s)^{-1} \begin{pmatrix} p_s \\ q_s \end{pmatrix} + \sqrt{\kappa_0}R(0)^{-1} \begin{pmatrix} p_{\text{vac}} \\ q_{\text{vac}} \end{pmatrix} \right]. \quad (\text{A.4})$$

A.2 Solutions for the intracavity field quadratures

Solving the system (A.4) for p_a and q_a and assuming that all quadratures are uncorrelated with each other one obtains the following solutions for the symmetrized spectral densities of the intra-cavity amplitude and phase quadratures S_{p_a} and S_{q_a} :

$$S_{p_a} = \frac{4/\kappa}{(1 + \bar{\Delta}^2)^2 + 2(1 - \bar{\Delta}^2)\bar{\Omega}^2 + \bar{\Omega}^4} \left[\frac{\kappa_{\text{ex}}}{\kappa} \left((1 + \bar{\Delta}^2 + \frac{\bar{\Omega}^2}{1 + \bar{\Delta}^2})S_{p_s} + \frac{\bar{\Delta}^2\bar{\Omega}^2}{1 + \bar{\Delta}^2} S_{q_s} \right) + \frac{\kappa_0}{\kappa} ((1 + \bar{\Omega}^2) S_{p_{\text{vac}}} + \bar{\Delta}^2 S_{q_{\text{vac}}}) + 4\frac{\bar{a}^2}{\kappa} \bar{\Delta}^2 g^2 S_x \right], \quad (\text{A.5})$$

$$S_{q_a} = \frac{4/\kappa}{(1 + \bar{\Delta}^2)(\bar{\Delta}^4 + 2\bar{\Delta}^2(1 - \bar{\Omega}^2) + (1 + \bar{\Omega}^2)^2)} \left[\frac{\kappa_{\text{ex}}}{\kappa} (\bar{\Delta}^2\bar{\Omega}^2 S_{p_s} + (1 + \bar{\Omega}^2 + 2\bar{\Delta}^2 + \bar{\Delta}^4) S_{q_s}) + \frac{\kappa_0}{\kappa} (\bar{\Delta}^2(1 + \bar{\Delta}^2) S_{p_{\text{vac}}} + (1 + \bar{\Omega}^2)(1 + \bar{\Delta}^2) S_{q_{\text{vac}}}) + 4\frac{\bar{a}^2}{\kappa} (1 + \bar{\Omega}^2)(1 + \bar{\Delta}^2)g^2 S_x \right]. \quad (\text{A.6})$$

For better readability, the reduced Fourier frequency $\bar{\Omega} = 2\Omega/\kappa$ and detuning $\bar{\Delta} = 2\Delta/\kappa$, normalized by the cavity field decay rate $\kappa/2$ were introduced.

Using the above expression, the spectral density of the intracavity photon number fluctuations S_N as well as the phase fluctuations of the intracavity field S_φ can then be calculated:

$$S_N = \bar{a}^2 \cdot S_{p_a}, \quad (\text{A.7})$$

$$S_\varphi = \frac{1}{4\bar{a}^2} \cdot S_{q_a}. \quad (\text{A.8})$$

A.3 Solution for the output field quadratures

Inserting the quadrature components according to expression (1.32) into Eq. (1.13) and including its hermitian conjugate one obtains the following system of equations which describes the quadrature fluctuations p_{out} and q_{out} of the output field s_{out} :

$$\begin{pmatrix} p_{\text{out}} \\ q_{\text{out}} \end{pmatrix} = R(\varphi_{s_{\text{out}}}) \left[R(\varphi_s)^{-1} \begin{pmatrix} p_s \\ q_s \end{pmatrix} - \sqrt{\kappa_{\text{ex}}}R(0)^{-1} \begin{pmatrix} p_a \\ q_a \end{pmatrix} \right]. \quad (\text{A.9})$$

Substituting p_a and q_a with the solutions of (A.4) yields:

$$\begin{pmatrix} S_{p_{\text{out}}} \\ S_{q_{\text{out}}} \end{pmatrix} = C \begin{pmatrix} A_1 & B_1 & B_2 & B_3 & B_4 \\ A_2 & B_2 & B_1 & B_4 & B_3 \end{pmatrix} \begin{pmatrix} S_x \\ S_{p_{\text{in}}} \\ S_{q_{\text{in}}} \\ S_{p_{\text{vac}}} \\ S_{q_{\text{vac}}} \end{pmatrix}, \quad (\text{A.10})$$

where

$$C = [(1 + \bar{\Delta}^2) ((1 - 2\eta_c)^2 + \bar{\Delta}^2) (1 + (\bar{\Delta} - \bar{\Omega})^2) (1 + (\bar{\Delta} + \bar{\Omega})^2)]^{-1} \quad (\text{A.11})$$

$$A_1 = 64 \left(\frac{g}{\kappa}\right)^2 \eta_c^2 \bar{\Delta}^2 (4(1 - \eta_c)^2 + \bar{\Omega}^2) \frac{P}{\hbar\omega} \quad (\text{A.12})$$

$$A_2 = 64 \left(\frac{g}{\kappa}\right)^2 \eta_c^2 \left(((1 - 2\eta_c) - \bar{\Delta}^2)^2 + (1 - 2\eta_c)^2 \bar{\Omega}^2 \right) \frac{P}{\hbar\omega} \quad (\text{A.13})$$

$$B_1 = \bar{\Omega}^2 \left[((1 - 2\eta_c) + \bar{\Delta}^2)^2 \bar{\Omega}^2 + 2((1 - 2\eta_c)^2 - \bar{\Delta}^4) (\eta_c^2 + (1 - \eta_c)^2 + \bar{\Delta}^2) \right] \\ + (1 + \bar{\Delta}^2)^2 ((1 - 2\eta_c)^2 + \bar{\Delta}^2)^2 \quad (\text{A.14})$$

$$B_2 = 4\bar{\Delta}^2 \eta_c^2 \bar{\Omega}^2 (4(1 - \eta_c)^2 + \bar{\Omega}^2) \quad (\text{A.15})$$

$$B_3 = 4\eta_c (1 - \eta_c) \left(((1 - 2\eta_c) - \bar{\Delta}^2)^2 + (1 - 2\eta_c)^2 \bar{\Omega}^2 \right) (1 + \bar{\Delta}^2) \quad (\text{A.16})$$

$$B_4 = 4\bar{\Delta}^2 \eta_c (1 - \eta_c) (4(1 - \eta_c)^2 + \bar{\Omega}^2) (1 + \bar{\Delta}^2) . \quad (\text{A.17})$$

Here, P , as in the main part of this thesis, is defined as the optical input power.

Appendix B

Experimental techniques for near-field cavity optomechanics

In this appendix several important experimental techniques used in chapter 2 will be described. Besides the microfabrication techniques also the experimental setup for coupling tapered optical fibre, toroid microresonator and nanomechanical oscillator will be discussed. Moreover, the optical homodyne detection scheme and the calibration of the corresponding acquired frequency noise spectra is shown in more detail.

B.1 Microfabrication techniques

In this section, the fabrication of toroid near-field sensors and strained silicon nitride nanostrings will be discussed.

B.1.1 Fabrication of toroid near-field sensors

In order to get physical access to the evanescent near-field of toroid microresonators these have to be fabricated at the edge of their silicon chip support. To this end, a few special steps have to be added to the fabrication of regular toroid microresonators [88].

Starting point are undoped 3'' silicon wafers with a $1\ \mu\text{m}$ film of thermally grown wet oxide (commercially obtained from Virginia Semiconductor). First, circular silica pads are created by UV lithography and subsequent wet-etching in buffered hydrofluoric acid (HF). At the beginning of this thesis, these standard steps which do not differ from the general recipe for fabricating toroid microresonators were carried out in the cleanroom facilities of the chair of solid state physics (Prof. Kotthaus) at LMU Munich. The following parameters were used:

- Spin-coating of adhesion promoter hexamethyldisilazane (HDMS) on the wafer at 3000 rpm for 20s
- Baking at $110\ ^\circ\text{C}$ for 60s

- Spin-coating of photoresist S-1813 on the wafer at 4000 rpm for 60 s
- Baking for 70 s at 110 °C
- Illuminating the wafer for 40 s using a MJB 3 mask aligner (Süss Microtech).
- Developing for 40 – 60 s using MF-319 developer
- Baking for 10 min at 110 °C
- Etching for 9 – 11 min using 5% buffered HF solution
- Cleaning with acetone and isopropanol

Later on, also samples fabricated in a similar manner on 4" wafers in the CMI cleanroom at the EPF Lausanne were used. The final fabrication of all samples, however, was performed in the cleanroom of MPQ:

First, the wafers are cleaved into $5 \times 15 \text{ mm}^2$ chips each containing a row of 35 silica pads. The subsequent fabrication steps are summarized in Fig. B.1. A layer of photoresist (S-1813) is spin-coated on these chips individually with the same parameters as mentioned above. After hardbaking for 10 min at 110 °C, the chips are cleaved again perpendicular to the row of silica pads in order to break the chip close to a silica pad. Typically, the distance of the outmost silica pad to the rim of the chip is on the order of 100 μm . It is critical that the cleave in this step is straight both along the cleave axis and perpendicular to the cleave axis.

In the next step, a pulsed flow of XeF_2 gas is used to etch the whole chip from the side, the photoresist serving as an etch mask. Silicon is thereby etched by XeF_2 according to the following reaction:



At the same time the chip is monitored from the top using a microscope such that the etching depth can be controlled to a precision of $\sim 1 \mu\text{m}$. The chip is etched continuously until the distance of the silica pad to the rim of the chip is approximately 5 μm . The previous hardbaking of the chip turns out to be critical for this etch, as without it the photoresist is very often penetrated by XeF_2 . Subsequently, the photoresist is removed using hot acetone and isopropanol. The result of this etching and cleaning step is depicted in Fig. B.1 (3). The best optical quality is obtained when the chip is additionally cleaned with oxygen plasma (typically 5 min at 250 W).

Now, the silica pad, located at the edge of the silicon chip is subjected to a second XeF_2 etch. The etching speed of silicon bound in silica is reduced by a factor of ~ 1000 and thus the silica pad is underetched isotropically. Two subtleties have, however, to be considered in order to obtain an isotropic underetch. First, in the used system the XeF_2 gas enters the circular etching chamber evenly from all sides. Due to saturation effects, thus the lateral faces of the chip will be etched more strongly. In order to compensate for

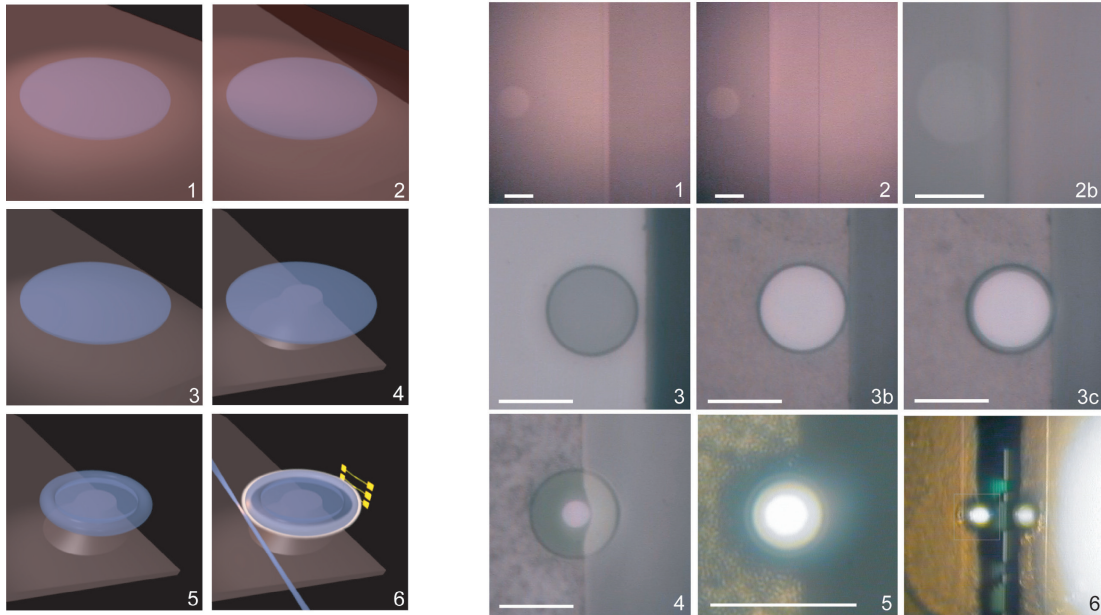


Figure B.1: Fabrication of microcavity near-field sensors. The left panel shows a rendering of the fabrication process. The right panel shows microscope images taken during the experimental fabrication process in the XeF_2 etching chamber (1-4) and the experimental vacuum chamber (5-6) (scale bars mark $50\ \mu\text{m}$ in (1)-(5); in (6) the contour of (5) is indicated). (1)-(2) show how the silicon chip (protected by photoresist) is etched from the side until the silica pad sits $\sim 5\ \mu\text{m}$ away from the edge of the chip. (3) shows the chip after removing the photoresist and in (3b-c) it is isotropically underetched. The etching at the initial stage (3b) progresses faster at the lateral face (as explained in the text) such that the $\sim 5\ \mu\text{m}$ gap is etched away before the silica pad is significantly underetched. In (4) the underetch is completed and the microtoroid created by laser-induced reflow is shown in (5). (6) shows the toroid in the experimental setup, together with a tapered optical fibre and an array of nanomechanical strings (right: a mirror image is reflected by the smooth silicon surface of the chip hosting the nanomechanical oscillators).

this and still obtain an isotropic underetch of the silica pad despite its location at the edge of the chip, it is advantageous to place an additional silicon chip next to the free side of the silica pad. Thus, a similar concentration of XeF_2 reaches the silica pad from all sides leading to an isotropic underetch. Second, during the first few etching pulses, the lateral faces of the chip are more strongly etched than the top faces which is attributed to a layer of oxide typically formed on the top face due to exposure to air. Thus, best results are obtained when the silica pads do not exactly sit at the edge of the silicon chip support but rather at a distance of approximately $5\ \mu\text{m}$. Then, the thin oxide layer on the top face is typically etched away exactly as the lateral face of the chip reaches the edge of the silica pad.

Finally, the underetched silica pad is illuminated with a 30 W CO_2 laser (Synrad) emitting at a wavelength of $10.6\ \mu\text{m}$. As at this wavelength silica strongly absorbs whereas the silicon substrate essentially acts as a mirror the silica pad heats up with the silicon chip serving as a heat sink. For sufficiently large laser power the silica melts at its periphery and due to surface tension an ultra-smooth toroid is formed. Typically less than 3 W of optical power are sufficient to induce this melting process. In order to obtain a highly symmetric toroid which supports whispering gallery modes with ultra-high optical Q a symmetric undercut of the silica pads is crucial. Moreover, a symmetric support also allows accessing sufficiently high mechanical quality such that the mechanical background noise floor caused by intrinsic mechanical toroid modes is suppressed (cf. section 2.5.2.2).

B.1.2 Fabrication of nanomechanical oscillators

The nanomechanical oscillators used in this thesis were initially fabricated at LMU Munich in the cleanroom facilities of the chair of solid state physics (Prof. Kotthaus). In the later phase also oscillators fabricated at EPF Lausanne were employed. Here, a brief overview of the fabrication of these nanomechanical strings will be given. The fabrication is shown in Fig. B.2. Starting point is a 4'' undoped silicon wafer with a $2\ \mu\text{m}$ layer of SiO_2 (e.g. from Virginia Semiconductor). After chemical cleaning, a 100 nm device layer of high stress silicon nitride is deposited on the oxide via low pressure chemical vapour deposition. After spin-coating a negative photoresist (Fig. B.2b), the pattern of the nanomechanical

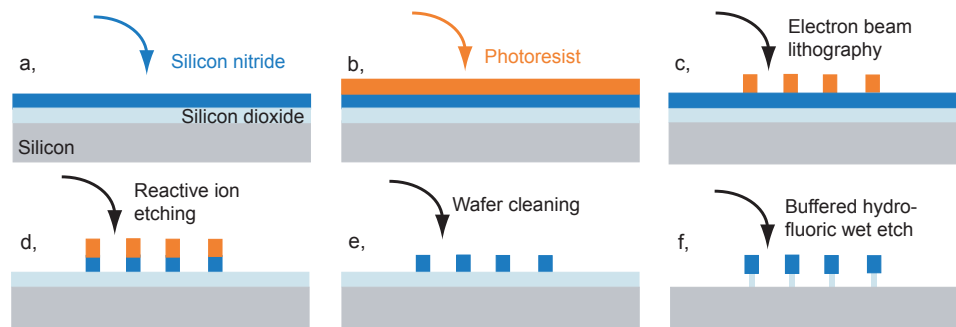


Figure B.2: Fabrication of silicon nitride nanomechanical oscillators. See text for details.

oscillators is written into the resist by electron beam lithography. The photoresist is developed (Fig. B.2c) and subsequently its pattern is transferred into the silicon nitride layer (Fig. B.2d) by reactive ion etching using C_4F_8 - CH_4 chemistry. Then, the resist is removed (Fig. B.2e) and the nanomechanical oscillators are released by a buffered HF etch that removes the sacrificial oxide layer underneath the oscillators (Fig. B.2f).

B.2 Experimental setup

In this section, the experimental setup will be described in somewhat more detail. The fabrication of compact tapered optical fibres and the coupling setup itself will be discussed.

B.2.1 Compact tapered optical fibres

The tapered fibre used for coupling light in and out of toroid microresonators is fabricated out of a standard single-mode fiber. Thereby, after stripping of the fibre's buffer, it is clamped at two points separated by approximately 10 mm. Melting the fibre in a hydrogen flame and at the same time pulling the clamping points apart allows adiabatically reducing the fibre's diameter from its original value $125\ \mu\text{m}$ down to a few hundred nanometres across a tapered region of typically 30 mm length. At the same time the transmission of the tapered part can be kept at values exceeding 99%. Fig. B.3a, shows the experimental setup used for fibre-pulling. In principle the fibre can be directly used for experiments after pulling. Due to space constraints within the experimental chamber, and in particular for enabling the microscope access necessary for coupling to nanomechanical oscillators, the fibre is transferred from the bulky holder used for pulling to a small u-shaped aluminium part for the experiments described in chapter 2. As shown in Fig. B.3b, the aluminium holder is positioned underneath the fibre until it slightly lifts up the tapered part. Subsequently, the taper is glued to the aluminium holder using standard ultraviolet-cured epoxy glue for optical elements (Thorlabs), cf. inset in Fig. B.3b. The aluminium holder and the glued fibre-taper are then mounted into the experimental chamber, as shown in Fig. B.3c.

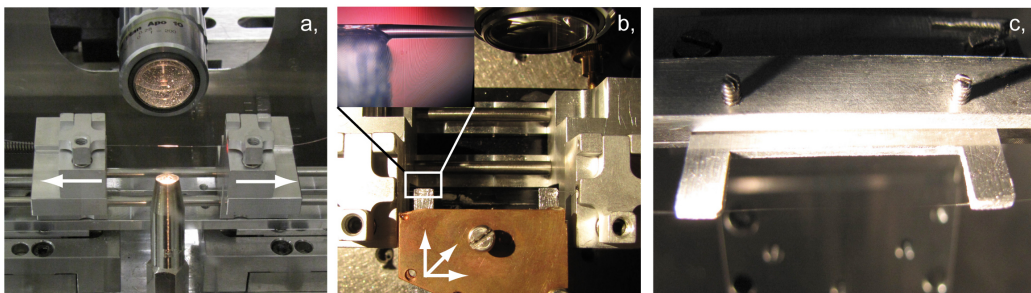


Figure B.3: Compact tapered optical fibre. a, After stripping off the fibre's buffer layer, it is cleaned using ethanol and clamped at two positions. A hydrogen flame is positioned underneath the fiber and the clamping points are pulled until the desired fibre diameter is reached. A microscope is used for monitoring the process. b, For the near-field experiments the taper is subsequently transferred onto a u-shaped aluminum piece onto which it is glued by a drop of ultraviolet-cured epoxy glue. The inset shows a zoom on the transition between free-hanging taper and glued region. c, The tapered fibre as used in the experimental chamber is shown.

B.2.2 Coupling setup

Fig. B.4 shows a drawing as well as a photograph of the experimental coupling region including the tapered optical fibre, the horizontal chip hosting the toroid microresonator as well as the vertical chip with the nanomechanical oscillators. As can be seen, careful translational and rotational alignment of all three elements with respect to each other has to be achieved. To this end, both the nanomechanical oscillator- and the toroid microresonator-chips are mounted on a common motor stage that allows coarse positioning of both elements with respect to the tapered optical fibre, as shown in Fig. B.4. The fibre in turn is mounted on a piezo cube that allows fine-tuning its position in the evanescent near-field of the microcavity. It can, moreover, be rotated around the two axes perpendicular to its own axis which is necessary for parallel alignment with both nano- and microchip. The nanomechanical oscillators' alignment with respect to the microtoroid is performed by three long-range piezo actuators on which the nanochip is mounted onto the motor stage. Their rotational degrees of freedom can be adjusted using a mirror mount on top of the piezo actuators.

The experimental coupling geometry and the mounting of the tapered optical fibre are designed in a compact way such that the actual coupling region resides sufficiently close to a vacuum window on top of it to allow optical access by a long-working distance (~ 25 mm) microscope objective. The positioning of the tapered fibre in the evanescent near-field is conveniently done using the microscope and in principle this would even be possible without the objective. Given the much smaller dimensions of the nanomechanical oscillators, the microscope objective, however, is indispensable for coarse positioning of the nanomechanical oscillators in the near-field of the toroids. The fine-positioning of the

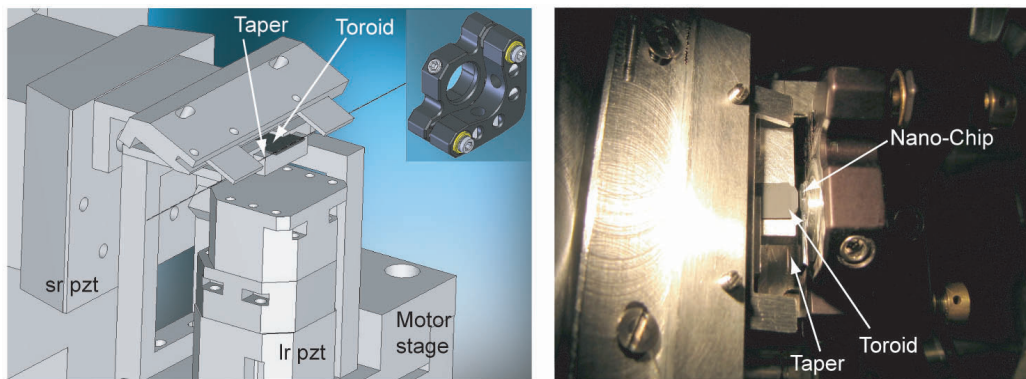


Figure B.4: Experimental setup. The left panel shows a drawing of the experimental setup. The tapered fibre is mounted on a short range piezo cube (sr pzt). Both the toroid and a stack of three long range piezo cubes (lr pzt) are mounted on a motorized translation stage. The nanomechanical oscillator chip is mounted on a mirror mount (inset) on top of the long range cubes. A photograph of the coupling region is shown in the right panel with the tapered fibre, the horizontal microresonator chip and the vertical nanomechanical oscillator chip which is attached to a mirror mount.

nanomechanical oscillators is performed using two further steps. First, the distinct optical response of the toroid microresonator's resonance to the presence of the dielectric in its evanescent field is used to optimize the nanomechanical oscillator's position. The silicon substrate produces a predominantly reactive shift in the microtoroid's optical resonances, i.e. the resonances are broadened whereas the dispersive frequency shift is very small. Thus, the presence of silicon or silicon nitride (which causes a predominantly dispersive frequency shift, as shown in section 2.2.1) in the evanescent near-field can be clearly distinguished. Once, the dispersive signal of a nanomechanical oscillator is found and both horizontal and vertical position are optimized accordingly, its position is further optimized in a second step. Thereby, the mechanical modes of the nanomechanical strings are used to fine tune the position. Minimizing the signal obtained for the second order mechanical modes (which exhibit a node at the centre of the strings) and at the same time maximizing the signal of the fundamental mode allows reliably tuning to the centre of the respective nanomechanical string.

B.3 Homodyne interferometer signal and frequency noise calibration

In this section the homodyne error signal, as employed in the setup described in chapter 2.5, will be derived. Moreover, the calibration of the thus measured frequency noise spectra is described in more detail.

B.3.1 Homodyne signal

The fields emerging from the signal and local oscillator arms (cf. Fig. 2.24), E_s and E_{lo} , are superimposed on a beam-splitter (denoted as PBS 5 in Fig. 2.24) using a half-wave plate. Thereby, the wave plate is adjusted such that both fields E_s and E_{lo} are split equally between both detectors of the balanced receiver. Thus, the fields impinging on each detector can be written as:

$$E_{\pm} = \frac{1}{\sqrt{2}}(E_{lo} \pm E_s). \quad (\text{B.2})$$

The phase shift of π between both fields is induced by the half-wave plate which rotates the orthogonally polarized fields onto each other in a 45° angle with respect to the following beam-splitter. At the balanced detector one then obtains a photocurrent of

$$I \propto |E_+|^2 - |E_-|^2. \quad (\text{B.3})$$

Assuming a relative phase of ϕ between E_s and the local oscillator field E_{lo} in the uncoupled case (i.e. for $\kappa_{ex} \rightarrow 0$) and taking into account the phase imprinted onto E_s by the optomechanical system (Eq. 1.13) the photocurrent as a function of the laser detuning evaluates to:

$$I = R \frac{2\sqrt{P_{lo}P_s}}{1 + 4\Delta^2/\kappa^2} \left[(1 + 4\Delta^2/\kappa^2 - 2\kappa_{ex}/\kappa) \cos(\phi) + 4\Delta\kappa_{ex}/\kappa^2 \sin(\phi) \right], \quad (\text{B.4})$$

where P_{lo} (P_s) is the power launched into the local oscillator (signal) arm and R denotes the responsivity (in A/W) of the employed detector. This expression is shown in Fig. B.5 as a function of normalized detuning. For optimizing the transduction of the phase quadrature at zero detuning, the relative phase ϕ is crucial. Experimentally, it is controlled by the length of the local oscillator arm. To this end, a piezo-driven motor stage is employed which allows matching the path-length of both arms with a precision of $\sim 1 \mu\text{m}$. Pumping the interferometer with a diode laser whose wavelength is scanned across its maximum tuning range and minimizing the concomitant change in homodyne signal has been a useful technique to closely match the path-lengths of both interferometer arms. The phase difference of both arms is moreover fine-tuned using a piezoelement that actuates the position of a movable mirror in the local oscillator arm. During measurements the phase difference ϕ is actively stabilized, as shown in Fig. 2.24 using a low frequency lock (bandwidth $< 10 \text{ kHz}$) applied to both elements. Choosing the phase $\phi = -\pi/2$ thereby

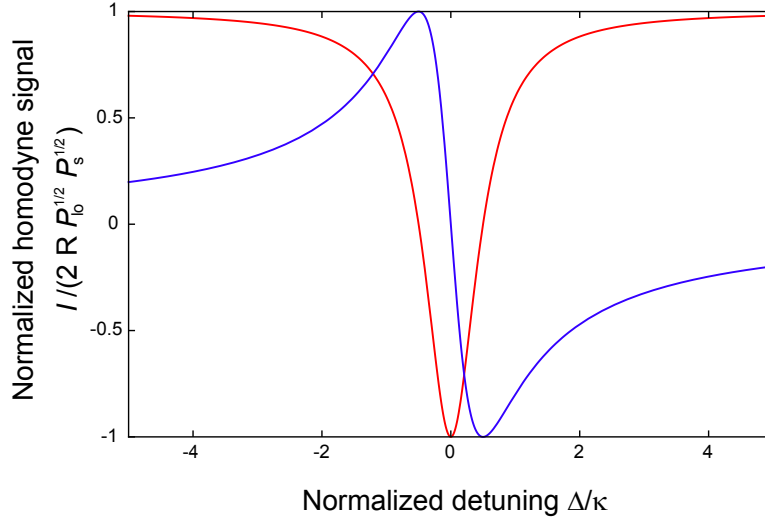


Figure B.5: Homodyne interferometer signal. Normalized photocurrent of the balanced homodyne receiver, as a function of the normalized laser-cavity detuning Δ/κ for $\phi = 0$ (red) and $\phi = -\pi/2$ (blue).

enables a dispersive homodyne signal, as shown in Fig. B.5. Correspondingly, at cavity resonance the phase fluctuations of E_s caused by the optomechanically induced cavity frequency fluctuations are probed.

B.3.2 Frequency noise calibration

In order to calibrate the measured cavity frequency noise spectra in absolute terms, a well-known frequency modulation is applied to the measurement laser using an electro-optic modulator. It can be shown that the transduction functions of both laser frequency modulation and cavity frequency fluctuations into the phase noise spectrum of E_s are equivalent. Thus, the knowledge of the applied frequency modulation's magnitude allows extracting a scale for the measured frequency noise spectra. First, the calibration of the applied frequency modulation is discussed. Then, it is shown how exactly the applied phase modulation is used to calibrate the measured spectra.

B.3.2.1 Calibrated phase modulation

By applying a bias-voltage to an electro-optic modulator, the phase of the light field transiting the modulator can be shifted. The modulators used in this thesis are all fibre-coupled, have typical bandwidths exceeding a GHz and typically the voltage necessary for a phase shift of π (V_π) is in the range of a few volts. The manufacturers typically specify the maximum value of V_π which can, however, range within individual devices. Therefore, each device has to be calibrated individually. To this end, a laser beam (with field E_0 , power P oscillating at angular frequency ω_d) is sent to the phase modulator and its wavelength

is scanned across the resonance of an optical cavity. At the same time, a sinusoidally modulated voltage $V \cos(\Omega_{\text{mod}}t)$ is applied to the modulator. The field exiting the phase modulator can be written as:

$$E = E_0 \cdot e^{i\beta(V)\cos(\Omega_{\text{mod}}t)}, \quad (\text{B.5})$$

where the phase modulation depth $\beta(V)$ depends on the amplitude of the applied voltage. It does not, however, depend on the modulation frequency $\Omega_{\text{mod}}/2\pi$ for the frequencies 1 – 100 MHz, well within the modulator bandwidth, considered here. Using the Jacobi-Anger identity¹, E can be written as

$$E = E_0 \left(J_0(\beta) + \sum_{n=1}^{\infty} i^n J_n(\beta) (e^{in\Omega_{\text{mod}}t} + e^{-in\Omega_{\text{mod}}t}) \right). \quad (\text{B.6})$$

From the linear expression (1.10), one can then obtain the total output field emerging from the cavity as a function of the laser detuning from cavity resonance $\Delta = \omega_d - \omega$ by summing the individual field components:

$$\bar{s}_{\text{out}}^{\text{tot}} = J_0(\beta) \bar{s}_{\text{out}}(\Delta) + \sum_{n=1}^{\infty} i^n J_n(\beta) (\bar{s}_{\text{out}}(\Delta + n\Omega_{\text{mod}})e^{in\Omega_{\text{mod}}t} + \bar{s}_{\text{out}}(\Delta - n\Omega_{\text{mod}})e^{-in\Omega_{\text{mod}}t}). \quad (\text{B.7})$$

Keeping only DC terms, one thus obtains a total DC photocurrent at the detector given by:

$$I = R \times P_{\text{in}} \sum_{n=-\infty}^{\infty} J_n^2(\beta) \left(1 - \frac{\kappa_{\text{ex}}(\kappa - \kappa_{\text{ex}})}{(\kappa^2/4 + \Delta - n\Omega_{\text{mod}})^2} \right). \quad (\text{B.8})$$

Thus, the transmitted field consists of the regular absorption dip at $\Delta = 0$ and symmetric sidebands at $\Delta = \pm n\Omega_{\text{mod}}$ all weighted by the respective Bessel-function $J_n(\beta)$. Fig. B.6a shows the transmission of a $\kappa/2\pi = 20$ MHz linewidth cavity using a frequency-modulated input laser. The transmission trace which clearly exhibits sidebands is fitted according to Eq. (B.8) up to second order which yields good agreement. Correspondingly the modulation index β can be extracted. Fig. B.6b shows the thus obtained modulation index as a function of voltage applied to the electro-optic modulator. A linear fit allows extracting $\beta(V) = \pi V/V_\pi$, with $V_\pi = (5.3 \pm 0.5)$ V.

B.3.2.2 Calibration of frequency noise spectra

The calibrated phase modulation which is applied to the measurement laser can now be used in order to calibrate the measured radio-frequency noise spectra in terms of frequency

¹ The Jacobi-Anger identity reads
 $e^{i\beta\cos(\phi)} = \sum_{n=-\infty}^{\infty} i^n J_n(\beta) e^{in\phi}$, $\beta, \phi \in \mathbb{R}$.

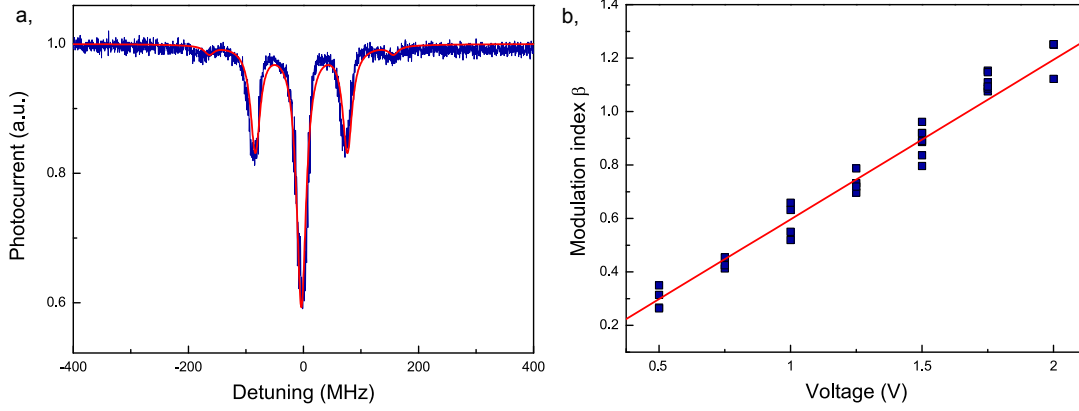


Figure B.6: Calibration of the electro-optic phase modulator. a, The transmission of a phase-modulated laser through a cavity resonance is shown as a function of the laser detuning. The data allows an excellent fit according to Eq. (B.8) and yields $\beta = 0.9$. b, The modulation index β measured as a function of the modulation voltage is shown. A linear fit through the origin allows extracting $V_\pi = 5.3$ V.

noise. It can be shown from Eqs. (A.10)-(A.17) that both cavity frequency noise S_ω and laser phase noise S_ϕ are transduced into fluctuations S_I of the cavity output field with the same transduction factor K [Ω] (see Ref. [3] for more details):

$$S_I[\Omega] = K[\Omega] (S_\phi[\Omega] + S_\omega[\Omega]/\Omega^2). \quad (\text{B.9})$$

Sending the signal S_I to a spectrum analyzer yields the following measured convolved spectrum:

$$S_{\text{meas}}[\Omega] = F[\Omega] * [K[\Omega] (S_\phi[\Omega] + S_\omega[\Omega]/\Omega^2)], \quad (\text{B.10})$$

where $F[\Omega]$ denotes the filter function of the electronic spectrum analyzer. Applying the previously calibrated phase modulation with modulation index β (as defined in Eq. B.5) leads to a delta distributed spectrum of the input laser phase:

$$S_\phi[\Omega] = \pi (\delta(\Omega - \Omega_{\text{mod}}) + \delta(\Omega + \Omega_{\text{mod}})) \beta^2/2. \quad (\text{B.11})$$

If the measured signal $S_{\text{meas}}[\Omega_{\text{mod}}]$ at the modulation frequency is dominated by $S_\phi[\Omega]$, the transduction factor $K[\Omega]$ can thus be calculated:

$$K[\Omega_{\text{mod}}] = 4 \text{ENBW} S_{\text{meas}}[\Omega_{\text{mod}}] / \beta^2, \quad (\text{B.12})$$

where ENBW denotes the effective noise bandwidth of the filter function $F[\Omega]$ ². Now, if the transduction factor is sufficiently flat across the frequency window of interest (which is

² The effective noise bandwidth is usually defined via $\text{ENBW} \cdot F[0] = \int_{-\infty}^{\infty} F[\Omega] \frac{d\Omega}{2\pi}$. For a normalized filter function one has thus: $\text{ENBW} = 1/F[0]$.

typically the case, since $\Gamma_m \ll \kappa$), the measured cavity frequency noise can be calibrated in absolute terms. If the ENBW is chosen much narrower than the spectral features in S_{meas} , using the above expressions one obtains:

$$S_{\omega}^{\text{ds}}[\Omega] = \frac{1}{S_{\text{meas}}[\Omega_{\text{mod}}]} \frac{\Omega_{\text{mod}}^2 \beta^2}{4 \text{ENBW}} \times S_{\text{meas}}[\Omega] , \quad (\text{B.13})$$

where the superscript in $S_{\omega}^{\text{ds}}[\Omega]$ emphasizes that we refer to a double-sided spectrum, here. Equivalently, for the single-sided spectrum one obtains:

$$S_{\omega}^{\text{ss}}[\Omega] = \frac{1}{S_{\text{meas}}[\Omega_{\text{mod}}]} \frac{\Omega_{\text{mod}}^2 \beta^2}{2 \text{ENBW}} \times S_{\text{meas}}[\Omega] . \quad (\text{B.14})$$

Appendix C

Fabrication of spoke-supported microresonators

In this appendix, the fabrication of spoke-supported microresonators is described. As depicted in Fig. C.1, it requires two UV-lithography steps. The first one is performed in the cleanroom of Prof. Kotthaus at LMU. Starting with an undoped silicon wafer with a $1 - 3 \mu\text{m}$ oxide layer (Virginia Semiconductor), first, the spokes pattern is etched into the oxide layer using UV-lithography and a buffered hydrofluoric wet etch. This fabrication step follows the same recipe as used for regular toroids and described in appendix B.1.1.

Now, a second lithography step is required. An immediate XeF_2 dry etch which is used to underetch the glass disks would also etch through the gaps which define the spokes patterns and thus make it difficult to achieve the desired geometry with free-standing spokes. In order to prevent this, a layer of photoresist (AZ 5214F) that does not react with XeF_2 is deposited on top of the silica disk and circular pads covering the gaps between the spokes are defined. This step which requires precise alignment of the spokes pattern and the photomask turned out to be very difficult to perform with the MJB 3 mask aligner used in the standard process. Therefore, this step was performed in the cleanroom of Prof. Feldmann and Prof. Kersting at LMU where a mask-aligner with a better microscope could be used (MA 6, Süss Microtech). The following recipe was used for fabricating the circular pads:

- Spin-coating of adhesion promoter HDMS on the wafer at 3000 rpm for 20s
- Baking at 110°C for 60s
- Spin-coating of photoresist AZ-5214 F on the wafer at 4000 rpm for 60s
- Baking for 70s at 110°C
- Illuminating the wafer for 35s using a MA 6 mask aligner (Süss Microtech).
- Developing for 40 – 60s using AZ-726 MIF developer

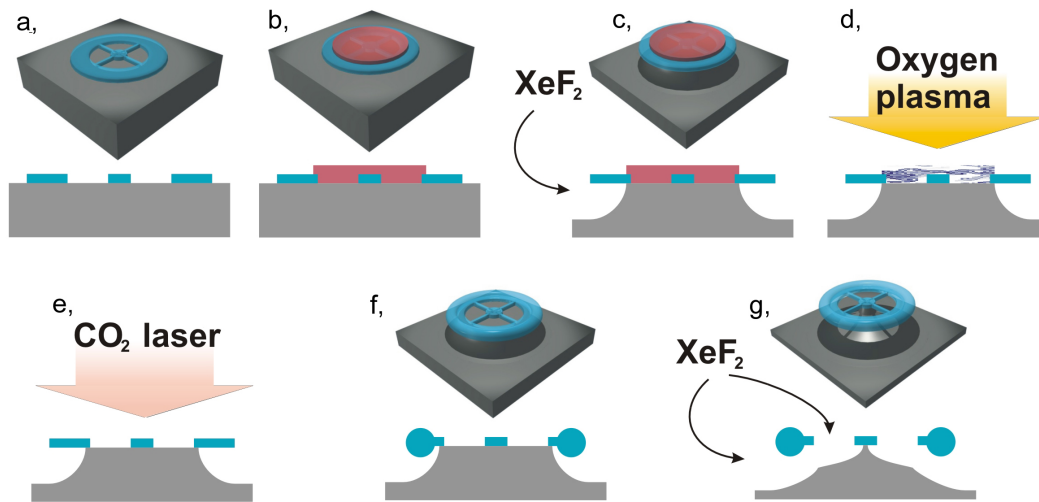


Figure C.1: Fabrication of spoke-supported microresonators. a, Silica disk with spokes on silicon wafer. b, A protective layer of photoresist is deposited on top of the spokes. c, The silica structure is underetched from the side using XeF_2 gas. d, The photoresist is removed with oxygen plasma. e, The silica structure is illuminated with a CO_2 laser melting the structure at its rims such that a toroid is formed f, via surface tension. g, A second XeF_2 etch releases the spokes such that the silica structure is only supported at its centre. Fig. adapted from Ref. [6]

Subsequently, the XeF_2 underetch can be performed as for regular toroids. Afterwards the protective photoresist pad is removed by acetone and oxygen plasma (Fig. C.1c). In order to obtain ultra-high optical Q-factors the rim of the spokes pattern is melted using a CO_2 laser-assisted reflow process. For this reflow process it has to be made sure that the spokes are still fully supported by the silicon substrate after the XeF_2 etch. Only that way, sufficient heat conduction from the silica to the silicon substrate is ensured, allowing controlled melting along the circumference of the silica disk. Doing so, it is possible to perform the full laser reflow process without harming the silica spokes even if these are very thin. By a final XeF_2 etching step the spokes sitting on the silica substrate are released and the desired relative undercut can be reached.

Appendix D

Code for FEM whispering gallery mode simulations

The following code is used for simulating the optical whispering gallery modes of a toroid microresonator with a dielectric nanomechanical oscillator present in its evanescent field. It is based on the code for axisymmetric problems supplied in Ref. [101].

```
% Input variables:
% - R:          Major toroid radius in micron
% - r:          Minor toroid radius in micron
% - modeM:      angular mode number l
% - nfusedsilica:refractive index of silica
% - startvalue: optical frequency used as start value
% - width:      thickness of the dielectric nanomechanical oscillator in micron
% - height:     width of the dielectric nanomechanical oscillator in micron
% - x0:         distance of the nanomechanical oscillator to the cavity in micron
%
% Output variables:
% - Field distribution (a.u.)
% - Resonance frequency in Hz
% - Mode volume in micron^3

function frequency(R,r,modeM,nfusedsilica,startvalue,width,height,x0)

% COMSOL version
clear vrsn
vrsn.name = 'COMSOL 3.2';
vrsn.ext = '';
vrsn.major = 0;
vrsn.build = 224;
vrsn.rcs = '$Name: $';
vrsn.date = '$Date: 2005/10/24 07:30:19 $';
fem.version = vrsn;

flclear fem
```

```

global fem

% Constants
fem.const = {'c','299792458', 'fc','4*pi^2/c^2', 'alpha','1', 'M',modeM, ...
'e1','n_silica^2', 'e2','n_SiN^2', 'e3','1.0', 'e4','1.0', 'e5','1.0', ...
'eperp1','9.2725', 'epara1','11.3486', 'eperp2','1.0', 'epara2','1.0', ...
'eperp3','1.0', 'epara3','1.0', 'eperp4','1.0', 'epara4','1.0', ...
'eperp5','1.0', 'epara5','1.0', 'n_silica',nfusedsilica, 'n_SiN','2.0'};

% Draw Geometry
g1=rect2(6+2*r,6+2*r,'base','corner','pos',[R-3-2*r,-r-3]);
g2=rect2(3+r,'1','base','corner','pos',{R-3-2*r,-1},'rot','0');
g3=ellip2(r,r,'base','center','pos',[R-r,0]);
g4=geomcomp({g2,g3},'ns',{g51,g52},'sf','g51+g52','edge','all');
g42=rect2(width,height,'base','corner','pos',{R+x0,-height/2},'rot','0');

clear s
s.objs={g1,g4,g42};
s.name={'R2','CO2','R3'};
s.tags={'g1','g4','g42'};

fem.draw=struct('s',s);
fem.geom=geomcsg(fem);

% Initialize mesh
fem.mesh=meshinit(fem, ...
    'hmaxfact',0.55, ...
    'hgrad',1.25, ...
    'hcurve',0.25, ...
    'hcutoff',0.0005);

%Refine mesh
fem.mesh=meshrefine(fem, ...
    'mcase',0, ...
    'boxcoord',[R-2*r R+3 -r-1 r+1], ...
    'rmethod','regular');

% (Default values are not included)
% Application mode 1
% Before using the code, REMOVE LINEBREAKS within curly brackets {} in equ.weak!
clear appl
appl.mode.class = 'FlPDEW';
appl.dim = {'Hrad','Hazi','Haxi','Hrad_t','Hazi_t','Haxi_t'};
appl.name = 'AxisymmetricDielectricResonatorSimulator';
appl.gporder = 4;
appl.cporder = 2;
appl.assignsuffix = '_AxisymmetricDielectricResonatorSimulator';
clear bnd
bnd.constr = {'Hrad*nx+Haxi*ny',{'Hazi';'-Haxi*nx+Hrad*ny'},0,{'-Hrad'; ...
'-Hazi';'-Haxi'}};
bnd.name = {'tangential_H','normal_H','null',''};

```

```

bnd.ind = [1,1,1,4,1,4,1,4,4,4,4,1,4,4,4,4];
appl.bnd = bnd;
clear equ
equ.weak = {'((test(Hazi)*Hazi-M*(test(Hazi)*Hrad+Hazi*test(Hrad))
+M^2*(test(Hrad)*Hrad+test(Haxi)*Haxi))/x+(test(Hazix)*(Hazi-M*Hrad)
+Haxix*(test(Hazi)-M*test(Hrad)))-M*(test(Haxi)*Hazi+Haxi*test(Hazi))
+x*(test(Hazix)*Haxix+(test(Haxix)-test(Hrady))*(Haxix-Hrady)
+Hazi*test(Hazi)))'); 'alpha*((test(Hrad)*Hrad-M*(test(Hazi)*Hrad
+Hazi*test(Hrad))+M^2*test(Hazi)*Hazi)/x+(test(Haxiy)
+test(Hradx))*(Hrad-M*Hazi)+(test(Hrad)-M*test(Hazi))*(Hradx+Haxiy)
+x*(test(Hradx)+test(Haxiy))*(Hradx+Haxiy))'}, ...
{'((test(Hazi)*Hazi-M*(test(Hazi)*Hrad+Hazi*test(Hrad))
+M^2*(test(Hrad)*Hrad+test(Haxi)*Haxi))/x+(test(Hazix)*(Hazi-M*Hrad)
+Haxix*(test(Hazi)-M*test(Hrad)))-M*(test(Haxi)*Hazi+Haxi*test(Hazi))
+x*(test(Hazix)*Haxix+(test(Haxix)-test(Hrady))*(Haxix-Hrady)
+Hazi*test(Hazi)))/e1'; 'alpha*((test(Hrad)*Hrad-M*(test(Hazi)*Hrad
+Hazi*test(Hrad))+M^2*test(Hazi)*Hazi)/x+(test(Haxiy)
+test(Hradx))*(Hrad-M*Hazi)+(test(Hrad)-M*test(Hazi))*(Hradx+Haxiy)
+x*(test(Hradx)+test(Haxiy))*(Hradx+Haxiy))'}, ...
{'((test(Hazi)*Hazi-M*(test(Hazi)*Hrad+Hazi*test(Hrad))
+M^2*(test(Hrad)*Hrad+test(Haxi)*Haxi))/x+(test(Hazix)*(Hazi-M*Hrad)
+Haxix*(test(Hazi)-M*test(Hrad)))-M*(test(Haxi)*Hazi+Haxi*test(Hazi))
+x*(test(Hazix)*Haxix+(test(Haxix)-test(Hrady))*(Haxix-Hrady)
+Hazi*test(Hazi)))/e2'; 'alpha*((test(Hrad)*Hrad-M*(test(Hazi)*Hrad
+Hazi*test(Hrad))+M^2*test(Hazi)*Hazi)/x+(test(Haxiy)
+test(Hradx))*(Hrad-M*Hazi)+(test(Hrad)-M*test(Hazi))*(Hradx+Haxiy)
+x*(test(Hradx)+test(Haxiy))*(Hradx+Haxiy))'}};

equ.dweak = 'fc*x*(Haxitt*test(Haxi)+Hazitt*test(Hazi)+Hradtt*test(Hrad))';
equ.name = {'dielectric_0:vacuum','isotrop_diel_1','isotrop_diel_2'};
equ.ind = [1,2,3];
appl.equ = equ;
fem.appl{1} = appl;
fem.border = 1;
fem.units = 'SI';

% Subdomain expressions
clear equ
equ.ind = [1,2,3];
equ.dim = {'Hrad','Hazi','Haxi'};
equ.expr = {'erel',{1,'e1','e2'}};
fem.equ = equ;

% Scalar expressions
fem.expr = {'DivH','(Hrad-Hazi*M+(Haxiy+Hradx)*x)/x', ...
'MagEnDens','Hrad*Hrad+Hazi*Hazi+Haxi*Haxi', ...
'Drad','(Haxi*M-Hazi*x)/x', ...
'Dazi','-Haxix+Hrady', ...
'Daxi','(Hazi-Hrad*M+Haxix*x)/x', ...
'Erad','Drad/erel', ...
'Eazi','Dazi/erel', ...

```

```

'Eaxi','Daxi/erel', ...
'ElecMagSqrD','Erad*Erad+Eazi*Eazi+Eaxi*Eaxi', ...
'ElecEnDens','Erad*Drad+Eazi*Dazi+Eaxi*Daxi'}];

% Descriptions
clear descr
descr.expr= {'Eaxi','axial el. field strength', 'DivH','div. of magn. field', ...
'ElecEnDens','el. energy density', ...
'ElecMagSqrD','el. field strength magnitude squared', ...
'Eazi','azimuthal el. field strength', 'Drad','radial el. displacement', ...
'Dazi','azimuthal el. displacement', 'Erad','radial el. field strength', ...
'Daxi','axial el. displ.', 'MagEnDens','logarithmic magn. energy density'}];
fem.descr = descr;

% Coupling variable elements
clear elemcpl

% Integration coupling variables
clear elem
elem.elem = 'elcplscalar';
elem.g = {'1'};
src = cell(1,1);
src{1} = {{},{},{}};
elem.src = src;
geomdim = cell(1,1);
geomdim{1} = {};
elem.geomdim = geomdim;
elem.var = {};
elem.global = {};
elem.maxvars = {};
elemcpl{1} = elem;
fem.elemcpl = elemcpl;

% Descriptions
descr = fem.descr;
descr.const= {'c','speed of light', 'n_SiN','refracvtive index of SiN', ...
'M','angular mode number', 'n_silica','refractive index of silica', ...
'fc','constant used internally --do not modify', ...
'e1','relative permittivity of isotropic_dielectric_1', ...
'alpha','penalty coefficient on Div H'}];
fem.descr = descr;

% Multiphysics
fem=multiphysics(fem);

% Extend mesh
fem.xmesh=meshextend(fem);

% Solve problem
fem.sol=femeig(fem, ...
'symmetric','on', ...

```

```
'solcomp', {'Hazi', 'Haxi', 'Hrad'}, ...
'outcomp', {'Hazi', 'Haxi', 'Hrad'}, ...
'neigs', 1, ...
'shift', startvalue, ...
'maxeigit', 2000, ...
'linsolver', 'spooles');

% Save current fem structure for restart purposes
fem0=fem;

% Get mode volume and frequency
I2=postint(fem, '2*pi*x*ElecEnDens', 'dl', [1]);
I3=postint(fem, '2*pi*x*ElecEnDens', 'dl', [2]);
I4=postint(fem, '2*pi*x*ElecEnDens', 'dl', [3]);

Energy=I2+I3+I4;
Engmax=postmax(fem, 'ElecEnDens');

fem.modevolume=Energy/Engmax;
fem.frequency=fem.sol.lambda*1e6;

% Visualise solution
postplot(fem, ...
    'tridata', {'log10(ElecMagSqr+1e-2)', 'cont', 'internal'}, ...
    'trimap', 'jet(1024)', ...
    'arrowdata', {'Erad', 'Eaxi'}, ...
    'arrowspacing', 15, ...
    'arrowyspacing', 13, ...
    'arrowscale', 1.2, ...
    'arrowtype', 'arrow', ...
    'arrowstyle', 'proportional', ...
    'arrowcolor', [1.0, 1.0, 1.0], ...
    'maxminsub', 'ElecEnDens', ...
    'title', 'log10(ElecMagSqr+1e-2)', ...
    'axis', [R-3-2*r, R+3, -r-3, r+3, -1, 1]);
```


Bibliography

- [1] G. Anetsberger and T. J. Kippenberg. Near-field cavity optomechanics. *in preparation* (2010).
- [2] G. Anetsberger, E. Gavartin, O. Arcizet, Q. P. Unterreithmeier, E. M. Weig, M. L. Gorodetsky, J. P. Kotthaus and T. J. Kippenberg. Measuring nanomechanical motion with an imprecision below the standard quantum limit. *Physical Review A* in press (2010).
- [3] M. L. Gorodetsky, A. Schliesser, G. Anetsberger, S. Deléglise and T. J. Kippenberg. Determination of the vacuum optomechanical coupling rate using frequency noise calibration. *Optics Express* **18**, 23236 (2010).
- [4] G. Anetsberger, O. Arcizet, Q. P. Unterreithmeier, R. Rivière, A. Schliesser, E. M. Weig, J. P. Kotthaus and T. J. Kippenberg. Near-field cavity optomechanics with nanomechanical oscillators. *Nature Physics* **5**, 909 (2009).
- [5] G. Anetsberger, R. Rivière, A. Schliesser, O. Arcizet and T. J. Kippenberg. Approaching the quantum world with nanospokes. *SPIE Newsroom* doi: 10.1117/2.1200901.1423 (2009).
- [6] G. Anetsberger, R. Rivière, A. Schliesser, O. Arcizet and T. J. Kippenberg. Ultralow-dissipation Optomechanical Resonators on a Chip. *Nature Photonics* **2**, 627 (2008).
- [7] A. Schliesser, G. Anetsberger, R. Rivière, O. Arcizet and T. J. Kippenberg. High-sensitivity monitoring of micromechanical vibration using optical whispering gallery mode resonators. *New Journal of Physics* **10**, 095015 (2008).
- [8] A. Schliesser, O. Arcizet, R. Rivière, G. Anetsberger and T. J. Kippenberg. Resolved-sideband cooling and position measurement of a micromechanical oscillator close to the heisenberg uncertainty limit. *Nature Physics* **5**, 509 (2009).
- [9] O. Arcizet, R. Rivière, A. Schliesser, G. Anetsberger and T. J. Kippenberg. Cryogenic properties of optomechanical silica microcavities. *Physical Review A* **80**, 021803 (2009).
- [10] A. Schliesser, R. Rivière, G. Anetsberger, O. Arcizet and T. J. Kippenberg. Resolved-sideband cooling of a micromechanical oscillator. *Nature Physics* **4**, 415 (2008).

-
- [11] R. Ma, A. Schliesser, P. Del’Haye, A. Dabirian, G. Anetsberger and T. J. Kippenberg. Radiation-pressure driven vibrational modes in ultrahigh-q silica microspheres. *Optics Letters* **32**, 2200 (2007).
- [12] R. Morrow, D. R. McKenzie, M. M. M. Bilek, C. L. MacDonald, M. Stindt, G. Anetsberger and A. S. Martin. Electric field effects on adsorption/desorption of proteins and colloidal particles on a gold film observed using surface plasmon resonance. *Physica B: Condensed Matter* **394**, 203 (2007).
- [13] K. D. Wise. Special Issue: Integrated Sensors, Microactuators, and Microsystems (MEMS). *Proceedings of the IEEE* **86**, 1529 (1998).
- [14] K. J. Vahala. Optical microcavities. *Nature* **424**, 839 (2003).
- [15] T. J. Kippenberg and K. J. Vahala. Cavity Optomechanics: Back-Action at the Mesoscale. *Science* **321**, 1172 (2008).
- [16] F. Marquardt and S. M. Girvin. Optomechanics. *Physics* **2**, 40 (2009).
- [17] I. Favero and K. Karrai. Optomechanics of deformable optical cavities. *Nature Photonics* **3**, 40 (2009).
- [18] A. Einstein. Die Grundlagen der allgemeinen Relativitätstheorie. *Annalen der Physik* **49**, 769 (1916).
- [19] B. P. Abbott et al. LIGO: the Laser Interferometer Gravitational-Wave Observatory. *Reports on Progress in Physics* **72**, 076901 (2009).
- [20] GEO 600 Collaboration. <http://www.geo600.uni-hannover.de/geocurves/>.
- [21] V. B. Braginsky and Y. I. Vorontsov. Quantum-mechanical limitations in macroscopic experiments and modern experimental technique. *Soviet Physics Uspekhi* **17**, 644 (1975).
- [22] C. M. Caves. Quantum-mechanical noise in an interferometer. *Physical Review D* **23**, 1693 (1981).
- [23] A. Dorsel, J. D. McCullen, P. Meystre, E. Vignes and H. Walther. Optical bistability and mirror confinement induced by radiation pressure. *Physical Review Letters* **51**, 1550 (1983).
- [24] V. B. Braginsky and A. B. Manukin. Ponderomotive effects of electromagnetic radiation. *Soviet Physics JETP* **25**, 653 (1967).
- [25] V. B. Braginskii, A. B. Manukin and M. Y. Tikhonov. Investigation of dissipative ponderomotive effects of electromagnetic radiation. *Soviet Physics JETP* **58**, 1550 (1970).

-
- [26] T. J. Kippenberg, H. Rokhsari, T. Carmon, A. Scherer and K. J. Vahala. Analysis of radiation-pressure induced mechanical oscillation of an optical microcavity. *Physical Review Letters* **95**, 033901 (2005).
- [27] T. Carmon, H. Rokhsari, L. Yang, T. J. Kippenberg and K. J. Vahala. Temporal behavior of radiation-pressure-induced vibrations of an optical microcavity phonon mode. *Physical Review Letters* **94**, 223902 (2005).
- [28] H. Rokhsari, T. J. Kippenberg, T. Carmon and K. J. Vahala. Radiation-pressure-driven micro-mechanical oscillators. *Optics Express* **13**, 5293 (2005).
- [29] S. Tallur, S. Sridaran, S. A. Bhave and T. Carmon. Phase noise modeling of optomechanical oscillators. *IEEE Frequency Control Symposium* 268 (2010).
- [30] X. L. Feng, C. J. White, A. Hajimiri and M. L. Roukes. A self-sustaining ultrahigh-frequency nanoelectromechanical oscillator. *Nature Nanotechnology* **3**, 342 (2008).
- [31] M. Hossein-Zadeh, H. Rokhsari, A. Hajimiri and K. J. Vahala. Characterization of a radiation-pressure-driven micromechanical oscillator. *Physical Review A* **74**, 023813 (2006).
- [32] O. Arcizet, P.-F. Cohadon, T. Briant, M. Pinarid and A. Heidmann. Radiation-pressure cooling and optomechanical instability of a micromirror. *Nature* **444**, 71 (2006).
- [33] S. Gigan, H. R. Bohm, M. Paternostro, F. Blaser, G. Langer, J. B. Hertzberg, K. C. Schwab, D. Bauerle, M. Aspelmeyer and A. Zeilinger. Self-cooling of a micromirror by radiation pressure. *Nature* **444**, 67 (2006).
- [34] A. Schliesser, P. Del’Haye, N. Nooshi, K. J. Vahala and T. J. Kippenberg. Radiation pressure cooling of a micromechanical oscillator using dynamical backaction. *Physical Review Letters* **97**, 243905 (2006).
- [35] I. Wilson-Rae, N. Nooshi, W. Zwerger and T. J. Kippenberg. Theory of ground state cooling of a mechanical oscillator using dynamical backaction. *Physical Review Letters* **99**, 093901 (2007).
- [36] F. Marquardt, J. P. Chen, A. A. Clerk and S. M. Girvin. Quantum theory of cavity-assisted sideband cooling of mechanical motion. *Physical Review Letters* **99**, 093902 (2007).
- [37] J. D. Thompson, B. M. Zwickl, A. M. Jayich, F. Marquardt, S. M. Girvin and J. G. E. Harris. Strong dispersive coupling of a high-finesse cavity to a micromechanical membrane. *Nature* **452**, 72 (2008).

- [38] J. D. Teufel, J. W. Harlow, C. A. Regal and K. W. Lehnert. Dynamical backaction of microwave fields on a nanomechanical oscillator. *Physical Review Letters* **101**, 197203 (2008).
- [39] S. Gröblacher, K. Hammerer, M. F. Vanner and M. Aspelmeyer. Observation of strong coupling between a micromechanical resonator and an optical cavity field. *Nature* **460**, 724 (2009).
- [40] Y.-S. Park and H. Wang. Resolved-sideband and cryogenic cooling of an optomechanical resonator. *Nature Physics* **5**, 489 (2009).
- [41] T. Rocheleau, T. Ndukum, C. Macklin, J. B. Hertzberg, A. A. Clerk and K. C. Schwab. Preparation and detection of a mechanical resonator near the ground state of motion. *Nature* **463**, 72 (2010).
- [42] A. D. O'Connell, M. Hofheinz, M. Ansmann, R. C. Bialczak, M. Lenander, E. Lucero, M. Neeley, D. Sank, H. Wang, M. Weides, J. Wenner, J. M. Martinis and A. N. Cleland. Quantum ground state and single-phonon control of a mechanical resonator. *Nature* **464**, 697 (2010).
- [43] K. Jensen, K. Kim and A. Zettl. An atomic-resolution nanomechanical mass sensor. *Nature Nanotechnology* **3**, 533 (2008).
- [44] A. Cleland and M. Roukes. A nanometre-scale mechanical electrometer. *Nature* **392**, 160 (1998).
- [45] D. Rugar, R. Budakian, H. J. Mamin and B. W. Chui. Single spin detection by magnetic resonance force microscopy. *Nature* **430**, 329 (2004).
- [46] C. K. Law. Interaction between a moving mirror and radiation pressure: A hamiltonian formulation. *Physical Review A* **51**, 2537 (1995).
- [47] J. Hofer, A. Schliesser and T. J. Kippenberg. Cavity optomechanics with ultrahigh-Q crystalline microresonators. *Physical Review A* **82**, 031804 (2010).
- [48] T. Corbitt, Y. Chen, E. Innerhofer, H. Müller-Ebhardt, D. Ottaway, H. Rehbein, D. Sigg, S. Whitcomb, C. Wipf and N. Mavalvala. An all-optical trap for a gram-scale mirror. *Physical Review Letters* **98**, 150802 (2007).
- [49] M. Eichenfield, R. Camacho, J. Chan, K. J. Vahala and O. Painter. A picogram- and nanometre scale photonic-crystal optomechanical cavity. *Nature* **459**, 550 (2009).
- [50] S. Gröblacher, J. B. Hertzberg, M. R. Vanner, G. D. Cole, S. Gigan, K. C. Schwab and M. Aspelmeyer. Demonstration of an ultracold micro-optomechanical oscillator in a cryogenic cavity. *Nature Physics* **5**, 485 (2009).

- [51] I. Favero, C. Metzger, S. Camerer, D. König, H. Lorenz, J. Kotthaus and K. Karrai. Optical cooling of a micromirror of wavelength size. *Applied Physics Letters* **90**, 104101 (2007).
- [52] Q. Lin, J. Rosenberg, X. Jiang, K. J. Vahala and O. Painter. Mechanical oscillation and cooling actuated by the optical gradient force. *Physical Review Letters* **103**, 103601 (2009).
- [53] M. Eichenfield, J. Chan, R. M. Camacho, K. J. Vahala and O. Painter. Optomechanical crystals. *Nature* **462**, 78 (2010).
- [54] I. Favero, S. Stapfner, D. Hunger, P. Paulitschke, J. Reichel, H. Lorenz, E. M. Weig and K. Karrai. Fluctuating nanomechanical system in a high finesse optical microcavity. *Optics Express* **17**, 12813 (2009).
- [55] M. Li, W. H. P. Pernice and H. X. Tang. Reactive cavity optical force on microdisk-coupled nanomechanical beam waveguides. *Physical Review Letters* **103**, 223901 (2009).
- [56] J. Teufel, T. Donner, M. Castellanos-Beltran, J. Harlow and K. Lehnert. Nanomechanical motion measured with an imprecision below that at the standard quantum limit. *Nature Nanotechnology* **4**, 820 (2009).
- [57] V. Giovannetti and D. Vitali. Phase-noise measurement in a cavity with a movable mirror undergoing quantum brownian motion. *Physical Review A* **63**, 023812 (2001).
- [58] C. W. Gardiner and M. J. Collett. Input and output in damped quantum systems: Quantum stochastic differential equations and the master equation. *Physical Review A* **31**, 3761 (1985).
- [59] Y. Hadjar. *Etude du couplage optomécanique dans une cavité de grande finesse. Observation du mouvement Brownien d'un miroir*. Ph.D. thesis, Université Paris VI (1998).
- [60] C. Fabre, M. Pinard, S. Bourzeix, A. Heidmann, E. Giacobino and S. Reynaud. Quantum-noise reduction using a cavity with a movable mirror. *Physical Review A* **49**, 1337 (1994).
- [61] M. Kitagawa and Y. Yamamoto. Number-phase minimum-uncertainty state with reduced number uncertainty in a kerr nonlinear interferometer. *Physical Review A* **34**, 3974 (1986).
- [62] H. A. Haus. *Waves and Fields in Optoelectronics*. Prentice Hall (1983).
- [63] A. Heidmann and S. Reynaud. Photon noise reduction by reflection from a movable mirror. *Physical Review A* **50**, 4237 (1994).

- [64] K. Jacobs, P. Tombesi, M. J. Collett and D. F. Walls. Quantum-nondemolition measurement of photon number using radiation pressure. *Physical Review A* **49**, 1961 (1994).
- [65] M. Pinard, C. Fabre and A. Heidmann. Quantum-nondemolition measurement of light by a piezoelectric crystal. *Physical Review A* **51**, 2443 (1995).
- [66] A. Heidmann, Y. Hadjar and M. Pinard. Quantum nondemolition measurement by optomechanical coupling. *Applied Physics B: Laser and Optics* **64**, 173 (1997).
- [67] V. B. Braginsky, Y. I. Vorontsov and K. S. Thorne. Quantum non-demolition measurements. *Science* **209**, 547 (1980).
- [68] V. B. Braginsky and F. Y. Khalili. *Quantum Measurement*. Cambridge University Press (1992).
- [69] A. A. Clerk, F. Marquardt and K. Jacobs. Back-action evasion and squeezing of a mechanical resonator using a cavity detector. *New Journal of Physics* **10**, 095010 (2008).
- [70] J. B. Hertzberg, T. Rocheleau, T. Ndukum, M. Savva, A. A. Clerk and K. C. Schwab. Back-action-evading measurements of nanomechanical motion. *Nature Physics* **6**, 213 (2010).
- [71] S. Stenholm. The semiclassical theory of laser cooling. *Reviews of Modern Physics* **58**, 699 (1986).
- [72] C. Genes, D. Vitali, P. Tombesi, S. Gigan and M. Aspelmeyer. Ground-state cooling of a micromechanical oscillator: Comparing cold damping and cavity-assisted cooling schemes. *Physical Review A* **77**, 033804 (2008).
- [73] D. J. Wineland and W. M. Itano. Laser cooling of atoms. *Physical Review A* **20**, 1521 (1979).
- [74] A. A. Clerk and S. Bennett. Quantum nanoelectromechanics with electrons, quasiparticles and Cooper pairs: effective bath descriptions and strong feedback effects. *New Journal of Physics* **7**, 238 (2005).
- [75] V. B. Braginsky, S. E. Strigin and S. P. Vyatchanin. Parametric oscillatory instability in Fabry-Perot interferometer. *Physics Letters A* **287**, 331 (2001).
- [76] V. B. Braginsky and S. P. Vyatchanin. Low quantum noise tranquilizer for Fabry-Perot interferometer. *Physics Letters A* **293**, 228 (2002).
- [77] F. Marquardt, J. G. E. Harris and S. M. Girvin. Dynamical multistability induced by radiation pressure in high-finesse micromechanical optical cavities. *Physical Review Letters* **96**, 103901 (2006).

- [78] M. Ludwig, B. Kubala and F. Marquardt. The optomechanical instability in the quantum regime. *New Journal of Physics* **10**, 095013 (2008).
- [79] C. Metzger, M. Ludwig, C. Neuenhahn, A. Ortlieb, I. Favero, K. Karrai and F. Marquardt. Self-induced oscillations in an optomechanical system driven by bolometric backaction. *Physical Review Letters* **101**, 133903 (2008).
- [80] M. Hossein-Zadeh and K. J. Vahala. Observation of injection locking in an optomechanical rf oscillator. *Applied Physics Letters* **93**, 191115 (2008).
- [81] K. Vahala, M. Herrmann, S. Knünz, V. Batteiger, G. Saathoff, T. W. Hänsch and T. Udem. A phonon laser. *Nature Physics* **5**, 682 (2009).
- [82] I. S. Grudinin, H. Lee, O. Painter and K. J. Vahala. Phonon laser action in a tunable two-level system. *Physical Review Letters* **104**, 083901 (2010).
- [83] S. Knünz, M. Herrmann, V. Batteiger, G. Saathoff, T. W. Hänsch, K. J. Vahala and T. Udem. Injection locking of a trapped-ion phonon laser. *Physical Review Letters* **105**, 013004 (2010).
- [84] J. P. Gordon, H. J. Zeiger and C. H. Townes. The maser—new type of microwave amplifier, frequency standard, and spectrometer. *Physical Review* **99**, 1264 (1955).
- [85] A. L. Schawlow and C. H. Townes. Infrared and optical masers. *Physical Review* **112**, 1940 (1958).
- [86] K. J. Vahala. Back-action limit of linewidth in an optomechanical oscillator. *Physical Review A* **78**, 023832 (2008).
- [87] B. Sheard, M. Gray, C. Mow-Lowry, D. McClelland and S. Whitcomb. Observation and characterization of an optical spring. *Physical Review A* **69**, 051801 (2004).
- [88] D. K. Armani, T. J. Kippenberg, S. M. Spillane and K. J. Vahala. Ultra-high-Q toroid microcavity on a chip. *Nature* **421**, 925 (2003).
- [89] T. J. Kippenberg, S. M. Spillane and K. J. Vahala. Kerr-nonlinearity optical parametric oscillation in an ultrahigh-Q toroid microcavity. *Physical Review Letters* **93**, 083904 (2004).
- [90] P. Del’Haye, A. Schliesser, O. Arcizet, T. Wilken, R. Holzwarth and T. J. Kippenberg. Optical frequency comb generation from a monolithic microresonator. *Nature* **450**, 1214 (2007).
- [91] P. Del’Haye, O. Arcizet, A. Schliesser, R. Holzwarth and T. J. Kippenberg. Full stabilization of a microresonator-based optical frequency comb. *Physical Review Letters* **101**, 053903 (2008).

- [92] T. J. Kippenberg, S. M. Spillane, D. K. Armani and K. J. Vahala. Ultralow-threshold microcavity raman laser on a microelectronic chip. *Optics Letters* **29**, 1224 (2004).
- [93] A. M. Armani, R. P. Kulkarni, S. E. Fraser, R. C. Flagan and K. J. Vahala. Label-free, single-molecule detection with optical microcavities. *Science* **317**, 783 (2007).
- [94] S. M. Spillane, T. J. Kippenberg, K. J. Vahala, K. W. Goh, E. Wilcut and H. J. Kimble. Ultrahigh-Q toroidal microresonators for cavity quantum electrodynamics. *Physical Review A* **71**, 013817 (2005).
- [95] T. Aoki, B. Dayan, E. Wilcut, W. P. Bowen, A. S. Parkins, T. J. Kippenberg, K. J. Vahala and H. J. Kimble. Observation of strong coupling between one atom and a monolithic microresonator. *Nature* **443**, 671 (2006).
- [96] B. Dayan, A. S. Parkins, T. Aoki, E. P. Ostby, K. J. Vahala and H. J. Kimble. A photon turnstile dynamically regulated by one atom. *Science* **319**, 1062 (2008).
- [97] A. N. Oraevsky. Whispering gallery waves. *Quantum Electronics* **32**, 377 (2002).
- [98] F. Treussart. *Etude expérimentale de l'effet laser dans des microsphères de silice dopées avec des ions néodyme*. Ph.D. thesis, Université Paris VI (1997).
- [99] M. L. Gorodetsky and A. E. Fomin. Geometrical theory of whispering-gallery modes. *IEEE Journal of Quantum Electronics* **12**, 33 (2006).
- [100] V. S. Ilchenko, M. L. Gorodetsky, X. S. Yao and L. Maleki. Microtorus: a high-finesse microcavity with whispering-gallery modes. *Optics Letters* **26**, 256 (2001).
- [101] M. Oxborrow. 2.5-d simulation of axi-symmetric electromagnetic structures. <http://www.npl.co.uk/science-technology/time-frequency/microwave-frequency-standards/research/2.5-d-simulation-of-axi-symmetric-electromagnetic-structures>.
- [102] S. Haroche and J.-M. Raimond. *Exploring the quantum: Atoms, Cavities, and Photons*. Oxford University Press (2006).
- [103] H. Walther, B. T. H. Varcoe, B.-G. Englert and T. Becker. Cavity quantum electrodynamics. *Reports on Progress in Physics* **69**, 1325 (2006).
- [104] J. T. Robinson, C. Manolatou, L. Chen and M. Lipson. Ultrasmall mode volumes in dielectric optical microcavities. *Physical Review Letters* **95**, 143901 (2005).
- [105] V. B. Braginsky, M. L. Gorodetsky and V. S. Ilchenko. Quality-factor and nonlinear properties of optical whispering-gallery modes. *Physics Letters A* **137**, 393 (1989).
- [106] J. C. Knight, G. Cheung, F. Jacques and T. A. Birks. Phase-matched excitation of whispering-gallery-mode resonances by a fiber taper. *Optics Letters* **22**, 1129 (1997).

-
- [107] S. M. Spillane, T. J. Kippenberg, O. J. Painter and K. J. Vahala. Ideality in a fiber-taper-coupled microresonator system for application to cavity quantum electrodynamics. *Physical Review Letters* **91**, 043902 (2003).
- [108] A. Abramovici et al. Improved sensitivity in a gravitational wave interferometer and implications for ligo. *Physics Letters A* **218**, 157 (1996).
- [109] Y. Hadjar, P.-F. Cohadon, C. G. Aminoff, M. Pinard and A. Heidmann. High-sensitivity optical measurement of mechanical brownian motion. *European Physics Letters* **47**, 545 (1999).
- [110] R. G. Knobel and A. N. Cleland. Nanometre-scale displacement sensing using a single electron transistor. *Nature* **424**, 291 (2003).
- [111] M. D. LaHaye, O. Buu, B. Camarota and K. C. Schwab. Approaching the quantum limit of a nanomechanical resonator. *Science* **304**, 74 (2004).
- [112] A. Naik, O. Buu, M. D. LaHaye, A. D. Armour, A. Clerk, M. P. Blencowe and K. C. Schwab. Cooling a nanomechanical resonator with quantum back-action. *Nature* **443**, 193 (2006).
- [113] N. E. Flowers-Jacobs, D. R. Schmidt and K. W. Lehnert. Intrinsic noise properties of atomic point contact displacement detectors. *Physical Review Letters* **98**, 096804 (2007).
- [114] C. A. Regal, J. D. Teufel and K. W. Lehnert. Measuring nanomechanical motion with a microwave cavity interferometer. *Nature Physics* **4**, 555 (2008).
- [115] S. Etaki, M. Poot, I. Mahboob, K. Onomitsu, H. Yamaguchi and H. S. J. van der Zant. Motion detection of a micromechanical resonator embedded in a d.c. SQUID. *Nature Physics* **4**, 785 (2008).
- [116] R. C. Dunn. Near-field scanning optical microscopy. *Chemical Reviews* **99**, 2891 (1999).
- [117] V. B. Braginsky and S. P. Vyatchanin. On the quantum-non-demolition measurement of the energy of optical quanta. In *Quantum Optics, Experimental Gravity, and Measurement Theory*. Plenum Press (1983).
- [118] M. M. Burns, J.-M. Fournier and J. A. Golovchenko. Optical binding. *Physical Review Letters* **63**, 1233 (1989).
- [119] M. M. Burns, J.-M. Fournier and J. A. Golovchenko. Optical matter: Crystallization and binding in intense optical fields. *Science* **249**, 749 (1990).
- [120] M. Povinelli, S. Johnson, M. Loncar, M. Ibanescu, E. Smythe, F. Capasso and J. Joannopoulos. High-Q enhancement of attractive and repulsive optical forces between coupled whispering-gallery- mode resonators. *Optics Express* **13**, 8286 (2005).

- [121] P. T. Rakich, M. A. Popović, M. Soljacić and E. Ippen. Trapping, corralling and spectral bonding of optical resonances through optically induced potentials. *Nature Photonics* **1**, 658 (2007).
- [122] M. Eichenfield, C. P. Michael, R. Perahia and O. Painter. Actuation of micro-optomechanical systems via cavity-enhanced optical dipole forces. *Nature Photonics* **1**, 416 (2007).
- [123] A. Ashkin. Acceleration and trapping of particles by radiation pressure. *Physical Review Letters* **24**, 156 (1970).
- [124] A. Ashkin. *Optical Trapping and Manipulation of Neutral Particles Using Lasers*. World Scientific, Singapore (2007).
- [125] T. W. Hänsch and A. L. Schawlow. Cooling of gases with laser radiation. *Optics Communications* **13**, 68 (1975).
- [126] D. Van Thourhout and J. Roels. Optomechanical device actuation through the optical gradient force. *Nature Photonics* **4**, 211 (2010).
- [127] M. Li, W. H. P. Pernice, C. Xiong, T. Baehr-Jones, M. Hochberg and H. X. Tang. Harnessing optical forces in integrated photonic circuits. *Nature* **456**, 480 (2008).
- [128] Q. P. Unterreithmeier, E. M. Weig and J. P. Kotthaus. Universal transduction scheme for nanomechanical systems based on dielectric forces. *Nature* **458**, 1001 (2009).
- [129] T. J. Kippenberg, S. M. Spillane and K. J. Vahala. Modal coupling in traveling-wave resonators. *Optics Letters* **27**, 1669 (2002).
- [130] J. G. E. Gardeniers, H. A. C. Tilmans and C. C. G. Visser. LPCVD silicon-rich silicon nitride films for applications in micromechanics, studied with statistical experimental design. *Journal of Vacuum Science & Technology A* **14**, 2879 (1996).
- [131] S. S. Verbridge, J. M. Parpia, R. B. Reichenbach, L. M. Bellan and H. G. Craighead. High quality factor resonance at room temperature with nanostrings under high tensile stress. *Journal of Applied Physics* **99**, 124304 (2006).
- [132] P. J. French, P. M. Sarro, R. Mollé, E. J. M. Fakkeldij and R. F. Wolffenbuttel. Optimization of a low-stress silicon nitride process for surface-micromachining applications. *Sensors and Actuators A* **58**, 149 (1997).
- [133] H. J. Lee, C. H. Henry, K. J. Orlowsky, R. F. Kazarinov and T. Y. Kometani. Refractive-index dispersion of phosphosilicate glass, thermal oxide, and silicon nitride films on silicon. *Applied Optics* **27**, 4104 (1988).
- [134] D. P. Poenar and R. F. Wolffenbuttel. Optical properties of thin-film silicon-compatible materials. *Appl. Opt.* **36**, 5122 (1997).

- [135] T. J. Kippenberg, S. M. Spillane and K. J. Vahala. Demonstration of ultra-high-Q small mode volume toroid microcavities on a chip. *Applied Physics Letters* **85**, 6113 (2004).
- [136] D. J. Wilson, C. A. Regal, S. B. Papp and H. J. Kimble. Cavity optomechanics with stoichiometric SiN films. *Physical Review Letters* **103**, 207204 (2009).
- [137] A. Mazzei, S. Götzinger, L. de S. Menezes, G. Zumofen, O. Benson and V. Sandoghdar. Controlled coupling of counterpropagating whispering-gallery modes by a single rayleigh scatterer: A classical problem in a quantum optical light. *Physical Review Letters* **99**, 173603 (2007).
- [138] T. J. Kippenberg, A. L. Tchebotareva, J. Kalkman, A. Polman and K. J. Vahala. Purcell-factor-enhanced scattering from si nanocrystals in an optical microcavity. *Physical Review Letters* **103**, 027406 (2009).
- [139] M. Pinard, Y. Hadjar and A. Heidmann. Effective mass in quantum effects of radiation pressure. *European Journal of Physics D* **7**, 107 (1999).
- [140] W. Weaver, S. P. Timoshenko and D. H. Young. *Vibration Problems in Engineering*. John Wiley and Sons (1990).
- [141] E. D. Black. An introduction to Pound–Drever–Hall laser frequency stabilization. *American Journal of Physics* **69**, 79 (2001).
- [142] A. Schliesser. *Cavity Optomechanics and Optical Frequency Comb Generation with Silica Whispering-Gallery-Mode Microresonators*. Ph.D. thesis, Ludwig-Maximilians Universität München (2009).
- [143] D. R. Southworth, R. A. Barton, S. S. Verbridge, B. Ilic, A. D. Fefferman, H. G. Craighead and J. M. Parpia. Stress and silicon nitride: A crack in the universal dissipation of glasses. *Physical Review Letters* **102**, 225503 (2009).
- [144] Q. P. Unterreithmeier, T. Faust and J. P. Kotthaus. Damping of nanomechanical resonators. *Physical Review Letters* **105**, 027205 (2010).
- [145] J. M. Dobrindt, I. Wilson-Rae and T. J. Kippenberg. Parametric normal-mode splitting in cavity optomechanics. *Physical Review Letters* **101**, 263602 (2008).
- [146] M. Zalalutdinov, A. Zehnder, A. Olkhovets, S. Turner, L. Sekaric, B. Ilic, D. Czaplewski, J. M. Parpia and H. G. Craighead. Autoparametric optical drive for micromechanical oscillators. *Applied Physics Letters* **79**, 695 (2001).
- [147] R. Rivière, S. Deléglise, S. Weis, E. Gavartin, O. Arcizet, A. Schliesser and T. J. Kippenberg. Optomechanical sideband cooling of a micromechanical oscillator close to the quantum ground state. *arXiv:1011.0290v1 [quant-ph]* (2010).

- [148] V. S. Ilchenko and M. L. Gorodetskii. Thermal nonlinear effects in optical whispering gallery microresonators. *Laser Physics* **2**, 1004 (1992).
- [149] T. Carmon, L. Yang and K. J. Vahala. Dynamical thermal behavior and thermal self-stability of microcavities. *Optics Express* **12**, 4742 (2004).
- [150] M. L. Gorodetsky and I. Grudinin. Fundamental thermal fluctuations in microspheres. *Journal of the Optical Society of America B* **21**, 697 (2004).
- [151] M. L. Gorodetsky and A. E. Fomin. Eigenfrequencies and Q factor in the geometrical theory of whispering-gallery modes. *Quantum Electronics* **37**, 167 (2007).
- [152] M. Li, W. H. P. Pernice and H. X. Tang. Broadband all-photonics transduction of nanocantilevers. *Nature Nanotechnology* **4**, 377 (2009).
- [153] N. Bansal and R. Doremus. *Handbook of glass properties*. Academic Press (1986).
- [154] D. B. Leviton and B. J. Frey. Temperature-dependent absolute refractive index measurements of synthetic fused silica. In *SPIE Astronomical Telescopes and Instruments Conference, 24-31 May 2006, Orlando, FL, United States* (2006).
- [155] S. S. Verbridge, H. G. Craighead and J. M. Parpia. A megahertz nanomechanical resonator with room temperature quality factor over a million. *Applied Physics Letters* **92**, 013112 (2008).
- [156] P. Verlot, A. Tavernarakis, T. Briant, P.-F. Cohadon and A. Heidmann. Scheme to probe optomechanical correlations between two optical beams down to the quantum level. *Physical Review Letters* **102**, 103601 (2009).
- [157] J. M. Dobrindt and T. J. Kippenberg. Theoretical analysis of mechanical displacement measurement using a multiple cavity mode transducer. *Physical Review Letters* **104**, 033901 (2010).
- [158] C. Zhao, L. Ju, Y. Fan, S. Gras, B. J. J. Slagmolen, H. Miao, P. BARRIGA, D. G. Blair, D. J. Hosken, A. F. Brooks, P. J. Veitch, D. Mudge and J. Munch. Observation of three-mode parametric interactions in long optical cavities. *Physical Review A* **78**, 023807 (2008).
- [159] D. S. Weiss, V. Sandoghdar, J. Hare, V. Lefèvre-Seguin, J.-M. Raimond and S. Haroche. Splitting of high-Q Mie modes induced by light backscattering in silica microspheres. *Optics Letters* **20**, 1835 (1995).
- [160] M. L. Gorodetsky, A. D. Pryamikov and V. S. Ilchenko. Rayleigh scattering in high-Q microspheres. *Journal of the Optical Society of America B* **17**, 1051 (2000).
- [161] W. Nagourney, J. Sandberg and H. Dehmelt. Shelved Optical Electron Amplifier: Observation of Quantum Jumps. *Physical Review Letters* **56**, 2797 (1986).

- [162] T. Sauter, W. Neuhauser, R. Blatt and P. E. Toschek. Observation of Quantum Jumps. *Physical Review Letters* **57**, 1696 (1986).
- [163] J. C. Bergquist, R. G. Hulet, W. M. Itano and D. J. Wineland. Observation of Quantum Jumps in a Single Atom. *Physical Review Letters* **57**, 1699 (1986).
- [164] S. Gleyzes, S. Kuhr, C. Guerlin, J. Bernu, S. Deléglise, U. B. Hoff, M. Brune, J.-M. Raimond and S. Haroche. Quantum jumps of light recording the birth and death of a photon in a cavity. *Nature* **446**, 297 (2006).
- [165] A. M. Jayich, J. C. Sankey, B. M. Zwickl, C. Yang, J. D. Thompson, S. M. Girvin, A. A. Clerk, F. Marquardt and J. Harris. Dispersive optomechanics: a membrane inside a cavity. *New Journal of Physics* **10**, 095008 (2008).
- [166] J. C. Sankey, C. Yang, B. M. Zwickl, A. M. Jayich and J. G. E. Harris. Strong and tunable nonlinear optomechanical coupling in a low-loss system. *Nature Physics* **6**, 707 (2010).
- [167] A. A. Clerk, F. Marquardt and J. G. E. Harris. Quantum measurement of phonon shot noise. *Physical Review Letters* **104**, 213603 (2010).
- [168] K. S. Novoselov, A. K. Geim, S. V. Morozov, D. Jiang, Y. Zhang, S. V. Dubonos, I. V. Grigorieva and A. A. Firsov. Electric field effect in atomically thin carbon films. *Science* **306**, 666 (2004).
- [169] K. S. Novoselov, D. Jiang, F. Schedin, T. J. Booth, V. V. Khotkevich, S. V. Morozov and A. K. Geim. Two-dimensional atomic crystals. *Proceedings of the National Academy of Sciences of the United States of America* **102**, 10451 (2005).
- [170] K. S. Novoselov, A. K. Geim, S. V. Morozov, D. Jiang, M. I. Katsnelson, I. V. Grigorieva, S. V. Dubonos and A. A. Firsov. Two-dimensional gas of massless Dirac fermions in graphene. *Nature* **438**, 197 (2005).
- [171] A. H. Castro Neto, F. Guinea, N. M. R. Peres, K. S. Novoselov and A. K. Geim. The electronic properties of graphene. *Reviews of Modern Physics* **81**, 109 (2009).
- [172] A. Balandin, S. Ghosh, W. Bao, I. Calizo, D. Teweldebrhan, F. Miao and C. N. Lau. Superior thermal conductivity of single-layer graphene. *Nano Letters* **8**, 902 (2008).
- [173] J. S. Bunch, A. M. van der Zande, S. S. Verbridge, I. W. Frank, D. M. Tanenbaum, J. M. Parpia, H. G. Craighead and P. L. McEuen. Electromechanical resonators from graphene sheets. *Science* **315**, 490 (2007).
- [174] D. Garcia-Sanchez, A. M. van der Zande, A. S. Paulo, B. Lassagne, P. L. McEuen and A. Bachtold. Imaging mechanical vibrations in suspended graphene sheets. *Nano Letters* **8**, 1399 (2008).

- [175] C. Lee, X. Wei, J. W. Kysar and J. Hone. Measurement of the elastic properties and intrinsic strength of monolayer graphene. *Science* **321**, 385 (2008).
- [176] A. K. Geim. Graphene: Status and Prospects. *Science* **324**, 1530 (2009).
- [177] J. S. Bunch, S. S. Verbridge, J. S. Alden, A. M. van der Zande, J. M. Parpia, H. G. Craighead and P. L. McEuen. Impermeable atomic membranes from graphene sheets. *Nano Letters* **8**, 2458 (2008).
- [178] C. Chen, S. Rosenblatt, K. I. Bolotin, W. Kalb, P. Kim, I. Kymissis, H. L. Stormer, T. F. Heinz and J. Hone. Performance of monolayer graphene nanomechanical resonators with electrical readout. *Nature Nanotechnology* **4**, 861 (2009).
- [179] A. K. Hüttel, G. A. Steele, B. Witkamp, M. Poot, L. P. Kouwenhoven and H. S. J. van der Zant. Carbon nanotubes as ultrahigh quality factor mechanical resonators. *Nano Letters* **9**, 2547 (2009).
- [180] A. C. Ferrari, J. C. Meyer, V. Scardaci, C. Casiraghi, M. Lazzeri, F. Mauri, S. Piscanec, D. Jiang, K. S. Novoselov, S. Roth and A. K. Geim. Raman spectrum of graphene and graphene layers. *Physical Review Letters* **97**, 187401 (2006).
- [181] R. R. Nair, P. Blake, A. N. Grigorenko, K. S. Novoselov, T. J. Booth, T. Stauber, N. M. R. Peres and A. K. Geim. Fine Structure Constant Defines Visual Transparency of Graphene. *Science* **320**, 1308 (2008).
- [182] A. B. Kuzmenko, E. van Heumen, F. Carbone and D. van der Marel. Universal optical conductance of graphite. *Physical Review Letters* **100**, 117401 (2008).
- [183] T. Hänsch and B. Couillaud. Laser frequency stabilization by polarization spectroscopy of a reflecting reference cavity. *Optics Communications* **35**, 441 (1980).
- [184] J. R. Clark, W.-T. Hsu, M. A. Abdelmoneum and C. T.-C. Nguyen. High-Q UHF micromechanical radial-contour mode disk resonators. *Journal of Microelectromechanical Systems* **14**, 1298 (2005).
- [185] A. N. Cleland. *Foundations of Nanomechanics*. Springer (2003).
- [186] F. R. Blom, S. Bouwstra, M. Elwenspoek and J. H. J. Fluitman. Dependence of the quality factor of micromachined silicon beam resonators on pressure and geometry. *Journal of Vacuum Science and Technology B* **10**, 19 (1992).
- [187] L. D. Landau and E. M. Lifshitz. *Fluid Mechanics, Volume 6 (Course of Theoretical Physics)*. Butterworth-Heinemann (1987).
- [188] I. Wilson-Rae. Intrinsic dissipation in nanomechanical resonators due to phonon tunneling. *Physical Review B* **77**, 245418 (2008).

- [189] V. B. Braginsky, V. P. Mitrofanov and K. V. Tokmakov. Energy dissipation in the pendulum mode of the test mass suspension of a gravitational wave antenna. *Physics Letters A* **218**, 164 (1996).
- [190] P. Willems, V. Sannibale, J. Weel and V. Mitrofanov. Investigations of the dynamics and mechanical dissipation of a fused silica suspension. *Physics Letters A* **297**, 37 (2002).
- [191] S. Gossler. *The GEO 600 suspension system*. Ph.D. thesis, Universität Hannover (2004).
- [192] C. T.-C. Nguyen. Mems technology for timing and frequency control. *IEEE transactions on ultrasonics, ferroelectrics, and frequency control* **54**, 251 (2007).
- [193] M. A. Abdelmoneum, M. U. Demirci and C. T.-C. Nguyen. Stemless wine-glass-mode disk micromechanical resonators. In *Proceedings of the 16th IEEE International MEMS Conference, Kyoto, Japan, Jan. 19-23* (2003).
- [194] G. D. Cole, I. Wilson-Rae, K. Werbach, M. Vanner and M. Aspelmeyer. Minimization of phonon tunneling dissipation in mechanical resonators. *arXiv: 1007.4948* (2010).
- [195] R. O. Pohl, X. Liu and E. Thompson. Low-temperature thermal conductivity and acoustic attenuation in amorphous solids. *Reviews of Modern Physics* **74**, 991 (2002).
- [196] P. W. Anderson, B. I. Halperin and C. M. Varma. Anomalous low-temperature thermal properties of glasses and spin glasses. *Philosophical Magazine* **25**, 1 (1972).
- [197] W. A. Phillips. Tunneling states in amorphous solids. *Journal of Low Temperature Physics* **7**, 351 (1972).
- [198] J. Jäckle. On the ultrasonic attenuation in glasses at low temperatures. *Zeitschrift für Physik A* **257**, 212 (1972).
- [199] J. Jäckle, L. Piché, W. Arnold and S. Hunklinger. Elastic effects of structural relaxation in glasses at low temperatures. *Journal of Non-Crystalline Solids* **20**, 365 (1976).
- [200] K. S. Gilroy and W. A. Phillips. An asymmetric double-well potential model for structural relaxation processes in amorphous materials. *Philosophic Magazine B* **43**, 735 (1981).
- [201] D. Tielbörger, R. Merz, R. Ehrenfels and S. Hunklinger. Thermally activated relaxation processes in vitreous silica: An investigation by Brillouin scattering at high pressures. *Physical Review B* **45**, 2750 (1992).
- [202] R. Vacher, E. Courtens and M. Foret. Anharmonic versus relaxational sound damping in glasses. II. Vitreous silica. *Physical Review B* **72**, 214205 (2005).

- [203] C. Zener. Internal friction in solids I. *Physical Review* **52**, 230 (1937).
- [204] C. Zener. Internal friction in solids II. *Physical Review* **53**, 90 (1938).
- [205] R. Lifshitz and M. L. Roukes. Thermoelastic damping in micro- and nanomechanical systems. *Physical Review B* **61**, 5600 (2000).
- [206] B. H. Houston, D. M. Photiadis, M. H. Marcus, J. a. Bucaro, X. Liu and J. F. Vignola. Thermoelastic loss in microscale oscillators. *Applied Physics Letters* **80**, 1300 (2002).
- [207] A. Duwel, J. Gorman, M. Weinstein, J. Borenstein and P. Ward. Experimental study of thermoelastic damping in MEMS gyros. *Sensors and Actuators A* **103**, 70 (2003).
- [208] A. Duwel, R. N. Candler, T. W. Kenny and M. Varghese. Engineering MEMS Resonators with low thermoelastic damping. *Journal of Microelectromechanical Systems* **15**, 1057 (2006).
- [209] A. I. Akhiezer. On the sound absorption in solids. *Journal of Physics (USSR)* **1**, 277 (1939).
- [210] V. B. Braginsky, V. P. Mitrofanov and V. I. Panov. *Systems with small dissipation*. The University of Chicago Press (1985).
- [211] E. Rat, M. Foret, G. Massiera, R. Violla, M. Arai, R. Vacher and E. Courtens. Anharmonic versus relaxational sound damping in glasses. I. Brillouin scattering from densified silica. *Physical Review B* **72**, 214204 (2005).
- [212] J. Hasson and A. Many. Observation of Akhiezer and Landau-Rumer Regimes in the Frequency Dependence of Shear-Wave Lattice Attenuation in CdS. *Physical Review Letters* **35**, 792 (1975).
- [213] H. Rokhsari, T. J. Kippenberg, T. Carmon and K. J. Vahala. Theoretical and experimental study of radiation pressure-induced mechanical oscillations (parametric instability) in optical microcavities. *IEEE Journal of Selected Topics in Quantum Electronics* **12**, 96 (2006).
- [214] G. S. Wiederhecker, L. Chen, A. Gondarenko and M. Lipson. Controlling photonic structures using optical forces. *Nature* **462**, 633 (2009).
- [215] J. Rosenberg, Q. Lin and O. Painter. Static and dynamic wavelength routing via the gradient optical force. *Nature Photonics* **3**, 478 (2009).
- [216] J. E.-Y. Lee and A. A. Seshia. 5.4-MHz single-crystal silicon wine glass mode disk resonator with quality factor of 2 million. *Sensors and Actuators A* **156**, 28 (2009).
- [217] C. Enss and S. Hunklinger. *Low-temperature physics*. Springer (2005).

Danksagung

Ich möchte mich zuvorderst bei Prof. Tobias Kippenberg bedanken, dass er diese Arbeit mit all seiner Tatkraft und Energie unterstützt und durch seine Intuition immer wieder entscheidend vorangebracht hat. Zudem bedanke ich mich für seine großzügige Unterstützung der unzähligen Konferenzbesuche und seine Erreichbarkeit zu sämtlichen Tages- und Nachtzeiten.

Ich möchte mich auch ganz herzlich bei Prof. Theodor Hänsch bedanken, dass er die Betreuung dieser Arbeit übernommen und dabei die Infrastruktur seiner Arbeitsgruppe bereitgestellt sowie größtmögliche Freiheiten gewährt hat.

Prof. Jörg Kotthaus gebührt mein besonderer Dank für das Initiieren des Nahfeld-Experiments und das große Interesse, das er dieser Arbeit gewidmet hat. Durch seine Initiative wurde der Hauptteil dieser Doktorarbeit überhaupt erst ermöglicht.

Darüberhinaus bedanke ich mich bei Olivier Arcizet, der durch sein experimentelles Können und seinen tiefen theoretischen Sachverstand die Projekte stets voranbrachte und zudem immer für positive Stimmung sorgte.

Zudem danke ich Eva Weig, dass sie das Nahfeld Projekt mitgetragen und unterstützt hat. Ich danke Albert Schliesser, der mich in das Forschungsgebiet eingeführt hat und sich dabei immer Zeit für Fragen und Diskussionen aller Art nahm.

Zudem danke ich Rémi Rivière, dessen Gewandtheit experimentelle Schwierigkeiten oft mit großer Leichtigkeit beseitigte und damit unter anderem für das Gelingen der erstmaligen Herstellung der Speichenproben sorgte.

Emanuel Gavartin und Quirin Unterreithmeier gebührt ein großes Dankeschön für die kompetente Fabrikation der Nanosaiten.

Ich bedanke mich bei Ignacio Wilson-Rae für fruchtbare Diskussionen über mechanische Dissipation.

Vielen Dank auch an Xiaoqing Zhou, Bastian Schröter, Jens Dobrindt, Pascal Del'Haye, Rui Ma, Tobias Herr, Stefan Weis, Christine Wang und Samuel Deléglise für das meist äußerst angenehme Arbeitsklima und die hilfsbereite Zusammenarbeit.

Zudem danke ich Michael Gorodetsky für das Interesse für die Nahfeld Experimente und die fruchtbare Zusammenarbeit.

Ich danke auch Pierre Verlot, der sich von den Nahfeld Experimenten überzeugen ließ und diese nun weiterführen wird.

Mein Dank gebührt auch Markus Schenk, Alexander Kubanek, Holger Specht, Katharina Predehl und Birgitta Bernhardt für das nette Miteinander am MPQ, technische Hilfe mit

dem MBR Laser System und die gemeinsamen Konferenzreisen.

Ich bedanke mich zudem bei den Sportlern vom SV MPQ Quantenkick, die in unzähligen Matches am Campus enorm zum Freizeitwert am MPQ beitrugen.

Helmut Brückner, Karl Linner und ganz besonders Wolfgang Simon, der für jedes noch so vertrackte Problem immer eine schnelle Lösung parat hat, danke ich für Ihre stets zügige und kompetente Hilfe bei technischen Anliegen aller Art. Auch Philipp Altpeter gilt mein Dank für die Unterstützung im Reinraum.

Ich danke Christina Becker für Ihre stete Unterstützung mit Herzblut. Mein Dank gebührt auch Ingrid Hermann, Gabriele Gschwendtner, Patricia Marti-Rochat und der leider viel zu früh verstorbenen Rosemarie Lechner, die stets ein offenes Ohr hatten. Zudem danke ich allen Mitarbeitern am MPQ und an der LMU, die durch ihren oft großen Einsatz das Gelingen dieser Arbeit ermöglicht haben.

Auch möchte ich mich an dieser Stelle bei Prof. Gerhard Buchalla und Prof. Heinrich Steinlein für ihre Unterstützung während meines Studiums bedanken.

Der größte Dank aber gilt meiner Familie, insbesondere meinen Eltern, meinen Großeltern, der Familie Carzburg und Aida Nurispahić, die mich in all den Jahren stets unterstützt und mir zudem viel Freiraum ermöglicht haben, auch wenn die gemeinsame Zeit oft knapp war.